

Effect of Cellulose Nanofibrils on Some Common Durability Issues of Cement-Based Systems

by

Jose Roberto Albuquerque Goncalves

A thesis submitted in partial fulfillment of the requirements for the degree of

Doctor of Philosophy

in

Structural Engineering

Department of Civil and Environmental Engineering
University of Alberta

© Jose Roberto Albuquerque Goncalves, 2019

ABSTRACT

The most common detrimental processes that lead to reduction in durability in reinforced concrete elements are shrinkage, sulphate attack and chloride attack. Shrinkage is a dimensional instability chiefly caused by a loss of moisture in the hydrating cement paste. Soluble sulphate ions take part in ettringite-induced expansive reactions in concrete, while chloride ions trigger the corrosion process in embedded steel reinforcement.

Cellulose nanofibrils (CNFs) possess unique characteristics, including hydrophilicity, nano-dimensions, and excellent chemical tunability. These features confer upon CNF the ability to control internal moisture movement and also mitigate the ingress of harmful agents, including sulphate and chloride ions, into the cementitious system. A thorough review of the literature confirms that the proposed study is a novel scientific approach.

This study explores the feasibility and demonstrates successfully the ability of CNF to address these three durability concerns. Three types of CNFs were used in the study, each one with a distinct amount of carboxylate grafted upon the fibre surface. The CNF was incorporated in cement-based paste and mortar mixtures at various volume fractions. The mixtures were cast to the same workability and water-to-cement ratio, and the mortars had a fixed cement-aggregate ratio.

Results show that adding CNF moderately increased the shrinkage as measured at 2-days using image analysis. Similar growth in the drying shrinkage was observed in 90-day trials performed according to ASTM C596. However, CNF additions significantly alleviated bleeding and the

shrinkage behavior was strongly influenced by CNF's ability to retain water in the early hours of hydration. Further evidence from the gas-sorption analyses reveals that this water accumulated in fresh mixtures due to CNF led to a larger volume of capillary pores and an increase mainly in the pore gel phase. As seen in the long-term trials, when this cumulative water was lost, there was a rise in shrinkage. This study reveals a retardation in hydration upon adding CNF. However, the samples containing CNF uniformly showed less cracking, which is likely due to fibres bridging the micro- and nano-cracks.

The mortars mixtures when dosed with CNF uniformly exhibited noticeable reduction in the ingress of sulphates ions and again, for chlorides ions. Under sulphate exposure, the CNF visibly reduced the penetration of sulphate ions and effected a marked reduction in ettringite as well as the associated ettringite-induced expansion, measured as per ASTM C1012/C1012M. The decrease in the ettringite content (as measured by X-ray analysis) in the CNF-loaded Type GU Portland cement paste mixtures even after 90 days in sulphate solution was comparable to that seen with Type HS Portland cement. At the same time, the compressive strength of CNF-cement mortars was enhanced. Similar improvement was observed in the resistance of mortars loaded with CNF against chlorides ion ingress, as substantiated by the results of the rapid chloride penetrability test (as described in ASTM C1202) and the silver nitrate-based colorimetric method.

The performance verified here can be credited to physical and chemical mechanisms triggered by CNF. Despite a slight increase in the capillary pores ranging from 100 nm – 10 µm as seen from the analysis of SEM images, the porosity in the range of 10 nm to 140 nm was moderately reduced as increasingly amounts of CNF were added to cement pastes. As a result, the pore network in this

range experienced a rise in the tortuosity and a reduction in the connectivity, which ultimately hindered the ingress of sulphate ions and chloride ions. Concurrently, the negatively charged ionic groups of CNF chemically scavenged some of the calcium cations soluble in the aqueous phase (as evident from the thermogravimetric analysis), which are essential to the ettringite phase formation. This further explains why CNF loadings slowed down the ettringite content. However, the pH of CNF-cement pastes remained unaltered, notwithstanding the reduction in the calcium content in the pore solution. It is safe to say that CNF will not break the protective passive film of the embedded steel bars. The results show CNF as an all-round promising additive to hamper the ingress of deleterious agents in cement-based systems.

PREFACE

This thesis is an original work of Jose Roberto Albuquerque Goncalves. The CNF gels containing 1 wt.% of cellulose nanofibres with carboxylate content of 0.7 mmol/g of fibre and containing 3 wt.% of cellulose nanofibres with 1.13 mmol of carboxylate/g of fibre used in the current study (see CHAPTER 3) were developed at the University of Alberta and manufactured at the InnoTech Alberta facilities by Dr. M. El-Bakkari, who was Dr. Vivek Bindiganavile's post-doctoral fellow.

No part of the thesis has been previously published, except by two matters. The cracking area data reported in Section 5.4.1 of CHAPTER 5 was published as El Bakkari, M., Bindiganavile, V., Goncalves, J., & Boluk, Y. (2019). Preparation of cellulose nanofibers by tempo-oxidation of bleached chemi-thermomechanical pulp for cement applications. *Carbohydrate polymers*, 203, 238-245. In this regard, I was accountable for the research design, testing, data collection and analysis. Dr. M. El-Bakkari prepared the manuscript, which was edited by Dr. V. Bindiganavile and Dr. Y. Boluk. And the sulphate attack behavior of mixtures containing CNF #0.13, as described in CHAPTER 6, was published as the following reference: Goncalves, J., El-Bakkari, M., Boluk, Y., & Bindiganavile, V. (2019). Cellulose nanofibres (CNF) for sulphate resistance in cement-based systems. *Cement and Concrete Composites*. 99, 100-111. I was responsible for the design of the pH analysis research program besides the development of the mixtures, performance of experiments, data collection, data analysis and manuscript composition. Dr. V. Bindiganavile delineated the sulphate-attack research program and edited the manuscript. Dr. Y. Boluk also contributed to manuscript edits and design of the CNF gel manufacturing program, which was implement and developed by Dr. M. El-Bakkari.

Dr. V. Bindiganavile, Dr. Y. Boluk, Dr. C. Cruz Noguez, and Dr. D. Panesar (from the University of Toronto) also contributed to review the manuscript of the current thesis.

ACKNOWLEDGEMENTS

First of all, I have to express my sincere gratitude to my supervisor, Dr. V. Bindiganavile, for his expertise in cement-based systems, guidance and encouragement over the whole course, as he conducted me to successfully complete my research and my PhD course. I extend my thanks to Dr. Y. Boluk, my co-supervisor, for giving me the opportunity to learn a little bit of his invaluable know-how, particularly about nanocellulose fibres and rheology. I would like to acknowledge the University of Alberta, InnoTech Alberta, and National Institute of Nanotechnology for providing me their updated research facilities to develop my research. This acknowledgment also extends to the support given by Dr. D. M. Naveiros (in memoriam), Dr. F. C. Rizzo (both from the National Institute of Technology in Brazil), and to the sponsorship given by Dr. R. Kennedy (LeHigh Hanson Cement), Dr. S. Lord (Millar Western) and Dr. B. Ahvazi (InnoTech Alberta).

The completion of this research program was feasible thanks to the technical support provided by the staff of several laboratories at the University of Alberta, as follows: (i) Mr. R. Mariano deserves my first and especial thanks due to his technical support during the specimen preparation and durability testing carried out at the Concrete Laboratory; (ii) Dr. M. El-Bakkari, my supervisor's post-doctoral fellow, for the knowledge on cellulose nanofibres preparation; (iii) Mr. D. Zhao for assisting me during the sulphate content analysis at the Environmental Laboratory; (iv) Dr. M. Secanell for authorizing me to operate the environmental chamber at Energy System Design Laboratory to conduct my experiments; (v) Mr. M. Labbe, from the Thin Section Laboratory, for specimen preparation to the back-scattered electron microscopy analysis; (vi) Dr. N. Gerein, from Scanning Electron Microscopy Lab, for his outstanding assistance with the SEM micrographs used for pore size distribution analysis; (vii) Dr. N. Zhang (NanoFAB) for training me on B.E.T. theory

and the Autosorb Quantachrome 1Mp operation; (viii) Mrs. Mihaela Istratescu, Lab Coordinator of the Enhanced of Oil and Gas Recovery and Characterization Research Group, for allowing me to use the 1,000°C furnace; (ix) Dr. J. Trivedi (School of Mining and Petroleum Engineering) for giving access to the Petroleum Laboratory to expose the specimens to the environmental chamber; and ultimately (x) Mr. G. Miller and Mr. C. West, technicians of the I. F. Morrison Structural Laboratory, for the technical support and training in various lab equipment used to extract samples for sulphate content analysis and prepare the mortar specimens for chloride diffusivity trials. I am thankful to my colleagues Mr. C. Yi, Mr. C. Ou, Mr. D. Orozco, Ms C. Gu, and Ms H. Al Shereida for taking part in this PhD research project. My thanks are also addressed to the National Institute of Nanotechnology, in the persons of: (i) Dr. S. Launspach, Senior Technical Officer in X-Ray Diffraction Lab, by his first-class services and by lending me his outstanding expertise for accomplishing the crystallography analysis of my samples; and (ii) Dr. M. Xia, Supervisor at the Organic and Inorganic Synthesis Lab, for the training me to operate the TGA Q50.

This acknowledgement would be incomplete without expressing my unconditional gratitude to my dear wife, Renata Amerio Goncalves, for her emotional support, patience during the toughest moments, and encouragement in pursuing my dreams, who I formally share this conquest; as well as to my children, Felipe Amerio Albuquerque Goncalves and Victoria Amerio Albuquerque Goncalves, for understanding my temporary absence of their lives during the doctoral program period, in spite of my efforts in contrary. To finish, my fuller appreciation to my beloved parents (in memoriam), Iris Albuquerque Goncalves and Aluisio Goncalves, for all guidance, hearting, teaching, and being the motivating force during my life.

TABLE OF CONTENTS

ABSTRACT	ii
PREFACE	v
ACKNOWLEDGEMENTS	vii
TABLE OF CONTENTS	ix
LIST OF TABLES	xiv
LIST OF FIGURES	xvii
LIST OF ABBREVIATIONS	xxviii
CHAPTER 1. Introduction	1
1.1. Background	1
1.2. Problem Statement	3
1.3. Hypothesis	5
1.4. Objectives	5
1.5. Research Significance	6
1.6. Scope	6
1.7. Organization	9
CHAPTER 2. Literature review	11
2.1. Introduction	11
2.2. Durability of Cement-Based Systems	11
2.2.1. Shrinkage Mechanism	12
2.2.1.1. Plastic Shrinkage.....	12
2.2.1.2. Drying Shrinkage	14
2.2.1.3. Other Forms of Shrinkage.....	17
2.2.2. Sulphate Attack Mechanism	19
2.2.2.1. Sources of Sulphate.....	19
2.2.2.2. Classical Ettringite Formation	20
2.2.2.3. Delayed Ettringite Formation (DEF)	24
2.2.2.4. Salt Hydration Formation	24
2.2.2.5. Sulphate-Related Expansive Reactions.....	25
2.2.3. Chloride Attack Mechanism	27

2.2.3.1. Corrosion in Reinforced Concrete	27
2.2.3.2. Passivation Phenomenon	30
2.2.3.3. Source and Transport of Chloride.....	31
2.2.3.4. Chloride-Induced Corrosion	34
2.3. Nanomaterials in Cement-Based Systems	36
2.4. Cellulose Nanomaterials	39
2.5. Cellulose Nanofibres	44
2.6. Cellulose Nanofibres in Cement-Based Systems	49
2.6.1. Mix Proportions	51
2.6.2. Fresh Properties	53
2.6.2.1. Setting time	53
2.6.2.2. Workability	54
2.6.2.3. Rheology	54
2.6.3. Hardened Properties.....	55
2.6.3.1. Compressive strength.....	55
2.6.3.2. Tensile strength.....	56
2.6.3.3. Flexural strength, toughness and fracture energy	56
2.6.3.4. Thermal properties	58
2.6.4. Durability.....	58
2.6.4.1. Decaying of cellulose nanofibres in alkaline environments	58
2.6.4.2. Shrinkage	59
2.6.5. Degree of hydration	59
2.7. Concluding Remarks	60
CHAPTER 3. Mix Design	61
3.1. Introduction.....	61
3.2. Raw Materials	62
3.2.1. CNF	62
3.2.2. Portland Cement	66
3.2.3. Other Materials.....	68
3.3. CNF-based Cement Mortar Mixtures.....	69
3.4. CNF-based Cement Paste Mixtures	77

3.5. Concluding Remarks	81
CHAPTER 4. Microstructure of CNF-based Cement Pastes.....	83
4.1. Introduction.....	83
4.2. Degree of Hydration	83
4.2.1. Introduction.....	83
4.2.2. Experimental Procedure	85
4.2.3. Results and Discussion.....	90
4.3. Porosimetry Analysis.....	95
4.3.1. Gas Sorption Analysis.....	95
4.3.1.1. Introduction.....	95
4.3.1.2. Experimental Procedure.....	97
4.3.1.3. Results and Discussion	100
4.3.2. Scanning Electron Microscope (SEM) Image Analysis.....	104
4.3.2.1. Introduction.....	104
4.3.2.2. Experimental Procedure.....	106
4.3.2.3. Results and Discussion	109
4.4. Mineralogical Analysis	113
4.4.1. Introduction.....	113
4.4.2. Experimental Procedure	114
4.4.3. Results and Discussion.....	115
4.5. Concluding Remarks	116
CHAPTER 5. Shrinkage in CNF-based Cement Pastes	118
5.1. Introduction.....	118
5.2. Overall Shrinkage	119
5.2.1. Introduction.....	119
5.2.2. Experimental Procedure	120
5.2.3. Results and Discussion.....	123
5.3. Drying Shrinkage.....	127
5.3.1. Experimental Procedure	127
5.3.2. Results and Discussion.....	128
5.4. Further Investigations	132

5.4.1. Cracking Analysis	132
5.4.1.1. Experimental Procedure.....	132
5.4.1.2. Results and Discussion	134
5.4.2. Bleeding.....	136
5.4.2.1. Standard Test Method.....	139
5.4.2.1.1. <i>Experimental Procedure</i>	139
5.4.2.1.2. <i>Results and Discussion</i>	140
5.4.2.2. Turbiscanner Analysis	143
5.4.2.2.1. <i>Experimental Procedure</i>	143
5.4.2.2.2. <i>Results and Discussion</i>	145
5.4.3. Evaporation Rate	150
5.4.3.1. Experimental Procedure.....	150
5.4.3.2. Results and Discussion	153
5.5. Concluding Remarks	159
CHAPTER 6. Sulphate Attack in CNF-based Cement Mortars.....	162
6.1. Introduction.....	162
6.2. Sulphate Penetration	165
6.2.1. Experimental Procedure	165
6.2.2. Results and Discussion.....	168
6.3. Linear Dimensional Change.....	175
6.3.1. Experimental Procedure	175
6.3.2. Results and Discussion.....	177
6.4. Further Investigations	184
6.4.1. Relative Content of Ettringite.....	185
6.4.1.1. Introduction.....	185
6.4.1.2. Experimental Procedure.....	185
6.4.1.3. Results and Discussion	188
6.4.2. Portlandite Content	191
6.4.2.1. Introduction.....	191
6.4.2.2. Experimental Procedure.....	193
6.4.2.3. Results and Discussion	194

6.4.3. Evaluating the pH	199
6.4.3.1. Introduction.....	199
6.4.3.2. Experimental Procedure.....	201
6.4.3.3. Results and Discussion	203
6.4.4. Compressive Strength Analysis	205
6.4.4.1. Introduction.....	205
6.4.4.2. Experimental Procedure.....	207
6.4.4.3. Results and Discussion	207
6.5. Concluding Remarks	210
CHAPTER 7. Chloride Penetration in CNF-based Cement Mortars	213
7.1. Introduction	213
7.2. Experimental Procedures	217
7.2.1. Materials, Mix Proportions and Specimens	217
7.2.2. Rapid Chloride-Ion Permeability Method	219
7.2.3. Silver Nitrate-Based Colorimetric Method	221
7.3. Results and Discussion	224
7.4. Concluding Remarks	230
CHAPTER 8. Conclusions and Recommendations	232
8.1. Summary of the Findings	232
8.2. Applications of the Findings	235
8.3. Recommendations for Further Studies	236
REFERENCES	238
APPENDIX	262

LIST OF TABLES

Table 2.1	Chemical composition of some wood and non-wood cellulose-containing sources [Khalil et al., 2012]:.....	42
Table 2.2	Succinct comparison between CNF and CNC [⁽¹⁾ Saito et al., 2007; ⁽²⁾ Xu et al. 2013; ⁽³⁾ Boluk et al. 2014; ⁽⁴⁾ Sofla et al. 2016; ⁽⁵⁾ Fu et al., 2017; ⁽⁶⁾ Nasir et al., 2017]......	42
Table 2.3	Some characteristics of the CNs [⁽¹⁾ Saito et al., 2007; ⁽²⁾ Eichhorn et al., 2010; ⁽³⁾ Boluk et al., 2014; ⁽⁴⁾ Fu et al., 2017; ⁽⁵⁾ Nasir et al., 2017; ⁽⁶⁾ Hisseine et al., 2018; ⁽⁷⁾ Barhoum et al., 2018]	43
Table 2.4	Tensile strength and Young’s modulus of CNF films according to various authors.	49
Table 3.1	Some characteristics of the CNFs.....	65
Table 3.2	Physical and chemical characteristics of the cements, and their mineral composition. The relevant chemical elements for sulphate attack are in bold. Data provided by Lehigh Hanson.	67
Table 3.3	Mix proportions of the GU-cement mortars containing different CNF loadings.	71
Table 3.4	Mix proportion of the HS-cement mortars, HE-cement mortars and GUb-cement mortars containing different CNF #0.13 fractions.....	74
Table 3.5	Procedure for mixing the control cement mortar and the CNF-based cement mortars.	74
Table 3.6.	The minimum stirring speeds [r.p.m.] assumed to dilute CNF gel in mixing water.	74
Table 3.7	Absorption, density and voids of the CNF #0.13-based GU cement hardened mortars.	75
Table 3.8	Compressive strength at 28 days of mortars mixed with various cement types and CNF #0.13 ranges.	75
Table 3.9	Procedure for mixing the control cement paste and the CNF-based cement pastes.	78
Table 3.10	Mix proportions of the GU-cement pastes containing different CNF fractions.	79

Table 5.1	Efficiency of each CNF #1.13 fraction in mitigating the cracking caused by shrinkage.....	135
Table 5.2	Mix proportions of cement pastes incorporating various CNF #1.13 loadings and no superplasticizer and 1.2% CNF #1.13-cement pastes with increments in superplasticizers dosages.....	138
Table 5.3	Environmental exposures.	151
Table A.1	Superplasticizer dosage and flow of the CNF-based cement mortars.	262
Table A.2	Superplasticizer dosage and flow of the CNF-based cement pastes.....	262
Table A.3	Plastic shrinkage of CNF-based cement pastes exposed to a severe environment.	262
Table A.4	Drying shrinkage for 12 weeks of CNF-based cement pastes with growing CNF fractions.	263
Table A.5	Cracking analysis of the cement pastes with CNF #1.13 loadings.....	263
Table A.6	Bleeding of CNF-based cement pastes as per ASTM C232/C232M [ASTM, 2014].....	264
Table A.7	Bleeding of CNF-cement pastes with and without superplasticizer as per Turbiscan [®] analysis.	264
Table A.8	Bleeding of cement pastes containing a fixed amount of 1.2 vol.% CNF #1.13 and variable quantities of superplasticizer as per Turbiscan [®] analysis.	265
Table A.9	Bleeding rate (BR) and evaporation rate (ER) of the control paste and CNF-based cement pastes with and without SP exposed to a different period of severe environment.	265
Table A.10	Evaporation rate of the volatile raw materials used to prepare the CNF-based cement pastes exposed to mild environment (ME), severe environment (SE) and extreme environment (EE).....	265
Table A.11	Length change (LC) of CNF-based cement mortars after 12 weeks exposure in sulphate solution and the absolute LC (i.e. the LC in sulphate solution deducted from the LC in water). ‘Positive’ values mean expansion.....	266
Table A.12	Sulphate penetration in CNF-based cement pastes prepared with various binders after 8 and 12 weeks in sodium sulphate solution solution.	267

Table A.13	Relative ettringite content at different times of exposure in sodium sulphate, Na_2SO_4 , solution.	267
Table A.14	Contents of calcium hydroxide ($W_{Ca(OH)_2}$), calcium carbonate (W_{CaCO_3}) and calcium hydroxide corrected ($W_{Ca(OH)_2,corrected}$) with the calcium from calcium carbonate.....	267
Table A.15	Potential of hydrogen (pH) of the pore solution of CNF-based cement pastes.	268
Table A.16	Degree of hydration (DOH) of CNF-based pastes by the conventional method... ..	268
Table A.17	Accumulative porosity of CNF-based cement pastes by BSEM image analysis. .	268
Table A.18	Resistance of cement mortars containing various CNF fractions and different CNF types to chloride ion penetration measured by RCPT and by colorimetric methods.....	269

LIST OF FIGURES

Figure 2.1	Backscattered electron images show the morphology of (a) ettringite needles (left side), the platy shape of portlandite (at centre-right) and (b) the foil-like mixed with bundles of <i>C – S – H</i> fibres. Reprinted from Figs. 174 and 175 published in Walker et al. [2006] (p. 223).	23
Figure 2.2	Loss of cohesion, delamination and fragmentation observed at the top-end cylinder with the sides coated with epoxy resin after being submitted to Na_2SO_4 solution for one year.	26
Figure 2.3.	(a) TEM image showing the rod-like particles of CNC. Reprinted from Fig. 1 published in Boluk et al. [2014] (p. 4). (b) Illustration of the ‘short circuit diffusion’ mechanism. Reprinted from Fig. 12.b published in Cao et al. [2015] (p. 81). (c) Sketch of the CNF and the CNC bridging microcracks in a polymeric matrix. Reprinted from Fig. 15 published in Xu et al. [2013] (p. 3006).	43
Figure 2.4	Flow illustrating the cellulose raw materials and the main stages in the manufacture of cellulosic nanoparticles.	44
Figure 2.5	Hierarchical structure from lignocellulosic plant-based biomass to CNF, and its respective dimensional features. Adapted from Fig. 1 published in Isogai et al. [2011] (p. 72).	46
Figure 2.6	TEMPO CNF in water suspension shown on two scales: (a) the gel-like aspect in a macroscopic view; and (b) the individualized nanofibres and bundles of them (at the top) displayed in a SEM image. Reprinted from Fig. 4.a published in El-Bakkari et al. [2019] (p. 243).	47
Figure 2.7	Pockets of cellulose nanofibres in a cement paste dosed with 0.4 wt.% CNF shown by (a) an optical microscope micrograph, and (b) a SEM micrograph. Reprinted from Fig. 6.b and Fig. 6.c published in Onuaguluchi et al. [2014] (p. 123), respectively.	58
Figure 3.1	General view of the main steps used in CNF preparation. The (a) TEMPO pretreatment is applied to (b) BCMT pulp followed by (c) mild disintegration in the ‘supermasscolloider’, and finally (d) yielding CNF.	63
Figure 3.2	Visual images of the (a) CNF #0.13, (b) CNF #0.7, and (c) CNF #1.13.	64

Figure 3.3	SEM images of the (a) CNF #0.13 and (b) CNF #1.13.	64
Figure 3.4	View of the (a) pycnometer and (b) solid content system used in the CNF gel analysis.	65
Figure 3.5	The X-ray diffractograms of the oven-dry samples of CNF displayed an extensive amorphous phase for diffraction angles (2θ) between 5° and 30°	66
Figure 3.6	The grain size distribution of (a) the quartz sands #2075, #4075 and #7030, and (b) the optimized blend of these sands meeting the grading limits of ASTM C33/C33M [ASTM, 2015].	68
Figure 3.7	View of the flow table test apparatus used to determine the consistency of mortars.	69
Figure 3.8	Effect of CNF loadings on: (a) superplasticizer demand, (note: the insert text in red offers the reasons for the CNF limit); and (b) flow of CNF-based GU-cement mortars, showing the acceptable consistency limits in red dashed lines.	72
Figure 3.9	View of the (a) high-intensity mixer used to mix the mortars, and (b) stirring mixer utilized to pre-mix the CNF gel and mixing water.....	76
Figure 3.10	CNF #0.13 gel and mixing water (a) before and (b) after the mixing. And CNF #1.13 (c) before and (d) after the same procedure. In both cases, a homogeneous mixture is visually obtained.....	76
Figure 3.11	View of the superplasticizer (a) before and (b) after the manual mixing with around 1/3 of the CNF-mixing water pre-mixture.....	77
Figure 3.12	View of the (a) the 200 mL-volume flow cone apparatus, (b) 110 mL mark in the graduate tube, and (c) the mixer used as per ASTM C305 [ASTM, 2014]......	79
Figure 3.13	Effect of CNF loadings on: (a) superplasticizer demand, (note: the insert text in red offers the reasons for the CNF limit); and (b) flow of CNF-based GU-cement pastes, showing the acceptable consistency limits in red dashed line.	80
Figure 4.1	View of the sealed vials containing the 1-year paste samples.....	88
Figure 4.2	Removal of the evaporable water from pore structure of pastes by solvent exchange: (a) sample in isopropanol alcohol; and (b) vacuum aspirating the solvent at most from the sample. View of the sample (c) before and (d) after being vacuum aspirated.	89

Figure 4.3	View of (a) the oven used to dry, and (b) the furnace to ignite the samples. (c). View of the porcelain crucibles containing the ignited samples cooling down inside of the desiccator.	89
Figure 4.4	View of the thermal analyzer <i>TA Instruments TA Q50</i>	89
Figure 4.5	TGA and its respective DTG curves showing the weight and the temperature of the paste samples at the borders of the dehydration, dehydroxylation and decarbonation phases.	90
Figure 4.6.	(a) Degree of hydration (DOH) of cement pastes affected by a range of CNF loadings using LOI measurements based the furnace trials. (b). Same DOH shown in (a), but now, deducted by the bound water coming from the pre-hydrated cement and the CO ₂ of carbonated cement paste.	92
Figure 4.7	Degree of hydration (DOH) of cement pastes affected by a range of CNF loadings based on TGA data, which the initial temperature was (a) room temperature (RT), or (b) 105 °C.	93
Figure 4.8	Linear correlation between the DOH dataset of CNF #0.13- and CNF #1.13-based mixtures acquired by TGA and furnace-based methods.	93
Figure 4.9	Decomposition phases of hardened cement pastes by TGA: (a) dehydration starting at room temperature, 20 °C, and (b) at 105 °C; (c) dehydroxylation; and (d) decarbonation.	94
Figure 4.10	View of (a) the cutting machine used to slice the cylinder made of hardened CNF-based cement paste. View of (b) the cut slices and (c) the sandpapering process... ..	99
Figure 4.11	View of (a) the manual crushing of CNF-based cement pastes and the ground sample (b) during and (c) after the removal of free residual water thorough solvent exchange.	99
Figure 4.12	View of (a) the gas sorption analyser used, and (b) the adsorption-desorption isotherm of control paste. P/P_0 is the sample pressure-to-saturation pressure ratio of the adsorbed nitrogen.	100
Figure 4.13.	(a) Specific surface area (SSA), and (b) average pore size of cement pastes loaded with a range of fractions of CNF #0.13 and CNF #1.13. Both data were based on adsorption isotherms.	101

Figure 4.14	Pore size distribution (PSD) of (a) CNF #0.13- & (b) CNF #1.13-cement pastes based on desorption isotherms. Same plots limited to pore sizes less than (c),(d) 50 nm and (e),(f) 10 nm.....	102
Figure 4.15	Accumulated pore size distribution (PSD) of (a) CNF #0.13-cement pastes, and (b) CNF #1.13-cement pastes based on the desorption isotherms.....	103
Figure 4.16.	(a) Overall pore volume of CNF-based cement pastes. Pore volume less than (b) 50 nm in diameter and (c) 10 nm in diameter. Data based on desorption isotherms.....	103
Figure 4.17	View of the (a) cut slices; (b) cutting; (c) sample ready to be embedded in epoxy resin; (d) carbon coat machine; (e) ready-for-analysis sample; and (f) <i>Zeiss Sigma Field Emission SEM</i>	108
Figure 4.18	View of BES image (a) before and (b) after being processed by ‘Fiji’ program. .	109
Figure 4.19.	(a) Pore fraction and (b) accumulative porosity of cement pastes affected by a range of CNF #0.13 loadings. Accumulative porosity (c) less than and (d) greater than 10 nm in diameter.	111
Figure 4.20.	(a) Pore fraction and (b) accumulative porosity of cement pastes affected by a range of CNF #1.13 loadings. Accumulative porosity (c) less and (d) greater than 10 nm in diameter.	112
Figure 4.21	Porosity associated to different pore ranges of cement pastes affected by various doses of (a) CNF #0.13, and (b) CNF #1.13.....	113
Figure 4.22	View of (a) the SEM; (b) the cut slice; and (c) the crushed pieces of sample used in the SEM analysis. View of (d) the SEM sample holder ready to be inserted in SEM.	114
Figure 4.23	Sequence of SEM images increasing the magnification from 1 mm to 2 μ m.	115
Figure 4.24.	(a) Acicular ettringite [E] growing inside of a void. (b). Fibres of ettringite [E] and needle-like <i>C – S – H</i> [C] stacks in the middle of hydrated products of cement poorly crystallized. (c). Columns of hexagonal plates of the $Ca(OH)_2$ crystals [P]. And (d) growth of <i>C – S – H</i> [C] needles on the plate shape of $Ca(OH)_2$ [P].....	116
Figure 5.1	Some steps of the overall shrinkage experiment: (a) molds covered with wax paper; (b) ink marks to arrange the specimens and to measure the length change	

	(LC) at specimen surface; (c) instruments used to control the environmental conditions inside the chamber; and (d) apparatus to photograph the specimen surface.....	121
Figure 5.2	View of the chamber equipped with fan-forced heater at one end, which blows heated air into the compartment containing specimens used for overall shrinkage and evaporation rate.....	122
Figure 5.3	Specimen photographs taken after (a) 30 minutes and (b) 48 hours of severe exposure in the chamber used to determine the length change of specimens by image analysis.....	122
Figure 5.4	Screen-print of the 'ImageJ' software tool used to obtain the calibration factor. .	123
Figure 5.5	Overall shrinkage of CNF-based cement pastes exposed to 48-hour severe environment.	126
Figure 5.6.	(a) View of the gradual darkening in shades of gray presented by slab-specimens loaded with CNF #0.13. (b) View in detail of the alligator skin-like cracking pattern observed in the surface of paste specimen containing 0.4 vol.% CNF #0.13 and overdose of superplasticizer.....	127
Figure 5.7	Curling observed in the slab-like specimen: (a) side view, and (b) end view.	127
Figure 5.8	Environmental chamber used to expose the specimens to a controlled mild condition.	128
Figure 5.9	Drying shrinkage of cement pastes containing (a) CNF #0.13, (b) CNF #0.7, and (c) CNF #1.13. CNFs effect on (d) 12-week drying shrinkage. Error bars covered by markers.	131
Figure 5.10	Slab specimens after (a) 30 min. and (b) 24 hours of severe exposure in the environmental chamber.	133
Figure 5.11	Cracking patterns exhibited by the pastes with various CNF #1.13 dosages after trials.	133
Figure 5.12	View of (a) the sandpaper, (b) the mold ready for casting, and (c) the paste specimen without the mold sides and the sandpaper ends fastened with screws to mold base.....	134
Figure 5.13.	(a) Cracking area and (b) max crack width of CNF #1.13-cement pastes.....	136

Figure 5.14	View of the different sedimentation levels after 40 minutes as a function of the dosage of polycarboxylate admixtures. Reprinted from Autier et al. [2014] (p. 38).....	138
Figure 5.15	View of (a) the adapted ASTM C232/C232M [ASTM, 2014] apparatus, and (b) the system assembled to acquire photos. View in detail of the bleeding heights in cement paste containing 0.8 vol.% CNF #1.13 at (c) 5 minutes, and (d) 240 minutes.....	140
Figure 5.16	Bleeding rates over four first hours of cement pastes loaded with (a) CNF #0.13, and (b) CNF #1.13. (c) Bleeding of CNF-based cement pastes after four-hour trial.....	142
Figure 5.17.	View of the clear-light turbid bleed water in the control paste after 4-hour trail..	143
Figure 5.18	View of the <i>Turbiscan</i> ^{LAB} analyser used in the turbidity analysis.	144
Figure 5.19	The white line demarks the top-limit of sedimentation cake of a cement paste with w/c ratio of 0.5, the black line the top of clear bleed water, and the red line the top of surfactant-oil combination. A thin layer composed by floating fine-cement particles is delineated between the red and blue lines. It is possible to see the meniscus softening in the top of bleed water layer.....	144
Figure 5.20	Bleeding heights in cement pastes loaded with 0-0.4 vol.% dry CNF #0.13 after 4 hours trial.....	145
Figure 5.21	Bleeding of cement pastes containing (a) CNF #0.13, and (b) CNF #1.13 over 4 hours. (c) Bleeding of CNF-based pastes after 4 hours. All mixtures contain superplasticizer and show an efflux time in the range of 6 ± 0.5 secs.	147
Figure 5.22	Correlation between the bleeding data acquired as per adapted ASTM C232/232M [ASTM, 2014] and Turbiscan analysis.	148
Figure 5.23	Bleeding of cement pastes containing (a) CNF #0.13, and (b) CNF #1.13 over 4 hours. (c) Bleeding of CNF-based cement pastes after four hours. Same mixtures shown in Figure 5.22 without superplasticizer (SP). Paste flows out of the 6 ± 0.5 secs range.....	149
Figure 5.24.	(a) Bleeding of cement pastes loaded with a fixed fraction of 1.2 vol.% dry CNF #0.13 and a growing dosage of superplasticizers (SP). (b) Effect of SP on bleeding after 4 hours. Paste flows out of the 6 ± 0.5 secs range.....	150

Figure 5.25	Evaporation rate apparatus set for automatic acquisition of weight-sample data in the environmental chamber (top). View of the balance-table weighing system (bottom-left), and in detail of the weighing table in the chamber compartment with a specimen on it (bottom-right).	152
Figure 5.26	Automatic sample weight acquisition system.	152
Figure 5.27	Specimen surface after 20 hours trial in severe environment. ‘SP’ = superplasticizer.	153
Figure 5.28	View of the CNF #1.13 gel at various times (t) of severe exposure.....	153
Figure 5.29	Evaporation rates of control paste and CNF #1.13-cement pastes containing and not containing superplasticizers (a) over 20 hours, (b) after 20 hours, and (c) after 4 hours in severe exposure. (d) Evaporation rate at a peak.	156
Figure 5.30	Evaporation rates of the control paste and the 1.2% CNF #1.13-cement pastes containing and not containing (SP) after 20 hours in severe exposure and their respective flow.....	157
Figure 5.31	Evaporation rates of CNF #1.13 gel and water over 8 hours exposed to mild (left), severe (centre), and extreme (right) conditions.	157
Figure 5.32	Evaporation rates of control paste and 1.2% CNF #1.13-cement pastes containing and not containing superplasticizer (SP) over 20 hours in severe exposure compared with rates of CNF #1.13 gel and water over the same time period and exposure conditions.	158
Figure 5.33	Bleeding rates of CNF-based cement pastes after 4-hour trial measured as per standard method – replotted from Figure 5.16.(c) – and evaporation rates of CNF #1.13 gel and water. All samples exposed to mild condition.	158
Figure 5.34	Gradual 3D volumetric shrinkage of CNF #1.13 gel (severe exposure) at different times: (a) 1 hour, (b) 4 hours, and (c) 20 hours	159
Figure 6.1.	(a) Side view and (b) top-end view of the cylinder sides partially coated with epoxy resin. (c) Cylinders immersed in Na_2SO_4 solution. (d) Bench drill press used to (e) drill samples from the top-end cylinder. (f) Measuring sample depths. (g). Top-end cylinder after sample collection up to 9 mm depth.	167
Figure 6.2.	(a) Sample digesting in HCl , and (b) filtrating the $BaSO_4$ precipitate.	167

Figure 6.3	Sulphate (SO_4^{2-}) contents at different depths in Type GU cement mortars dosed with 0-0.5 vol.% dry CNF #0.13 over 12 weeks of exposure in Na_2SO_4 solution. The mix identified as 'GU & 0%' is the control mixture prepared with GU cement and no CNF.	171
Figure 6.4	Sulphate (SO_4^{2-}) content at distinct depths in mortars as affected by 0-0.2 vol.% dry CNF #0.13 over 12 weeks of exposure in Na_2SO_4 solution for various cement-based binders (a) Type HS cement, (b) Type HE cement, and (c) blended Type GUb cement. The mixes identified as 'HS & 0%', 'HE & 0%' and 'GUb & 0%' are the control mortars prepared with 'HS', 'HE' and 'GUb' cements, respectively.	172
Figure 6.5	Sulphate (SO_4^{2-}) content at various depths in GU cement-based mortars having 0-0.5 vol.% CNF #1.13 over the period of 12 weeks of exposure in Na_2SO_4 solution. 'GU & 0%' is the control mortar.	173
Figure 6.6	Sulphate (SO_4^{2-}) content at 3mm depth in various mortars affected by (a) CNF #0.13 loadings after 12 weeks of exposure in Na_2SO_4 solution, and (b) CNF #1.13 loadings after 8 and 12 weeks of exposure in Na_2SO_4 solution.	173
Figure 6.7	Sulphate (SO_4^{2-}) content at 3 mm depth after 12 weeks in Na_2SO_4 solution in Type GU mortar series affected by CNF #0.13 dosage compared with those mixtures affected by CNF #1.13.	174
Figure 6.8	Porosity of CNF-based cement pastes in the range of 10 nm-140 nm. Dataset based on the gas sorption analysis shown in Figure 4.16.(a).	174
Figure 6.9	Porosity of cement pastes containing several CNF fractions ranging between 100 nm – 10 μ m measured by SEM image analysis. Dataset based on Figure 4.21.(a) and Figure 4.21.(b).	175
Figure 6.10	View of (a) the sealed container, (b) the prisms immersed in Na_2SO_4 solution, and (c) the length comparator used to measure the length change of prisms.	176
Figure 6.11	Water purifier <i>Milli-Q[®] Integral</i>	176
Figure 6.12	Length change (LC) measured in CNF #0.13-mortar mixtures prepared with distinct binders, (a) Type GU cement, (b) HS, (c) HE, and (d) GUb, over 12 weeks of exposure in Na_2SO_4 solution. Note that 'positive' values mean expansion.	180

Figure 6.13	Absolute length change (LC) measured in CNF #0.13-cement mortars prepared with (a) Type GU cement, (b) HS, (c) HE, and (d) GUb over 12 weeks in Na_2SO_4 solution. The blue-dashed line shows the benchmark expansion in HS mortars. Note that '+' values mean expansion.	181
Figure 6.14.	(a) Length change (LC) of CNF #1.13-GU-cement mortars over 12 weeks in Na_2SO_4 solution. (b) Absolute LC of the same mixtures. The blue-dashed line shows the benchmark expansion in HS cement mortars. Note that positive values mean expansion.	182
Figure 6.15.	(a) Length change (LC) of CNF #1.13-cement mortars prepared with distinct binders after 12 weeks in Na_2SO_4 solution. (b) Absolute LC of the same mixtures. The blue-dashed line indicates the benchmark expansion observed in HS cement mortars. Positive values mean expansion.	182
Figure 6.16.	(a) Length change (LC) of CNF #1.13-GU cement mortars after 12 weeks in Na_2SO_4 solution. (b) Absolute LC of the same mixtures. The blue-dashed line defines the benchmark expansion verified in HS cement mortars. Note that positive values mean expansion.	183
Figure 6.17	Comparison between the normalized (a) length change (LC) of GU-cement mortar mixtures dosed with different CNF types and fractions exposed to 12 weeks in Na_2SO_4 solution, and (b) the absolute LC of the same mixtures. Note that positive values mean expansion.	183
Figure 6.18.	(a),(b),(c). Sequence showing the sides of paste cylinder being coated with epoxy resin. (d) Cylinders submerged in Na_2SO_4 solution in a sealed container for 12 weeks.	186
Figure 6.19	Sequence showing the sample preparation: (a) bench saw cutting machine used to slice the cylinder; (b) cut slices; (c) sandpapering; (d) grinding; and (e) sieving the sample.	187
Figure 6.20	View of (a) the powder sample and (b) the diffractometer.	188
Figure 6.21.	(a) Relative ettringite content of cement pastes affected by various CNF fractions in distinct time intervals of Na_2SO_4 solution exposure. (b) Same plot, now, rearranged per CNF dosage. (c) Growth of ettringite content as a function of its initial amount at time zero of exposure.	190

Figure 6.22	Schematic representation of the chemical reaction between the COO^- groups on the CNF surface and the soluble Ca^{2+} in pore solution of cement pastes.	193
Figure 6.23	TGA curves of dry CNF #0.13 and dry CNF #1.13.	196
Figure 6.24	TGA/DTG curves showing the temperature limits for decomposition of (a) dry CNF #0.13 and (b) dry CNF #1.13.	197
Figure 6.25	View of the TGA plots of (a) the cement pastes dosed with 0-0.4 vol.% of CNF #0.13. (b). $Ca(OH)_2$ content of pastes affected by various dosages of CNF #0.13. (c). $Ca(OH)_2$ content corrected with the parcel of Ca^{2+} from the carbonation phase of cement pastes.	198
Figure 6.26	Calcium hydroxide, $Ca(OH)_2$, content in cement pastes affected by CNF dosage based on the dehydroxylation data shown in Figure 4.9.(c).	199
Figure 6.27	Sample preparation for pH analysis: (a) grinding; (b) stirring the powder dispersed in distilled water; (c) soaking period; and (g) filtrating the solid part of the dispersion.	202
Figure 6.28.	(a) pH-meter (and the pH-indicator strips). (b) Probe sensor of pH-meter inserted in the filtrated to measure the pH. (c) pH-indicator strips immersed in the filtered. (d) Measurement of pH by matching the colours of the indicator strip with the shades in the colour chart.	203
Figure 6.29	Potential of hydrogen (pH) of cement pastes loaded with various dosages of CNF #0.13 and CNF #1.13 measured by ex-situ leaching technique using pH-paper strip and pH-meter.	205
Figure 6.30.	(a) Compressive strength at 28 days ($f_{c,28\ days}$) of mortar specimens prepared with distinct cement types and CNF #0.13 fractions. (b) Compressive strength of these same CNF #0.13-cement mixtures exposed to 12-week Na_2SO_4 solution ($f_{c,12\ weeks\ in\ Na_2SO_4\ sol.}$). (c) $f_{c,12\ weeks\ in\ Na_2SO_4\ sol.} / f_{c,28\ days}$ ratio.	209
Figure 7.1.	(a) Marginal amount of macro entrapped air voids seen in the specimen surface cast with mortar dosed with 0.2 vol.% dry CNF #0.13; and (b) Large number and size of entrapped voids in the mortar slice containing 0.5 vol.% dry CNF #0.13.	218
Figure 7.2.	(a) Two cut slices with 50 mm height for RCPT and one with 100 mm height for colorimetric method. (b) View in detail of the cut slide sides coated with epoxy resin.	218

Figure 7.3	Some stages of RCPT: (a) sample drying with a vacuum pump; (b) sample soaking in de-aired distilled water; (c) sample soaking in vacuum; (d) ready-to-test sample in a rubber gasket; (e) specimen in the two half-acrylic cells, one filled with <i>NaCl</i> solution and the other with <i>Na(OH)</i> sol.; and (f) $60 \pm 0.1V$ applied to the solutions in the half-cells, which temperature is continuously monitored by a thermometer.....	220
Figure 7.4	Stages of the <i>AgNO₃</i> -based colorimetric method: (a) 100-mm mortar slice diked; (b) specimen top-end covered with wax film to avoid evaporation of the 20-mm height dike of <i>NaCl</i> solution; (c) specimen free bottom face to allow moisture evaporation; (d) environmental chamber; (e) splitting the slice 90-day exposure in <i>NaCl</i> solution; (f) slice split in two halves; (g) fractured surface after spraying <i>AgNO₃</i> solution, showing the chloride-contaminated white zone and the chloride-free brown zone; (h) apparatus to take photos of specimen cross-section; and (i) image used to measure the chloride depth by image analysis.....	223
Figure 7.5	Schematic representation of the readings taken from the chloride ion front by the caliper method (left) and the image analysis (right).....	224
Figure 7.6.	(a) Electrical resistance to chloride ion ingress (RCPT) in mortars dosed with various CNF fractions and CNF types. (b) Free chloride depths of CNF #1.13-based mortars measured by <i>AgNO₃</i> -based colorimetric method in post-RCPT specimens.....	228
Figure 7.7	Free-chloride depth in mortars dosed with various CNF fractions as per <i>AgNO₃</i> -based colorimetric method.....	228
Figure 7.8	Agreement between (a) the data based on the two colorimetric methods: image analysis and caliper method. Comparison between the data acquired by RCPT and colorimetric method in (b) the same specimen, and (c) different specimens.	229
Figure 7.9	Porosity of cement pastes containing various CNF fractions measured by (a) gas sorption analysis in the 10 nm – 140 nm range, and (b) SEM image analysis in the 100 nm–10 μ m range.	229
Figure 7.10	Apparent coefficient of chloride diffusion (D_{app}) of cement mortars as affected by CNF additions and types.....	230

LIST OF ABBREVIATIONS

<i>AFt</i>	alumina, ferric oxide, tri-sulfate or $Al_2O_3 - Fe_2O_3 - tri$
<i>AFm</i>	alumina, ferric oxide, mono-sulfate or $Al_2O_3 - Fe_2O_3 - mono$
<i>BC</i>	Bacterial cellulose
<i>BCTMP</i>	Bleached chemi-thermomechanical pulp
<i>BJH</i>	Barret–Joyner–Halenda
<i>BR</i>	Bleeding rate
<i>BSE</i>	Backscattered electron
<i>BSEM</i>	Backscattering electron microscopy
<i>CI</i>	Crystalline index
<i>CF</i>	Cellulose filament
<i>CMF</i>	Cellulose microfibrils
<i>CN</i>	Cellulose nanoparticle
<i>CNC</i>	Cellulose nanocrystal
<i>CNF</i>	Cellulose nanofibre
<i>CNF #0.13</i>	Cellulose nanofibre with 0.13 mmol of carboxylate / g of fibre
<i>CNF #0.7</i>	Cellulose nanofibre with 0.7 mmol of carboxylate / g of fibre
<i>CNF #1.13</i>	Cellulose nanofibre with 1.13 mmol of carboxylate / g of fibre
<i>CNW</i>	Cellulose nanowhisker
<i>C₃A</i>	Tricalcium aluminate or $3CaO.Al_2O_3$
<i>C₄AF</i>	Tetra-calcium aluminoferrite or $4CaO.Al_2O_3.Fe_2O_3$
<i>C₃S</i>	Tricalcium silicate or Alite or $3CaO.SiO_2$
<i>C₂S</i>	Dicalcium silicate or Belite or $2CaO.SiO_2$
<i>C – S – H</i>	Calcium silicate hydrate
<i>DEF</i>	Delayed ettringite formation
<i>DOH</i>	Degree of hydration
<i>DTG</i>	Derivative thermogravimetry
<i>ER</i>	Evaporation rate
<i>GU</i>	General use cement
<i>GUb</i>	General use cement blended with supplementary cement material

<i>HE</i>	High early strength cement
<i>HS</i>	High sulphate resistant cement
<i>LC</i>	Length change
<i>LOI</i>	Loss on Ignition
<i>MFC</i>	Microfibrillated cellulose
<i>MCC</i>	Microcrystalline cellulose
<i>MS</i>	Moderate sulphate resistant cement
<i>NFC</i>	Nanofibrillated cellulose
<i>pH</i>	Potential hydrogen
<i>PSD</i>	Pore size distribution
<i>QPA</i>	Qualitative phase analysis
<i>RCPT</i>	Rapid chloride-ion permeability test
<i>RT</i>	Room temperature
<i>SEM</i>	Scanning electron microscope
<i>SP</i>	Superplasticizer
<i>SSA</i>	Specific surface area
<i>TEMPO</i>	(2,2,6,6-tetramethylpiperidine-1-oxyl radical)-mediated oxidation
<i>TGA</i>	Thermogravimetric analysis
<i>TSA</i>	Thaumasite sulphate attack
<i>XRD</i>	X-ray diffraction
<i>WRV</i>	Water retention value
<i>w/c</i>	Water to cement ratio
<i>3D</i>	Tri-dimensional

CHAPTER 1. Introduction

1.1. Background

A sustainable development is without doubt a key word for construction industry in 21st century. Under this context, the lifetime extension of constructed infrastructure and the life cycle enhancement of new structures are a challenge set to engineers. The construction industry has a large carbon footprint – 60% of the natural resources are consumed by this industrial sector. Most of these resources are converted to building materials [Kibert 1994; Kline & Barcelo, 2012]. Portland cement-based concrete is the most consumed man-made construction material in the world. The concrete annual production is estimated in 0.7-1.0 ton per capita [Sonebi, Ammar & Diederich, 2016].

Cement-based systems have their lifetime shortened by unavoidable deleterious interactions with external agents – and more rarely even with internal agents. Fire exposure, overload, freeze-thaw cycles, abrasion, weathering, and shrinkage are some examples of the aggressive physical mechanisms. And alkali-aggregate reaction, carbonation, sulphate attack, and chloride attack are only part of the possible detrimental chemical mechanisms. All these mechanisms impose high economic, environmental, and social costs upon society. Ueda & Takewaka [2007] revealed that the expenditure with the maintenance and repair of existing structures is equal or even higher than with new structures. As an example, a sum of over 2 trillion dollars is required to maintain the current US's surface transportation infrastructure in the next years [American Society of Civil Engineers (ASCE), 2016].

Among the several deleterious processes, the most common are the shrinkage in fresh and hardened concrete, the sulphate attack in hardened concrete, and the chloride attack in the steel bars of reinforced concrete. Shrinkage is closely associated with the moisture loss caused by evaporation or cement hydration. This process occurs all over the lifetime of concrete. Sulphate attack is a decaying process of the cement paste matrix provoked by expansive reactions, which are usually triggered by the late and continuous ingress of sulphate in hardened concrete. And the chloride attack speeds up the electrochemical corrosion of steel bars embedded in concrete. All

these harmful processes reduce the durability of concrete structures and elements [Metha & Monteiro, 2013].

The advent of nanomaterials has opened doors for a new class of innovative, nanosized products with potential for enhancing target properties. Nanosilicas, nanoclays [Sobolev, Flores, Hermosillo, & Torres-Martínez, 2006], carbon nanotubes [Sanchez & Sobolev, 2010], and calcareous nanomaterials [Pacheco-Torgal & Jalali, 2011] are just some examples of nanomaterials recently developed to improve strength, durability, and sustainability of the cementitious materials. However, the relative high cost, hydrophobic nature, chemical inflexibility, and toxicity have limited their application in building materials [Sobolev et al., 2006; Sanchez et al., 2010; Pacheco-Torgal et al., 2011].

In response, researches at Purdue University [Cao, Zavaterra, Youngblood, Moon, & Weiss, 2015] and at the University of Alberta [Dousti, 2018] in the last couple of years have examined the role of cellulosic nanomaterials, particularly cellulose nanocrystals (CNC), on cement-based systems. The high aspect ratio, high elastic modulus, high tensile strength, low density, and water-dispersibility confer upon CNC the capacity to improve the mechanical properties and increase the degree of hydration [Cao et al., 2015; Fu, Montes, Suraneni, Youngblood, & Weiss, 2017]. CNC is derived from cellulose fibres [Hamad, 2017]. Cellulose is the most abundant biopolymer on Earth [Einhorn, Dufresne, Aranguren, Capadona, Rowan, Weder, & Veigel, 2010; Isogai, Saito, & Fukuzumi, 2011]. Therefore, cellulose offers an alternative relatively inexpensive and sustainable for replenishable nanomaterial towards engineering the materials for construction.

As CNC, cellulose nanofibril (CNF) is the result of chemical and/or mechanical treatments to defibrillate the cellulose. CNF possesses unique characteristics. The anionic groups present on CNF's surface associated with its nanoscale assure to CNF a high hydrophilicity and an excellent chemical tunability [Jiao et al., 2016; Isogai et al., 2011]. These features may favour CNF to work as a strategic water reservoir inside of concrete; retaining mixing water at early ages to avoid premature evaporation and releasing water at later ages to seed cement hydration. Both resulting in positive implications for the mechanical strength and durability of concrete. Besides, the

nanoscale and nanofiber shape of CNF may suitably alter not only the porosimetry of capillary pores in cement paste, but also their interconnectivity [Jiao et al., 2016], with clear benefits for concrete durability. Moreover, the fibre shape of CNF may generate a bridging effect on cracks at nano level, resulting in enhanced flexural strength and toughness properties [Hoyos, Cristia, & Vazquez, 2013]. Other possibility to be considered is that CNF may interfere in the chemical attacks of concrete by electrostatically scavenging the aggressive elements, such as sulphate, and extending its lifetime.

The literature review about CNF in cementitious materials, shown somewhere else in the thesis, confirms the unprecedented character of this matter. The very few papers found addressed chiefly the mechanical aspects of CNF addition in cementitious materials, whereas the durability issues were not approached.

In view of the foregoing, the current doctoral research aims to evaluate CNF as an agent to mitigate the most usual harmful mechanisms acting in reinforced concrete: (i) shrinkage, (ii) sulphate attack and (iii) chloride attack.

1.2. Problem Statement

The mixing water added to cement and aggregates in concrete has two basic purposes: one is to hydrate the cement grains to provide the required mechanical and durability properties, and the other is to give the required workability. The quantity of mixing water in concrete – usually expressed in terms of water-to-cement (w/c) ratio – is hence fundamental for its performance. Most of the w/c ratios in concrete vary from 0.4 to 0.6; notwithstanding, the stoichiometric w/c ratio necessary to hydrate the whole amount of cement particle is between 0.22 and 0.26. The exact quantity depends on the cement type and its chemical composition. The remaining water is indispensable to fresh cement-based systems acquires the proper workability for casting. Although, sooner or later, this free water inexorably lost mostly by evaporation. Only 20-25% of the drying shrinkage of concrete takes place until 2 weeks [Metha et al., 2013]. Gradients of humidity between concrete and the external environment lead to a loss of water from the capillary pores and even from some hydrated products of cement. This process shrinks the concrete and may drive to cracks.

The resultant cracking process turns concrete still more vulnerable to ingress of harmful agents, such as chloride and sulphate among others. Thus, the shrinkage mechanism (by loss of water) and the deformations associated with that along the lifetime of concrete shall not be neglected in design, otherwise the serviceability of the structure or construction can be reduced.

The cement hydration process is one of the determinant factors in the gradual construction of the crystalline structure of cementitious materials. The internal spaces not filled by the hydrated products of cementitious materials are named capillary voids. The volume, size, and connectivity of them depend not only on the degree of hydration, but also on the content of evaporable water. For this reason, concrete is inherently a porous material. And the several deleterious chemical elements penetrate the cement-based systems through these interlinked capillary pores – mostly between 50 nm and 10 μm (or 50 μm) – and microcracks [Metha et al., 2013]. One of the most common aggressive elements is sulphate. Once a (external or internal) source of sulphate is available and constantly feeds the pore solution of hardened concrete, a sequence of detrimental chemical reactions takes place and goes unchecked. In other words, the sulphate ions turn Portlandite (or calcium hydroxide, $\text{Ca}(\text{OH})_2$) into gypsum, which one reacts with monosulphoaluminate and precipitates expansive ettringite in the pores, causing microcracks in the cement paste. This continuous volumetric increase disintegrates the cement paste. Other aggressive chemical element is chlorides. As sulphate, the origin of chloride can be the raw materials of concrete and/or the environment. Once chloride ions are available in high concentrations in pore solution around the steel bars, the protective passive film of reinforced bar is broken and the corrosion rate speeds up. In brief, aside the presence of the sulphates and chlorides, the key factors for the development of these detrimental mechanisms are the porosity, which depends on the availability of water and the chemical processes in the cement-based systems.

In brief, in these three deleterious mechanisms mentioned above, moisture movement and penetration of sulphates and /or chlorides ions within or into cement-based materials provoke harmful physical and chemical reactions.

1.3. Hypothesis

CNF's singular characteristics create an expectancy in extending the durability of reinforced concrete structures, as well as their serviceability. Its unique hydrophilic capacity provided by the active carboxyl and hydroxyl groups permits to presume that CNF may control the water movements inside and to outside of concrete. It may attenuate the rate of bleeding water and hence the moisture loss by free-water evaporation. Both processes head to mitigate the deleterious drying shrinkage mechanism. Concomitantly, CNF may improve the cement hydration by 'short-circuit diffusion'. This process was originally observed in cement pastes containing CNC. The CNC facilitates the transport of water through the high-density calcium-silicate hydrate shell that covers the unhydrated cement particles [Cao et al., 2015]. Improvements in the cement hydration are followed by lower porosity, pore refinement, and increase in pore tortuosity of cement paste matrix. In addition, the fiber shape of CNF may also modify the pore size distribution and the capillary pore connectivity, as seen in macro- and micro-fibre concrete. Accordingly, by means of physical effects, CNF can hamper not only the ingress of sulphate ions and chloride ions, but also their internal movement. Another aspect to be examined is if CNF can chemically minimize the sulphate attack. The ionized carboxylate, COO^- , groups disposed on CNF surface may potentially react with the calcium cations, Ca^{2+} , available in pore solution [Jiao et al., 2016] and in consequence of that, slow down the formation of expansive-ettringite phase. In this regard, these expected anionic exchange are substantiated on the higher affinity between sulphate anions, SO_4^{2-} , and carboxylate anions, COO^- .

Therefore, without doubt, it is essential to examine the role of the anionic groups of CNFs on the aforementioned durability issues. All these hypotheses were examined, and certain new scientific approaches have been employed in this thesis.

1.4. Objectives

The primary targets of this thesis were to study CNF as an agent to mitigate:

- (i) shrinkage in hardened cement-based pastes;
- (ii) sulphate attack in hardened cement-based mortars; and
- (iii) chloride penetration in hardened cement-based mortars.

In addition, two secondary targets were also established:

- (i) to examine the effect of CNF's carboxylate content on these durability issues; and
- (ii) to understand how CNF affects the physical and chemical microstructure of cement paste.

A preliminary short-term goal was to ensure that all paste and mortar mixtures used in this study, with and without CNF loadings, have identical water/cement ratio and workability.

1.5. Research Significance

Cement-based systems incorporating CNF is a nascent technology. From the scope proposed by this thesis, only few articles about shrinkage were found in the scientific literature. Thus, this PhD study may thereby be deemed entirely novel.

The outcome of the current study may be taken as basis for the development of innovative, cheap and sustainable CNF cementitious materials, admixtures and building products capable to extend the lifetime of the future reinforced concrete elements and protect the old ones from the deleterious effects of shrinkage and the aggressive ionic attacks of sulphates and chlorides. Considering that, all those suggested possibilities may also be naturally followed by claiming patents based on the original character of the products with embodied CNF.

1.6. Scope

Tenths of variables may affect the results of this study. Therefore, the focus was limited to the more relevant materials, properties, and parameters.

The principal goal of the research is to examine the effect of CNF on the durability of cement-based systems. Among the innumerable harmful physical-chemical mechanisms, drying shrinkage, sulphate-expansive reaction, and chloride penetration were chosen exactly because are the most usual in structural and non-structural concrete elements.

The key-raw material in this study is CNF. The concentration and the carboxyl group content of dry CNF in water suspension are the most relevant characteristics for the study, since that these features directly affect CNF's capability to retain water and chemical reactivity. For this reason, CNF gel with low and high nanofibre concentrations (1 wt.% and 3 wt.% by mass) and different carboxylate contents (0.13 mmol/g, 0.7 mmol/g and 1.13 mmol/g) were examined.

The most popular cement type, which is general use (GU), coming from the same batch and supplier was utilized as reference cement in the whole study to minimize the interference in the results. Other cements types than GU cement were also applied in the study of sulphate attack, given that their distinct characteristics interfere in the outcome of the research.

In total, 16 paste mixtures and 22 mortar mixtures were used in the whole study. All mixtures were designed in such way that the w/c ratio (0.485), the mortar proportion (1 :2.75), and the workability (6 ± 1 sec for pastes and $30 \pm 5\%$ for mortars) remained constant. A standard quartz sand graded meeting the requirements of ASTM C33/C33M [ASTM International (ASTM), 2016] was used in the mortar series. For this reason, the influence of these parameters in the final performance were discarded. The CNF was added as a volume fraction of the mixture in increments of 0.1% dry CNF as a volume fraction of the mixture. The maximum CNF content added to the mixture varied according to the CNF characteristics. The limit reached for CNF with carboxylate content of 0.13 mmol/g was 0.5% in pastes and 0.3% in mortars; for CNF with 0.7 mmol/g was 0.2% in mortars; and for CNF having 1.13 mmol/g was 1.2% in pastes and 0.5% in mortars. Considering that CNF reduces the workability, a superplasticizer was added in all mixtures containing CNF to maintain the equal workability.

The shrinkage performance was evaluated solely in cement pastes, since that this is the most affected phase of concrete in terms of dimensional stability. The length change was measured in paste specimens submitted to 2 days of severe exposure and over 90 days of standard mild exposure. The first trials intend to verify CNF as a mixing-water retainer mainly during the fresh stage of cement paste and the second experiments as a hydration seeder.

Bleeding, cracking area, evaporation rate, and pore size distribution analyses provided additional data to subsidize an adequate evaluation of the shrinkage phenomena in fresh pastes dosed with CNF fractions. Two CNFs were incorporated in the cement pastes used in these complementary studies: the CNF having carboxylate content of 0.13 mmol/g and the CNF with 1.13 mmol/g.

The mixtures were exposed to different environmental conditions according to the trial to verify the water-retaining potential of CNF under various ambient. They were: (i) ‘mild’ conditions in the bleeding analysis; (ii) ‘severe’ ambient in the cracking area analysis and in the evaporation rate trials; and (iii) ‘mild’, ‘severe’ and ‘extremely severe’ conditions in the evaporation rate tests. Temperature, relative humidity and wind speed of each one of these environmental conditions are detailed in CHAPTER 5. According to the correlate literature [Metha et al., 2013], the pore size distribution lower than 50 nm are the most appropriated characteristics of the paste mixtures to explain their shrinkage performance. Thus, the porosity in cement paste series was measured by gas sorption technique.

The sulphate attack behaviour was evaluated by building the profile of sulphate penetration and by length change experiments of 28-day-moist-cured CNF-mortar mixtures exposed to sodium sulphate solution (i.e. 50 g sodium sulphate per litre of solution) over 90 days. Nevertheless, only part of the soluble sulphates combines with the soluble calcium ions, Ca^{2+} , (coming from portlandite, that is, $Ca(OH)_2$) in the aqueous soluble to precipitate as expansive ettringite. Moreover, CNF may partially scavenge these Ca^{2+} and for this reason, mitigate the ettringite precipitation. Thus, the relative ettringite content was quantified by X-ray diffraction analysis and the portlandite content by thermogravimetric analysis. Considering the hypothesis that a low-calcium content may lead to an alkalinity in the paste mixture capable to trigger a corrosion process, a pH analysis was proceeded.

The same mortar series used to the sulphate study were also employed to the chloride ingress analysis. To this end, the profile of chloride depth was delineated in 28-day-moist-cured mortar specimens after being submitted to 90-day sodium chloride solution (i.e. 3 wt.% of sodium chloride solution), alongside the resistance to chloride ion penetration by electrical indication in 56-day-moist-cured mortar specimens.

The permeability to sulphates ions and chlorides ions is intrinsically related to the solid phase of the microstructure and its porosimetry, especially with pore sizes over 50 nm [Metha et al., 2013]. Accordingly, the degree of hydration was evaluated by thermogravimetric analysis and the porosity by gas sorption technique and SEM image analysis gas sorption in cement paste series. To this end, the CNFs with the smallest and the largest carboxylate contents (0.13 mmol/g and 1.13 mmol/g, respectively) were individually incorporated in the cement pastes.

Overall, two distinct test methods with similar objectives were employed to evaluate each one of three main target issues of the study. One of the two is preferably based on an ASTM standard, while the other on a more sophisticated or innovative test method. That way, it is intended to cross the testing results and eliminate any possible interference of the methodology on the final evaluation.

1.7. Organization

The present CHAPTER, CHAPTER 1, briefly describes the principal durability issues of concrete, the advanced nanomaterials used in cementitious materials, and the CNF unique characteristics. Besides, this CHAPTER is designed to connect all these matters to highlight the CNF potentialities as an agent to enhance the concrete sustainability through lifetime extension. This CHAPTER also define the target problems, the hypothesis studied, and the objectives pursued on this research program. Finally, the scope defines the research limits and the general lines assumed for the research methodology in this thesis.

CHAPTER 2 lists a comprehensive review of the relevant literature about the issues approached by this research. The deleterious mechanisms of shrinkage, sulphate attack and chloride attack are depicted in detail. Along with a general approach concerning the use of nanomaterials in construction sector, and a critical review about CNF and CNF's background on cement-based systems.

The raw materials, the mix design criteria and the mix proportion containing or not CNF, as well as their respective characteristics, are reported in CHAPTER 3.

Before approaching the main issues of this thesis, CHAPTER 4 provides essential data about the impact of CNF on hydration process and microstructure to figure out the mechanisms through which CNF affects the principal questions related to the durability of cement-based systems.

The main focus of this research project was subdivided in three CHAPTERS. The testing methods, the respective experimental data, an extensive discussion about the findings, and the concluding remarks on how CNF affects shrinkage, sulphate attack and chloride intrusion in cement-based systems are reported in CHAPTER 5, CHAPTER 6 and CHAPTER 7, respectively. In addition, each of these CHAPTERS presents further studies about associated properties to help decipher the CNF role on the durability.

The findings and the concluding remarks collected from CHAPTER 3, CHAPTER 4, CHAPTER 5, CHAPTER 6 and CHAPTER 7 are condensed in CHAPTER 8. Besides, this CHAPTER provides a list of suggested applications and recommendations to ongoing and further studies on the durability of CNF-based cementitious materials.

Lastly, in the Appendix are found Tables containing the dataset used to plot all graphs presented in the thesis, except for those in which there is a massive amount of data, such as X-ray diffractograms and 90-day drying shrinkage test.

CHAPTER 2. Literature review

2.1. Introduction

This CHAPTER presents a detailed state-of-art based on the available published literature about various essential aspects for the adequate understanding of the current study. At the outset, each one of the major concerns on durability of concrete, i.e. shrinkage, sulphate attack and chloride attack, are unraveled. The principal focus is on describing the deleterious mechanisms. There is first a detailed explanation on how these detrimental processes evolve physically and chemically. It is followed by a brief report of the advantages and disadvantages of employing nanomaterials in cement-based systems is related; as well as their applications in the building materials sector. Then, a succinct depiction of cellulose along with a comprehensive portrayal of CNF and its characteristics are presented. And lastly, the findings on cementitious materials containing CNF as reported in the few articles that precede the present study are discussed.

2.2. Durability of Cement-Based Systems

Reinforced concrete is a multi-phase structural material. Here, the reinforcement and the concrete are the main phases. Concrete is a by a three-phase material: (i) paste matrix; (ii) coarse aggregate phase; and (iii) the transition zone between paste and coarse aggregate. Each one of them presents different chemical, mineralogical and mechanical properties; consequently, each phase is susceptible to a distinct deleterious process. The signs of degradation are several, including cracking, spalling, surface wear and efflorescence. And, various harmful physical and/or chemical mechanisms can be ascribed to them, of which leaching, freeze-thaw damage, steel corrosion and alkali-aggregate reactions are some examples. Some of these mechanisms act on the cementitious matrix, whereas others on the embedded steel bars. Cracking due to changes in the volume of concrete, sulphate attack on cement paste and corrosion of the embedded steel bars are responsible for most of the deterioration phenomena seen in concrete structures [Metha et al., 2013]. Many processes are associated with dimensional instability in concrete. Without doubt, shrinkage is the most relevant. This deleterious process affects primarily the cement paste matrix of concrete. The major cause for that is the loss of mixing water, either in the fresh state or in hardened state. Several deleterious elements, such as sulphate ions and chloride ions, penetrate through the shrinkage

cracking and damage the reinforced concrete structures. The hardened cement paste may be attacked by sulphate ions, as well. The expansive reaction resulting from this process literally disintegrates the concrete. The corrosion of steel bars in concrete is a complex electrochemical process subjected to a variety of conditioning factors. And the soluble chloride ions in pore solution of concrete take an essential part on accelerating this mechanism. All these mechanisms have in common a significant capacity to drastically reduce the durability of concrete; and consequently, its life expectancy. Therefore, these very important debilitating phenomena cannot be neglected in designing concrete structures and construction practices. That is why, most of the major concerns on durability issues are addressed to shrinkage, sulphate attack and chloride attack.

2.2.1. Shrinkage Mechanism

Macroscopic volume instabilities are an inherent characteristic of cement-based materials. These instabilities may be attributed to loading in structural elements, intense amount of chemical reactions, and gradients of temperature and humidity in the materials. However, only those mechanisms that are strictly associated with the loss of moisture (and water movement, in general) shall be treated in greater detail in this thesis. There are different ways in which water can be lost; thus, shrinkage is a complex phenomenon that is described by diverse ‘shrinkage types’. They are plastic shrinkage, drying shrinkage, autogenous shrinkage, chemical shrinkage, carbonation shrinkage and thermal shrinkage. Carbonation shrinkage is a variation of chemical shrinkage in which there is no water consumption; though for the holistic understanding of the subject, it too will be described albeit, briefly. Thermal shrinkage is outside the scope of the present thesis. Many of these phenomena overlap each other up to a certain extent, as it will be seen ahead. The next Sections depict all the shrinkages types.

2.2.1.1. Plastic Shrinkage

Plastic shrinkage is the volume reduction of concrete caused by the loss of free mixing water during the fresh concrete. The mixing water added to concrete has two main functions. Firstly, to hydrate the cement particles and provide the designed strength and durability. And secondly, to impart the desired workability in the fresh state. In the first case water ends up bonded to hydrated cement phases and it is not easily lost; while in the other the water remains free and gradually migrates from the interior of fresh concrete to the surface. The driving mechanism for that is the difference

between the density of water (i.e. lighter) and the other solid particles (i.e. heavier). The inability of the solid particles to retain water plays another important role during this process. This phenomenon is named bleeding. The rate at which the water bleeds depends upon the amount of free-mixing water available in the mixture and the obstacles present to hinder the path of water upward to the surface (e.g. coarse aggregates and fibres). Once at the concrete surface, the bleed water progressively evaporates. The water evaporation rate is function of the temperature gradient, relative humidity of ambient, wind action or combination of them. The loss of moisture in the concrete may be intensified by water suction from concrete to subbase or absorbent formworks; although the water evaporation through concrete surface is predominant. The geometry of certain concrete elements may also accelerate the evaporation. For example, pavements, slabs, bridge decks, tunnel linings are more susceptible due to the extensive evaporation surface in comparison with the concrete volume [Neville, 1995]. This rate is the factor, which determines crack formation – also referred as plastic shrinkage cracking. If the rate of evaporation exceeds the bleeding rate, the free water in the capillary pores near the concrete surface are drained gradually. Lerch [1957] reported evaporation rates in concrete of about $0.5 \text{ kg/m}^2/\text{h}$. ACI Committee 305 [2014] recommends precautions be taken against plastic shrinkage cracking in cases in which the evaporation rate reaches $1.0 \text{ kg/m}^2/\text{h}$. The correlation between plastic shrinkage and loss of moisture is explicit, though the correlation between plastic shrinkage and bleeding is not. If the setting time of paste is postponed by any retardant (for instance, high dosages of some superplasticizers), the bleeding is accelerated, as it is the plastic shrinkage. On the other hand, the thickening of the bleed water layer may prevent a fast drying of concrete surface, so that the plastic shrinkage is then mitigated [Neville, 1995]. In case water evaporates from the capillary pores in the vicinities of the concrete surface, these pores (as concrete volume) tend to shrink; and consequently, create internal drying strains [Jennings, Thomas, Rothstein, & Chen, 2002; Serpukhov & Mechtcherine, 2015]. If the stress induced by the shrinkage strains surpasses the tensile strength capacity of paste, the concrete cracks. That is why the plastic shrinkage initiates at very early ages of concrete, i.e. when the tensile strength is still very low to resist to these shrinkage strains [Lerch 1957; Ramachandran & Beaudoin, 2001; Jennings et al., 2002; Metha et al., 2013; Sayahi, Emborg, & Hedlund, 2014]. The cracks are spread over in size, from a few tens of millimetres to the whole cross section and parallel to one another transverse to the largest dimension of the concrete element. Cracking may also occur over obstacles (e.g. steel

reinforcement and large coarse aggregates) to uniform plastic settlement in fresh concrete subjected to excessive bleeding [Neville, 1995]. Harmful chemicals (e.g. soluble sulphates and chlorides) may enter the concrete through these cracks, whereupon, the service life of concrete is vastly shortened. One way to mitigate plastic shrinkage is to keep concrete hydrated during the very first hours, and avoid premature moisture loss [Metha et al., 2013].

Plastic shrinkage is affected by mix design, constituent materials and their water retention. Chemical admixtures, supplementary cementitious materials, construction practice and the environmental conditions. Popular remedies for mitigating the plastic shrinkage are to: (i) apply curing compounds on the surface of fresh concrete in order to slowdown the evaporation rate; (ii) design concrete with low cement content and low w/c ratio; (iii) reduce the exposure of surface concrete to high temperature and speed winds (e.g. rapid placement of concrete in formworks); and use synthetic non-metallic microfibres (e.g. nylon, polyester, glass, polypropylene, and cellulose), supplementary cementitious materials (e.g. silica fume), chemical additives (e.g. water reducers) and water adsorbent materials to mitigate water evaporation [Neville, 1995; Mindess, Young, & Darwin, 2003; Banthia & Gupta, 2006].

2.2.1.2. Drying Shrinkage

Drying shrinkage is a deformation that occurs in hardened concrete. It is essentially related to the removal of water from small capillary pores and hydrated components (i.e. mainly calcium silicate hydrate, $C - S - H$, gel particles) of hardened cement paste. The intensity with which the water is withdrawn from concrete in this type of shrinkage is intimately associated with the relative humidity balance between the pores of the concrete and the external environment [Jennings et al., 2002].

At 100% air humidity, no moisture loss happens; hence, no drying shrinkage takes place. Between 100% and approximately 50-45%, the absorbed water is gradually removed by evaporation from the capillary pores of hardened cement paste at and near the concrete surface to the environment. The loss of the liquid phase increases the negative capillary pressure; which in turn, provokes compressive stresses in the solid phase (that may achieve tens of MPa). Moreover, the surface tension of water rises substantially and then contracts the wall of fine water-filled capillary pores

(i.e. pores from 2.5 to 50 nm size). Capillary pores larger than 50 nm are unaffected. As a result of that, the hardened paste shrinks (as well as concrete) [Hansen 1987; Neville, 1995; Jennings et al., 2002; Ramachandran et al., 2001; Hewlett et al., 2003; Metha et al., 2013]. Metha et al. [2013] claimed that voids lower than 50 nm (which are referred by the authors as micropores) play a decisive role in drying shrinkage. Jennings et al. [2002] revealed that gas sorption is the best methodology to determine pore size distribution in a range less than 50 nm.

In the range of 45-11% relative humidity, the absorbed water on the surface of $C - S - H$ gel is ever so slowly moved to the surrounding pores [Jennings et al., 2002]. The thinning out of this water film (that pull apart the gel particles) decreases remarkably the disjoining pressures among the $C - S - H$ gel particles. These swelling forces counterbalance the attractive van der Waal forces and the surface tension; the latter is just appreciable for air humidity less than 30% [Jennings et al., 2002]. With the weakening of these forces, the solid phase of cement paste contracts (and concrete as a whole) [Hansen 1987; Neville, 1995; Jennings et al., 2002; Ramachandran et al., 2001; Hewlett et al., 2003; Metha et al., 2013]. It is worth noting that the initial width of this water layer on the $C - S - H$ gel particles depends on the w/c ratio (i.e. mixing water content) of concrete mixture. The higher w/c ratio, the thicker the absorber water; and vice versa. Between this and that, cement pastes with elevated w/c ratios (or water contents) leads to substantial drying shrinkage [Jennings et al., 2002]. Neville [1995] estimates that cement pastes entirely dried at 11% exhibit a linear change in dimensions of the order of 10,000 ($\times 10^{-6}$) per cent; although, values up to 4,000 ($\times 10^{-6}$) % are reported [Neville, 1995].

Environmental conditions with air humidity less than 11% are extremely rare. Only concrete elements submitted to sustained elevated temperatures as in fire exposure may face such extreme circumstances. In cases like these, the interlayer water of $C - S - H$ gel migrates to the neighboring capillary pores or even away causing not just the shrinkage, but also the complete disintegration of the gel phase [Hansen 1987; Neville, 1995; Jennings et al., 2002; Ramachandran et al., 2001; Metha et al., 2013]. The portion of the total shrinkage resulting from the dehydration this gel phase is irreversible; differently from the reversible shrinkage that may occur when exposed to environments with normal relative humidity, that is, above 11%. Under this relative humidity, the shrinkage may be partially reverted or even inverted to a swelling process depending

upon the direction of the water flux. If the external humidity is higher than the internal moisture of cement paste, the water flux is from outside to inside and concrete swells; and vice versa. However, the reversibility phenomenon recovers just part of the total shrinkage; it seems that the first drying shrinkage permanently develops additional silicate bonds within the microstructure of $C - S - H$ gel, even in a partial shrinkage. Although, the subsequent wet and dry cycles are reversible [Jennings et al., 2002; Metha et al., 2013].

The resultant cracks are randomly distributed along the concrete surface. In reality, some features of drying shrinkage cracking are somewhat similar to the plastic shrinkage, what turns the visual identification misleading. At large, the cracks originated from drying shrinkage occurs after concrete has reached the final setting time and presents a considerable degree of bonding between paste and aggregate. The brittle fracture controls the cracking process, so that drying shrinkage forms more linear cracks across the concrete volume and leave the aggregate surface relatively clean, i.e. very few or no parts of hardened paste is found firmly attached to the aggregate. In contrast, the plastic shrinkage cracking is developed at in a malleable and weak fresh concrete. Generally, the cracks are tortuous due to the distortion caused by the shrinkage tensile forces, and exhibit layers of paste on aggregate surface in one of the crack side. Sometimes, little bridges of paste linking both sides of the crack can visually be seen. The typical cracking associated to plastic shrinkage displays a V-shape, i.e. the crack opening at or near the concrete surface is wide and gradually narrows down as reaches its deep end [Walker, Lane, & Stutzman, 2006].

This debilitating process can go on over the entire lifetime of concrete. For that reason, drying shrinkage deformation is considered for many authors [Hansen 1987; Jennings et al., 2002; Page & Page, 2007; Metha et al., 2013; Ulm, Jennings, & Pellenq, 2013] the most important in terms of durability and design of concrete.

Several factors may affect drying shrinkage. Low cement content, reduced w/c ratios, and addition of water reducers and fibres are some of the necessary measures to achieve a concrete resistant to shrinkage [Neville, 1995; Ramachandran et al., 2001; Metha et al., 2013]. However, above all, the relative humidity of air and the aggregate content are the most impacting agent to restrain the shrinkage development in hardened concrete [Neville, 1995]. The behaviour of drying shrinkage

is, by and large, proportional to the loss of moisture in cement pastes (as well as in plastic shrinkage phenomenon); notwithstanding the fact that the scenario is slightly different in concrete. The presence of aggregates in concrete are an additional element to restrain the shrinkage. The restraint capacity of aggregate is basically defined by its content and mineralogy [Neville, 1995].

2.2.1.3. Other Forms of Shrinkage

The macroscopic volume reduction of cement-based materials is determined by the consumption of water available in the pores during the chemical reactions of hydration with the unreacted cementitious grains. It is denominated autogenous shrinkage and is a self-desiccation phenomenon [Tazawa, Miyazawa, & Kasai, 1995; Jennings et al., 2002; Metha et al., 2013; Tazawa 2014]. In spite of the fact that the hydration of cement particles begins at the moment that water is put in contact with mixing water, the autogenous shrinkage is only measured from the initial setting time of cement paste onwards. On this account, this shrinkage type is associated to hardened concrete; plastic shrinkage is excluded [Tazawa 2014]. Drying shrinkage encompasses the autogenous shrinkage nonetheless, given that the parcel of water that takes part of hydration is also account for drying shrinkage.

Chemical shrinkage is based essentially on the fact that the absolute volume of hydrated products in cement paste is smaller than the volume of reactants involved in the hydration reactions. The reactants are the cementitious materials and the water available in the capillary pores and gel pores. In other words, the volume of liquid and solid phases before hydration is less than the solid skeleton of paste microstructure formed after hydration [Tazawa et al. 1995; Jennings et al., 2002; Metha et al., 2013; Tazawa 2014]. This is mainly due to the formation of voids (or porosity) during hydration process. For that reason, chemical shrinkage is always higher than autogenous shrinkage [Tazawa et al., 1995]. Besides cement hydration, the pozzolanic reactions between some hydrated cement products – more specifically calcium hydroxide and calcium silicate hydrate – and the alumino-silicates (e.g. silica fume) can also interfere with this phenomenon.

The chemical shrinkage is more intense in a fresh concrete, when hydration of cement particles is at a peak; although this shrinkage may permanently occur as long as water is available to react in the pores with the unhydrated cement in paste [Tazawa et al., 1995; Tazawa 2014]. Compared with

the typical numbers found for autogenous shrinkage – e.g. $100 (x10^{-6})$ % for a five-year age concrete with conventional w/c ratio, chemical shrinkage is much higher [Neville, 1995; Tazawa 2014].

The cracking coming from these interrelated types of shrinkage develops along the whole volume of concrete. They are notably relevant in concretes with low w/c ratio, high content of cementitious materials, cements with high fineness, and cements with high aluminate phases content [Neville, 1995]. As can be noted, the cementitious paste governs both forms of shrinkage; thereby the degree of hydration matters the most [Tazawa et al., 1995; Neville, 1995, Jennings et al., 2002; Tazawa 2014].

Carbonation shrinkage is a special case of chemical shrinkage, given that the deformations are equally provoked by chemical reactions. However, in this case, the shrinkage is strictly related to carbonation reactions. This reaction is a deleterious chemical reaction between calcium hydroxide ($Ca(OH)_2$ or portlandite) in hardened cement paste and the carbon dioxide (CO_2) coming from the atmosphere dissolved in the pore solution of concrete; this reaction precipitates calcium carbonate ($CaCO_3$ or calcite) as follows [Neville, 1995; Metha et al., 2013; Silva, 2013]:



This phenomenon is highly dependent on the carbon dioxide gas dissolution in pore solution. The soluble carbon dioxide moves principally by capillary suction through the interconnected capillary pores of cement paste [Ramachandran et al., 2001]. The capillary suction is the main mechanism of transport in concretes with moderate relative humidity (i.e. from 50-75%).

Carbonation is mostly restricted to concrete exposed to an environment of intermediate relative humidity and rich in carbon dioxide [Neville, 1995; Ramachandran et al., 2001; Jennings et al., 2002]. At this point, it is important to clarify that some alkali-active materials with low calcium content, such as fly ash, promote the carbonation; and not mitigates it [Ramachandran et al., 2001].

2.2.2. Sulphate Attack Mechanism

The expansive mechanism of sulphate attack is composed of a multitude of swelling physico-chemical reactions that occur concurrently or sequentially in both the fresh and the hardened cement paste. These reactions may manifest themselves in three different ways: (i) the ‘classical’ ettringite formation; (ii) the delayed ettringite formation (DEF); and (iii) the salt hydration. The former mechanism is called ‘classical’ because, in spite of the complexity of the physical and chemical reactions involved, there is a reasonable consensus in the scientific circles that the sulphate attack is predominantly associated with formation of expansive ettringite (calcium aluminate trisulphate 32-hydrate, $CaO.Al_2O_3.3CaSO_4.32H_2O$) precipitated by the chemical reaction between sulphate anions (SO_4^{-2}) and some compounds of cement [Mindess et al., 2003; Jennings et al., 2002; Marchand, Odler, & Skalny, 2003; Metha et al., 2013]. ACI Committee 201[2016] also recognizes gypsum formation as another form of sulphate expansion, besides ettringite. Yet, the ettringite expansion is predominant over gypsum, whose expansive effect is limited. In addition, ettringite forms at comparatively low concentrations of soluble sulphate, while gypsum demands a reasonable concentration, i.e. over 3,000 ppm [Marchand et al., 2003; ACI Committee 201, 2016]. For that reason, the gypsum expansion mechanism will not be approach in this thesis.

This Section presents some of the most common sources of sulphate ions to concrete and a summary detailing the essential information on each of the above sulphate attack mechanisms.

2.2.2.1. Sources of Sulphate

Several factors can affect sulphate attack, but the availability of sulphate anions (SO_4^{-2}) inside concrete is most crucial. Only sulphate salts soluble in gas or liquid phases may take part in the sulphate attack. The sources of sulphate in the concrete can be internal or external; but the development of the expansive chemical reactions is independent of the sulphate source [Marchand et al., 2003].

Portland cement, supplementary cementitious materials, aggregates, chemical admixtures and even mixing water are the most probable internal sources. Amongst all, the Portland cement and

some mineral admixtures are the most probable suppliers of sulphate in concrete. Actually, the sulphate present in the raw materials used to manufacture cement (e.g. Portland clinker and gypsum, i.e. calcium sulphate hydrate or $CaSO_4 \cdot 2H_2O$) accomplishes important role in cement performance. The sulphate phase prevents flash setting and increases the early mechanical strength of cement-based materials. In this respect, the sulphate speeds up the hydration of calcium silicate compounds in cement. Fly ash and blast furnace slag arising from furnaces with sulphur fuels may contain high sulphate amounts. Furthermore, gypsum and sulfide phases, such as pyrite (FeS_2), can be present in the aggregates [Neville, 1995; Jennings et al., 2002; Marchand et al., 2003; Metha et al., 2013]. And some chemical admixtures may also contain sulphates (e.g. sodium lignosulphonate- and calcium lignosulphonate-based superplasticizers) [Ramachandran, 1996]. Water is an unlikely source of sulphates, though Marchand et al. [2003] highlighted that even tap water may contain dangerous quantities of sulphate for concrete.

The external sources of sulphate ions are many. The primary ones are the sodium sulphate (Na_2SO_4), potassium sulphate (K_2SO_4), magnesium sulphate ($MgSO_4$), and gypsum ($CaSO_4 \cdot 2H_2O$) present in soil and dissolved in ground water. The ammonium sulphate ($(NH_4)_2 \cdot SO_4$) of some fertilizers is often found in contaminated agricultural soil as well. Solid industrial wastes, such as bottom ash, pulverized fuel ash and blast-furnace slag, usually are another source of sulphates for concrete. Ultimately, even sulphates carried out by precipitations contaminated with atmospheric pollution may trigger sulphate attack in concrete [Jennings et al., 2002; Marchand et al., 2003; Metha et al., 2013; Whitaker et al., 2015].

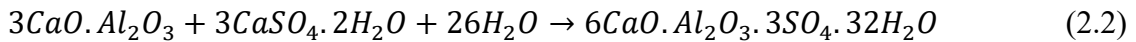
The internal sulphate attack provokes a uniform volume change in concrete initiated by the classical ettringite formation and/or DEF-related expansions. On the other hand, external sulphate attack is restricted to the surface layer of concrete in contact with the solid and/or liquid sulphate sources. In this situation, the conventional ettringite formation and salt hydration are the main deleterious processes [Marchand et al., 2003].

2.2.2.2. Classical Ettringite Formation

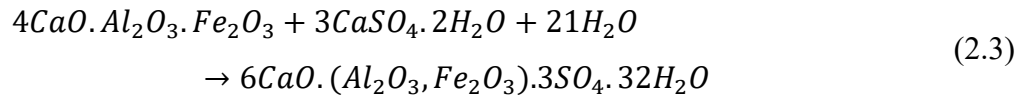
The classical sulphate attack is primarily based on ettringite formation; and possible on gypsum [Metha et al., 2013]. Ettringite initially crystallizes as a result of the cement hydration at early

ages; later may be dissolved and then recrystallizes once more, according to the sulphate availability in concrete and the local physico-environmental conditions in which the chemical reactions proceed.

In the first step of ettringite formation, the key compounds of anhydrous cement are gypsum and aluminate-bearing phases, i.e. tricalcium aluminate ($3CaO.Al_2O_3$ or C_3A , where ‘C’ is CaO and ‘A’ is Al_2O_3) and tetra-calcium aluminoferrite ($4CaO.Al_2O_3.Fe_2O_3$ or C_4AF , where ‘F’ is Fe_2O_3). The other two, alite (tricalcium silicate, $3CaO.SiO_2$ or C_3S , where ‘S’ is SiO_2) and belite (dicalcium silicate, $2CaO.SiO_2$ or C_2S) may or may not take part in the sulphate attack; it depends on the alkalinity and the soluble sulphate concentration in pore solution of cement paste. That is the reason why the standard specifications for cement around the world limit the aluminate-bearing phases. The C_3A content is limited in 8% for Type II Portland cement, and the C_3A and C_4AF quantities in 5% for Type V [Marchand et al., 2003]. The Canadian standard [CSA, 2013] adopts the same limits for equivalent cement types; these are the Portland cement having moderate sulphate resistance (MS type), and high sulphate resistance (HS Type) [Marchand et al., 2003; Metha et al., 2013], respectively. The hydration of C_3A with gypsum starts immediately after the contact with mixing water and precipitates ettringite, as follows [Taylor, Famy, & Scrivener, 2001; Marchand et al., 2003]:



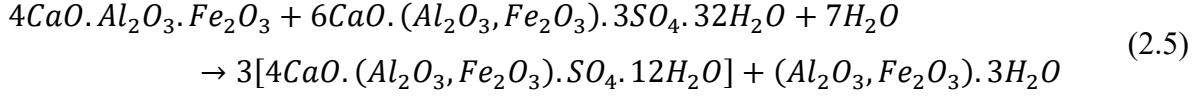
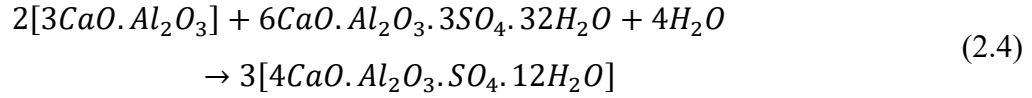
The C_4AF proceeds equal reactions, but at a lower rate, as shown below:



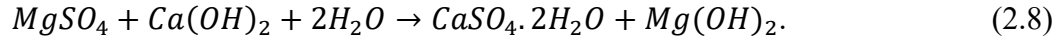
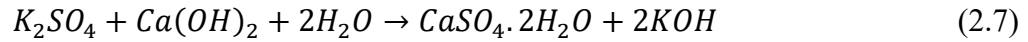
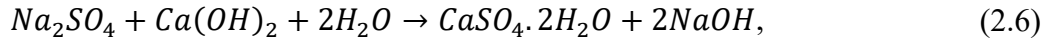
This ettringite is relevant for the internal sulphate attack. The cement paste may expand only if significant quantities of ettringite are deposited in a restrained microstructure. Hardened paste has little or no ability to withstand dimensional changes [Marchand et al., 2003]. Whereas the fresh paste has the plasticity to absorb any volume change.

The alumina-bearing phases keep continuous reacting until the complete depletion of gypsum. In absence of gypsum, the remaining amounts of C_3A and C_4AF combine with the primary ettringite

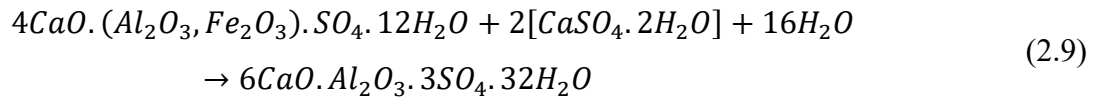
formed as in reactions (2.2) and (2.3), and precipitate calcium monosulphoaluminate hydrate ($4CaO \cdot Al_2O_3 \cdot SO_4 \cdot 12H_2O$) [Marchand et al., 2003; Metha et al., 2013], respectively, as follows:



Meanwhile, the alkali salts (Na_2SO_4 and K_2SO_4) and alkali earth salts ($MgSO_4$) coming from internal and external sources release soluble sulphates anions into the pore solution of paste. These anions react with portlandite ($Ca(OH)_2$) in presence of water; portlandite is one of the hydrated cement products. The following stoichiometric reactions describe these reactions accordingly to the salt source [Marchand et al., 2003; Metha et al., 2013]:



The newly formed gypsum may expand the hardened cement paste if significant quantities are deposited. However, as explained somewhere else above, the expansive effect of ettringite prevails upon gypsum. Particularly because the subsequent dissolution of this gypsum into pore solution of cement paste provides, once more, accessible sulphate anions to turn Ca-monosulphoaluminate phase instable. As a result, a secondary ettringite is formed, as follows:



The secondary ettringite is notably significant for the external sulphate attack. The associated expansion may or may not occur. The determinant factors are the quantity of deposited ettringite and the degree of restraint offered by the solid microstructure of paste [Marchand et al., 2003].

The high alkalinity of pore solution (i.e. pH over 12.5) is mostly kept by the portlandite phase; nonetheless, as previously demonstrated in reactions (2.6), (2.7) and (2.8), this phase is partially consumed by sulfate salts during the gypsum recrystallization. As a result, the alkalinity of pore solution is possible reduced. On the other hand, the alkaline by-products of reactions (2.6) and (2.7), i.e. $NaOH$ and KOH , reestablish the high alkalinity in pore solution. The maintenance of a highly alkaline environment is fundamental to maintain the stability of calcium silicate hydrate phase ($C - S - H$); as well as the aluminate and sulfo-aluminate phases [Ramachandran et al., 2001]. However, the same alkaline balance is not seen with brucite (magnesium hydroxide or $Mg(OH)_2$); the residual hydroxide of reaction (2.8). The high insolubility of brucite declines the hydroxyl group content in the liquid phase of pores; and at same pace, its alkalinity. In such situation, the existing $C - S - H$ is no longer stable; the sulphate ions from gypsum and the carbon dioxide (CO_2) from calcite (calcium carbonate or $CaCO_3$) break down the $C - S - H$ phase into thaumasite ($3CaO.SiO_3.CO_2.15H_2O$), as follows:

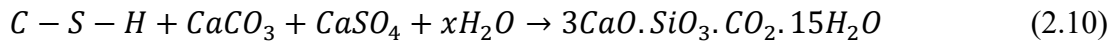


Figure 2.1.(a) portrays the morphology of the ettringite and portlandite crystals and Figure 2.1.(b) gives an idea about the $C - S - H$ gel.

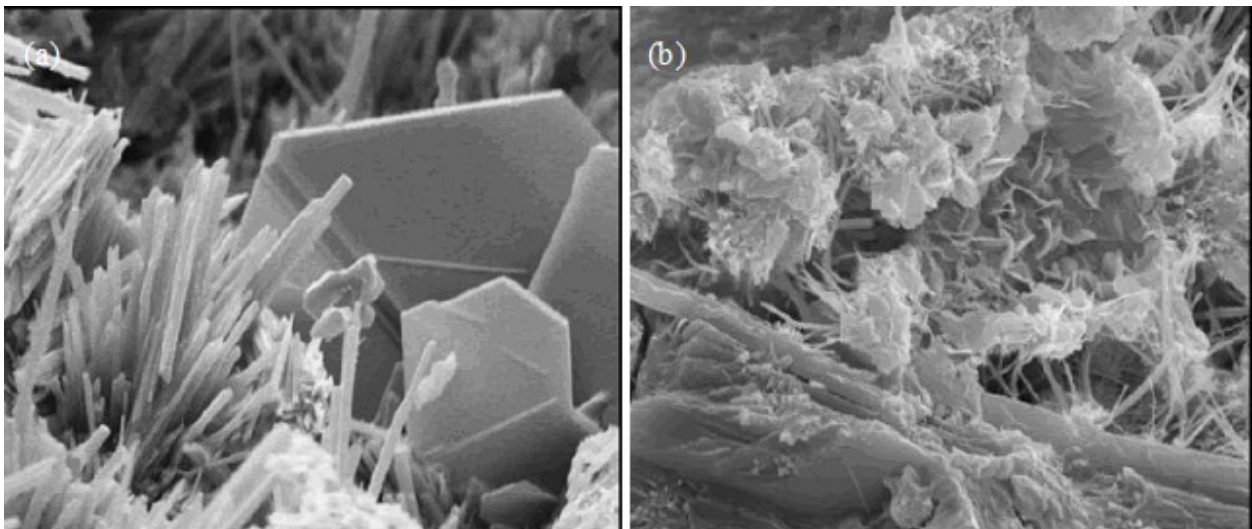


Figure 2.1 Backscattered electron images show the morphology of (a) ettringite needles (left side), the platy shape of portlandite (at centre-right) and (b) the foil-like mixed with bundles of $C - S - H$ fibres. Reprinted from Figs. 174 and 175 published in Walker et al. [2006] (p. 223).

Calcite is a product of the carbonation; this phenomenon is explained in Sections 2.2.1.3 and 2.2.3.1 and portrayed by reaction (2.1). Thaumassite sulphate attack (TSA) is the most aggressive case of sulphate aggression to concrete. TSA transforms the cement paste that keeps concrete a solid material in a white, incohesive mush [Marchand et al., 2003].

2.2.2.3. Delayed Ettringite Formation (DEF)

The DEF phenomenon was first observed by Heinz and Ludwig [1986; 1987] after performing a series of steam-induced sulphate attack experiments in laboratory. According to Marchand et al. [2003], several alleged DEF-related damages took place in Canada and United States. Since then, DEF has been studied and discussed by many researchers; nevertheless, DEF remains uncommon and mostly associated with post curing of steam-cured precast concrete products.

Ettringite is known not to be stable at temperatures higher than 65°C. Under elevated humidity, ettringite phase is decomposed and subsequently converted in Ca-monosulphoaluminate phase as demonstrated in reactions (2.4) and (2.5). At the same time and environmental conditions, sulphate anions dissolved from internal sources go into pore solution of cement paste. Later, under service conditions, ettringite recrystallizes as demonstrated in reaction (2.9). The poorly crystalline secondary ettringite initially fills the empty voids, pores and existing microcracks of concrete; until they are thoroughly occupied [Ramachandran et al., 2001; Metha et al., 2013]. From this point on, the sulphate-related damages start by swelling and/or ettringite-crystal growth [Marchand et al., 2003].

In short, DEF is an internal sulphate attack based on ettringite decomposition in environments with high temperature and humidity followed by late recrystallization of expansive ettringite [Ramachandran et al., 2001].

2.2.2.4. Salt Hydration Formation

Hitherto, only ettringite-related expansive mechanisms were discussed; although sulphate attack may express by itself. In other words, it may damage concrete by purely physical expansive cycles of salt dissolution and crystallization in localized regions at surface without reacting with hydrated products in cement paste [Marchand et al., 2003; Metha et al., 2013]. This phenomenon is termed

scaling salts or salt crystallization or salt hydration [Metha et al., 2013]. It has been observed in porous concrete submitted to hydratable salts; the most common are thenardite (Na_2SO_4) and its hydrated form, mirabilite (sodium sulphate hydrate or $Na_2SO_4 \cdot 10H_2O$). Thenardite becomes mirabilite at 20 °C temperature and 75% relative humidity; and vice versa according to local conditions of temperature and humidity. This dynamic balance between the rate at which water evaporates through the exposed surface of concrete and the rate at which the salt is supplied by pore solution is the basic mechanism behind the salt hydration process. If the salt resupply rate is lower than the water evaporation rate, the salt recrystallization occurs outside (i.e. on concrete surface) and no damage takes place in concrete. On the other hand, if the rate of water evaporation is higher, the salt recrystallizes inside of capillary pores, voids and microcracks of cement paste. The salt recrystallization occurs at just few millimeters distance from surface. This process promotes a substantial, though localized, volumetric expansion at concrete surface. Wetting-drying cycles may repeat this process several times, even daily. Therefore, a progressive deterioration of concrete surface takes place leading to cracking, surface wear and spalling [Collepardi 2003; Taylor et al., 2001; Marchand et al., 2003; Metha et al., 2013; Whitaker et al., 2015]. As can be noted, the DEF may be considered as a particular case of the classical sulphate attack.

2.2.2.5. Sulphate-Related Expansive Reactions

Marchand et al. [2003] described in detail the possible hypothesis for the expansive mechanisms in sulphate attack. In brief, they are: (i) the pressure exerted in surrounding crystalline microstructure by oriented crystal growth of the new-formed solid phases at the spaces initially occupied by the original chemical products; (ii) the increase in the overall volume of the sulphate-related solid phases, despite that these expansive reactions generate chemical shrinkage; and (iii) the swelling phenomena induced by the additional water adsorbed on the hydrophilic surfaces of the sulphate-related crystalline lattices and interlayer spaces of supersaturated pores. Metha et al. [2013] suggested that the ettringite-related expansion in sulphate attack is caused by: (i) the crystalline pressure provoked by the ettringite growth; and (ii) the swelling of poorly crystalline ettringite induced by the adsorbed water coming from the alkaline solution in the pores of cement paste.

The general visual effects of sulphate-related damages are: (i) decrease in the alkalinity of pore solution in cement paste; (ii) concrete expansion; (iii) increase in the capillary porosity of paste; (iv) softening of paste matrix of concrete; (v) spalling; (vi) surface delamination; and (vii) loss of mechanical and durability properties of concrete [Marchand et al., 2003; Metha et al., 2013; Whitaker et al., 2015]. The usual damages seen in heat-induced sulphate attack (i.e. DEF) are map cracking, longitudinal cracking, spalling and localized warping of concrete elements [Marchand et al., 2003]. Figure 2.2 portrays some of these damages.



Figure 2.2 Loss of cohesion, delamination and fragmentation observed at the top-end cylinder with the sides coated with epoxy resin after being submitted to Na_2SO_4 solution for one year.

Common precautions to avoid sulphate attack are (i) to meet the limits and tolerances established in the correlate recommendations and standards for concrete mix design and construction; (ii) to consider the atmospheric conditions in concrete mix design; (iii) to design concrete mixtures with low cement content, low w/c ratios and water reducer in order to enhance the concrete impermeability; (iv) to control the sulphate content in all mixture ingredients; (v) to use cement with low C_3A content, i.e. MS or HS type; (vi) to add supplementary cementitious materials able to reduce the portlandite content in hydrated cement; and (vii) to adopt the best manufacturing and curing practices of concrete structures [Neville, 1995; Mindess et al., 2003; Marchand et al., 2003;

Metha et al., 2013]. In addition, temperature control is the main measure adopted to mitigate the DEF-related expansion issues [Taylor et al., 2001; Ramachandran et al., 2001; Marchand et al., 2003; Metha et al., 2013; Whitaker et al., 2015].

2.2.3. Chloride Attack Mechanism

Corrosion of embedded steel bars is, without doubt, one of the major causes of damage in reinforced concrete structures in many parts of the world [Neville, 1995; Silva, 2013]. According to Broomfield [2003], the annual cost of the maintenance of reinforced concrete in US highway bridge decks and substructures due to corrosion attack is estimated in US\$4 billion. Metha et al. [2013] emphasized that steel corrosion was the immediate cause of the collapse of several reinforced and prestressed steel concrete structures in England during 1974 and 1978.

In short, the corrosion is a phenomenon that requires: (i) the existence of an electrochemical cell; (ii) the availability of oxygen and water in the concrete around steel bar; and (iii) the breakdown of the thin protective layer that coats the steel bar. The collapse of the protective film happens in carbonated concrete and chloride-induced corrosion. In this CHAPTER, only the role of chloride in reinforced concrete corrosion is discussed.

This Section provides a brief discussion with emphasis on: (i) the general steel corrosion mechanism; (ii) the formation of passive film; (iii) the sources and transport of chlorides; and ultimately (iv) the chloride-induced corrosion mechanism in concrete. This basic knowledge about how chlorides ions interact in a steel corrosion process is sufficient for the proper understanding of the current dissertation.

2.2.3.1. Corrosion in Reinforced Concrete

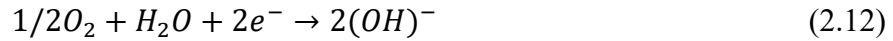
The four components necessary to establish an electrochemical process are: (i) anode; (ii) cathode; (iii); electrolyte; and (iv) a metallic conductor. The anode is where the steel loses electrons (i.e. oxidation), whereas the cathode is where there is a gain of electrons (i.e. reduction). This oxidation-reduction cell may chiefly be created by chemical gradients in pore solution of hardened cement paste in the vicinities of the steel bar; the most common examples are differences in the alkalinity or in the concentration of chloride ions. Furthermore, even a simple physical contact between

metallic materials with distinct chemical compositions may trigger the corrosion mechanism. Interestingly, the presence of rust on the steel surface during the manufacture of a concrete element does not interfere in the corrosion process; provided that no rust is loose. The electrolytes are the liquid phase with soluble cations in pore solution of the hardened cement paste surrounding steel bar. These soluble cations are calcium (Ca^{2+}), sodium (Na^+) and potassium (K^+). They arise, respectively, from $Ca(OH)_2$, sodium hydroxide ($NaOH$) and potassium hydroxide (KOH). The fourth, and last, component is the steel bar, as the metallic conductor [Helene 1993; Neville, 1995; Metha et al., 2013; Silva, 2013].

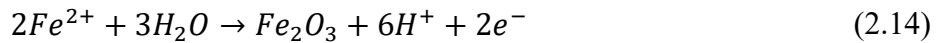
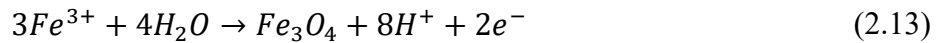
Once the conditions for the electrochemical cell are met, the electric potential in reinforcement steel is triggered. At anodic region, the oxidation of superficial metallic iron (of the steel bar) takes place. It dissolves the iron and releases negatively charged electrons, via reaction (2.11).

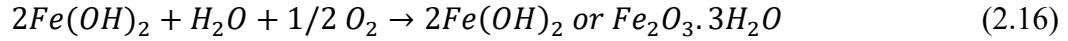
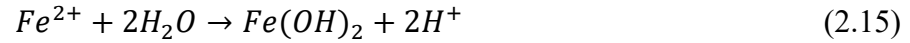


The electrons travel from anode to cathode through the steel bar. Induced by these charges, the reduction reactions of oxygen happen in the pore solution at proximities of cathodic region; it results in hydroxide anions (OH)⁻, as reported in reaction (2.12).



It shall be noted that the ingress of oxygen and the presence of water are crucial for the reduction reactions; without which will not occur. In order to maintain the positive balance of charges neutral at anode (i.e. provoked by Fe^{2+} or Fe^{3+} cations), the hydroxide anions (OH)⁻ move from cathode towards the anode; this anionic flux takes place through the electrolytes in pore solution in the vicinities of steel bar [Neville, 1995; Ramachandran et al., 2001; Metha et al., 2013; Silva, 2013]. Moreover, this flux is highly dependent of the concrete electric resistivity; differently from the electron flux (in reverse direction) through the conductor; the larger the resistivity, the lower the potential rate [Neville, 1995]. There, at the anode, the hydrolysis of metallic iron precipitates a complex mixture of ferrous-ferric compounds, accordingly the following reactions [Silva, 2013]:





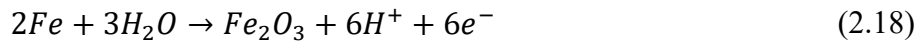
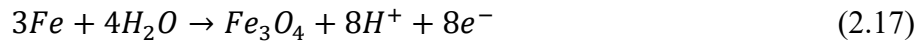
The formation of the rust type depends on oxygen content, pH, and temperature and moisture close to the embedded steel bar in concrete. The principal difference among them relies on the volume of each one; the volume of $Fe(OH)_3 \cdot 3H_2O$ is almost double that of the $Fe(OH)_2$. At this point, it worth mentioning that the rust volume is from 2 to 6 times greater than the steel products involved in the its formation; it is, thus, a rather expansive reaction. Nonetheless, the extension of the damages in reinforced concrete caused by rust precipitation is conditioned to the place where the iron cations are available for reaction. If in high concentrations around the anodic region, the soluble iron cations may be transported through the pore solution by capillary suction; and even reach the concrete surface in wet concretes. Once exposed to an external environment, these cations oxidize and precipitate as hydrated ferric oxides ($Fe_2O_3 \cdot xH_2O$); these red-brownish rust stains are visible on the concrete surface. The aggressiveness to concrete of this rust form is low; given that, merely the steel bar is affected. On the other hand, if the moisture in concrete is low, the hydrolysis of iron cations proceeds inside of concrete; i.e. the rust precipitates on or by the anodic region of the reinforcement. The continuous accumulation of rust on steel surface meaningfully increases the tensile stresses at the steel bar-concrete interface; when the stress is higher than the tensile strength capacity of concrete, the concrete cover cracks [Neville, 1995; Ramachandran et al., 2001; Metha et al., 2013; Silva, 2013]. Thereafter, a spiral of deleterious events takes place up to compromise the reinforced concrete integrity. The sequence of events are: (i) more aggressive elements, such as water, oxygen, carbon dioxide and chlorides, penetrates into concrete; (ii) more iron cations are removed from steel surface; (iii) the cross section of steel bar is progressively reduced; (iv) more expansive rust is, then, formed on steel surface; and (v) more reddish stains, cracking and spalling show up in concrete [Helene 1993; Neville, 1995; Ramachandran et al., 2001; Metha et al., 2013].

The ACI Committee 222.3 R11 [2011] provides recommendations for designing and constructing safer structures against corrosion in reinforced concrete.

2.2.3.2. Passivation Phenomenon

Initially, in the early hours of hydration, the steel bar is embedded in freshly poured concrete not contaminated with harmful external agents, such as carbon dioxide, sulphates, and chlorides. The environment around the steel is consequently poor in oxygen and highly alkaline. It favours a very low (or low) electric potential. The elevated alkalinity at early ages is due to high alkali content in pore solution of cement paste. Silva [2013] considered the alkalinity of pore solution high if the pH is minimally equal to 12.5, and Ramachandran et al. [2001] if the pH of a chloride-free concrete is from 9.5 to 12.5. Under such conditions, the steel is at a passive state; and may be considered practically immune to corrosion, i.e. neither iron dissolves nor reacts with water to form iron oxides.

This scenario is about to change with the gradual increase in the potential, which moves the steel from passivity to activity. At first, the anodic current growth is rapid and, in turn, leads to the dissolution of metallic iron at steel surface, as shown in reaction (2.11), and the subsequent deposition of (mostly) iron oxide compounds (i.e. Fe_2O_3 and Fe_3O_4) on the steel surface, as seen in reactions (2.17) and (2.18) [Neville, 1995; Metha et al., 2013; Silva, 2013]:



This is the starting point for the formation of the passive iron oxide film. As it grows, the anionic current in the steel progressively slows down until reaching a negligible rate; though the steel remains being dissolved at a very slow rate. On average, the passive film attains 1-5 nm thick. This very thin protective layer forms rapidly during the early ages of concrete and protects the steel bar against corrosion [Ramachandran et al., 2001; Silva, 2013]. This phenomenon is known as passivation.

However, the protective layer can be weakened, or it may even collapse in two different ways: (i) carbonation; and (ii) chloride-induced corrosion [Neville, 1995; Mindess et al., 2003; Metha et al., 2013; Silva, 2013]. The first was briefly described in Section 2.2.1.3. It is once again reintroduced very briefly in this Section, in order to recover important concepts about carbonation and better

clarify its role in the steel despassivation. The latter, chloride attack, will now be treated in Section 2.2.3.4.

The carbonation is a deleterious chemical reaction between portlandite and carbon dioxide (CO_2), which precipitates calcite, as demonstrated in reaction (2.1). The carbon dioxide comes from the atmospheric air and permeates mainly through the capillary pores. The portlandite maintains the high alkalinity in pore solution of cement paste. When carbonation reduces the portlandite phase it in turn reduces the alkalinity of cement paste [Neville, 1995; Metha et al., 2013; Silva, 2013]. According to Ramachandran et al. [2001], the condition of fully carbonated paste is achieved if the pH is equal or less than 8.7. The advance of carbonation from the surface to the interior of concrete depends on the rate at which carbon dioxide enters, dissolves, permeates and reacts in concrete. As soon as the carbonation front reaches the embedded steel bar in concrete, the despassivation of the protective layer takes place. Without the protection given by the passive film, the steel bar is, then, subjected to electrochemical corrosion; even in the absence of chloride ions in concrete [Neville, 1995; Ramachandran et al., 2001; Metha et al., 2013; Silva, 2013].

The Pourbaix diagram, also known as equilibrium diagram, provides information about the electrochemical stability for different states of a metal as a function of pH and potential. Each metal has its own diagram. The diagram of steel used for reinforcement in concrete indicates that the immunity region for corrosion is progressively reduced for pHs beyond around 8 [Silva, 2013].

2.2.3.3. Source and Transport of Chloride

The sources of soluble chloride anions can be internal and/or external to concrete. Mixing water, aggregates and chemical admixtures (e.g. de-icing agents) are usual internal sources; and brackish water and seawater are examples of the most common external sources that may potentially provide chlorides through the contact with concrete surface.

Concrete is a porous material and possesses several microcracks [Neville, 1995; Metha et al., 2013]. The ingress and transport of soluble chloride anions (as well as oxygen, which presence is fundamental for corrosion) take place principally through the liquid phase of interconnected capillary pores; especially those ranging between 10 nm and 10 μm . Pore sizes over 10 μm play

little influence, as well as the microcracks [Bertolini & Redaelli, 2004; Metha et al., 2013; Silva, 2013]. The chief mechanisms for chloride anions transport are: (i) suction from the wet concrete surface to the dried (or partially dried) one by surface tension of the liquid phase in the capillary pores; (ii) ionic diffusion through the saturated pores by changes in the concentration of ions over time; and (iii) gravitation action [Silva, 2013]. The latter mechanism is only meaningful for ionic transport by means of the macropores and microcracks of concrete. The ionic diffusion is the most relevant transport mean for chloride ions. But compared with capillary suction, it is a slower process; given that a continuous liquid phase in interconnected capillary pores is a crucial factor for the development of ionic diffusion. Thereby, the soluble-chloride transport is at maximum rate in submerged concrete, whilst it is negligible for concrete moisture less than 50%. In contrary, the peak rate of oxygen penetration (by capillary suction) in concrete occurs at low-moisture environments (i.e. less than 70); given that the oxygen transport speeds up in empty air-filled pores [Nilsson et al., 1996; Silva, 2013]. Under such circumstances, the optimum range for corrosion takes place is 70-80% relative humidity; relatively dry concrete (i.e. less than 50-70% humidity) and submerged concrete develop no or negligible corrosion rates [Neville, 1995].

The availability of free chloride ions in concrete can be mitigated. There are two basic mechanisms to refrain the internal movement of soluble chlorides and impede their participation in the corrosion process. The main manner is to bind chloride ions by chemical reaction, i.e. soluble chlorides react to aluminate phases of cement (C_3A and C_4AF) to form calcium chloroaluminate ($3CaO \cdot Al_2O_3 \cdot CaCl_2 \cdot 10H_2O$), also referred in the literature as Friedel's salt [Neville, 1995; Nilsson et al. 1996; Silva, 2013]. The other mechanism is by adsorption of chloride ions on capillary pore walls [Nilsson et al., 1996; Metha et al., 2013; Silva, 2013]. The free chloride ion (Cl^-) present in pore solution may vary from 20% to more than 50% of the total chloride content; the difference is bound by hitherto cited mechanisms [Neville, 1995].

The critical chloride value (also known as chloride threshold value) at the steel-concrete interface that initiates the breakdown of passivation (and as a result, the chloride-induced corrosion of the reinforcement in concrete) is still an object of controversy. At present, no general consensus on its value has been achieved in the related literature. Even the possibilities of expressing this value are many. This threshold content can be expressed in terms of total or free chloride concentration in

the pore solution as weight percent of binder (cement), mortar, and concrete; or even as the molar ratio of chloride ion concentration to hydroxide ion concentration, Cl^-/OH^- [Angst, Elsener, Larsen, & Vennesland, 2009a; Angst, Vennesland, & Myrdal, 2009b; Cao et al., 2015]. Angst et al. [2009a] revealed that this molar ratio shows the fundamental relationship between the chloride ion activity and the pH of pore solution (here represented by the OH^- content) to the reinforcement corrosion mechanism. These authors [Angst et al., 2009a] consider that the critical value should be expressed by the free-chloride content (not by the total value) in pore solution or related to the weight of cement (or concrete); this assumption considers the fact that the bound chloride does not participate in the corrosion process.

The ACI Committee 318 [2018] sets several water-soluble chloride limits for concrete. The European standard EN 2016 define the critical values as 0.2-0.4%, by mass of binder, for reinforced concrete [Angst et al., 2009a]. Some authors [Neville, 1995; Ramachandran et al., 2001] reported that the maximum acceptable is 0.2%, by weight of cement, and 0.6% for Cl^-/OH^- ratio. In a comprehensive study, Angst et al. [2009a; 2009b] and more recently Cao, Gehlen, Angst, Wang and Yao [2019] summarized a broad range of critical values associated with the despassivation of reinforcement found in the literature, i.e. free chloride contents by weight of binder ranging between 0.04-8.34%, and by weight of concrete between 0.025%-0.18%. These authors also showed that the Cl^-/OH^- molar ratio varied from 0.01-45. These numbers were obtained from distinct methods and from experiments performed under outdoor conditions of exposure (or actual structures) or in steel specimens or embedded steel in cement-based systems submerged in chloride solutions under controlled conditions of laboratory [Angst et al., 2009a].

This large variety of results relies on the fact that the deleterious free-chloride threshold depends on innumerable factors; for instance, steel-concrete interface, pH of the pore solution, cement type, surface condition of steel, moisture content, oxygen ingress, w/c ratio of concrete, concrete resistivity, chemical composition of steel, temperature and chloride source [Angst et al., 2009a].

Besides the control of chloride content in the raw materials, the more effective way to hamper the chloride ingress is, as a rule, improving the impermeability of concrete. Some examples to do so are to: (i) extend the curing time of fresh concrete; (ii) select blended cement types; (iii) select

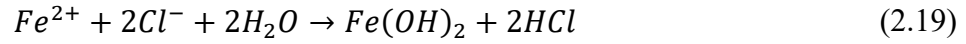
(chloride-free) water reducers; (iv) add supplementary cementitious materials with high or intermediate calcium content; and (v) design concrete mixtures with low w/c ration and high concrete cover of steel bars [Neville, 1995; Metha et al., 2013; Mindess et al., 2003; ACI Committee 318, 2014].

2.2.3.4. Chloride-Induced Corrosion

As seen so far, an electrochemical cell, water and oxygen are essential ingredients in the corrosion mechanism. Furthermore, carbonation is fundamental to collapse the passive film and then the corrosion process arises; even in absence of chloride. As with carbonation, so with chlorides: the chloride ions can remove the protective iron oxide film around the steel bar in concrete. In fact, chloride is the most common cause of the passive layer breakdown. The mechanism by which it occurs continue not fully understood, notwithstanding several efforts in this regard [Neville, 1995]. Despite that, the breakdown of the passive film may be described in three sequential steps: (i) the penetration; (ii) the breaking; and (iii) the adsorption [Silva, 2013].

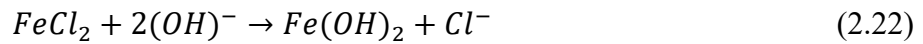
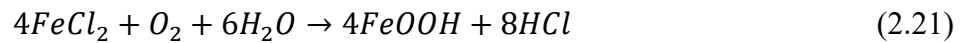
The chloride ions available in concrete from different sources migrate in direction to the steel bar. If the free chloride ions accumulated in the vicinities of reinforcement steel achieve a threshold, the steel turns from passive state to active state in terms of the corrosion potential. As reported in Section 2.2.3.3, the critical free chloride content for that is controversial. Once the free chloride concentration exceeds the threshold, these anions penetrate through the passive layer towards to the steel bar surface. This movement is driven by the high difference in the potential across the passive film. Discontinuities in the film (e.g. microcracks) at anodic region provide direct access of chloride ions to steel surface. At these pits, the gradual adsorption of chloride by the passive iron oxide film conducts to a progressive thinning until its entire dissolution; consequently, the passivity of the layer is broken [Silva, 2013]. There, at the pit, the metallic iron is dissolved, as depicted in reaction (2.11), and the electron flux moves to cathode through the steel bar. At the cathode, the hydroxide anions – formed by reduction reactions shown in reaction (2.12) – and surrounding chlorides anions are transferred through the electrolytes in pore solution of cement paste to anodic pit; in order to preserve the electroneutrality of the anode-cathode balance. At the anode, the hydrolysis of the soluble iron cations (Fe^{2+} and Fe^{3+}) precipitates several forms of

rust, as described in the reactions (2.13)-(2.16) and (2-19), and iron dichloride ($FeCl_2$), as reaction (2.20) [Helene 1993; Neville, 1995; Metha et al., 2013; Silva, 2013].



Normally, the negatively charged hydroxide ions (OH^{-}) would migrate to the anionic pit in order to balance the hydrogen cations (H^{+}) released from the iron hydrolysis, as listed in reactions (2.13)-(2.16). Nonetheless, the acid environment in the pit region blocks its possible repassivation; and moreover, boosts the movement of more free chloride ions to the pit. It means more hydrochloric acid (HCl) and less alkalinity, which further stimulate the iron dissolution and subsequent reactions. The HCl is a by-product of the reduction of iron, as displayed in reaction (2.19) [Neville, 1995; Silva, 2013].

The iron-chloride compounds coming from reaction (2.20) are unstable in environments rich in hydrogen and oxygen, as it is in the pit region. As a result, rust is precipitated, and chloride ions are released for further attack, as follows [Neville, 1995; Silva, 2013]:



Goethite, $FeOOH$, is just one of the many possible ferric compounds [Neville, 1995].

The continuous precipitation of expansive rust cracks and spalls concrete cover at the anodic region; and then more detrimental agents (e.g. oxygen, water, carbon dioxide and chloride; not mentioning the sulphate salts necessary for the formation of expansive ettringite) intrude into concrete. This detrimental cycle, described in more details in Section 2.2.3.1, reduces significantly the durability and serviceability of the reinforced concrete.

Summarizing, chlorides can collapse the protective film, accelerate the corrosion rate and even so, they still remain available for taking part in new corrosion reactions.

2.3. Nanomaterials in Cement-Based Systems

The development of structural cementitious materials along the last two millenniums is narrowly associated with the successive introduction of innovative technologies and new materials. From the use of pozzolans to improve the Roman millennial structures passing by the bicentennial Portland cement invention until the recent new generations of chemical admixtures and alkali-activated materials, the concrete history is rich in successful examples of novel materials that little by little corrected its 'defects' and gave rise to new attributes, such as self-compaction and ultra-high performance. Many of these concrete innovations were only feasible thanks to the important role performed by super-fine scale of these new materials [Sobolev et al., 2006]. Nowadays, the demand of society is by efficient, sustainable and durable building materials. In the last few years, the advent of nanomaterials has been the new frontier in the search for novel and/or superior functionalities [Jongvisuttisun, Negrello, & Kurtis, 2013].

The European Union Commission [2011] defines nanomaterials as:

A natural, incidental or manufactured material containing particles, in an unbound state or as an aggregate or as an agglomerate and where, for 50 % or more of the particles in the number size distribution, one or more external dimensions is in the size range 1 nm - 100 nm. (p. 1)

Although, Norhasri, Hamidah, and Fadzil [2017] stated that for concrete applications the nanosized materials are the sub-500 nm size particles. These authors also refer to nanoconcrete as a concrete in which nanomaterials are used or added.

Sanchez et al. [2010] claimed that nanoscience and nanoengineering of complex materials are the basis for nanotechnology exploitation in concrete. In brief, nanoscience measures the material properties at nanoscale, and nanoengineering tailors the materials microstructure at nanometer scale to incorporate new functions or enhance the material performance [Sanchez et al., 2010]. According to Hisseine, Omran, and Tagnit-Hamou [2018]:

Nanomodification of concrete refers to incorporating nanosized objects into concrete to manipulate its nanostructure and control its macro behavior [Jennings et al., 2008] in order

to develop a new generation of tailored and multifunctional composites with superior mechanical performance and durability [Sanchez et al., 2010] (p. 04018109-2).

The growing interest on nanomaterials has attracted the attention of several researchers. Zhu, Bartos, and Porro [2004] and Ghosal, and Chakraborty [2017] listed a number of new nanotechnology-based products commercially available in the market to improve the performance of cementitious products. According to Silvestre, Silvestre, and De Brito [2016], the annual number of indexed publications in SCI Web of Knowledge linked to the keywords ‘concrete and nano’ jumped from 1, in 2000, to 133, in 2013. As a result, a range of nanomaterials has been developed to strategically interact, at nanoscale, with the physicochemical of solid phase, liquid phase or interface between both cementitious material [Garboczi 2009; Sanchez et al., 2010; Silvestre et al., 2016; Norhasri et al., 2017; Hisseine et al., 2018]. Nanoiron oxides [Li, Xiao, & Ou, 2004], nanoclays [Chang, Shih, Yang, & Hsiao, 2007; Farzadnia, Ali, Demirboga, & Anwar, 2013], nanosilicas [Sobolev et al., 2006; Quercia, Spiesz, Hüsken, & Brouwers, 2014; Sonebi, García-Taengua, Hossain, Khatib, & Lachemi, 2015; Wu, Shi, Khayat, & Wan, 2016; Lazaro, Yu, & Brouwers, 2016; Hisseine et al., 2018], nanotitanium dioxides [Hashimoto, Irie, & Fujishima, 2005; Folli, Pade, Hansen, De Marco, & Macphee, 2012; Sanchez et al., 2010; Lazaro et al., 2016; Hisseine et al., 2018], calcareous nanomaterials [Sanchez et al., 2010; Lazaro et al., 2016; Wu et al., 2016], nanoalumina oxides [Li et al., 2006; Behfarnia, & Salemi, 2013; Barbhuiya, Mukherjee, & Nikraz, 2014; Hisseine et al., 2018], and nanolime [Otero, Charola, Grissom, & Starinieri, 2017] are some examples of nanosized particles currently examined for nanomodification of concrete. By and large, the majority of the benefits of aforementioned nanomaterials come from the extremely high surface area to volume ratio, which intensifies the chemical reactivity in cement pastes [Sobolev et al., 2006; Sanchez et al., 2010].

The use of nanosilicas and nanoclays have been predominantly guided by enhancements in the mechanical properties of concrete [Silvestre et al., 2016]; principally nanomontmorillonite [Chang et al., 2007] and halloysite nanoclay [Farzadnia et al., 2013] among the various possibilities of nanoclays. And have been examined in ultra-high-performance concrete [Norhasri et al., 2017]. Their high chemical reactivity provokes pore refinement and $C - S - H$ gel densification in the

microstructure of cement paste, which in turn, enhances the durability and mechanical properties [Porro et al., 2005; Ozyildirim & Zegetosky, 2010; Sanchez et al., 2010; Lazaro et al., 2016]; in the case of nanosilicas, these improvements occur mainly at early ages of concrete [Sobolev et al., 2006; Maheswaran et al., 2012]. Nanoalumina increases the durability of cement paste through the densification of microstructure, although compressive strength remains unaltered [Barbhuiya et al., 2014].

Other nanomaterials also provide limited or even negligible advantages for the mechanical properties of concrete, but in compensation they bring special features. Nanoiron oxides can confer a self-monitoring property upon the concrete structures [Li et al., 2004]. Overloads and/or any other damage may be detected by changes in the electrical resistance as the loading is applied to concrete [Silvestre et al., 2016]. The self-cleaning and self-disinfection are qualities provided by nanotitanium dioxides; their photocatalytic activity (i.e. photoreactions provided by ultraviolet irradiation from sunlight) activates the nanoparticles to absorb (due to their hydrophilicity) and decay inorganic substances [Hashimoto et al., 2005; Folli et al., 2012; Silvestre et al., 2016]. Nanolime is a consolidant employed in the preservation treatments of historic limestone works or recovery of calcareous-based materials [Otero et al., 2017].

Besides these nanomaterials, nanoreinforcements (e.g. single-walled carbon nanotubes, multi-walled carbon nanotubes and carbon nanofibres) have also attracted the attention of many researchers; especially due to their peculiar features, such as exceptionally high aspect ratio (i.e. length-to-diameter ratio up to 132,000,000), remarkable tensile strength (i.e. hundred times greater than steel) [Pacheco-Torgal et al., 2011; Gdoutos, Konsta-Gdoutos, Danoglidis, & Shah, 2016] and superior elastic modulus [Silvestre et al., 2016]. Nano-reinforced cement-based materials attain high mechanical properties, toughness and crack-growth resistance [Konsta-Gdoutos, Metaxa, & Shah, 2010; Gdoutos et al., 2016; Pacheco-Torgal et al., 2011; Kumar, Kolay, Malla, & Mishra, 2012; Lazaro et al., 2016; Urkhanova, Lkhasaranov, Buyantuev, & Kuznetsova, 2016; Norhasri et al., 2017].

Silvestre et al. [2016] reported that, among all nanomaterial, nanosilica is the most effective in increasing the compressive strength of concrete; whilst nanotitanium dioxide is the best choice if

the concerns are addressed to environmental and health effects. For these reasons, most of the studies have targeted nanosilicas and nanotitanium dioxides [Sanchez et al., 2010; Lazaro et al., 2016].

In general, the nanomaterials may augment the mechanical properties, durability and sustainability of cementitious materials beyond incorporating novel attributes; but at same time, their relative high cost (e.g. nanosilica), hydrophobic nature (e.g. carbon nanotube), strong self-attraction (e.g. nanoreinforcements), chemical inflexibility (e.g. carbon nanofibres), flocculating tendency (e.g. nanosilica and nanoclays), low availability in certain regions (e.g. nanoalumina), environmental issues (e.g. nanosilica) and toxicity (e.g. nanotitanium dioxide) are limitations to be overcome in order to turn feasible their use in cement-based systems [Lee, Mahendra, & Alvarez, 2010; Sanchez et al., 2010; Silvestre et al., 2016; Norhasri et al., 2017]. In response to these drawbacks, cellulose nanomaterials may offer an attractive alternative to extend the lifetime of reinforced concrete structures.

2.4. Cellulose Nanomaterials

Cellulose is an organic carbohydrate, $(C_6H_{10}O_5)_n$, largely used by industries to manufacture a wide variety of commodities (e.g. food, paints and medicaments), in vogue for several years [Nasir, Hashim, Sulaiman, & Asim, 2017]. It was made into functional polymers at an industrial scale as early as 1870 [Gao, 2013]. The cellulose molecule is chemically formed by a long linear polymer chain of linked β -D-glucose units [Khalil, Bhat, & Yusra, 2012]; many cellulose molecules assembled together create fibrils, which in turns, it is the elementary unit of cellulose microfibrils. The smallest microfibrils may display similar dimensions to an individual fibril, that is, 2-20 nm wide by few micrometres long [Fu et al., 2017]; nevertheless, the average diameter is typically less than 200 nm [Laukkanen et al., 2015]. These microfibrillar cellulose are the elementary unit of cellulose nanomaterials (CNs), also called as nanocellulose.

The interest in this naturally synthesized nanomaterial has growing exponentially during the recent years. The driving reasons are its biocompatibility, good mechanical properties and tailorable surface chemistry capacity [Nasir et al., 2017]; without mentioning that cellulose is the most abundant and renewable polymer on Earth [Eichhorn et al., 2010; Isogai et al., 2011; Jiao et al.,

2016; Nasir et al., 2017]. Furthermore, the pulp and paper industry are an important social and economic segment in Canada. In 2017, this industrial sector contributed \$ 8.9 billion to Canada's nominal GDP and employed tens of thousands of Canadian workers [Natural Resources Canada, 2019].

There are two distinct ways to obtain CNs. One is a direct method, in which the CNs are the harvest of cellulose-producing microorganisms (e.g. *Acetobacter*, *Agrobacterium*, *Rhizobium*, *Pseudomonas* or others [Laukkanen et al., 2015]). These CNs are also known as bacterial celluloses (BCs) [Fu et al., 2017; Nasir et al., 2017; Barhoum, Li, Chen, Cheng, Yang & Dufresne, 2018]. And in the other, the CNs are derived from the disintegration of any plant-based materials that contain cellulose fibres (i.e. any wood or non-wood biomass) or wood pulps. The fibre content of these cellulosic materials varies according to the native source, as shown in Table 2.1 [Khalil et al., 2012]. The non-wood sources (and specially cotton, which is almost pure cellulose fibres) show higher fibre contents and lower costs than the wood biomass; notwithstanding the higher availability of the wood-derived sources [Nasir et al., 2017]. Besides cellulose fibres, these biomass sources contain some impurities, such as lignin, hemicellulose, pectin, oils and other substances. The removal of these impurities yields the wood pulp, also known as cellulose pulp. The delignification and purification treatments of the lignocellulosic-containing biomass are carried out by chemical, mechanical, thermomechanical or chemi-thermomechanical pulping processes [Nasir et al., 2017; Barhoum et al., 2018]. The pulp is typically composed by poorly crystalline cellulose fibres with thickness of 10-25 μm and few millimeters long [Fu et al., 2017]. Santos et al. [2015] claimed that the magnitude of these dimensions are smaller, i.e. 1-5 μm and 10-50 μm , respective. The defibrillation of these cellulose fibres by distinct synthesis techniques originates a variety of CNs [Nasir et al., 2017]. In this regard, the scientific literature presents divergences and unclear descriptions [Saito, Kimura, Nishiyama, & Isogai, 2007; Eichhorn et al., 2010; Boluk & Danumah., 2014; Khalil et al., 2012; Onuaguluchi, Panesar, & Sain, 2014; Fu et al., 2017; Nasir et al., 2017; Hisseine et al., 2018; Landis, Alyaseen, Ahmed, & Kolour, 2018; Barhoum et al., 2018]. Despite this, the CNs may be roughly grouped in consonance with certain similarities in 'cellulose microfibril' and 'cellulose whiskers'.

The ‘microfibrils group’ is composed by cellulose nanofibre (CNF), nanofibrillated cellulose (NFC), microfibrillated cellulose (MFC), and cellulose filaments (CF). All of them are formed by mechanical disintegration and refinement of the cellulose fibres into a network of cellulose microfibrils (i.e. individual and bundles of microfibrils); nonetheless, each one with a size of a different order of magnitude [Nasir et al., 2017; Hisseine et al., 2018]. CNF is the smallest one; it may show dimensions equal to a single fibril [Fu et al., 2017]. In addition to the mechanical processes, chemical treatments or a combination of chemical pretreatment followed by mechanical are also used to the obtainment of CNF [Fu et al., 2017]. Several authors [Nasir et al., 2017; Santos et al., 2015; Khalil et al., 2012] claimed that CNF is also known as NFC, MFC and cellulose microfibrils (CMF). Fu et al. [2017] reached the same conclusion, but only in regard to the terms CNF and CMF; nevertheless, the author pointed out that CNF production requests a chemical pretreatment to facilitate the defibrillation process. All microfibril-based CNs are flexible, given that the microfibrils alternates rigid crystalline segments and some flexible amorphous regions.

The other group (i.e. the ‘cellulose whiskers’) is basically composed by cellulose nanowhisker (CNW) or cellulose nanocrystal (CNC). These CNs are a rigid needle-like in structure almost totally crystalline obtained by acid hydrolysis of cellulose fibres. Such CNC features are instanced in Figure 2.3.(a). It worth mentioning that Cao et al. [2015] revealed the CNC systems exhibit the phenomenon of ‘short-circuit diffusion’. In this mechanism, the CNC particles ease the passage of water through the dense ring of hydrated products around the unhydrated cement particles improving their hydration, as shown in Figure 2.3.(b). CNF may have similar potentialities, given the hydrophilic nature and nanoscale likeness between them. Besides that, Xu et al. [2013] demonstrated the CNF capability of ‘bridging’ microcracks in a polymeric matrix, as illustrated in Figure 2.3.(c).

Table 2.2 briefly compares CNC and CNF properties and characteristics. And Figure 2.3.(a) and Figure 2.6.(b) in the next Section show, respectively, CNC and CNF at nanoscale. Figure 2.4 displays a concise flow with a description of the above-mentioned principal steps in CNs manufacture. Table 2.3 summarizes the CNs dimensional characteristics.

Khalil et al. [2012] considered microcrystalline cellulose (MCC) as a CN. MCC is a rod-like crystalline structure, similar to CNC, with over 1 μm in diameter and length. However, by definition, nanomaterials have at least one dimension less than 100 nm; hence MCC is not taken as a CN for the purpose of this thesis.

Table 2.1 Chemical composition of some wood and non-wood cellulose-containing sources [Khalil et al., 2012]:

<i>Biofibre Type</i>	<i>Composition [%]</i>				
	<i>Native Source</i>	<i>Cellulose Fibre</i>	<i>Hemicellulose</i>	<i>Lignin</i>	<i>Others</i>
<i>Wood</i>	Hardwood	43-47	25-35	16-24	2-8
	Softwood	40-44	25-29	25-31	1-5
<i>Non-Wood</i>	Cotton	95	2	1	0.4
	Sunn	80	10	6	3
	Sisal	73	14	11	2
	Jute	71	14	13	2
	Flax (retted)	71	21	2	6
	Hemp	70	22	6	2
	Bagasse	40	30	20	10

Table 2.2 Succinct comparison between CNF and CNC [⁽¹⁾ Saito et al., 2007; ⁽²⁾ Xu et al. 2013; ⁽³⁾ Boluk et al. 2014; ⁽⁴⁾ Sofla et al. 2016; ⁽⁵⁾ Fu et al., 2017; ⁽⁶⁾ Nasir et al., 2017].

<i>Characteristic</i>	<i>CNF</i>	<i>CNC</i>
<i>Defibrillation process</i>	Mechanical or chemical & mech. ⁽⁴⁾	Acid hydrolysis ⁽²⁾⁽⁴⁾
<i>Defibrillation residues</i>	Bleaching agents ⁽⁴⁾	Sulphate groups ⁽⁴⁾
<i>Structure morphology</i>	65-95 % ⁽¹⁾	$\approx 100\%$ ⁽³⁾
<i>Width [nm]</i>	5-20 nm ⁽⁵⁾	4-15 nm ⁽³⁾
<i>Length [nm]</i>	$>1 \mu\text{m}$ ⁽⁶⁾	0.1-0.3 μm ⁽³⁾
<i>Particle morphology</i>	Rope-like in structure ⁽²⁾⁽⁴⁾	Needle-like in structure ⁽⁴⁾
<i>Particle distribution</i>	Ind. & bundle of micro & nanofibrils ⁽⁴⁾	Uniform nanoparticles ⁽⁴⁾
<i>Specific Surface Area</i>	Lower ⁽⁴⁾	Higher ⁽⁴⁾
<i>Hydrophilic property</i>	Equal ⁽⁴⁾	Equal ⁽⁴⁾
<i>Strength</i>	Higher ⁽²⁾	Lower ⁽²⁾
<i>Young's Modulus</i>	Higher ⁽²⁾	Lower ⁽²⁾
<i>Fracture toughness</i>	Higher ⁽²⁾	Lower ⁽²⁾

Table 2.3 Some characteristics of the CNs [(¹) Saito et al., 2007; (²) Eichhorn et al., 2010; (³) Boluk et al., 2014; (⁴) Fu et al., 2017; (⁵) Nasir et al., 2017; (⁶) Hisseine et al., 2018; (⁷) Barhoum et al., 2018]

<i>Cellulose Nanomaterials</i>	<i>Width</i>	<i>Length</i>	<i>Crystallinity</i>
<i>Cellulose Nanofibres</i>	5-20 nm (⁴)	>1 μm (⁵)	65-95 % (¹)
<i>Nanofibrillated Cellulose</i>	1-100 nm (⁶)	0.5-2 μm (⁶)	-
<i>Cellulose Filaments</i>	30-400 nm (⁶)	100-2,000 μm (⁶)	-
<i>Microfibrillated Cellulose</i>	10-1,000 nm (⁴)	0.5-10 μm (²)	-
<i>Cellulose Nanocrystal</i>	4-15 nm (³)	0.1-0.3 μm (³) (⁷)	$\approx 100\%$ (³) (⁴)
<i>Bacterial Cellulose</i>	6-10 nm (²)	30-50 nm (²)	65-90% (⁴)

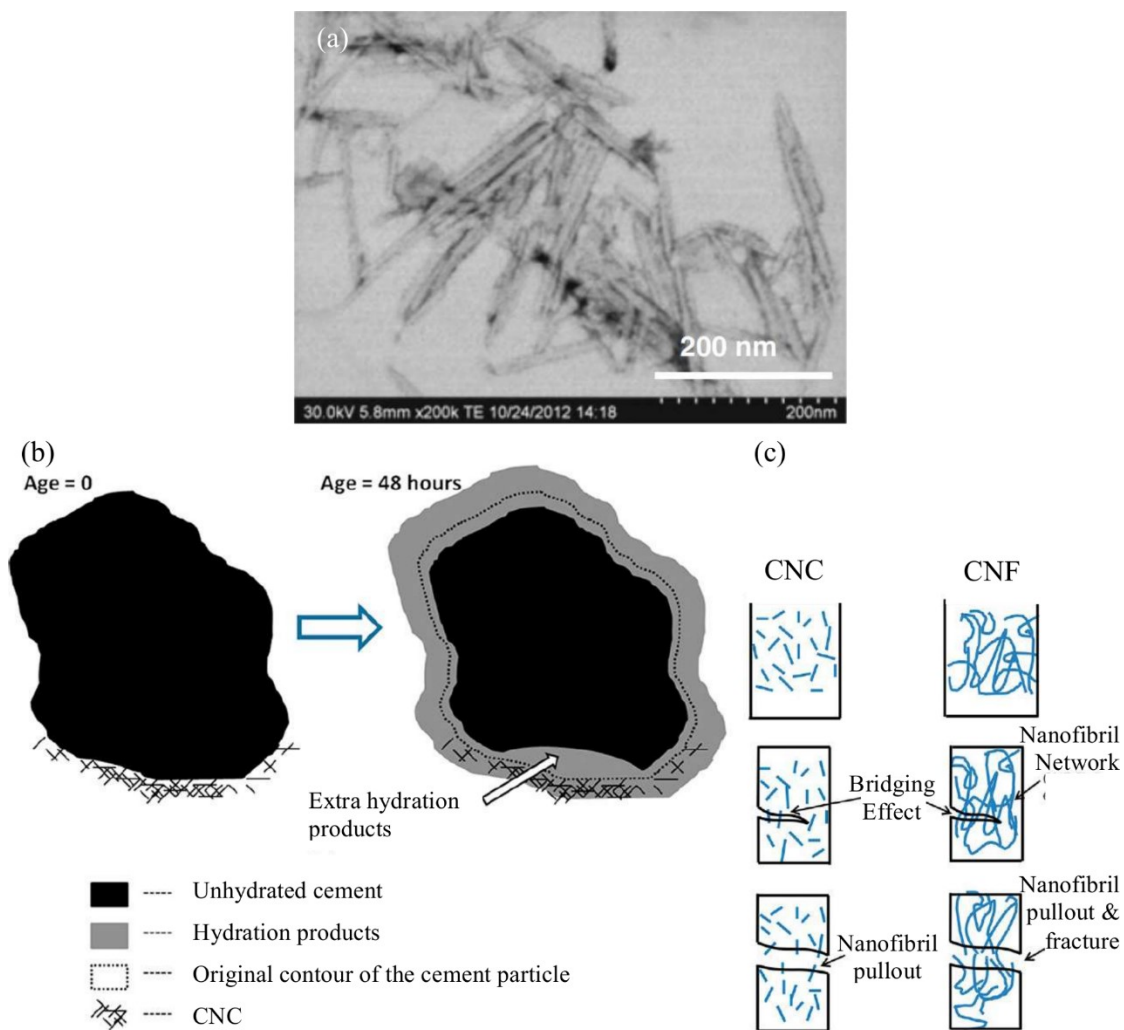


Figure 2.3.(a) TEM image showing the rod-like particles of CNC. Reprinted from Fig. 1 published in Boluk et al. [2014] (p. 4). (b) Illustration of the 'short circuit diffusion' mechanism. Reprinted from Fig. 12.b published in Cao et al. [2015] (p. 81). (c) Sketch of the CNF and the CNC bridging microcracks in a polymeric matrix. Reprinted from Fig. 15 published in Xu et al. [2013] (p. 3006).

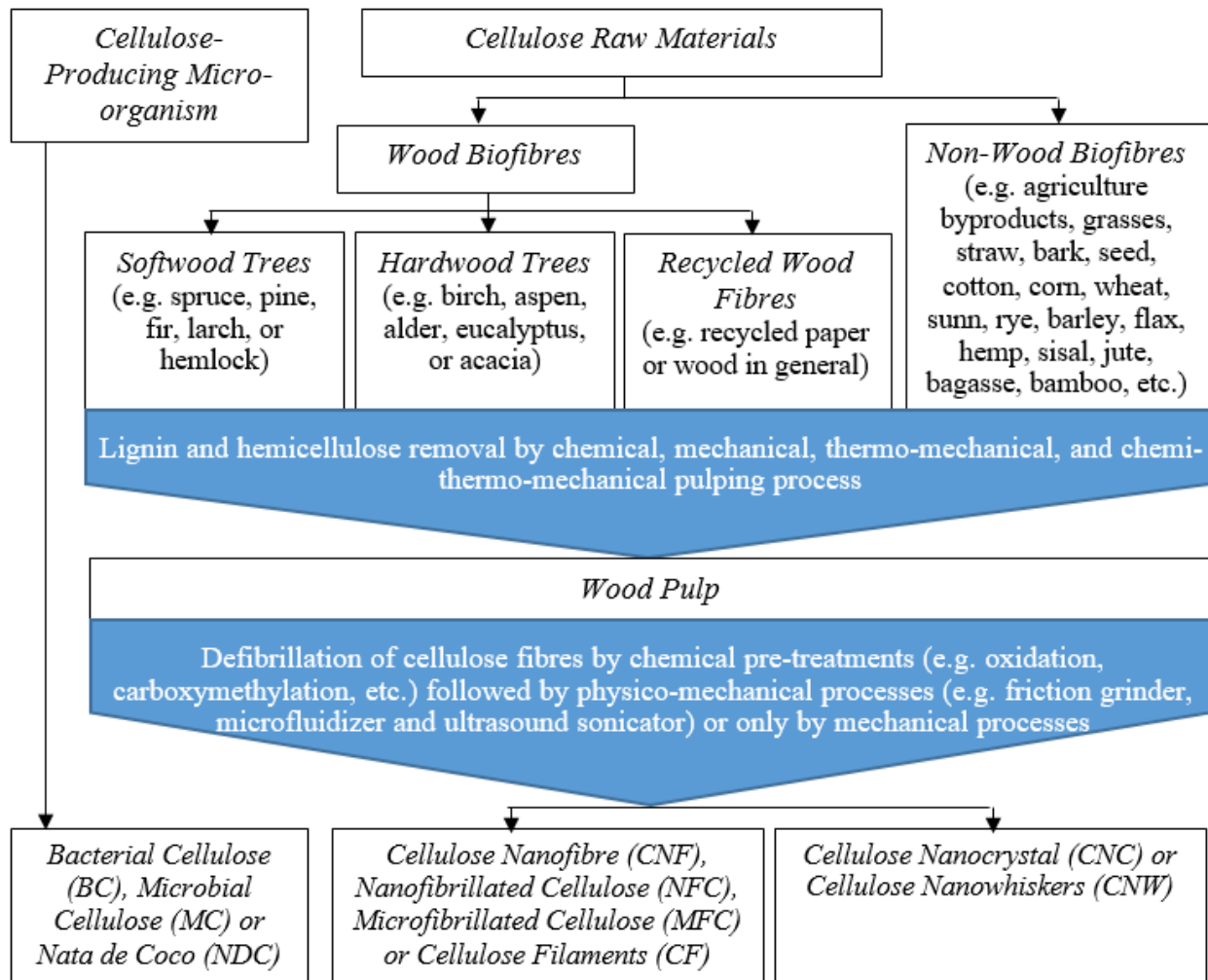


Figure 2.4 Flow illustrating the cellulose raw materials and the main stages in the manufacture of cellulosic nanoparticles.

2.5. Cellulose Nanofibres

Cellulose nanofibre (CNF) is a relatively new nanocellulose. The first articles on the isolation of cellulose microfibrils from pulp date back to the early 1980s [Turbak, Snyder, & Sandberg, 1984; Khalil et al., 2012; Gao, 2013]. Since then, its unique properties have enabled applications in different industrial segments [Postek, Moon, Rudie, & Bilodeau, 2013; El-Bakkari, Bindiganavile, Goncalves, & Boluk, 2019]; among others, medical, automotive, electronics, packaging and construction. More recently, CNF has attracted increasing attention to other range of uses, such as cement-based systems [Nasir et al., 2017].

The TAPPI standard nomenclature is CNF, but it is also referred in several scientific papers as NFC and MFC [Gao, 2013].

CNF is a low-cost material [Gao, 2013; Onuaguluchi et al., 2014; Landis et al., 2018], low-toxicity [Barhoum et al., 2018] new type of renewable [Onuaguluchi et al., 2014; Nasir et al., 2017; Fu et al., 2017; Landis et al., 2018] bio-based nanofibres naturally found in large amounts in nature [Sun, Wu, Lee, Qing, & Wu, 2016; Nasir et al., 2017; Fu et al., 2017; Barhoum et al., 2018; Landis et al., 2018]. In addition, it is compatible with hydrophilic matrices [Khalil et al. 2012; Isogai, 2018], such as cement-based systems. Landis et al. [2018] estimated the cost of CNF in US\$ 2.76/kg CNF slurry and Serra et al. [2017] in EU€ 9.29-14.94/kg for CNFs prepared by a chemical pretreatment known as TEMPO, i.e. (2,2,6,6-tetramethylpiperidine-1-oxyl radical)-mediated oxidation, with different carboxyl group contents; prices for Spanish market.

This cellulosic nanomaterial is obtained through mechanical refinement and homogenization processes of cellulose fibres without impurities, which were removed by means of mechanical, chemo-mechanical or thermo-chemo-mechanical processes [Isogai et al., 2011; Nasir et al., 2017; El-Bakkari et al., 2019]. High-pressure homogenization, microfluidization, ultrasonification, high speed disintegration and grinding are the most common mechanical mechanism used to defibrillate the cellulose fibres [Fu et al., 2017; Nasir et al., 2017; El-Bakkari et al., 2019].

However, they are high energy-consuming processes and thus pricey [Fu et al., 2017; Nasir et al., 2017]; beyond relatively inefficient to achieve individual microfibrils [Iwamoto, Lee, & Endo, 2014]. These facts turn the massive production of CNF for construction applications not feasible [El-Bakkari et al., 2019]. In response, chemical pre-treatments weaken the numerous inter-fibrillar hydrogen bonds that keep the microfibrils strongly attached to one another facilitating their subsequent mechanical disintegration [Nasir et al., 2017; El-Bakkari et al., 2019].

The most common chemical-assisted nano-fibrillation process is TEMPO or (2,2,6,6-tetramethylpiperidine-1-oxylradical)-mediated oxidation; another process is enzymatic hydrolysis [Saito et al., 2007; Iwamoto et al., 2014; Nasir et al., 2017; Landis et al., 2018; El-Bakkari et al., 2019]. TEMPO replaces hydroxyl groups onto CNF surface with carboxyl groups [Saito et al.,

2007; Isogai et al., 2011; El-Bakkari et al. 2019]. Consequently, TEMPO associated with a mild mechanical defibrillation – more moderate than without any chemical pretreatment – demonstrates high efficiency in yielding individualized microfibrils [Landis et al., 2018; El-Bakkari et al., 2019]. The result of these treatments is a homogeneous gel with CNF dispersed in water; if TEMPO is applied, this gel becomes more transparent [El-Bakkari et al., 2019].

Figure 2.5 illustrates the various aforementioned refinement stages and Figure 2.6 portrays a macro- and nano-view of CNF produced by TEMPO-mediated oxidation and mechanical disintegration at the facilities of Alberta Innovates as part of another research project at the University of Alberta.

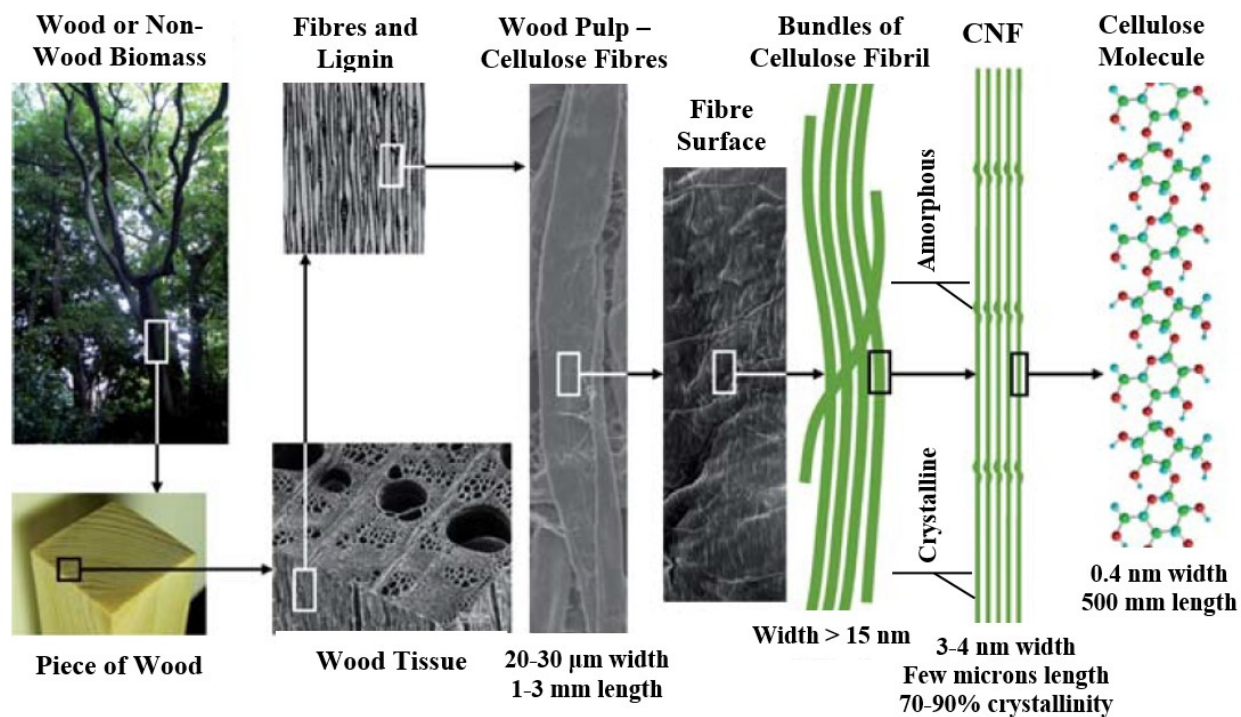


Figure 2.5 Hierarchical structure from lignocellulosic plant-based biomass to CNF, and its respective dimensional features. Adapted from Fig. 1 published in Isogai et al. [2011] (p. 72).

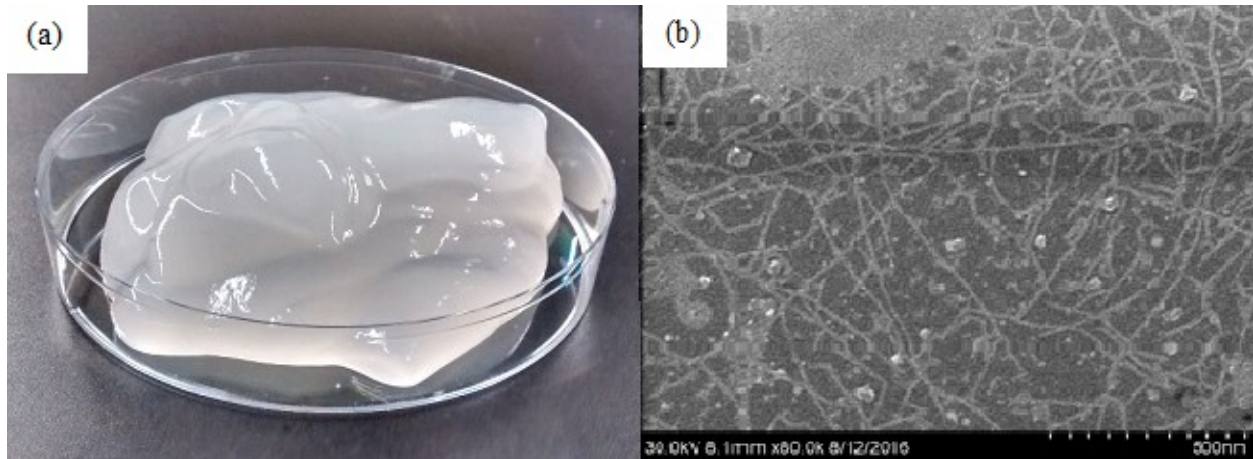


Figure 2.6 TEMPO CNF in water suspension shown on two scales: (a) the gel-like aspect in a macroscopic view; and (b) the individualized nanofibres and bundles of them (at the top) displayed in a SEM image. Reprinted from Fig. 4.a published in El-Bakkari et al. [2019] (p. 243).

CNFs are constituted by individualized microfibrils with 3-20 nm in wide [Saito et al., 2007; Isogai et al., 2011; Iwamoto et al., 2014; Sun et al., 2016; Mejdoub, Hammi, Suñol, Khitouni, & Boufi, 2017; Fu et al., 2017; Barhoum et al., 2018; El-Bakkari et al., 2019] and few micrometres long [Saito et al., 2007; Isogai et al., 2011; Sun et al., 2016; El-Bakkari et al., 2019] and by microfibril bundles containing 65-95 % crystallinity [Gao, 2013; Saito et al., 2007; El-Bakkari et al., 2019]; some authors [Iwamoto et al., 2014; Fu et al., 2017] estimated the microfibril length in 0.5-2 μm . Such micro- and nano-dimensions lead to a high aspect ratio between 30-300 [Xu et al., 2013; Iwamoto et al., 2014; Sun et al., 2016; Landis et al., 2018] and a very high free-dried specific surface areas from 140-160 m^2/g according to Sun et al. [2016] and 172-317 m^2/g as Serra et al. [2017]. Compared with the surface area of cement, that is 300-500 m^2/kg measured by Blaine method [Neville, 1995], CNF is 1000-1500 times higher.

Besides that, the active groups on CNF surface provide an electrostatic negative charge [Saito et al., 2007; Gao, 2013; Jiao et al., 2016; Isogai et al., 2011]. The higher the carboxyl group content, the greater the chemical reactivity of CNF [Serra et al., 2017]. The combination of these two features (i.e. high surface area and anionic charge) enables CNFs to a uniform dispersion [Fu et al., 2017], high chemical reactivity [Jiao et al., 2016], colloidal stability [Yang, 2011], tunability [Eichhorn et al., 2010], and exceptional hydrophilicity [Pei, Butchosa, Berglund, & Zhou, 2013; Landis et al., 2018; El-Bakkari et al., 2019]. From these features, two shall be highlighted. One is

the achievement of tuned performances by nanomodification of the anionic groups on CNF surface through chemical reactions with grafting agents or physical adsorption of molecules [Missoum, Belgacem, & Bras, 2013].

The other remarkable characteristic is the inherent hydrophilic nature, which capacitates CNF to retain high quantities of water. Serra et al. [2017] found water retention values varying from 3.9-11.4 g/g fibril for CNFs with carboxylic contents between 40-1392 $\mu\text{eq.g/g}$, respectively. El-Bakkari et al. [2019] obtained similar results, i.e. 3.62 g/g fibril for a carboxylate content of 0.13 mmol/g fibril and 13.4 g/g fibril for 1.13 mmol/g fibril. This capability in particular allows the manufacture of CNF concentrations of up to 3 wt.% in stable aqueous suspensions, as obtained by El-Bakkari et al. [2019].

Other physical characteristics are dry density oscillating from 1.15-1.51 g/cm^3 [Fujisawa, Okita, Fukuzumi, Saito, & Isogai, 2011; Ferrara et al., 2015; Serra et al., 2017], gel density of approximately 1 g/cm^3 [Landis et al., 2018], and density of pure cellulose around 1.5 g/cm^3 [Yang, 2011]. In terms of thermal properties, CNF presents a low coefficient of expansion, i.e. 7-10 k^{-1} [Abe, Iwamoto, & Yano, 2007]. And the degradation temperature occurs at about 200 °C with the decarboxylation of the carboxyl groups [Isogai, 2018]. Table 2.4 sums up some of the mechanical properties of CNF found in the literature review; the wide range of values reported reflects the use of distinct lignocellulosic raw materials and defibrillation methodologies in CNF preparation. Yang [2011] disclosed that the maximum theoretical elastic modulus of a microfibril is 27 GPa. The properties listed in the Table highlights the reinforcing potentials of CNF by means of the nanofibre bridging effects on micro-cracking propagation [Pei et al., 2013; Jiao et al., 2016; Eichhorn et al., 2010; Fu et al., 2017; El-Bakkari et al., 2019]. Such phenomenon is commonly perceived in macro and microfibre-reinforced concrete.

Needless to add, this suite of attributes confers upon CNF tremendous promise as a performance enhancing nano-additive to the cement and concrete industry.

Table 2.4 Tensile strength and Young's modulus of CNF films according to various authors.

<i>Tensile Strength [MPa]</i>	<i>Young's Modulus [GPa]</i>	<i>Reference</i>
54.7-145.9	11.05-13.00	Serra et al., 2017
-	145.2 ± 31.3	Jiao et al., 2016
312	2-6	Sun et al., 2016
200-300	-	Isogai et al., 2011
95-214	7.4-14.7	Yang et al. 2011
-	140-160	Eichhorn et al., 2010
312	2-6	Saito et al., 2007; Saito et al., 2007
222-233	6.2-6.9	Fukuzumi et al. 2008
129-214	10.4-13.7	Henriksson et al. 2008
104	14	Henriksson et al. 2007
180	13	Leitner et al. 2007

2.6. Cellulose Nanofibres in Cement-Based Systems

Cowie, Bilek, Wegner, and Shatkin [2014] reckoned the global market of cellulose nanofibres in cement-based products may reach an average of 4.13 million metric tonnes on a global basis; these numbers, according to the authors, correspond to only 25% of the potential market. Shatkin, Wegner, Bilek, and Cowie [2014] indicated the construction sector, and prestressed and precast concrete as those with the highest potential for high-volume applications of cellulose nanomaterials.

The future breakthroughs of concrete-related nanomaterials were analyzed by Sobolev et al. [2006] and Birgisson, Taylor, Armaghani, and Shah [2010]. Some of them are strictly addressed to durability issues, as follows: (i) internal moisture-controlling nanomaterials to mitigate the shrinkage (micro or nano)cracks and/or achieve non-shrinking concretes; and (ii) extremely high impermeable microstructures to attain more than 100-year service life in nano-modified concrete structures. As noted in the previous Section, CNF may meet such expectancies. The high chemical reactivity and hydrophilicity of CNF may afford special functionalities for cement-based systems. For example, CNF may impart the ability to control the water movements in benefit of the durability of CNF-cement-based materials. In other words, CNF may hold the water when this is abundant and thus mitigate the early-age shrinkage. And may release the water at late ages, when

is scarce, enhancing the impermeability through a denser microstructure. Moreover, CNF may also interfere in the deleterious chemical reactions scavenging key-elements (e.g. soluble calcium in pore solution) or even aggressive elements to concrete. And finally, the CNF tendency to form strong entangled network with up to several microns long associated to its reasonable intrinsic mechanical strength and natural flexibility may confer a nanoreinforcement capacity to expansive mechanisms as those observed in the sulphate attack on concrete and the corrosion of embedded bars.

Note that cellulose fibres have long been used in cement-based systems as rheology modifiers, viscosity enhancers or reinforcing agents. Indeed, the coarser cellulose microfibrils have proven themselves in (i) controlling plastic shrinkage, cracking development [Toledo Filho & Sanjuan, 1999; Banthia et al., 2006; Boghossian & Wegner, 2008; Pacheco-Torgal et al., 2011], drying shrinkage [Toledo Filho, Ghavami, Sanjuán, & England, 2005; Kawashima & Shah, 2011; Banthia, Bindiganavile, Azhari, & Zanotti, 2014] and autogenous shrinkage [Kawashima et al., 2011]; and (ii) enhancing tensile strength [Banthia, Moncef, Chokri, & Sheng, 1994], flexural strength [Metha et al., 2013], elastic modulus [Eichhorn et al., 2010], ductility, toughness, impact resistance [Banthia et al., 1994; Pacheco-Torgal et al., 2011], permeability [Banthia & Bhargava, 2007a], free-chloride penetration resistance [Sappakittipakorn & Banthia, 2011] and shotcrete pumpability [Banthia, Bindiganavile, Jones, & Novak, 2012a]. However, certain drawbacks come together with the addition of cellulose fibres. A less workable concrete due to CNF hydrophilicity and aspect ratio is an example [Onuaguluchi & Banthia, 2016]. Another is inconsistency in the fibre properties [Toledo Filho et al., 1999]. And ultimately to complete the list, the fibre depolymerization in alkaline environment of cement paste (or by means of weathering) [Ardanuy, Claramunt, García-Hortal, & Barra, 2011; Onuaguluchi et al., 2016] and the delay in setting time of paste as a result of sugar release from alkaline hydrolysis of fibres [Toloni et al., 2007].

Cement-based systems containing CNF have become a topic of study in the last 15 years. Thus, CNF trials are strictly nascent. The effect of CNF on the cementitious materials performance and respective physical and chemical mechanisms are still under analysis. This Section presents the state-of-art of knowledge on CNF in fresh and hardened cement-based systems. These studies concern hybrid micro- and nano-cellulose fibres or CNF. Cellulose filaments and bacterial

nanocelluloses, such as those examined by Peters, Rushing, Landis, and Cummins [2010], Claramunt, Ardanuy, Arévalo, Parés, & Tolêdo Filho [2011], Ardanuy, Claramunt, Arévalo, Parés, Aracri, and Vidal [2012], Hisseine et al. [2018], Cengiz, Kaya, & Bayramgil [2017] and da Costa Correia, Santos, Teixeira, and Junior [2018], are not covered by this literature review, because the length of these two cellulose nanoparticles is quite different from the CNF, i.e. they are too long or too short in length, respectively – see Table 2.3.

There are very few papers on this subject in the literature and some report conflicting conclusions. As a result, many issues remain unresolved. More research is required to clarify those unclear subject matters. Also, the majority of the literature focused on the mechanical properties of cement-based mixtures to evaluate CNF as a nanoreinforcement. Some authors investigated CNF as a curing agent in cement pastes; under this scope, early age and late age shrinkage was examined. In spite of the chemical reactivity made possible due to its nanosized dimension, no scientific literature has focused on CNF for durability enhancement in cement-based systems. Nor was the potential decay of CNF in alkaline environment considered. Therefore, to the authors' knowledge, this study marks a first in utilizing CNF's potential towards enhancing the durability of cement-based composites. Specifically, this study takes advantage of CNF's (i) high water retention, (ii) exposed abundantly with active hydroxyl and carboxyl groups and (iii) nanoscale dimension, to function at once, as both a chemical sink and a mechanical reinforcement towards effectively mitigating the adverse effects of sulphate and chloride attacks.

2.6.1. Mix Proportions

The earliest study on the effect of CNF upon the properties of cementitious materials was by Peters et al. [2010]. That study investigated the performance of micro- and nanocellulose, as well as the hybrid mixture of both, in ultra-high reactive powder cement mortars containing chemical additives. In 1% increment, up to 5% of CNF, by cement weight, were added to a control mortar. As a result of the CNF addition, the water-to-cement ratio of the 5% CNF mix design increased 11.2% in comparison with the control mortar ($w/c = 0.2172$ and 2.8 g of chemical admixture per kg of cement), and the growth of superplasticizer attained 39% to maintain a reasonable workability, as stated by the authors. The CNF concentration in water suspension was 3 wt.%.

Stephenson [2011] also developed ultra-high-performance concrete based on CNF-cement mixtures. The designed mix proportions were loaded with 0.5% and 1.0%, by cement weight. Superplasticizers were added to not change significantly the water-to-cement ratio. As the predecessor authors, Claramunt, Ardanuy, Arévalo, Parés and Tolêdo Filho [2011] and Ardanuy et al. [2012] incorporated 3.3 wt.% of nanofiber cellulose in cement mortars. According to Ardanuy et al. [2012], this nanocellulose content was the maximum possible to make a homogeneous mixture; superplasticizers were also added to aid workability. NFC was obtained after 6-hour mechanical refinement of sisal pulp.

Bindiganavile, Boluk, Saha and Mamun [2014] studied the effect of CNFs and CNCs in the shrinkage of pastes. The authors introduced two different CNFs in GU-cement pastes having 0.35 of water-to-cement ratio. The maximum fraction added was 0.3 vol.% for one CNF and 0.4 vol.% for the other. In this range, the optimum dosage was achieved, respectively, at 0.3 vol.% and 0.2 vol.%. These CNF contents were expressed as a fraction of the volume. Both CNFs were dispersed in water. One appeared as a cotton-like paste containing 10.6 wt.% of nanofibrils with 100 nm in width and 4-7 μm long. And the other was obtained by nano-fibrillation through multiple passes in the microfluidizer. The outcome of this refinement process was a star-branched network of nanofibrils with 40 nm in diameter and more than 10 μm in length. With a carboxylate content of 0.9 mmol/g of fibre. No superplasticizer was applied to the mixtures.

Onuaguluchi et al. [2014] worked with CNF-cement pastes with CNF dosages of 0.05%, 0.1%, 0.2% and 0.4%, by mass of cement. The CNF was in water suspension and the water-to-cement ratio was 0.5. The water content of CNF suspension was 98.1 wt.%. Besides, a superplasticizer at a maximum dosage of 1.6%, by mass of cement, was used to help the nanofibres dispersion.

Ferrara et al. [2015] mixed 2.3% cellulose nanofibres, by cement weight, along with 5.5 wt.% superplasticizer and other conventional raw materials to prepare a cement mortar. The concentration of nanofibres was 1.5 wt.%/litre of water.

Sun et al. [2016] examined oil well cement class H pastes loaded with 0.04 wt.%, 0.12 wt.%, 0.2 wt.% and 0.28 wt.% and water-to-cement ratio equal to 0.38; the percent was expressed by weight

of cement. The sulphuric acid hydrolysis of bleached wood pulp followed by high-pressure homogenization in a microfluidizer resulted in the CNF in water suspension used in the study.

Jiao et al. [2016] studied ordinary-cement pastes prepared with CNF fractions of 0.10%, 0.15%, 0.25% and 0.40%, by weight of cement. The water-to-cement ratio used was 0.35 for all mixtures. And the CNF suspension was obtained by a combination of TEMPO-mediated oxidation and mechanical homogenization. Mejdoub et al. [2017] also studied nanofibre cellulose produced by TEMPO followed by high pressure homogenization from eucalyptus pulp in cement pastes. The quantities added were 0.01%, 0.05%, 0.1%, 0.2%, 0.3% and 0.5% of NFC, by cement weight. The nanofibre cellulose concentration in water suspension was 1.5 wt.% and the carboxylic groups content 1.5 mmol/g fibre.

Differently from other authors, a concrete was produced by Machado et al. [2017]. The mixture with water-to-cement ratio of 0.23 contained 0.1%, 0.2% and 0.25% of CNF and 0.04% of superplasticizer; both materials expressed by weight of cement. The gel-like CNF encloses 2.5% of nanofibres in aqueous solution. Landis et al. [2018] added CNF not only into cement pastes, but also into concrete. A wide range of CNF (i.e. 0.05%, 0.1%, 0.2%, 0.5%, 1.0%, 1.5% and 3%, by volume) was incorporated in pastes with a large variety of water-to-cement ratios (i.e. 0.35, 0.4, 0.45 and 0.5). Similarly, 0.1-0.5%, by volume, of CNF was introduced in concrete. The water-to-cement ratio of concrete varied between 0.45 and 0.55. The concentration of the CNF in suspension was 3%, by weight.

2.6.2. Fresh Properties

2.6.2.1. Setting time

Jiao et al. [2016] reported that incorporating CNF in cement pastes delays the initial and final setting time in the region of 100 minutes and 90 minutes, respectively. As explained by the authors, the numerous active hydroxyl and carboxyl groups on nanofibre react with the calcium cations available in pore solution of cement paste and form a ring of hydrophilic complexes around the unhydrated cements particles. This ring hampers access to water slowing down the formation of hydrated products and lastly extends the setting time. As a consequence, the peak heat flow of the

paste with 0.15 wt.% of CNF was put off up to 8 hours. On the other hand, Mejdoub et al. [2017] observed that the nanofibre cellulose addition up to 0.5 wt.% accelerated the setting time of cement pastes; the initial and final setting times of control paste (estimated in 90 minutes and 230 minutes, respectively) were shortened in up to 38% and 23%, respectively.

2.6.2.2. Workability

Most of the authors declared the need to add high range water-reducing admixtures (e.g. superplasticizers) in cementitious mixtures containing CNF, in order to aid the workability [Peters et al. 2010; Stephenson 2011; Claramunt et al. 2011; Ardanuy et al., 2012; Onuaguluchi et al., 2014; Machado et al. 2017]. Jiao et al. [2016] suggested that additions of CNF in cement pastes should be followed by the use of superplasticizers.

Stephenson [2011] declared that 1.0 wt.% of CNF content was the limit achievable for a usable cementitious mixture in terms of workability, that is, pourable at fresh state. Still according to the author, minimal changes in superplasticizer content and water-to-cement ratio may considerably modify the fresh and hardened properties of ultra-high-performance CNF-cement-based concretes.

Jiao et al. [2016] experienced an increase in the water consistency of cement pastes as the fraction of CNF grows. The author claimed that the CNF aggregation reduces the workability. The same findings were observed by Machado et al. [2017] in CNF-reactive powder-based concretes. Both authors pointed the inherent hydrophilic nature of CNF and its high surface area as responsible for such behaviour. In the same manner, Landis et al. [2018] noticed that increments in CNF content dropped the workability of cement pastes and concretes; since that the hydrophilicity of CNF, besides its poor dispersion, limited the accessibility to free mixing water in fresh mixtures. According to those authors, an extra-mixing water amount of 5-8% per each 0.1% of CNF was added to maintain the concrete consistency.

2.6.2.3. Rheology

As reported in Section 2.6.2.2, adding CNF adversely affects the workability of the mixtures; although an increase in the CNF's carboxylate content greatly mitigates this drop in workability, as demonstrated in Sections 3.3 and 3.4. The reason of that is clarified by the rheological flow of

CNF-cementitious mixtures. Experiments in rheology of oil well cement class H pastes performed by Sun et al. [2016] indicated that the shear stress and shear rate increased with increments in CNF loadings. The plastic viscosity and yield stress followed the same trend. The best fitting data for the behaviour of flow rheology was Vom Berg model. Through this model, Sun et al. [2016] concluded that pastes with increasing CNF loadings presents shear-thinning effect. Alyaseen [2017] reported opposite findings. The author claimed that CNF-cement pastes exhibited a shear thickening behaviour (depending on the flow index) in accordance with Herschel-Bulkley rheological model. In consequence of this, the shear rate rose, and the workability declined. However, Alyaseen [2017] also presented an increase in the yield stress and viscosity as CNF dosage in cement paste rises, as observed by Sun et al. [2016] and Landis et al. [2018].

As the previous authors, Tang et al. [2019] also found that adding increments of CNF (at a concentration of 1 wt.% of gel) ranging between 0-0.2 wt.% of dry-cement raises the yield stress and the plastic viscosity of slurries with water-to-oil well cement ratio of 0.5. In addition, these rheological parameters showed a growth still higher if a finer CNF with a less entangled network is incorporated into the slurries. These findings were valid for all three mathematical models applied, i.e. Bingham, Modified Bingham, Herschel-Bulkley and Power law; although among these models, the Modified Bingham's model and Power law model demonstrated the most accurate fitting data. The authors [29] attributed the increase in the flow properties to a bridging effect provoked by the fibrils of CNF among the cement particles.

2.6.3. Hardened Properties

2.6.3.1. Compressive strength

Stephenson [2011] investigated the compressive strength of cementitious mixtures with CNF ranging from 0 to 1.0%, by weight of cement. The results indicated a marginal increase in compressive strength. To the same extend, Jiao et al. [2016] and Mejdoub et al. [2017] observed an increase in compressive strength for all CNF fractions examined. The best 28-day resistance performance achieved by Jiao et al. [2016] was at 0.15 wt.% of CNF loading for a range of 0-0.4 wt.% and by Mejdoub et al. [2017] at 0.3 wt.% of CNF for trials varying from 0-0.5 wt.%. These authors ascribed the paste strengthening to a denser paste microstructure. The hydrophilic nature,

nanoscale and high reactivity of carboxylic groups of NFCs intensified the formation of all hydration products; as a consequence, the degree of hydration was enhanced and porosity reduced. According to Mejdoub et al. [2017], high contents of NFC led to agglomeration zones that weaken the strength by means of stress concentration and premature cracking; despite the improvements in the dispersion of nanofibres proportionated by the anionic groups present on the NFC surface. Nonetheless, Jiao et al. [2016] observed an increase in the compressive strength only at late ages; given that the early-age strength slightly declined for all hardened paste trials. Inversely to that, Landis et al. [2018] exhibited a generalized drop in the 28-day compressive strength for cement pastes and concretes with different water-to-cement ratios and CNF quantities. The same reduction in compressive strength of concretes with CNF loadings up to 0.25 wt.% was revealed by Machado et al. [2017]. Other results from the same authors demonstrated equal scaling down for Young's modulus and flexural strength. Once more, the nanoscale and hydrophilicity of CNF were blamed for downgrading these mechanical properties.

2.6.3.2. Tensile strength

The CNF-cement mixtures of ultra-high performance concrete prepared by Stephenson [2011] demonstrated an increment in tensile strength. No further data was found in the literature.

2.6.3.3. Flexural strength, toughness and fracture energy

Peters et al. [2010] verified a marginal increase in toughness and fracture energy of CNF-cement mortars compared with the control mortar (without CNF). On the other hand, Stephenson [2011] found enhancements in the fracture energy only for the mixture containing 0.5 wt.% of CNF. The poor performance reported for the addition of 0.1 wt.% was imputed to an insufficient quantity of CNF and for 1.0 wt.% to a deficient workability and CNF agglomeration.

Claramunt et al. [2011] and Ardanuy et al. [2012] observed a meaningful decrease in toughness of cement mortars prepared with NFC from sisal pulp in comparison with the results of sisal pulp microfibrils; notwithstanding a slight increase in the flexural strength and flexural modulus. The growth in strength was attributed to a better stress transfer in fibre-matrix interface provoked by the hydrogen bonds between the hydroxyl of NFC and the cement hydrated products. On the other hand, this embrittlement of cement matrix associated to the low crack-bridging capacity lowered

the toughness. In this context, Eichhorn et al. [2011] stated that the aspect ratio (i.e. length by diameter) between 50 and 100 ensures an efficient nano-reinforcement.

In contrast, Onuaguluchi et al. [2014] verified an enhancement not only in fracture energy, but also in flexural strength of cement pastes ranging from 0.05-0.2 wt.% of CNF. At the optimum dosage of 0.1 wt.%, the authors found values more than three times higher for the energy absorption and twice the original strength when compared with the cement paste without nanofibres. The single exception was the mixture containing 0.4 wt.% of CNF, in which values were a bit smaller than the reference paste. Onuaguluchi et al. [2014] understood that the better mechanical behaviour was credited to a higher degree of hydration (at late ages) observed in the paste matrix and an improved nanofibre-paste bond; both boosted by the high specific surface area of CNF allied to its natural hydrophilicity. The downtrend in the properties ascertained for CNF contents over 0.1 wt.%, was accounted for an embrittled nanofibre-paste interface and fibre agglomeration [Onuaguluchi et al., 2014]. Figure 2.7 illustrates the non-homogeneous dispersion of CNF in the cement paste.

Analogous results for 28-day flexural strength were experienced by Sun et al. [2016] and Jiao et al. [2016]. In this case, the most advantageous CNF dosages were 0.04 wt.% and 0.15 wt.%, respectively. These authors reckoned that the strengthening of mechanical properties was assigned to improvements in the degree of hydration of cement paste induced by the hydrophilic nature, high surface area and a plentiful amounts of hydroxyl groups onto CNF surface; as also described by Onuaguluchi et al. [2014] and Mejdoub et al. [2017]. In addition to them, Sun et al. [2016] considered that the large aspect of CNF diverts and mitigates microcrack propagation, i.e. provides the 'bridging effect'. The weakening in resistance was ascribed by Sun et al. [2016] and Jiao et al. [2016] to the stress concentration in weak zones created by CNF agglomeration. However, it should be noted that Jiao et al. [2016] reported similar strengths at 3 days for pastes with and without CNF loadings. Thus, the increase in the strength at late ages is not observed at early ages. Here, the authors blamed the CNF reactions with the hydrated products of cement by the postponement of hydration period.

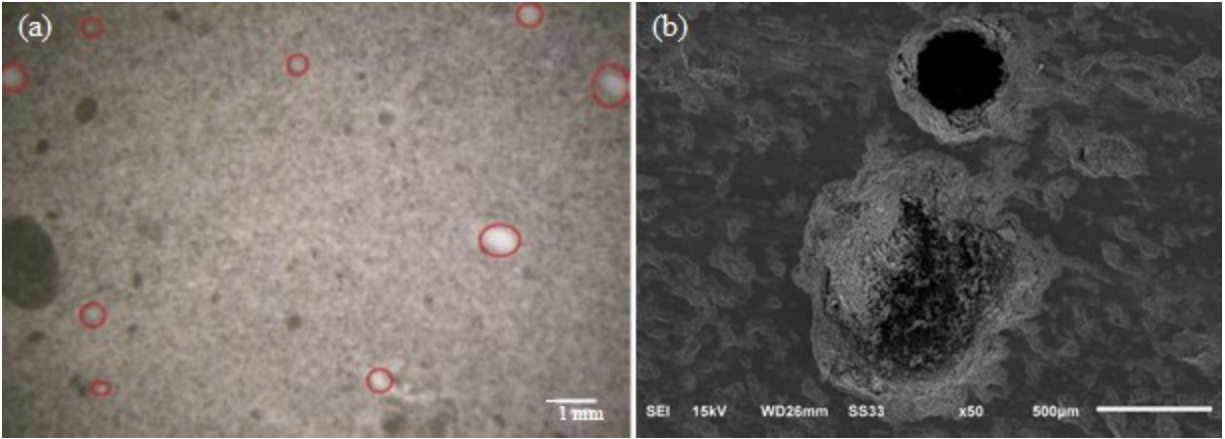


Figure 2.7 Pockets of cellulose nanofibres in a cement paste dosed with 0.4 wt.% CNF shown by (a) an optical microscope micrograph, and (b) a SEM micrograph. Reprinted from Fig. 6.b and Fig. 6.c published in Onuaguluchi et al. [2014] (p. 123), respectively.

2.6.3.4. Thermal properties

The increase in the thermal conductivity and the coefficient of thermal expansion of cement pastes with up to 0.3 wt.% NFC was attributed by Mejdoub et al. [2017] to a densification of paste promoted by the cellulose nanofibres.

2.6.4. Durability

2.6.4.1. Decaying of cellulose nanofibres in alkaline environments

The deterioration of cellulose microfibrils in alkaline environments, is an important concern. In such conditions, the lignin, pectin and other soluble sugars contents in nanofibres may potentially be decomposed by alkaline hydrolysis and thus reduce the durability of cementitious materials [Peters et al., 2010]. Although Jiao et al. [2016] made this concern explicit for CNF, note that the available studies address cellulose fibres (not CNF) [Marikunte & Soroushian, 1995; Mohr, Hood, & Kurtis, 2009] and come to conflicting conclusions. Nevertheless, as remarked by Marikunte et al. [1995], when the non-cellulosic component in the fibres is negligible, as it is in TEMPO CNF, it imparts CNF in cement-based systems with a better resistance to the alkaline environment.

2.6.4.2. Shrinkage

Stephenson [2011] claimed that the CNF mitigated the shrinkage during the curing period in ultra-high-performance mixtures. Bindiganavile et al. [2014] examined the performance of two different CNFs as curing agent in cement pastes. Both CNFs successful reduced the overall shrinkage (carried out in an accelerated experiment) for additions up to 0.3 vol.% of one CNF (in a range of 0-0.4%) and 0.2 vol.% of the other CNF (in a range of 0-0.3%); beyond that fraction, the shrinkage increased. The authors deemed the higher aspect ratio of the first CNF as the main reason for its superior effectiveness compared with the second one. Ferrara et al. [2015] verified a moderate increase in the drying shrinkage of cement mortars containing 2.3 wt.% cellulose nanopulps, notwithstanding a slight decreased in the autogenous shrinkage. Moreover, the authors concluded that the cellulose microfibrils of sisal and eucalyptus pulps fulfilled the role of curing agents better than the nanopulp. The findings of Landis et al. [2018] demonstrated a relative similar tendency, but in a different intensity. By and large, CNF increments had little positive effect on autogenous shrinkage and increased drying shrinkage. This behaviour was repeatedly verified in a wide range of CNF additions (i.e. 0.05-3.0 wt.%) and water-to-cement ratios (i.e. 0.35-0.55). As a result, only paste mixtures with low water-to-cement ratios (i.e. 0.35 and 0.40) and low-CNF contents (i.e. 0.01-0.2 wt.%) exhibited 90-day shrinkage performance rather similar to or better than the reference paste. Landis et al. [2018] understood that CNF performed a role similar to internal curing agents; that is, CNF enhances cement hydration at late ages and hence drops capillary porosity.

2.6.5. Degree of hydration

Onuaguluchi et al. [2014], Sun et al. [2016], Jiao et al. [2017] and Mejdoub et al. [2017] reported an increase in the degree of hydration for cement pastes as CNF fraction grows. All these authors credit this improvement to the superior curing conditions brought in by CNF. They claimed that CNF releases water to the vicinity's regions improving the hydration of cement particles not yet hydrated in prolonged ages, when the water is scarce. Jiao et al. [2016] attributed the lower to negligible effect of CNF in the early-age hydration rate of the hardened cement pastes to a delay in the cement hydration induced by the reactions between active hydroxyl and carboxyl groups of cellulose molecules and calcium ions soluble in pore solution. Onuaguluchi et al. [2014] found the

hydration peak of CNF-cement mixtures was postponed in about 7 hours, as well as the initial hydration of cement. Similarly, Jiao et al. [2016] reported that the peak of heat flow in cement pastes with CNF was moved to 8 hours later. Distinctively from Jiao et al. [2016], Onuaguluchi et al. [2014] attributed this delay to the interference of the products released in the alkaline hydrolysis of cellulose microfibrils in cement hydration. On the contrary, Mejdoub et al. [2017] reported a higher degree of hydration in cement pastes up to 3 days than at later ages as the CNF fraction increases. In this case, the early-age betterment was ascribed by the author to an enhanced CNF dispersion in paste and the capacity of CNF to promote cement hydration.

2.7. Concluding Remarks

The overall shrinkage of concrete may roughly be represented by the plastic shrinkage and drying shrinkage. The latter encompasses the autogenous shrinkage. Nonetheless, the most important volume reduction in concrete is drying shrinkage. The bleeding, loss of moisture and evaporation rate of cement paste are some of the most relevant parameter to measure shrinkage in concrete. Sulphate ions from internal and external sources to concrete take part in a series of interdependent, complex and superimposing physical-chemical reactions with the hydrated products of cement paste. These undesirable reactions may damage concrete through several expansive mechanisms, such as conventional ettringite expansion, delayed ettringite formation and salt hydration expansion. On top of that, chloride ions are equally disastrous to concrete integrity. These tiny ions may disintegrate the protective film that covers the steel bars and intensify the corrosion process.

In recent years, a new range of innovative nanomaterials have been developed to improve strength, durability and sustainability in cementitious materials. However, several disadvantages have hampered their application.

CNF is a novel type of nanocellulose with outstanding hydrophilic characteristics and nanoscale chemical activity. The use of CNF in cementitious materials is a rather new matter. Just few related papers were found. The majority of them focus on the potentialities of CNF as a nanoreinforcement and a curing agent. No one approached durability issues, such as attack of sulphates and chlorides in reinforced cement-based materials.

CHAPTER 3. Mix Design

3.1. Introduction

The present study aims to investigate the effect of CNF as an agent to mitigate the effect of some common aggressive physical and chemical sources of distress in cement-based systems. The most common Portland cement types were chosen to represent the cementitious mixtures that encounter such distress. Accordingly, the binders were chosen to possess special features, such as high sulphate resistance. CNFs with distinct morphology and carboxyl group content were mixed in various amounts in the reference plain cement-based mixture. The superplasticizer and fine aggregate used were the commonly available ones. All raw materials employed in the research came from a unique batch and from the same supplier, to minimize any variation in the results.

A series of cement pastes and cement mortars were produced as part of this study. The object of the paste series was to maximize the deleterious mechanisms that govern shrinkage and related phenomena, as explained in the previous CHAPTER 2. Besides, it is to examine the effect of CNF on the physico-chemical microstructure of cement paste. On the other hand, mortars are required by most current standards and test methods to evaluate the outcome of the sulphate attack and the chloride action. Mortar specimens were also employed to evaluate the ionic ingress of chloride, instead of concrete as recommended by the respective standard method.

In this CHAPTER are found the relevant characteristics of the raw materials and the mix proportions of the pastes and mortars with different CNF fractions. Furthermore, the criterion adopted to mix the CNF-based cement mixtures are described. The procedure to mix the raw materials and, in particular, to prepare CNF before the mixing are reported, in detail. And lastly, some physical properties of the mixtures are presented. In total, 14 distinct paste mixtures and 19 different mortar mixtures were developed for the present study.

3.2. Raw Materials

3.2.1. CNF

The Cellulose Nanofibres (CNF) were used in their never-dried state (i.e. in gel state or in water suspension) and are termed simply CNF henceforth in this thesis. The fibres were in water suspension, so as to prevent any hornification among the nanofibrils. The most important characteristics of CNF analyzed in this research were the concentration of nanofibres in water suspension and their carboxyl group content. These characteristics are together believed to be key parameters that affect the performance of conventional cementitious mixtures.

Three different CNFs were used, all in water suspension. Each one with a different carboxylate content, i.e. 0.13 mmol/g of fibre, 0.7 mmol/g of fibre and 1.13 mmol/g of fibre, as demonstrated in Table 3.1. The first was a commercially sourced nanofibre, while the other two were manufactured by Dr. M. El-Bakkari (Dr. V. Bindigavile's post-doctoral fellowship) at the Pilot Plant jointly set up by the University of Alberta, at the Alberta Innovates campus, as part of a separate research project mentored by Dr. Y. Boluk. These latter two CNFs were prepared from bleached chemi-thermomechanical pulp (BCTMP) subjected firstly to TEMPO-mediated oxidation and then to mechanical disintegration in the ultra-fine friction grinder (or 'supermasscolloider'). The entire procedure is depicted by El-Bakkari et al. [2019] and is illustrated in Figure 3.1. In this thesis, henceforward, these three CNFs are identified as CNF #0.13, CNF #0.7 and CNF #1.13, respectively, alluding to their individual carboxylate content. All CNFs were never-dried and showed a gel-like aspect. The CNF #0.13 presented a cotton-like appearance, whereas the TEMPO-oxidized CNFs are gels, being relatively transparent, as portrayed in Figure 3.2.

The morphological structure of CNF #0.13 and CNF #1.13 is revealed by the scanning electron microscope (SEM) micrographs shown in Figure 3.3. As visualized in Figure 3.3.(a), CNF #0.13 consists of a mix of (mostly) microfibrils and nanofibrils, many in bundles. Figure 3.3.(b) reveals a different picture for CNF #1.13. Here, a network of uniformly distributed nanofibrils with 5 nm – 20 nm in width and a few microns long, is seen.

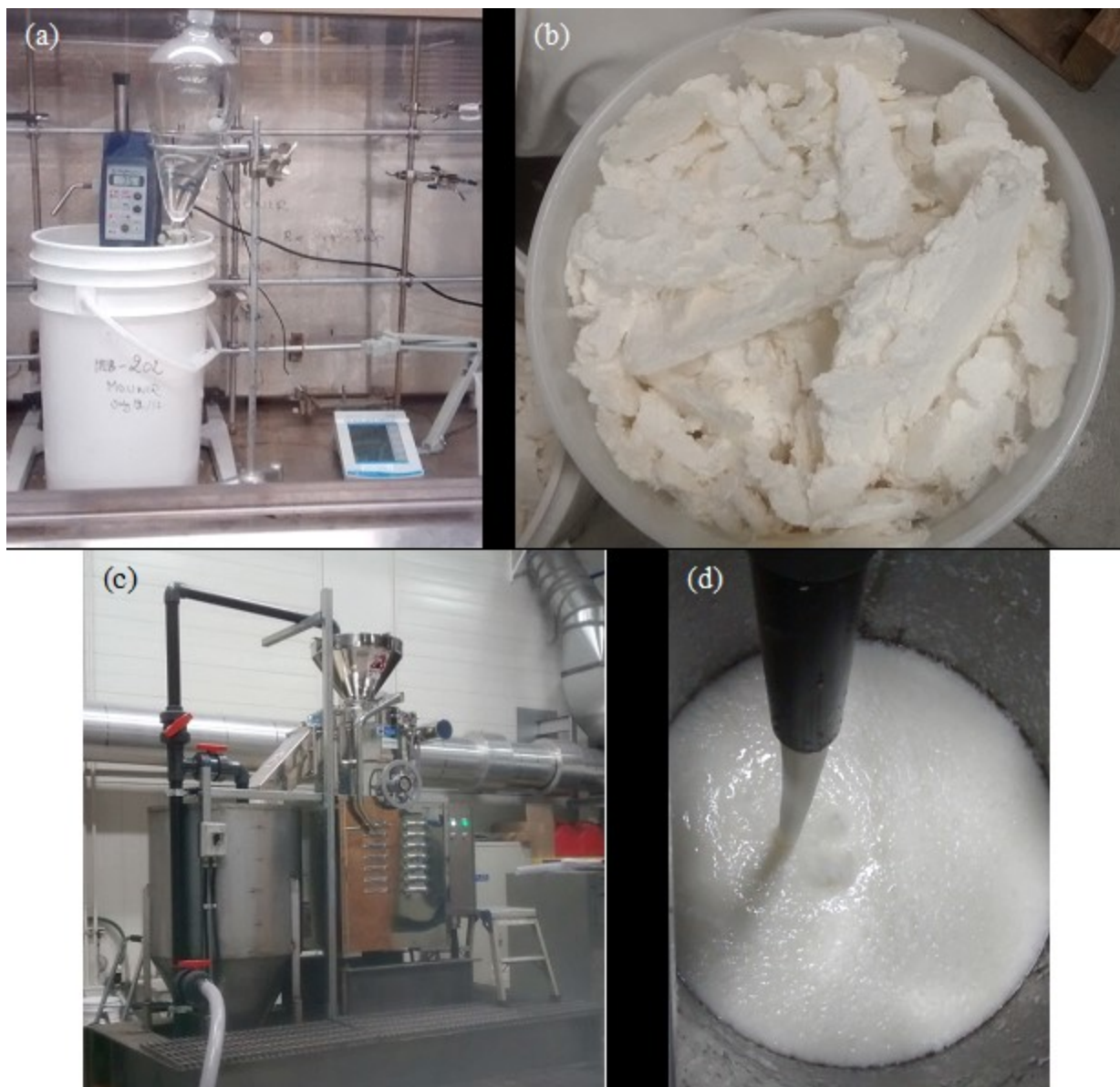


Figure 3.1 General view of the main steps used in CNF preparation. The (a) TEMPO pretreatment is applied to (b) BCMT pulp followed by (c) mild disintegration in the ‘supermasscolloider’, and finally (d) yielding CNF.

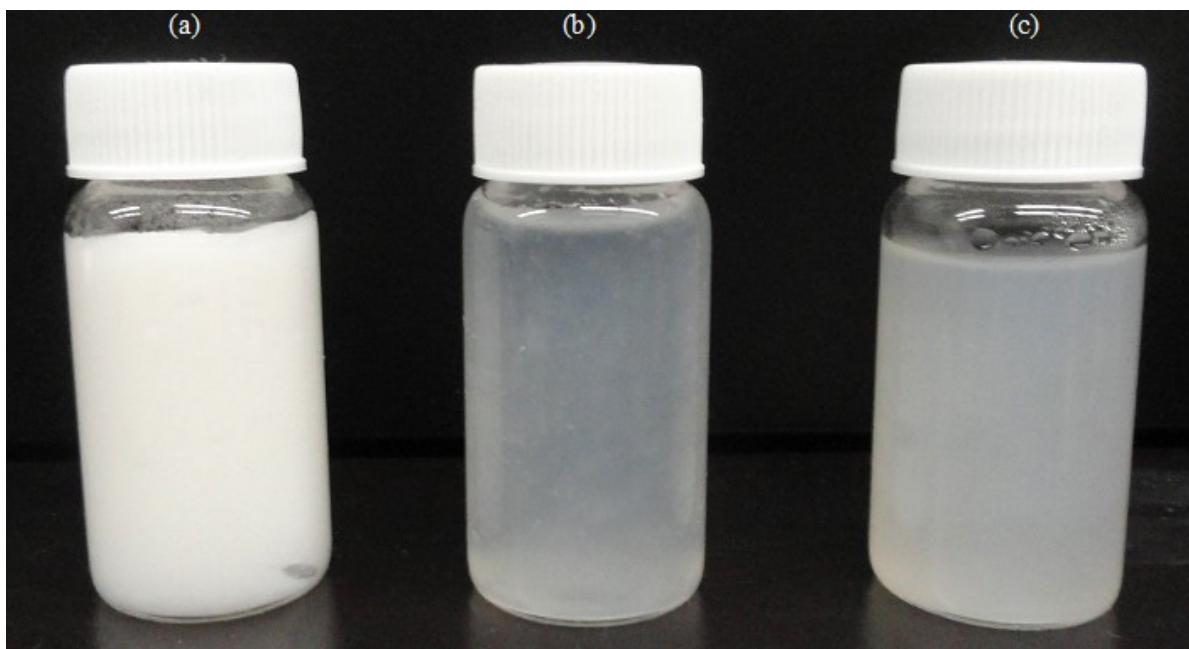


Figure 3.2 Visual images of the (a) CNF #0.13, (b) CNF #0.7, and (c) CNF #1.13.

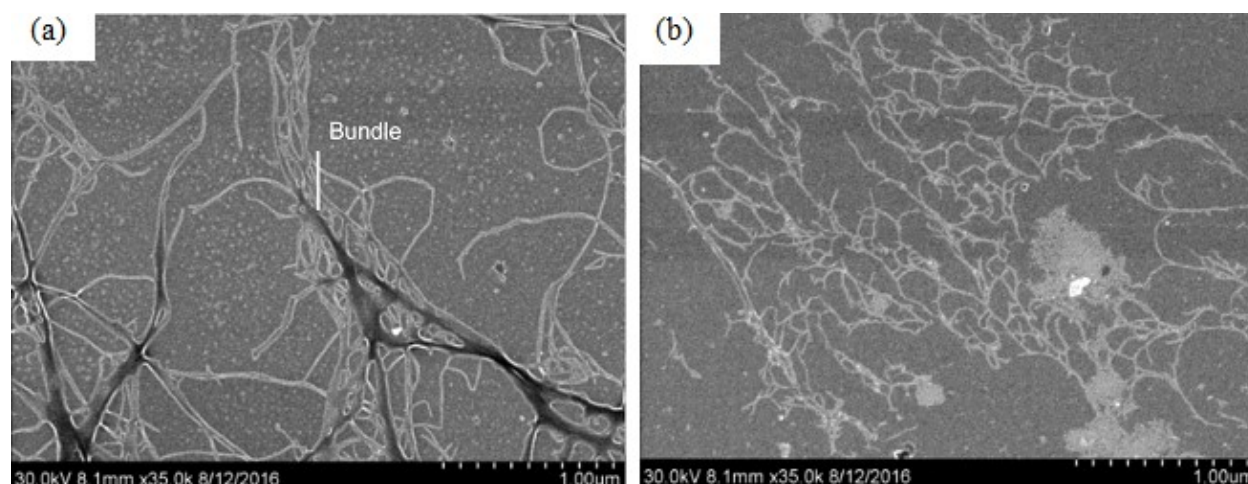


Figure 3.3 SEM images of the (a) CNF #0.13 and (b) CNF #1.13.

Some of the CNFs relevant characteristics are listed in Table 3.1. The densities of CNFs in water suspension were measured by pycnometer method with a pycnometer bottle of 25 mL – see Figure 3.4.(a); the density of dry-CNF was assumed 1.5 g/cm^3 [Fujisawa et al., 2011; Gao, 2013]. The solid content, expressed as a percentage of the total mass, was determined by drying the sample at $40 \pm 1^\circ\text{C}$ on a hot plate up to constant mass – see Figure 3.4.(b). The carboxylate content of the TEMPO-oxidized CNFs was determined by measuring the electric conductivity, using the titration method [Saito & Isogai, 2004] and the water retention value according to the method described by

Saito et al. [2007]. The carboxylate content and the water retention of the CNFs were computed by Dr. M. El-Bakkari, who was Dr. V. Bindigavile's post-doctoral fellowship. The calculation method of the crystallinity index was based on the amorphous area shown in the X-ray diffractogram (XRD) of an 8-hour vacuum oven-dried samples at $40 \pm 1^\circ\text{C}$, as described by Segal, Creely, Martin Jr, and Conrad [1959] – see Figure 3.5. The XRD analysis was carried out in a model Bruker D8 Discover with GADDS 2-dimensional detector workstation, with Copper-K α radiation (operated at 40kV and 40mA), with step size of 0.02° and with count time of 120 s/step from 5° to 112° diffraction angle.

Table 3.1 Some characteristics of the CNFs.

<i>CNF</i>	<i>Density</i>	<i>Solid Content</i>	<i>Carboxylate Content</i>	<i>WRV</i> ^(a)	<i>CI</i> ^(a)
<i>Identification</i>	<i>[g/cm³]</i>	<i>[%]</i>	<i>[mmol/g of fibre]</i>	<i>[g/g of fibre]</i>	<i>[wt.% crystal]</i>
<i>CNF #0.13</i>	1.0112	2.945	0.13	3.62	69.6
<i>CNF #0.70</i>	1.0036	0.714	0.70	6.28	-
<i>CNF #1.13</i>	1.0101	2.8528	1.13	8.39	69.0

^(a) The abbreviation 'WRV' means 'water retention value' and 'CI' 'crystallinity index'.

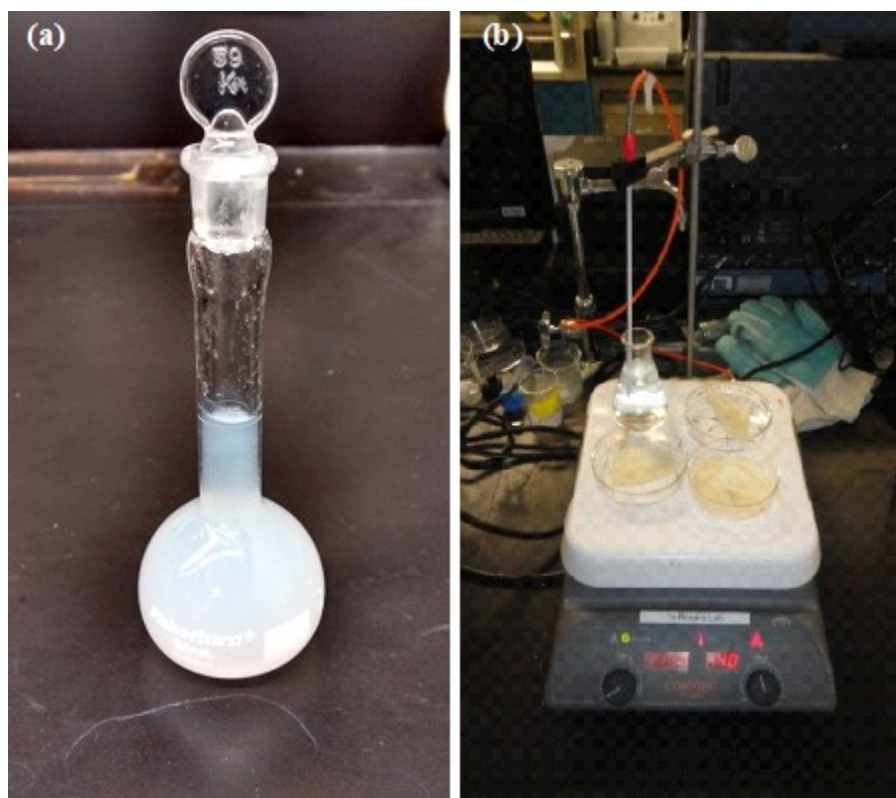


Figure 3.4 View of the (a) pycnometer and (b) solid content system used in the CNF gel analysis.

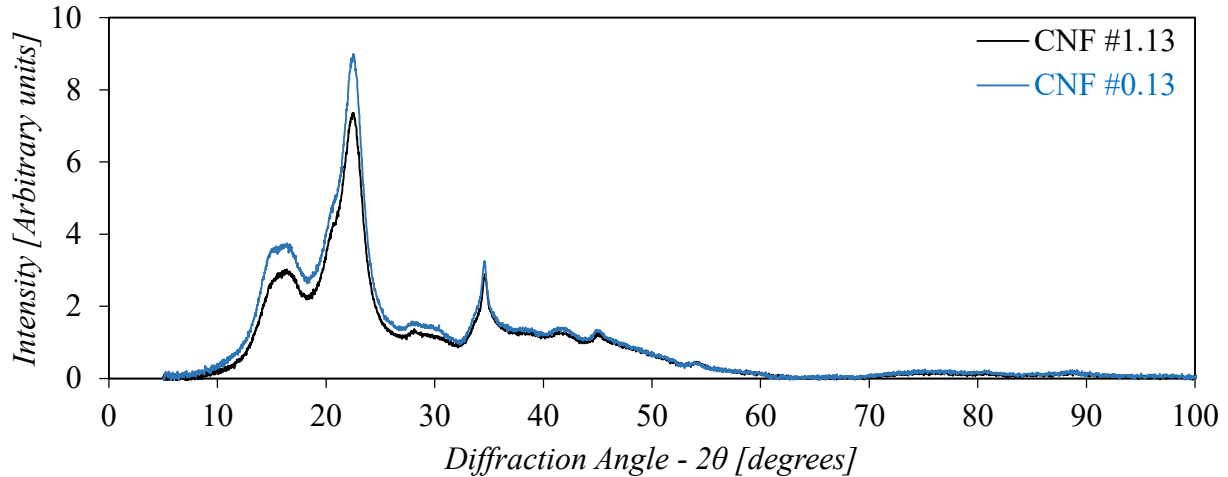


Figure 3.5 The X-ray diffractograms of the oven-dry samples of CNF displayed an extensive amorphous phase for diffraction angles (2θ) between 5° and 30° .

3.2.2. Portland Cement

The most commonly used cement type in Canada, that is, the Portland cement Type (GU) as per CSA A3000 [Canadian Standards Association (CSA), 2013], was utilized as the reference cement in the whole study. As well, in order to examine for the sulphate attack mitigation, three other cement types were employed. They were (i) a high-sulphate resistant Portland cement Type HS, (ii) high-early strength Portland cement Type HE, and (iii) a blended binder with 70% Type Portland cement and 30% Fly Ash (GUb).

The cement mineral composition and the sulphate ions content (from cement or from other sources) play a key role in the sulphate attack mechanism, as demonstrated in Section 2.2.2. The reference cement, Type GU, usually presents high tricalcium aluminate (C_3A) content; thus, it is more susceptible to sulphate attack. Type HS cement has the lowest C_3A content among all Portland cements. Type HE is the most reactive cement and often contains more gypsum (i.e. calcium sulphate dihydrate, $CaSO_4 \cdot 2H_2O$), than the other cement types, which makes Type HE vulnerable to sulphate attack. Given that only the Type GU fraction in the blend GUb contains any C_3A , the sulphate resistance of GUb is expected to be higher. The definition and requirements for the two Portland cements and the blended binder are listed in CSA A3000 [CSA, 2013]. The density for each of the Portland cement Types GU, HE and HS was assumed to be 3.15 Mg/m^3 and that for the blend GUb was taken as 2.88 Mg/m^3 .

Table 3.2 reports their physical and chemical characteristics. The cement and fly ash were supplied by Lehigh Hanson Canada.

Table 3.2 Physical and chemical characteristics of the cements, and their mineral composition. The relevant chemical elements for sulphate attack are in bold. Data provided by Lehigh Hanson.

<i>Portland Cement Type</i>		<i>GU</i>	<i>GUb</i>	<i>HE</i>	<i>HS</i>
<i>Chemical Analysis</i>					
<i>Silicon dioxide (SiO₂)</i>	[%]	20.0	-	20.2	21.1
<i>Aluminum oxide (Al₂O₃)</i>	[%]	4.6	-	4.8	3.5
<i>Iron oxide (Fe₂O₃)</i>	[%]	3.4	-	3.4	4.7
<i>Calcium oxide (CaO)</i>	[%]	62.6	-	62.1	62.1
<i>Magnesium oxide (MgO)</i>	[%]	2.7	-	2.7	2.5
<i>Sulphur trioxide (SO₃)</i>	[%]	2.7	2.7	3.3	2.2
<i>Loss on Ignition</i>	[%]	2.3	1.6	1.7	1.7
<i>Sodium oxide (Na₂O)</i>	[%]	0.2	-	0.2	0.3
<i>Potassium oxide (K₂O)</i>	[%]	0.4	-	0.4	0.5
<i>Insoluble residue</i>	[%]	0.5	-	-	0.4
<i>Total Alkalis</i>	[%]	0.5	0.3	0.5	0.6
<i>Mineral Composition calculated by Bogue Methodology</i>					
<i>Tricalcium silicate (C₃S)</i>	[%]	59	-	53	56
<i>Dicalcium silicate (C₂S)</i>	[%]	13	-	17	18
<i>Tricalcium aluminate (C₃A)</i>	[%]	6.5	-	6.9	1.4
<i>Tetra-calcium aluminoferrite (C₄AF)</i>	[%]	10	-	10	14
<i>Physical Properties</i>					
<i>Blaine</i>	[m ² /kg]	421	545	614	443
<i>Retained on 45µm sieve</i>	[%]	4.2	5.2	1.1	2.8
<i>Autoclave expansion</i>	[%]	0.110	0.013	0.073	0.035
<i>Vicat initial setting</i>	[min]	78	94	47	97
<i>Sulphate expansion</i>	[%]	-	-	0.0	0.0
<i>False setting</i>	[%]	75	78	-	73
<i>Air content</i>	[%]	8.2	5.7	-	8.3
<i>Compressive strength at 28 days</i>	[MPa]	43.1	38.4	43.7	40.5

3.2.3. Other Materials

The quartz sand used in the experiments meet the requirements established in ASTM C1012/C1012M [ASTM International (ASTM), 2015] and ASTM C 596 [ASTM, 2009], except by the grading requisites for fine aggregate defined in ASTM C778 [ASTM, 2013]. The grain size distribution complies with ASTM C33/C33M [ASTM, 2016] instead. In order to meet this standard grading limits, a blend of commercial quartz sands was optimized up to achieve the final proportion of 65% of sand Granusil 2075, 20% of sand Granusil 4075 and 15% of sand Granusil 7030, as seen in Figure 3.6. All these sands were supplied by UNIMIN Inc. In practical terms, the standard sand used was a bit coarser than that recommended by ASTM C778 [ASTM, 2013]. However, this is not expected to impact the experimental outcomes. The oven-dry relative density of sand was 2.635 Mg/m^3 and the bulk density 1.589 Mg/m^3 . They were determined, respectively, by ASTM C128 [ASTM, 2015] and ASTM C29/C29M [ASTM, 2016].

The polycarboxylate-based superplasticizer, MasterGlenium[®] 3030 [BASF Corporation, 2018], had a density of 1.048 g/cm^3 and solid content of 32.5%. These characteristics were evaluated by the same methodologies as used for analyzing the CNF. Distilled water was used only in the specimen preparation for chemical analysis.

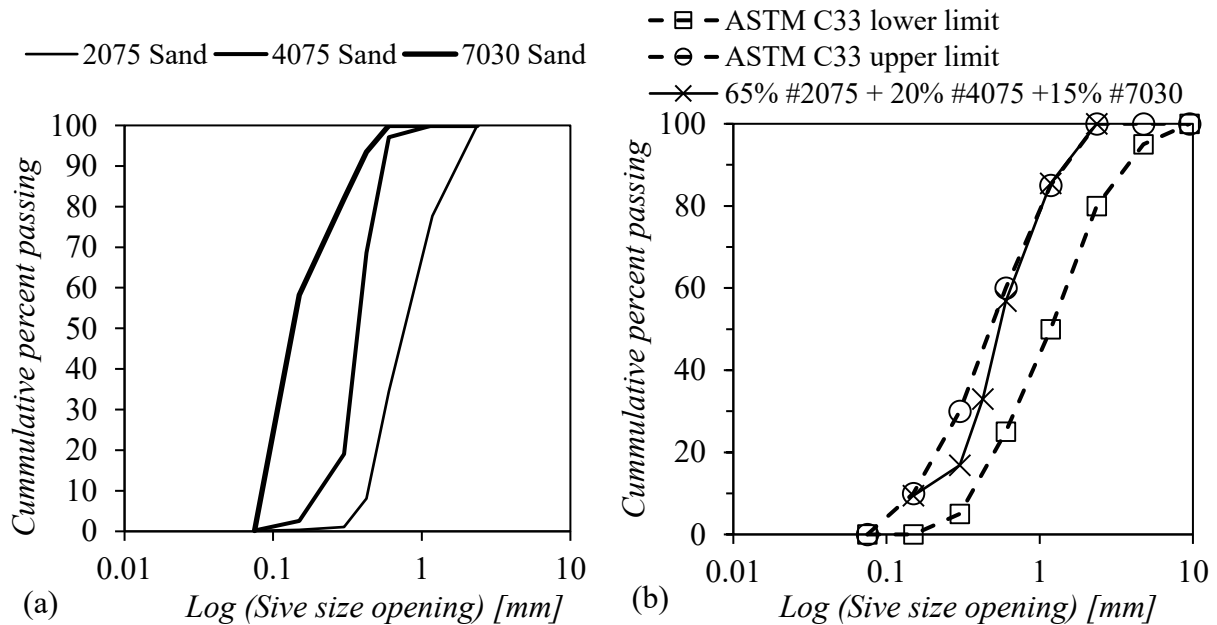


Figure 3.6 The grain size distribution of (a) the quartz sands #2075, #4075 and #7030, and (b) the optimized blend of these sands meeting the grading limits of ASTM C33/C33M [ASTM, 2015].

3.3. CNF-based Cement Mortar Mixtures

The ASTM standard test methods for evaluating drying shrinkage, sulphate penetration, sulphate expansion and chloride resistivity are oriented to cement mortars and cement concretes. Only two of the ASTM standard methods used to evaluate the performance of CNF-based cement mortars stipulate control mix proportions. Between them, the mix proportion defined in ASTM C 1012/C1012M [ASTM, 2015] was chosen, given that the other, ASTM C 596 [ASTM, 2009], does not specify a unique water-to-cement ratio; this ratio may vary according to the cement type. Therefore, the proportion of materials assumed for the control mortar in the whole study was 1-part cement to 2.75-part sand by mass and water-to-cement ratio by mass of 0.485.

The consistency of the control mortar made of type GU cement and sand ASTM C33/C33M [ASTM, 2016] was the reference to assume the typical flow range of $30 \pm 5\%$ for all mortar mixtures. The flow of mortars was determined in accordance with the ASTM C1437 [ASTM, 2015] – see Figure 3.7.



Figure 3.7 View of the flow table test apparatus used to determine the consistency of mortars.

The quantities of CNF gel added to the control mortars in increments of 0.1% were calculated based on the amount of dry CNF determined as a fraction of the volume of mixture, as follows:

$$V_{dry\ CNF} = v_{dry\ CNF} / v_{concrete} \quad (3.1)$$

where $V_{dry\ CNF} [\%]$ is the desired volume fraction of dry CNF, $v_{dry\ CNF} [dm^3]$ is the volume of dry CNF for a specific concrete volume $v_{concrete} [dm^3]$. The conversion of dry CNF in volume to CNF gel in mass was proceeded according to the following formula:

$$m_{CNF\ gel} = (v_{dry\ CNF} / (\gamma_{dry\ CNF} \times C_{dry\ CNF})) \times 100 \quad (3.2)$$

where $m_{CNF\ gel} [kg]$ is the mass of CNF gel, $\gamma_{dry\ CNF} [kg/dm^3]$ is the density of dry CNF, and $C_{dry\ CNF} [\%]$ is the concentration of nanofibres in CNF gel.

As shown in the literature review (see Section 2.6.2.2) of the thesis, the addition of CNF reduces the mortar workability, a superplasticizer was incorporated to maintain constant the flow of CNF-based cement mortars. The quantity of chemical admixture was defined by trial and error experiments until successfully meet the required flow range. These dosages varied according to the CNF loadings and CNF type. The limit for the high-range dosage of admixture recommended by the manufacturer is 1170 mL/100 kg of cementitious materials; notwithstanding this value may change according to specificities of each mixture.

The amount of water contained in the CNF gel and in the superplasticizer was discounted from the total mix water according to the following equations:

$$m_{water} = m_{water\ w/c} - m_{ded\ water} \quad (3.3)$$

$$m_{ded\ water} = m_{water\ w/c} - [m_{CNF\ gel} \times (1 - C_{dry\ CNF}/100) + m_{SP} \times (1 - C_{dry\ SP}/100)] \quad (3.4)$$

where $m_{water} [kg]$ is the mass of water added to the mixture, $m_{water\ w/c} [kg]$ is the mass of water calculated based on the water-to-cement ratio, $m_{ded\ water} [kg]$ is the deducted water mass, to account for that contained in the CNF gel and the superplasticizer, $m_{SP} [kg]$ is the mass of the superplasticizer, and $C_{dry\ SP} [\%]$ is the solid content in the superplasticizer. This way, the water-to-cement ratio for all mortars remained equal to 0.485. In terms of mix design, if the mixing water is completely replaced by the water coming from the CNF gel and the chemical admixture, it means that the maximum fraction of CNF was achieved. The limit reached for CNF #1.13 was 0.5030

vol.% (or 0.5% for the sake of the simplicity). CNF #1.13 loadings higher than this limit increases the water-to-cement ratio. The same limiting condition restrained the maximum CNF #0.7 fraction to 0.1551 vol.% (or, if rounded, 0.2%). The topmost fraction possible for CNF #0.13 was attained at 0.3 vol.% for GU cement and 0.2 vol. % for the other cement types. Here, the impediment to reach greater contents of CNF was the elevated dosage of superplasticizer, i.e. 6,000 mL/100 kg. Values greater than this led to a noticeable the postponement by at least 24 hours in the final setting time of mortar; notwithstanding this content exceeded by far the limit suggested by the supplier. However, to better compare the performance of CNF #0.13 with the CNF #1.13 (note that both of these CNF samples were prepared at a 3% solid nanofibre concentration in the gel), the maximum fraction of CNF #0.13-based GU cement mortars was extended up to 0.5 vol.%; that is, the same as reached by CNF #1.13. That said, the superplasticizer dosage was maintained the same for fibre volume beyond obtained for 0.3 % fraction. Hence, their workability was lower when compared to the other mixtures. Table 3.3 lists all 13 distinct mortar mixtures. Figure 3.8 portrays the impact of CNF fractions on the superplasticizer dosage and workability of mortars.

Table 3.3 Mix proportions of the GU-cement mortars containing different CNF loadings.

<i>CNF Type</i>	<i>Dry CNF</i> [vol.%]	<i>Materials [kg/m³]</i>						
		<i>Dry CNF</i>	<i>CNF gel</i>	<i>Cement</i>	<i>Water</i>	<i>Aggregate</i>	<i>SP</i>	<i>Deducted Water</i>
<i>Control</i>	0	0	0	541.3	262.6	1489	0	0
<i>CNF #0.13</i>	0.1	1.496	50.79	539.8	208.0	1485	6.750	53.85
	0.2	2.984	101.3	538.5	154.5	1481	12.34	106.7
	0.3	4.445	150.9	534.8	90.30	1471	33.43	169.1
	0.4	5.922	201.1	534.3	41.43	1469	33.40	217.7
	0.5	7.173	243.6	533.9	0	1468	33.38	258.9
<i>CNF #0.7</i>	0.1	1.499	210.0	540.9	52.88	1487	1.350	208.5
	0.2	1.875	262.8	540.7	0	1487	2.055	260.7
<i>CNF #1.13</i>	0.1	1.498	52.52	540.7	210.6	1487	0.9860	51.7
	0.2	2.992	104.9	540.1	158.5	1485	2.251	103.4
	0.3	4.483	157.1	539.3	106.2	1483	4.074	155.4
	0.4	5.968	209.2	538.5	53.76	1481	6.172	207.4
	0.5	7.494	262.7	537.7	0	1479	8.264	260.8

Note: 'SP' is superplasticizer.

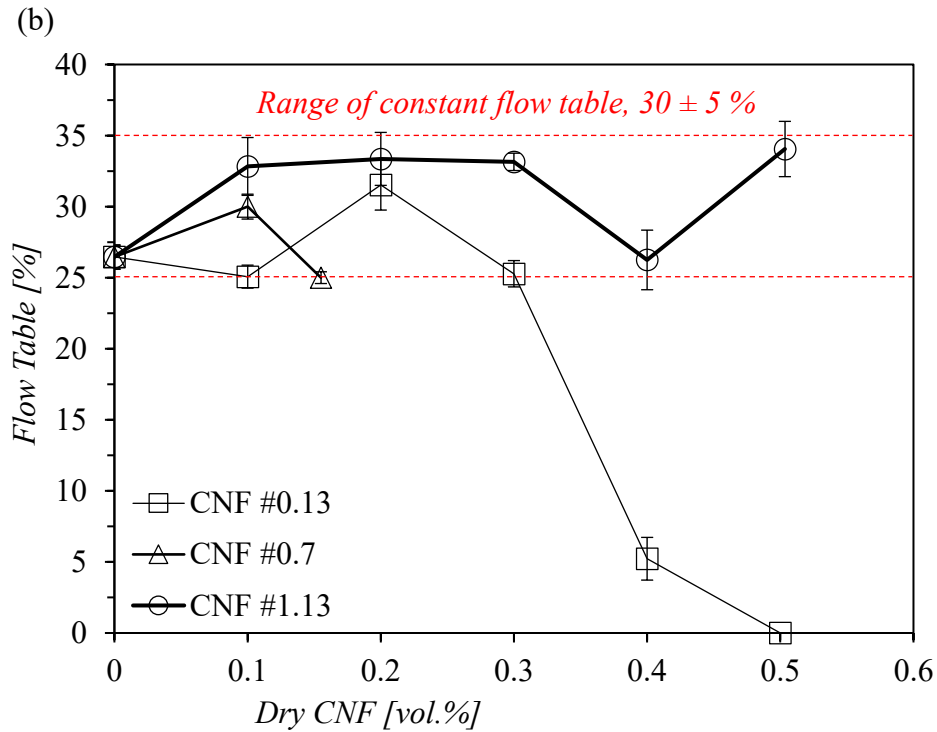
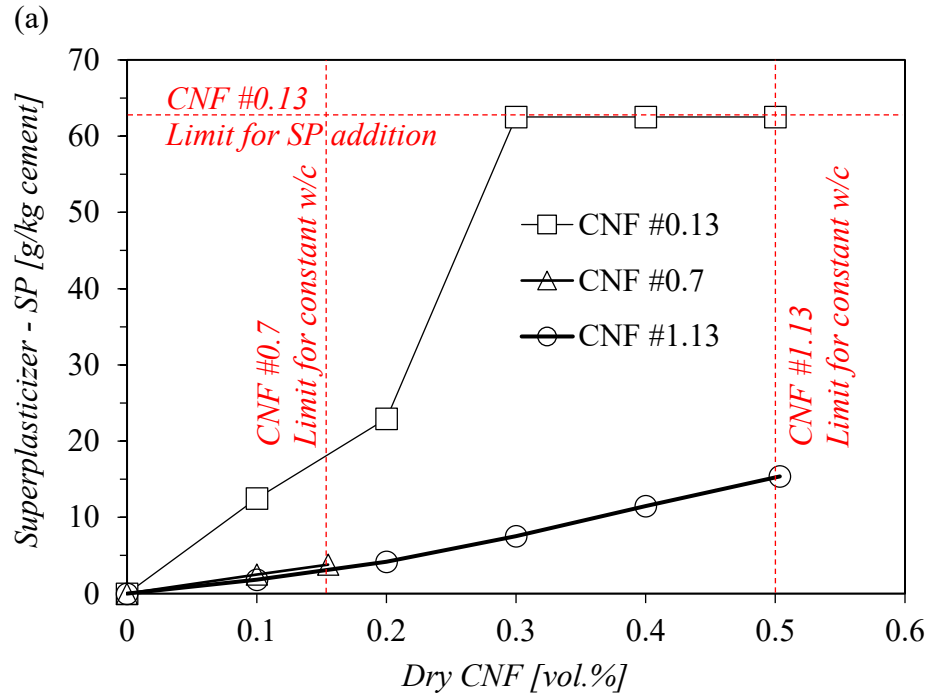


Figure 3.8 Effect of CNF loadings on: (a) superplasticizer demand, (note: the insert text in red offers the reasons for the CNF limit); and (b) flow of CNF-based GU-cement mortars, showing the acceptable consistency limits in red dashed lines.

The same procedure described above was applied to design the mortar mixtures based on other cement types (HS, HE and GUb) and containing various CNF #0.13 loadings. The maximum volume fraction of dry CNF #0.13 incorporated into the control mortar (maintained the water-to-cement in 0.485 and the flow table in $30 \pm 5\%$) was 0.2%. Table 3.4 reports these mix-proportions.

The raw materials used to prepare the control mortar were mechanically mixed in accordance with ASTM C109/C109M [ASTM, 2016], excluding the mixer. Instead, the high-intensity mixer shown in Figure 3.9.(a) with higher capacity of mortar production was employed. The appropriated rotational speeds were adjusted by trial and error, comparing the mortar consistency obtained by each mixer. The same procedure was adapted for mixing mortars loaded with CNF. Both procedures are delineated in Table 3.5.

Before to be introduced into the mixer bowl, the CNF in suspension was diluted in the mixing water in order to improve the CNF dispersion in the mortars. The general lines to proceed with pre-mixing was to blend together 500-800 mL of CNF gel and mixing water for at least 30 minutes in a stirring mixer with a steel four-blade propellers having 3" in diameter and 3/8" bore. The rotational speeds differ according to the CNF fraction and the CNF type, as demonstrated in Table 3.6. Figure 3.9.(b) shows the mixer and Figure 3.10 gives a visual idea of the mixing efficiency of the procedure.

Some of the physical characteristics of the cement mortars prepared with different cement types and CNF #0.13 loadings are shown in Table 3.7. These features were determined in accordance with ASTM C642 [ASTM, 2013]. Furthermore, the compressive strength of these same CNF #0.13-based mortar mixtures was measured at 28 days old as per ASTM C109/C109M. These results are recorded in Table 3.8.

Table 3.4 Mix proportion of the HS-cement mortars, HE-cement mortars and GUb-cement mortars containing different CNF #0.13 fractions.

<i>Cement Type</i>	<i>Dry CNF [vol.%]</i>	<i>Materials [kg/m³]</i>						
		<i>Dry CNF</i>	<i>CNF gel</i>	<i>Cement</i>	<i>Water</i>	<i>Aggregate</i>	<i>SP</i>	<i>Deducted Water</i>
<i>Control</i>	<i>0</i>	0	0	541.3	262.6	1489	0	0
<i>HS</i>	<i>0.1</i>	1.496	50.78	539.8	207.5	1484	7.36	54.26
	<i>0.2</i>	2.983	101.3	538.4	153.7	1481	14.5	107.4
<i>HE</i>	<i>0.1</i>	1.495	50.77	539.6	206.6	1484	8.59	55.07
	<i>0.2</i>	2.982	101.2	538.0	152.1	1480	15.7	108.9
<i>GUb</i>	<i>0.1</i>	1.520	51.62	539.9	207.6	1485	6.14	54.24
	<i>0.2</i>	3.033	103.2	538.7	153.7	1481	11.2	107.5

Note: 'SP' is superplasticizer.

Table 3.5 Procedure for mixing the control cement mortar and the CNF-based cement mortars.

<i>Control Cement Mortar</i>	<i>CNF-based Cement Mortars</i>
Place all the mixing water in the dry bowl.	Place about 2/3 of the CNF gel and the mixing water previously mixed (Figure 3.10) in the bowl.
Add the cement to the water and then start the mixer at 30 r.p.m. for 60 secs.	Add the cement to the water and then start the mixer at 30 r.p.m. for 60 secs.
Pour the sand over 30 secs and then increase the mixing speed to 45 r.p.m. for 60 secs.	Pour the sand over 30 secs and then increase the mixing speed to 45 r.p.m. for 60 secs.
Stop the mixer, scrap down any mortar on the bowl wall for 15 secs, cover the bowl with a lid and lastly let the mortar stand for more 75 secs.	Stop the mixer, scrap down any mortar on the bowl wall for 15 secs, add the superplasticizer manually mixed with the 1/3 left of the pre-mixture in the bowl (Figure 3.11), cover the bowl with a lid and let the mortar stand for 75 secs.
Turn on the mixer for more 60 secs at 45 r.p.m.	Turn on the mixer at 45 r.p.m. for 90 secs.

Table 3.6 The minimum stirring speeds [r.p.m.] assumed to dilute CNF gel in mixing water.

<i>CNF Type</i>	<i>Dry CNF [vol.%]</i>				
	<i>0.1%</i>	<i>0.2%</i>	<i>0.3%</i>	<i>0.4%</i>	<i>0.8%</i>
<i>CNF #1.13 gel</i>	500	550	600	650	700
<i>CNF #0.7 gel</i>	300	300	400	500	-
<i>CNF #0.13 gel</i>	600	700	850	1000	-

Table 3.7 Absorption, density and voids of the CNF #0.13-based GU cement hardened mortars.

<i>Cement-Dry CNF #013</i> [vol.%] Mix	<i>Absorption</i> ^(a) [%]	<i>Bulk density dry</i> [Mg/m ³]	<i>Apparent density</i> [Mg/m ³]	<i>Vol. permeable</i> <i>pores</i> [%]
<i>GU-0%</i>	5.59	2.134	2.423	11.93
<i>GU-0.1%</i>	5.26	2.157	2.433	11.34
<i>GU-0.2%</i>	5.32	2.128	2.399	11.32
<i>GU-0.3%</i>	5.79	2.118	2.414	12.27
<i>GU-0.4%</i>	5.72	2.126	2.420	12.16
<i>GU-0.5%</i>	6.77	2.108	2.459	14.26
<i>HS-0%</i>	5.26	2.163	2.441	11.39
<i>HS-0.1%</i>	5.07	2.124	2.380	10.76
<i>HS-0.2%</i>	5.00	2.132	2.387	10.65
<i>HE-0%</i>	5.43	2.106	2.378	11.43
<i>HE-0.1%</i>	4.93	2.092	2.332	10.31
<i>HE-0.2%</i>	5.26	2.082	2.338	10.96
<i>GUb-0%</i>	4.39	2.171	2.400	9.53
<i>GUb-0.1%</i>	4.55	2.107	2.331	9.58
<i>GUb-0.2%</i>	4.62	2.114	2.344	9.78

^(a) After immersion and boiling.

Table 3.8 Compressive strength at 28 days of mortars mixed with various cement types and CNF #0.13 ranges.

<i>Cement</i> <i>Type</i>	<i>28-day Compressive Strength [MPa]</i>					
	<i>Control</i>	<i>Dry CNF #0.13 [vol.%]</i>				
		<i>0.1</i>	<i>0.2</i>	<i>0.3</i>	<i>0.4</i>	<i>0.5</i>
<i>GU</i>	53.00	45.84	46.56	46.15	47.80	50.13
<i>HS</i>	53.02	43.98	44.07	-	-	-
<i>HE</i>	52.64	49.88	47.69	-	-	-
<i>GUb</i>	42.24	38.01	37.77	-	-	-

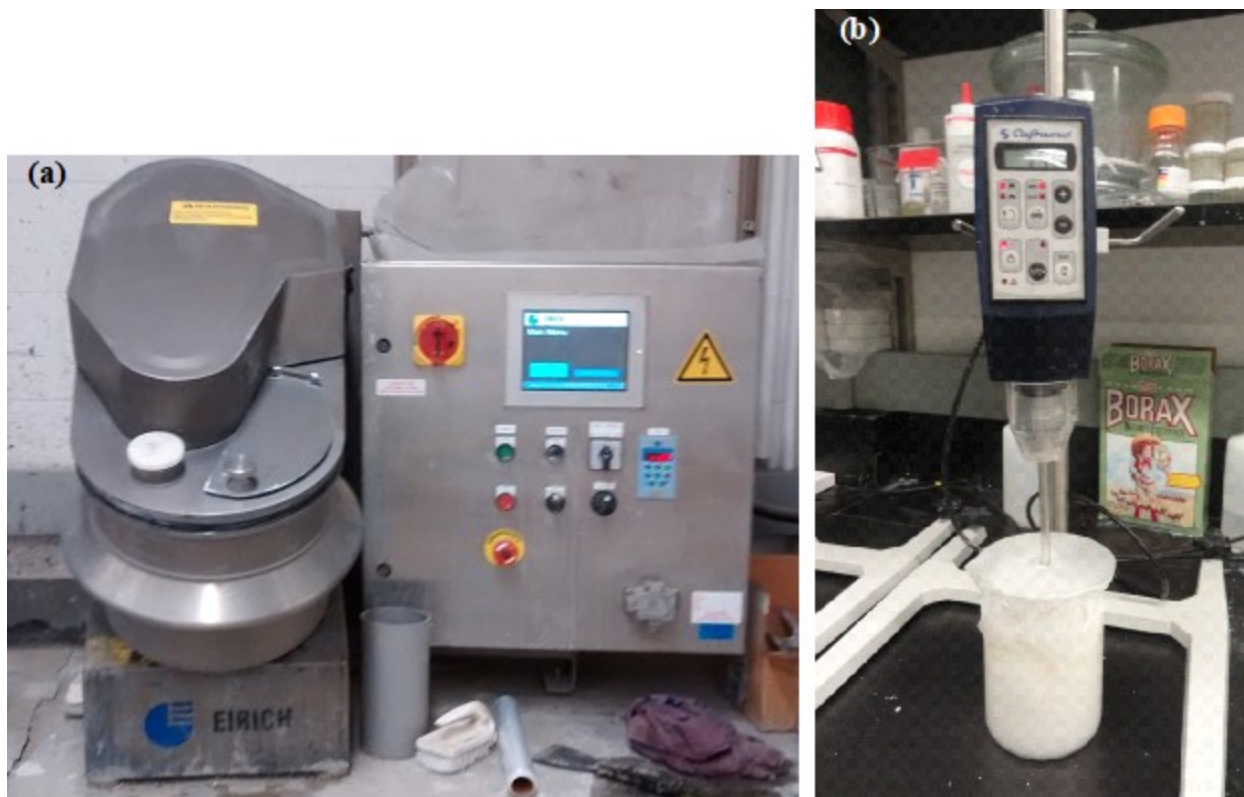


Figure 3.9 View of the (a) high-intensity mixer used to mix the mortars, and (b) stirring mixer utilized to pre-mix the CNF gel and mixing water.

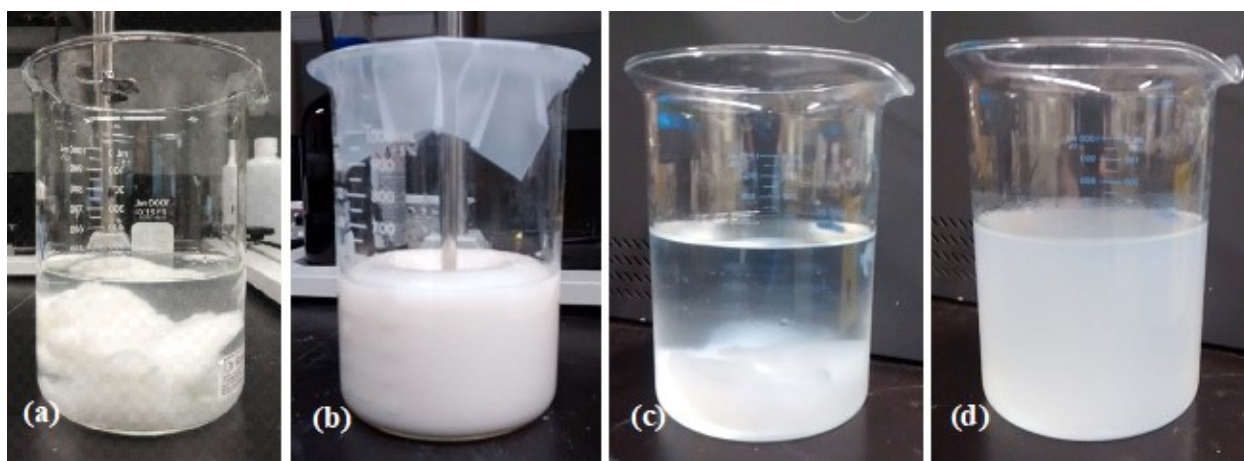


Figure 3.10 CNF #0.13 gel and mixing water (a) before and (b) after the mixing. And CNF #1.13 (c) before and (d) after the same procedure. In both cases, a homogeneous mixture is visually obtained.



Figure 3.11 View of the superplasticizer (a) before and (b) after the manual mixing with around 1/3 of the CNF-mixing water pre-mixture.

3.4. CNF-based Cement Paste Mixtures

As mentioned in Section 3.3, the ASTM standard test methods for measuring the drying shrinkage are not based on cement paste specimens. Thus, in the absence of any related guidance, the water-to-cement ratio was taken as 0.485, both for the control paste and the control mortar; this ratio was the same used for mortar mixtures.

The paste specimens were used to assess several properties, such as overall shrinkage, drying shrinkage, cracking area, bleeding rate, evaporation rate, degree of hydration, porosity and mineralogical composition. The paste was made by using Type GU. Dry CNF was incorporated to the control paste as a volume fraction of paste in increments of 0.1%. The quantities of dry-CNF and CNF gel were computed as described for mortars. All pastes shall have the same: (i) flow, and (ii) water-to-cement ratio of 0.485. The flow was determined as per the modified ASTM C939/C939M [ASTM, 2016]. The changes in the standard were in the methodology used to measure the efflux time and in the flow cone apparatus. The cone with 1725 ± 5 mL capacity and the paste discharge tube of 12.7 mm in diameter was substituted by a 250 mL glass funnel with a stem of 35 mm in length with a 19 mm diameter orifice. In brief, the efflux time was the elapsed time needed for the freshly prepared paste inside of the 250 mL glass funnel to fill the graduated tube up to the mark of 110 mL, as shown in Figure 3.12. The acceptable range for the efflux time of pastes was arbitrated in 6 ± 0.5 seconds based on the control paste results. A superplasticizer

was added to keep the time of efflux inside of the specified range. The water content of CNF gel and superplasticizer was taken off from the total mixing water. Figure 3.13 displays the flow and superplasticizer dosage of CNF-based cement pastes.

The maximum amount of CNF #0.7 gel and CNF #1.13 gel incorporated to the control paste meeting the design parameters were, respectively, 0.2932 vol.% (or simply 0.3%) and 1.184 vol.% (or 1.2%). At this CNF loadings, the mixing water added to the mixture was zero. Superior amounts conduct to water-to-cement ratios higher than 0.485. The maximum CNF #0.13 fraction was 0.4 vol.%. Distinctively from the other two CNFs, the attainment of the limit was due to the large content of superplasticizer, i.e. 5417 mL/100kg of cement, in spite of the fact that this value surpassed the suggest value by the manufacturer. For superior contents, the setting time was severely affected.

The mixing procedure for the control paste is defined in the ASTM C305 [ASTM, 2014]. For the CNF-based cement pastes, the methodology is essentially the same with few additional steps, as reported in Table 3.9. Before preparing the pastes, the blending of mixing water and CNF gel was proceeded as depicted in Table 3.6 and illustrated in Figure 3.10. Table 3.10 lists all paste mixtures.

Table 3.9 Procedure for mixing the control cement paste and the CNF-based cement pastes.

<i>Control Cement Paste</i>	<i>CNF-based Cement Pastes</i>
Place all the mixing water in the dry bowl.	Place about 2/3 of the CNF gel-water mixture (see Figure 3.10) in the dry bowl.
Add the cement to the water and then wait for 30 secs.	Add the cement to the mixture and then wait for 30 secs.
Start the mixer and mix at 140 ± 5 r.p.m. for 30 secs.	Start the mixer and mix at 140 ± 5 r.p.m. for 30 secs.
Stop the mixer and scrap down any paste on the bowl wall for 15 secs.	Stop the mixer and scrap down any paste on the bowl wall for 15 secs. In this time interval, add the superplasticizer manually mixed with the 1/3 left of the pre-mix in the bowl (see Figure 3.11).
Turn on the mixer and mix for more 60 secs at 285 ± 10 r.p.m.	Turn on the mixer, and mix at 285 ± 10 r.p.m. for 90 secs

Table 3.10 Mix proportions of the GU-cement pastes containing different CNF fractions.

CNF Type	Dry CNF [vol.%]	Materials [kg/m ³]					
		Dry CNF	CNF gel	GU Cement	Water	SP	Deducted Water
Control	0	0	0	1246	604.4	0	0
CNF #0.13	0.1	1.36	46.18	1245	558.5	0.652	49.15
	0.2	2.715	92.19	1243	510.7	3.69	99.74
	0.3	4.048	137.46	1235	451.1	21.58	159.6
	0.4	5.330	181	1218	368.5	69.12	237.3
CNF #0.7	0.1	1.478	207.2	1245	398.0	0.2966	205.9
	0.2	2.955	414.1	1244	191.8	0.7112	411.6
	0.3	4.328	606.6	1243	0	0.9475	602.9
CNF #1.13	0.1	1.478	51.82	1245	553.3	0.2174	55.47
	0.2	2.953	103.5	1244	502.2	0.5430	100.9
	0.4	5.894	206.6	1241	400.1	1.517	201.7
	0.8	11.73	411.3	1235	196.6	4.315	402.5

Note: 'SP' is superplasticizer.

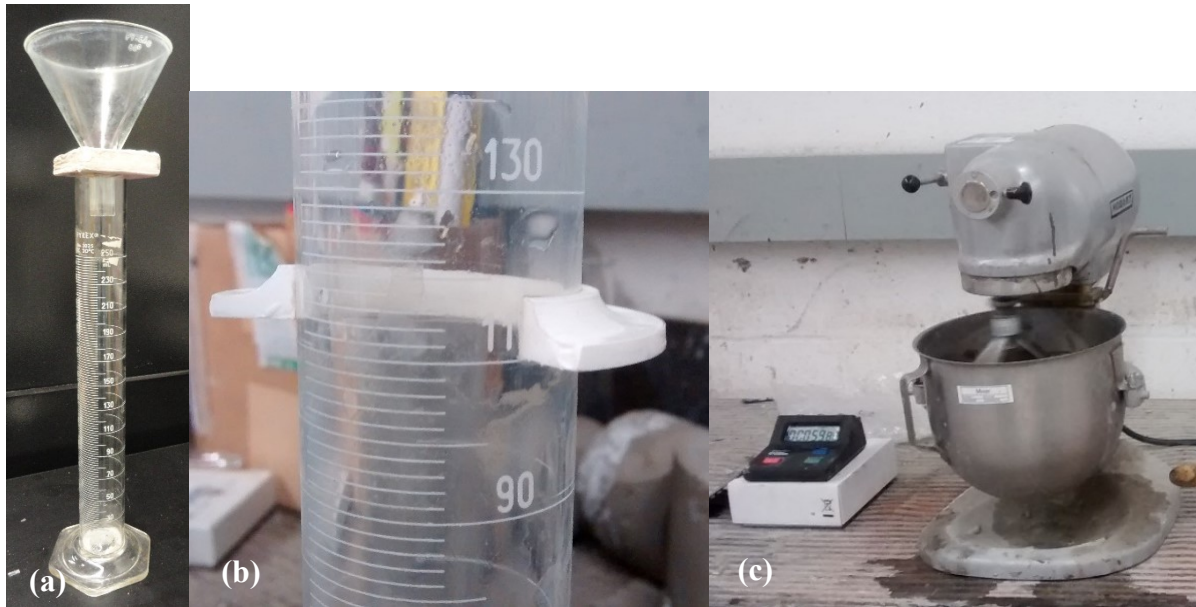


Figure 3.12 View of the (a) the 200 mL-volume flow cone apparatus, (b) 110 mL mark in the graduate tube, and (c) the mixer used as per ASTM C305 [ASTM, 2014].

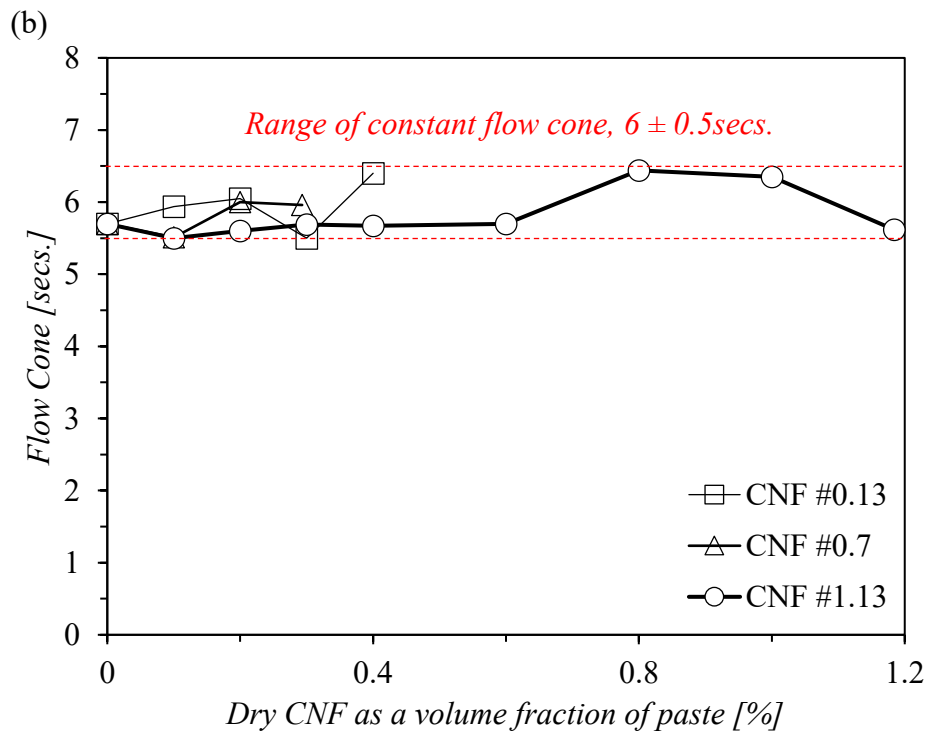
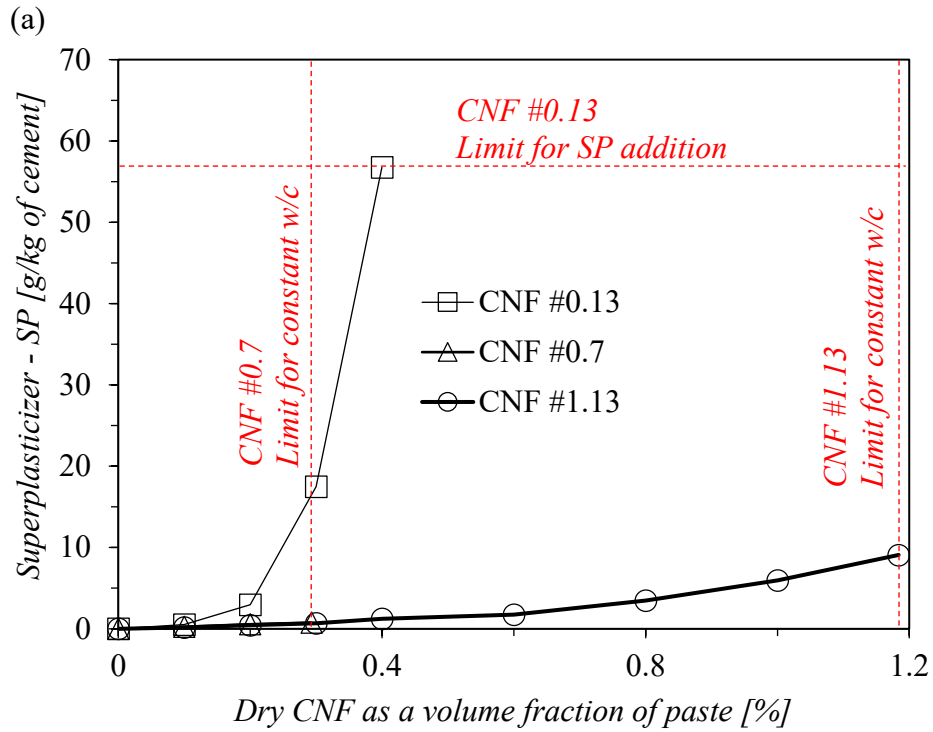


Figure 3.13 Effect of CNF loadings on: (a) superplasticizer demand, (note: the insert text in red offers the reasons for the CNF limit); and (b) flow of CNF-based GU-cement pastes, showing the acceptable consistency limits in red dashed line.

3.5. Concluding Remarks

CNF #0.13 gel was composed by around 3 wt.% of entangled microfibrils and nanofibrils with 0.13 mmol/g of fibre. CNF #0.7 presented higher carboxylate content, i.e. 0.7 mmol/g of fibre, but lower concentration of fibres, i.e. nearly 1 wt.%. CNF #0.13 shown the highest content of carboxylates (i.e. 1.13 mmol/g of fibre) and the largest concentration of dry cellulose nanofibrils (i.e. about 3 wt.%), which are homogeneously dispersed in water. It is worth mentioning that the great water retention capacity of these CNFs; that is, at least over 97 wt.% of water per litre of CNF gel.

The addition of CNF decreased the workability of the pastes and the mortars, as demonstrated in Figure 3.8 and Figure 3.13. The same finding was reported in several previous studies [Peters et al. 2010; Stephenson 2011; Claramunt et al. 2011; Ardanuy et al. 2012; Onuaguluchi et al., 2014; Jiao et al. 2016; Machado et al. 2017], as reported in Section 2.6.2.2 of this thesis. CNF #013 affected negatively the flow much more than the CNF #0.7 and CNF #1.13. The increase in the superplasticizer demand was exponential for increments in CNF #0.13. For this reason, the maximum fraction of CNF #0.13 was below than the theoretical limit, which it would be attained if CNF replaces thoroughly the total mixing water. The topmost fraction was obtained at 0.2% for mortars (0.3% for GU-cement mortars) and 0.4% for pastes. Nevertheless, the chemical admixture content 'versus' CNF #0.7 loadings relationship was roughly proportional, as well as for the CNF #1.13 loadings. At the highest fractions of these two CNFs, no mixing water was added, and the limit dosage proposed by the supplier of superplasticizer not exceeded. The maximum quantity of CNF #0.7 loadings was 0.2932% for pastes and 0.1551% for mortars; rather lower than for CNF #1.13, that was 0.5030% and 1.184%, respectively. The reason for that was the extremely high-water content retained in CNF #0.7 gel, which was 99.28%. Overall, CNF #1.13 demonstrated the best potential to incorporate cellulose nanofibrils in cementitious mixtures, i.e. 17.3 kg/m³ in paste and 7.49 kg/m³ in mortar – when the other dosing parameters were kept constant. Such remarkable performance was empowered by the highest concentration of nanofibrils, nearly 3% as well as CNF #0.13, and the very fine morphology.

It seems that the best performance for the workability of the mixtures is associated much more with the morphology of the CNF than with its carboxyl group content. In reality, the parcel of the water held by the carboxyl groups onto the surface of cellulose nanofibrils is not immediately

available to lubricate the solid particles in the fresh mixture; hence the workability is negatively affected. For this reason, an increase in the CNF loading is followed by a drop in the workability. Following this reasoning, the expectancy would be that CNFs with elevated carboxyl group content, as CNF #1.13 (and less CNF #0.7), should provoke a much higher negative impact in the workability than low-carboxyl group content CNFs, as CNF #0.13. However, the opposite was verified. The presence of microfibrils (with long lengths) and the higher level of entanglement verified for CNF #0.13 weighted heavier than the high-water retention capacity observed for CNF #0.7 or CNF #1.13.

The compressive strength declined marginally as increasingly amounts of CNF #0.13 were incorporated to the cement mortars. Apparently, the dissolution process of cement particles was slowed down a bit by the hydrophilicity of CNF during the first stages of hydration [Jiao et al., 2016]. Another factor that may have contributed to this performance is the chemical reactivity of CNF, which may react with some soluble cations in the pore solution, such as calcium, essentials to hydration mechanism [Jiao et al., 2016].

CHAPTER 4. Microstructure of CNF-based Cement Pastes

4.1. Introduction

The active hydroxyl and carboxyl groups on the CNF macromolecule retain water. This CNF property may interfere in the hydration kinetics of cement particles and hence in the pore system of cement paste. And as is well known, the microstructure characteristics affect fundamental macroproperties of concrete, such as mechanical strength and durability [Neville, 1995; Metha et al., 2013]. Mechanical strength relies on pore structure. Durability largely depends on porosity, pore sizes, pore connectivities and fluid movements (e.g. carbon dioxide, oxygen, water, or contaminated water with aggressive ions, such as sulphates, SO_4^{2-} , and chlorides, Cl^-) through the microstructure. The penetrability of aggressive ions by flow, diffusion or sorption occurs predominantly through large and medium capillary pores. And the dimensional instability is associated with pore gels [Neville, 1995]. Therefore, the degree of hydration (DOH) and porosimetry of cement pastes containing CNF were examined, respectively, in Sections 4.2 and 4.3, to provide additional data to explain the findings in shrinkage, sulphate attack and chloride ingress shown, respectively, in CHAPTER 5, CHAPTER 6 and CHAPTER 7.

Section 4.4 reports an attempt to identify CNF in the middle of hydrated cement products and/or any hydrophilic complex between CNF and Ca^{2+} adsorbed on cement particles.

4.2. Degree of Hydration

4.2.1. Introduction

Cao et al. [2015] proposed that the DOH increases when CNC is added to cement pastes. Recall again, that CNC refers to the nanocrystals as opposed to CNF, the nanofibers. These authors believed that such enhancement is related to two different mechanisms of CNC-cement interaction: (i) a better dispersion of the solid particles of cement; and (ii) a short circuit diffusion, [Cao et al., 2015]. The first mechanism is based on the same theoretical principles observed in many water reducers. And the second promotes further hydration of the unhydrated cement grains, as explained in Section 2.4 of the thesis. CNC and CNF are, both, cellulose nanomaterials with close

characteristics and properties. Accordingly, the active hydroxyl and carboxyl groups on CNF surface may interfere in the cement hydration, as well [Jiao et al., 2016].

The DOH provides valuable information about the hydration mechanism of cementitious materials. Bearing this in mind, the DOH is an important tool to better understand the effect of CNF on the cement hydration. Moreover, there is a strong relationship between DOH and porosity of the microstructure, which can be extrapolated to some relevant macroproperties of concrete, such as strength and (perhaps) durability. In reality, the DOH-durability correlation in concrete shall be analyzed under reservations, since the permeability to aggressive elements (e.g. SO_4^{2-} and chloride, Cl^-) is not uniquely associated with the porosity. Other factors, such as tortuosity and connectivity of pore network, shall be similarly taken into consideration.

The quantitative determination of the DOH of cement pastes is performed by several experimental techniques based on the non-evaporable water content, the isothermal heat of hydration [Pane & Hansen, 2005], the amount of calcium hydroxide, $Ca(OH)_2$, phase [Lam, Wong, & Poon, 2000; Feng, Garboczi, Bentz, Stutzman, & Mason, 2004] and even the strength of hardened cement paste [Lam et al., 2000]. Of these, the first one is the most usual method found in the literature review [Lam et al., 2000; Feng et al., 2004; Wong & Buenfeld, 2009; Yio, Phelan, Wong & Buenfeld, 2014; Deboucha, Leklou, Khelidj, & Oudjit, 2017].

In this method, the DOH is calculated by the ratio between the non-evaporable water (in gram per gram of anhydrous cement) to the chemically bound water at infinite time. The latter is theoretically estimated based on the stoichiometry of cement (or clinker) compounds [Lam et al., 2000; Deboucha et al., 2017]. The non-evaporable water embraces: (i) the ionic and covalent combined water with the hydrated products of cement; and the retained water in the intermolecular interaction of calcium silicate hydrate gel, $C - S - H$ [Jennings et al., 2002]. The bound water is usually determined by means of the loss on ignition (LOI) methods applied to hardened cement pastes with the free water previously removed from the capillary pores [Feng et al., 2004]. The LOI is performed at around 900-1,050°C using the conventional furnace-drying technique or the thermal analyzers.

In the course of heating the paste sample, the bound water is normally removed from the cement hydrates during two major thermal phases: dehydration and dehydroxylation. In the first phase, the dehydration of the gypsum occurs, followed by that of ettringite and part of the $C - S - H$ gel, among others, roughly from room temperature to 400 °C. Until 105 °C, only part of the water bound to the $C - S - H$ gel and the ettringite evaporates. The dehydroxylation of $Ca(OH)_2$ and a negligible amount of remnant $C - S - H$ takes place between 400-550 °C. In theory, all non-evaporable water of cement pastes vaporizes at 550 °C. Above this temperature, the decarbonation of calcium carbonate, $CaCO_3$, releases carbon dioxide, CO_2 , which is the main cause of loss of weight in this phase [Lothenbach, Durdziński, & De Weerd., 2016].

In order to improve the accuracy with which to estimate the DOH, any episodic pre-hydrated part of cement should be discounted from the LOI measurements [Fagerlund, 2009]. These methods discussed here are fully applied to plain cement-based materials, as the mixtures used in this research. For blended mixtures, the more complex chemical reactions between plain cement and reactive mineral admixtures requires alternative techniques, namely, the SEM point-counting technique [Feng et al., 2004] and/or proper equations, such as those suggested by Bhatti [1986] and Pane et al., [2005].

4.2.2. Experimental Procedure

The cement-paste mixtures used to cast the specimens are listed in Table 3.10 and were prepared with various doses of CNF fractions according to reported in Section 3.4. The CNFs with the highest and the lowest carboxyl group contents, CNF #0.13 and CNF #1.13, were added to paste mixtures, in order to examine the effect of CNF's water retention capacity upon the DOH of cement pastes. After mixing, the fresh pastes were poured into vials up to the edge, the vials sealed with caps and the specimens conditioned for 1 year in moist room as per ASTM C511 [ASTM International (ASTM), 2013] – see Figure 4.1.

At least 5 g of pulverized paste samples used to evaluate the DOH were extracted from the middle of the 1-year-old-moist-cured specimens by crushing, grinding and sieving as depicted and illustrated in Section 4.3.1.2. The particle size range of the sample was from 0.074 mm (sieve mesh

#200) to 0.15 mm (sieve mesh #100). Any free water that may be contained in the capillary pores of the powder sample was removed by solvent exchange, as detailed in Section 4.3.1.2 and shown in Figure 4.2.

The non-evaporable water measurements of the 1-year-old powder samples were obtained by LOI method using two different apparatus: a conventional electric furnace and a more accurate thermal analyzer. In the first experiment, the LOI was measured in at least 1.0 g of powdered sample ignited in the furnace at 1,000 °C for 1 hour – see Figure 4.3. This sample was oven-dried at 105 ± 5 °C for 20 ± 1 hours before starting the LOI trails. In the second, the LOI was ascertained by the thermal analyzer *TA Instruments TA Q50* shown in Figure 4.4 in a sample of 50 mg: (i) first, heated from room temperature (i.e. 20 °C) to 950 °C with a 10 °C per minute heating rate; and (ii) then, submitted to an isothermal of 950°C for 1 hour. The purging gas used was nitrogen with a flow of 60 mL/min. The non-evaporable water content on the ignited basis of the hydrated pastes was calculated according to the following equation [Fagerlund, 2009]:

$$w_n = (w_{t_{initial}} - w_{t_{ignited}}) \div w_{t_{ignited}} \quad (4.1)$$

where ' w_n ' is the non-evaporable water content [g/g of dry cement]; ' $w_{t_{initial}}$ ' is the initial sample weight [mg] measured at room temperature or at 105°C according to the case; and ' $w_{t_{ignited}}$ ' is the ignited weight [mg] of the sample after 1 hour at 950°C or 1,000°C depending on the apparatus used. The weighting at room temperature aims to include the parcel of bound water below 105 °C in the DOH analysis. The readings of weight and temperature were acquired by the software *TA Universal Analysis 2000 version 4.5A* of the thermal analyzer.

The bound water content was recalculated discounting any possible pre-hydrated fraction of the anhydrous cement [Lam et al., 2000] and CO_2 mass incorporated by carbonation of the hydrated paste during the sample preparation and storage, as follows [Lothenbach et al., 2016]:

$$w_{n,corrected} = w_n - w_{LOI\ cement} - w_{CO_2} \quad (4.2)$$

where ' $w_{n,corrected}$ ' is the corrected non-evaporable water [g/g of dry cement]; ' $w_{LOI\ cement}$ ' is the LOI of anhydrous Type GU cement [g/g of dry cement]; and ' w_{CO_2} ' is the CO_2 content released during the decarbonation of $CaCO_3$ [g/g of dry cement].

The LOI of cement was determined in accordance with a modified ASTM C114 [ASTM, 2015], using the following equation:

$$w_{LOI\ cement} = \left(w_{LOI,t_{initial}} - w_{LOI,t_{ignited}} \right) \div w_{LOI,t_{ignited}} \quad (4.3)$$

where ' $w_{LOI,t_{initial}}$ ' and ' $w_{LOI,t_{ignited}}$ ' are, respectively, the weights [mg] measured by an analytical balance at the beginning of the trial and after igniting the sample at 1,000 °C for 1 hour. The LOI value obtained for the anhydrous GU cement was 2.622 wt.%.

The w_{CO_2} was calculated as per the following equation [Lothenbach et al., 2016]:

$$w_{CO_2} = \left(w_{CO_2,t_{initial}} - w_{CO_2,t_{final}} \right) \div w_{ignited} \quad (4.4)$$

where ' $w_{CO_2,t_{initial}}$ ' and ' $w_{CO_2,t_{final}}$ ' are, respectively, the weights [mg] measured by the thermal analyzer at the beginning and at the end of the decarbonation phase, which occurs above 500 °C [Villain, Thiery, & Platret, 2007; Lothenbach et al., 2016; Deboucha et. al., 2017]. In this regard, the exact limits of the decarbonation were determined through derivative thermogravimetry (DTG) curves of the samples. The curves from thermogravimetric analysis (TGA) correspond to the cumulative weight loss in relation to the temperature, and the DTG plots are the derivative of these TGA curves. The DTG plots show the rate at which the sample weight varies under a constant heating ramp over the temperature. In the DTG curve, the peaks indicate a phase change in the hydrated components of cement. The volatile part of the dry CNF was neglected in the calculation of bound water, because it represents less than 1 wt.% of sample, in the worst scenario.

The DOH was calculated according to the following equation [Fagerlund, 2009; Deboucha et. al., 2017]:

$$\alpha = w_{n,corrected} / (w_n^0 / c) \quad (4.5)$$

where ' α ' is the DOH [%] based on the corrected amount of bound water, ' $w_{n,corrected}$ '; and ' w_n^0 / c ' is the theoretical DOH of cement. In other words, the ' w_n^0 / c ' is the bound water chemically combined with a fully hydrated cement paste at infinity time, which can estimate on the basis of the theoretical stoichiometry of cement. This hypothetical value ranges from 0.22 to 0.26

depending on the chemical composition of cement [Deboucha et al., 2017]. The stoichiometric calculation of ' w_n^0/c' ' was based on the chemical compounds of GU cement listed in Table 3.2 and assuming that (i) the entire cement is hydrated; (ii) the gypsum content is 3 wt.% of cement; (iii) the gypsum reacts with C_3A and tetra-calcium aluminoferrite (C_4AF) at the ratio of 2:1; (iv) 1/3 of the C_3A reactions are with gypsum; (v) the C_3A left undergoes hydrolysis and form hydrogarnets; and (vi) in case of the brownmillerite hydration, only 1/10 reacts with gypsum and the rest reacts directly with water [Czarnecki, Broniewski, & Henning, 1994; Brouwers, 2003; Wong et al., 2009]. The calculated values of ' w_n^0/c' ' for GU cement without gypsum was 0.2254 and for GU cement containing 3 wt.% of gypsum was 0.2588 [Czarnecki et al., 1994; Brouwers, 2003; Wong et al., 2009]. For the purpose of DOH calculation, the value of 0.2588 was used for ' w_n^0/c' '.

The temperature threshold of the three thermal decomposition phases of cement pastes, namely, dehydration, dehydroxylation and decarbonation, were determined using the DTG curves, as explained earlier in this Section and illustrated in Figure 4.5 [Lothenbach et al., 2016].



Figure 4.1 View of the sealed vials containing the 1-year paste samples.

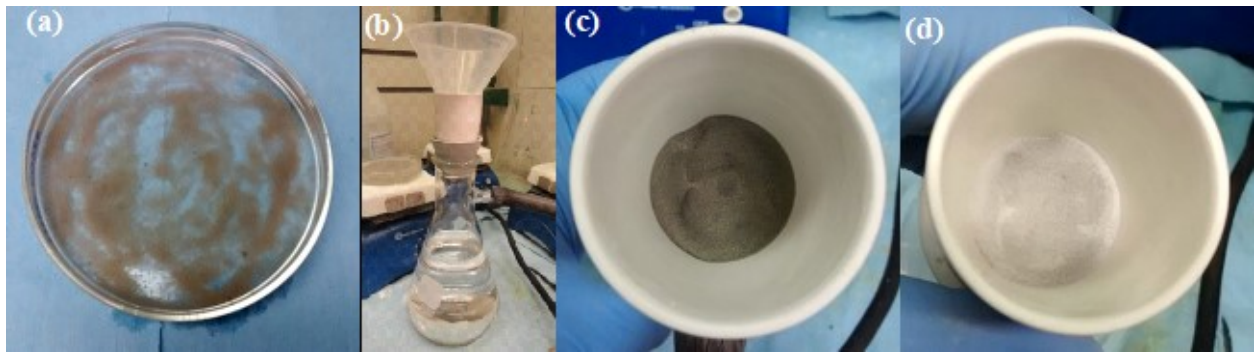


Figure 4.2 Removal of the evaporable water from pore structure of pastes by solvent exchange: (a) sample in isopropanol alcohol; and (b) vacuum aspirating the solvent at most from the sample. View of the sample (c) before and (d) after being vacuum aspirated.

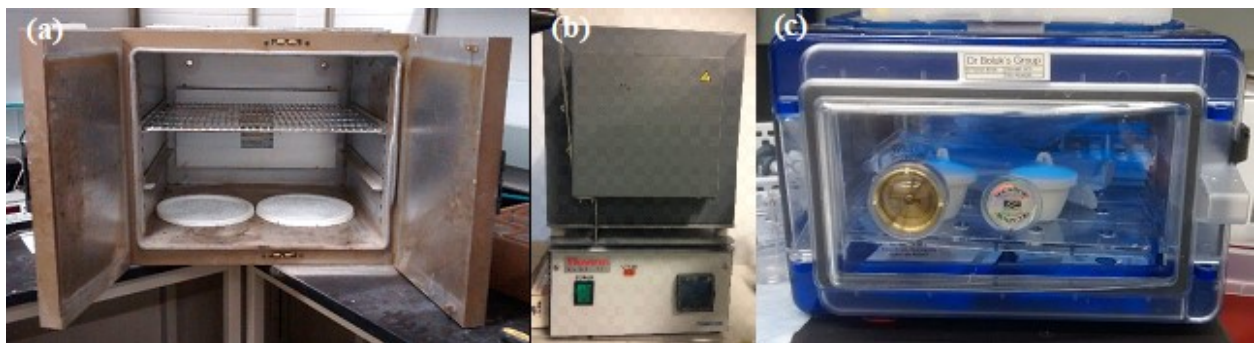


Figure 4.3 View of (a) the oven used to dry, and (b) the furnace to ignite the samples. (c). View of the porcelain crucibles containing the ignited samples cooling down inside of the desiccator.

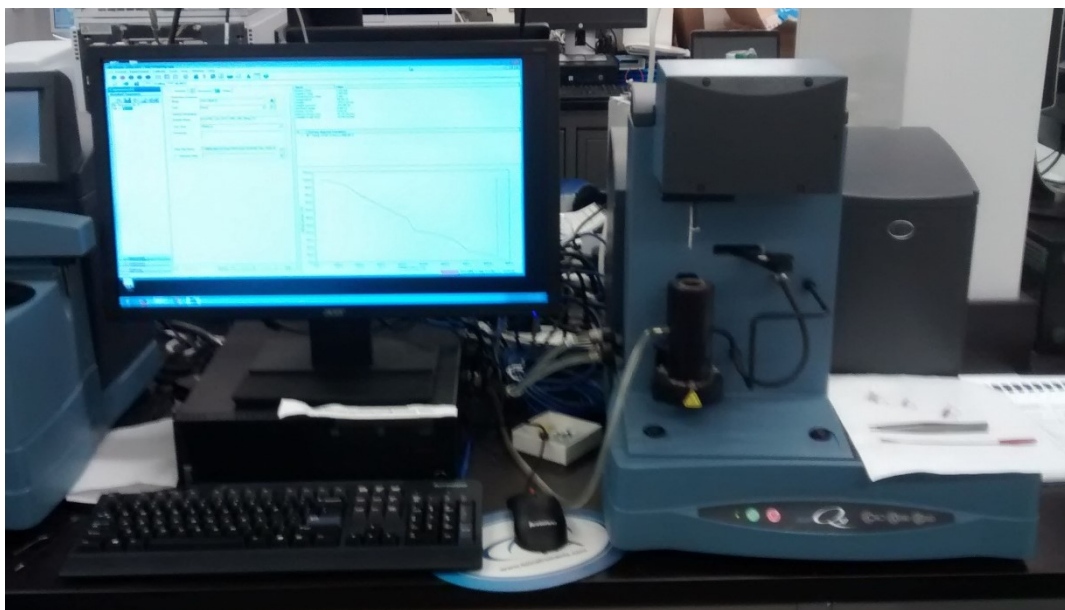


Figure 4.4 View of the thermal analyzer *TA Instruments TA Q50*.

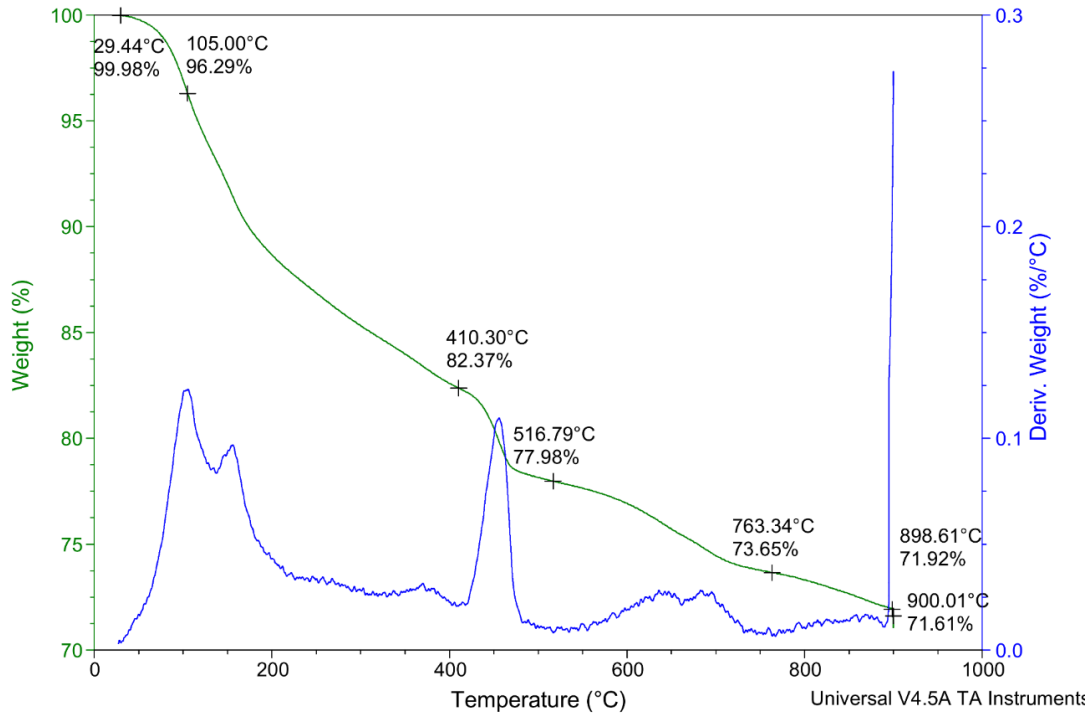


Figure 4.5 TGA and its respective DTG curves showing the weight and the temperature of the paste samples at the borders of the dehydration, dehydroxylation and decarbonation phases.

4.2.3. Results and Discussion

The DOH of cement pastes decrease by 12.4% for dry CNF dosages of 0.4 vol.% on the basis of the weight measurements using the electric furnace – see Figure 4.6.(a). This is true for both CNFs, CNF #0.13 and CNF #1.13. Nevertheless, incorporating fractions above 0.4 vol.% of CNF, which was possible only for CNF #1.13 due to its higher hydrophilicity, the reduction in the DOH raised a bit to 9.1%. The scenario remains nearly the same for values of DOH based on the weight loss of bound water corrected with the LOI of cement and the CO_2 weight loss, as shown in Figure 4.6.(b).

The DOH of CNF-cement pastes based on the TGA is plotted in Figure 4.7. The Figure 4.7.(a) tabulated the DOH considering the weight loss between the room temperature and 950 °C, and Figure 4.7.(b) from 105 °C to 950 °C. As before, Figure 4.7.(a) displays an initial reduction in DOH at low CNF doses, followed by a recovery of this loss after 0.4% vol. fraction of CNF. The reduction in the DOH (at 0.4% of CNF) was only less than 5%. Actually, a marginal increase was

observed in the DOH of pastes containing 1.2 vol.% of CNF #1.13. Both situations were compared with the performance of the control paste mixture. The enhancement in the numbers of the DOH of cement pastes loaded with CNF are still greater if taken from the initial weight at 105 °C. Based on Figure 4.7.(b), CNF loadings, at least, did not interfere in the DOH of cement pastes; despite the small reduction demonstrated in the CNF #0.13-cement pastes.

The linear model displayed in Figure 4.8 correlated the DOH dataset based on the TGAs with the LOI-in-furnace trials shown, respectively, in Figure 4.6.(b) and Figure 4.7.(b). The coefficient of determination (R-squared) CNF #1.13-based mixtures was 85%, whilst the R-squared of CNF #0.13-cement pastes was 55%. Both values demonstrate a moderate low variability between each series of data and their mean.

The difference in the performances exhibited in Figure 4.7.(a) and Figure 4.7.(b) essentially reflected the loss of bound water during two distinct temperature ranges of dehydration, as noticed in Figure 4.9. Figure 4.9.(a) shows the DOH considering the weight loss since about 20 °C, whereas Figure 4.9.(b) from 105 °C. Thus, part of the bound water of $C - S - H$ and ettringite (estimated in around 5 g/100 g of dry cement) was disregarded in the DOH calculation of the data plotted in Figure 4.7.(b). The impact of the dehydration phase in the DOH of cement pastes is about 2.5 times higher than dehydroxylation – see Figure 4.9.

Analyzing the DOH based on the decomposition phases in which the combined water is lost by heating, that are dehydration and dehydroxylation, allows to suggest that, overall, CNF loadings did not modify significantly the amount of hydrated structure of cement pastes, as ratified in the Figure 4.9.(b) and Figure 4.9.(c). The bound water loss during the dehydration of cement pastes maintained a relative plateau around 16.5-18.3 g/100 g of dry cement over the entire range of CNF dosages, as seen in Figure 4.9.(b). And during the dehydroxylation phase was observed a marginal decline from 6.65 to 5.70 g of bound water per 100 g of dry cement, as demonstrated in Figure 4.9.(c).

Thus, the proposition of ‘short-circuit diffusion’ be also attributed to the CNF, as it was for the CNC by Cao et al. [2015], seems not to be feasible. Nevertheless, in the literature review show in

Section 2.6.5 of the thesis, several authors [Onuaguluchi et al., 2014; Sun, Wu, Ren, & Lei, 2015; Jiao et al., 2016; Mejdoub et al., 2017] claimed that CNF loadings enhanced the DOH of cementitious materials.

Among all decomposition phases, the one in which was the largest reduction in the amount of weight loss relative to the control paste was found, was the decarbonation phase – see Figure 4.9.(d). The CO_2 loss was reduced from 7.17 to 3.80 g/100 g of dry cement (almost half) with increments in the CNF loadings.

Time and cost constraints limited by only one the number of TGA per mixture. Therefore, the TGA-based DOH data shown in Figure 4.7 and Figure 4.9 does not contain error bars. The same occurred with the furnace-based DOH data in Figure 4.6, but in this case due to restrictions on the availability of laboratory equipment.

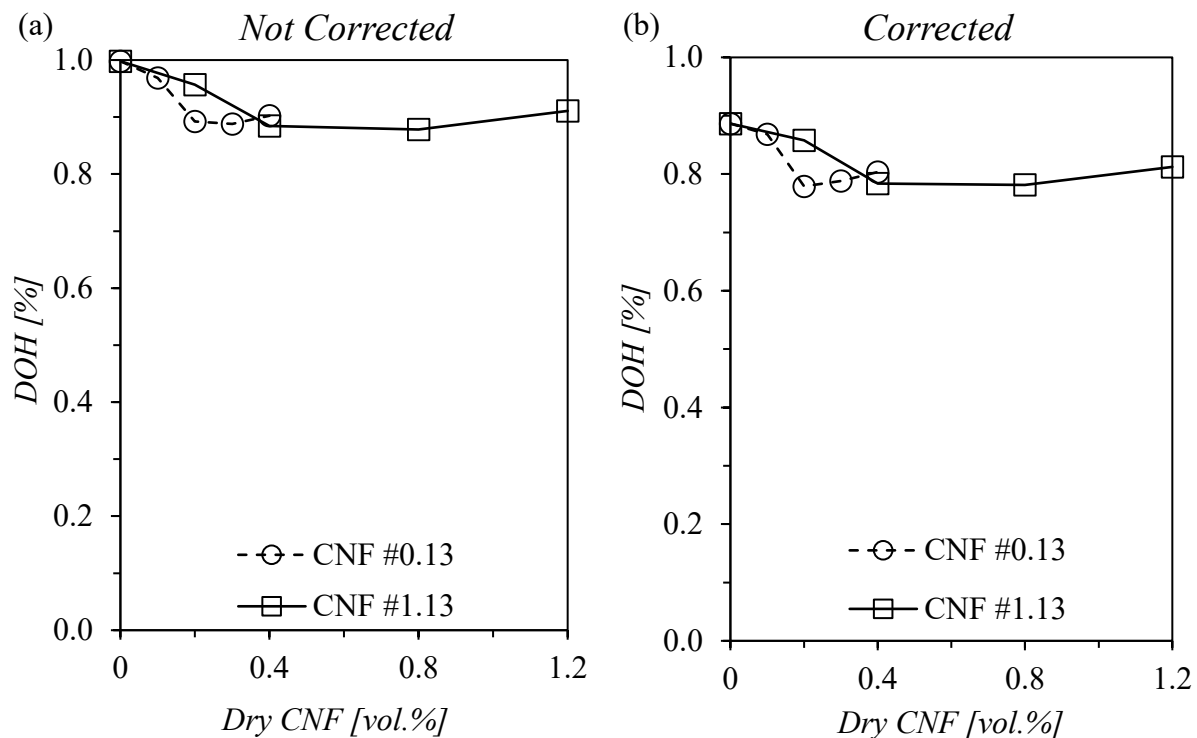


Figure 4.6.(a) Degree of hydration (DOH) of cement pastes affected by a range of CNF loadings using LOI measurements based the furnace trials. (b). Same DOH shown in (a), but now, deducted by the bound water coming from the pre-hydrated cement and the CO_2 of carbonated cement paste.

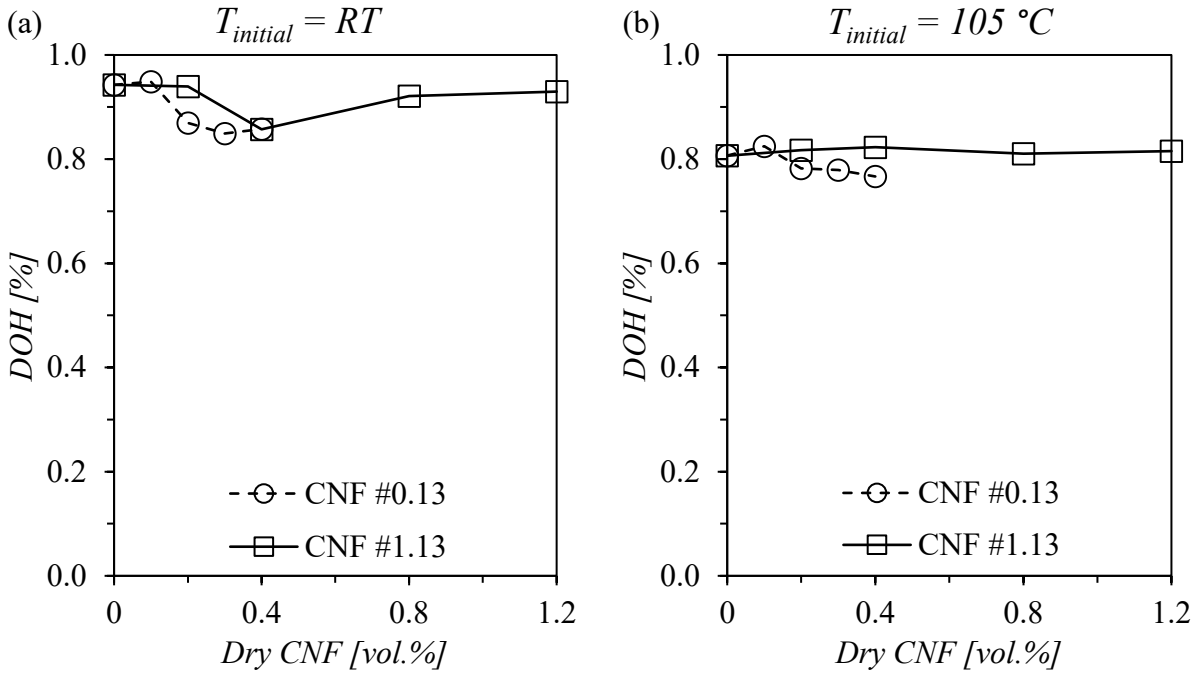


Figure 4.7 Degree of hydration (DOH) of cement pastes affected by a range of CNF loadings based on TGA data, which the initial temperature was (a) room temperature (RT), or (b) 105 °C.

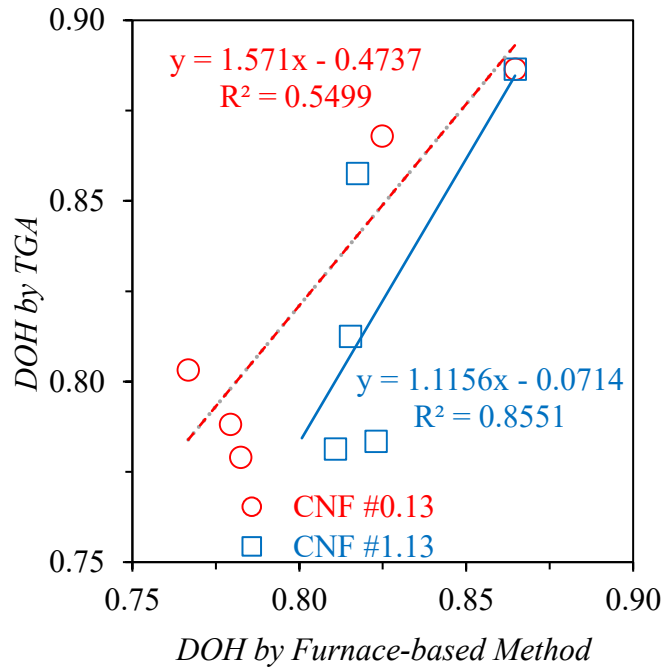


Figure 4.8 Linear correlation between the DOH dataset of CNF #0.13- and CNF #1.13-based mixtures acquired by TGA and furnace-based method.

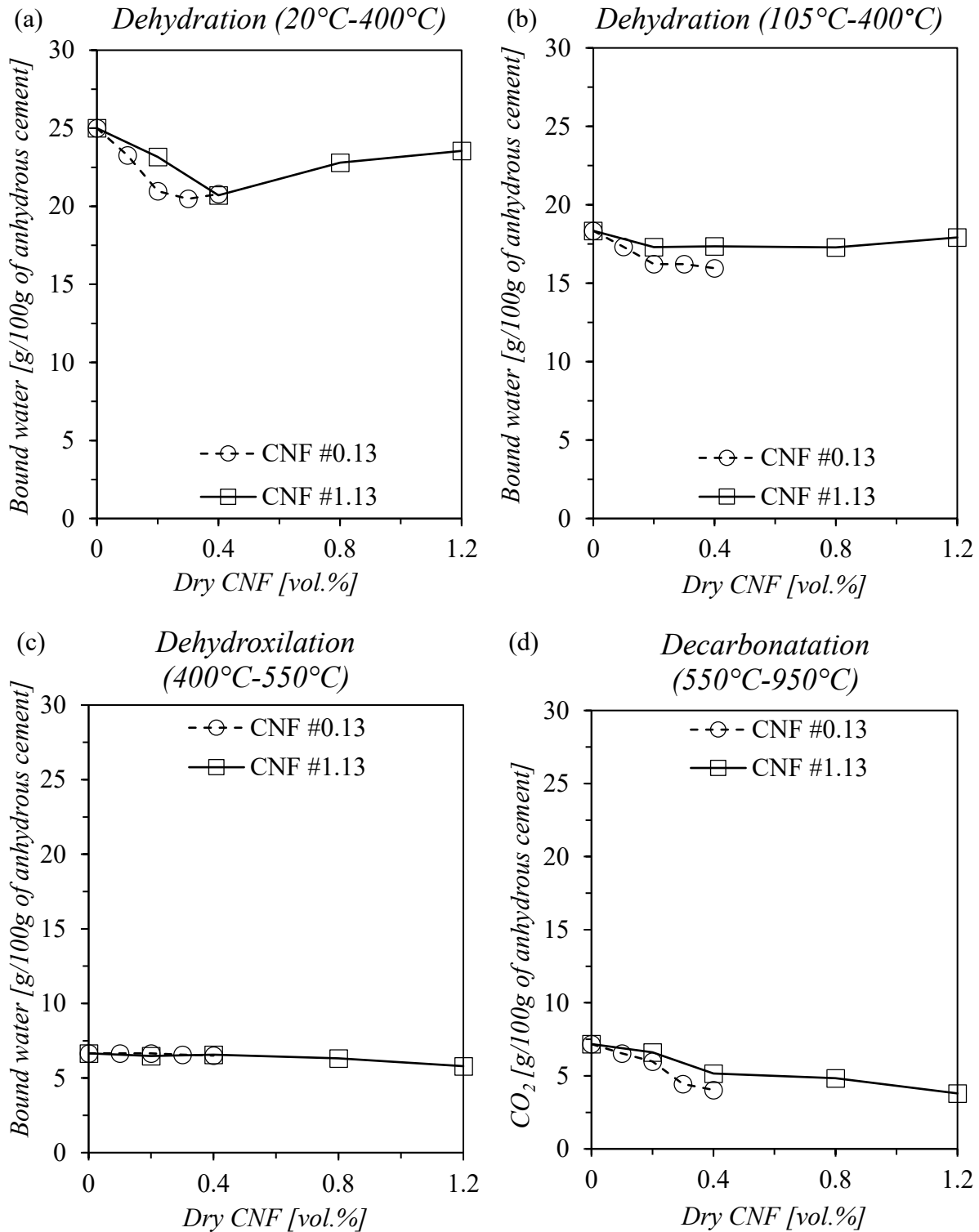


Figure 4.9 Decomposition phases of hardened cement pastes by TGA: (a) dehydration starting at room temperature, 20 °C, and (b) at 105 °C; (c) dehydroxylation; and (d) decarbonation.

4.3. Porosimetry Analysis

4.3.1. Gas Sorption Analysis

4.3.1.1. Introduction

Overall, the shrinkage of hardened cement pastes is controlled by pores less than 50 nm in size [Jennings, Thomas, Rothstein, & Chen, 2008; Metha et al., 2013]. Pores this size are categorized by the International Union of Pure and Applied Chemistry (IUPAC) as mesopores (between 50-2 nm in diameter), micropores (from 2-0.7 nm in diameter), ultra-micropores (less than 0.7 nm) and sub-micropores (less than 0.4 nm) [Zdravkov, Čermák, Šefara, & Janku, 2007]. Nonetheless, the pore size terminology in this thesis is the one conventionally taken in concrete technology, i.e. capillary pores (50-10 nm), gel pores (10-0.5 nm) and *C – S – H* interlayer (less than 0.5 nm) [Jennings et al., 2008]. In order to assess the pore size distribution (PSD) in cement paste are several radiation and fluid-based analytical methods are employed. Optical microscopy, small angles X-ray neutron scattering, nuclear magnetic resonance, image analysis of scanning electron microscope (SEM), mercury intrusion porosimetry, helium pycnometry, water immersion porometry and gas sorption analysis are some of the commonly used techniques [Lawrence & Jiang, 2017]. Each technique is best suited for a specific pore range. Gas sorption analysis accurately ascertains PSD under 100 nm [Berodier, Bizzozero, & Muller, 2016]. This range covers exactly the pore structure that has impact on the shrinkage performance. This technique has been extensively applied to evaluate the specific surface area (SSA) and PSD in colloidal and microporous materials, such as cement pastes, regardless the large variation in the results [Juenger & Jennings, 2001].

The gas sorption theory is essentially based on the volume of gas molecules (adsorbate) physically adsorbed by van der Waals forces onto the solid surface of the pore (adsorbent). Nitrogen and water are the most frequently adsorbates used in gas sorption analysis of cement pastes. Usually, nitrogen provides smaller results of SSA than water due to its bigger molecules, which are unable to penetrate into all small pores [Odler, 2003]. In spite of that, nitrogen is the most commonly used adsorbate in gas sorption experiments in cement pastes [Juenger et al., 2001]. Palacios, Kazemi-Kamyab, Mantellato, and Bowen [2016] consider nitrogen as the most suitable adsorbate for gas

sorption analysis of cement pastes. The physical adsorption of the adsorbate is only possible at cryogenic temperatures, as typically achieved by liquid nitrogen, that is, minus 196 °C. The volume of physisorbed molecules is the difference between a known volume of gas introduced into the cell containing the cement paste sample and the gas necessary to fill the empty spaces at the equilibrium pressure of 176 mmHg. This cycle is successively repeated by adding incremental quantities of gas into the cell after the equilibrium pressure is reached. The adsorption isotherm is progressively built with each cycle, which represents one dot in the plot of the isotherm curve [Palacios et al., 2016]. Palacios et al. [2016] recommends at least 10 cycles to obtain an accurate isotherm. Thus, briefly, the adsorption isotherm demonstrates the volume of adsorbed gas at fixed temperature as a function of the relationship between the sample pressure and the saturation pressure of the adsorbed gas (P/P_0). Desorption isotherm is obtained by inverse process, that is, the removal of all physisorbed molecules by degassing the cement paste sample. The adsorption-desorption isotherm provides information about PSD and porosity of cement pastes, given the hysteresis cycle in the isotherm is associated with the pore shape and tortuosity [Palacios et al., 2016].

The isotherms obtained for the pore structure of hardened cement pastes may be roughly classified as category IV in accordance with IUPAC classification. This group is typically composed of mesoporous materials with a strong interaction between adsorbate and adsorbent [Palacios et al., 2016; Lawrence et al., 2017]. It means that the gas sorption is an adequate technique for porosimetry analysis of hardened cement pastes.

The Brunauer, Emmett, and Teller (BET) theory is the most acceptable to calculate SSA in solid materials with open porosity, as cement pastes [Odler, 2003; Palacios et al., 2016]. According to this theory, the SSA can be estimated if the following are known: (i) the surface area covered by a single adsorbed gas molecule, and (ii) the amount of adsorbate necessary to form a hypothetical dense monomolecular layer on the surface of the pore structure of the sample [Beaudoin & Marchand, 2001]. The latter can be derived from the low-pressure region in the adsorption isotherm through the BET equation [Odler, 2003; Lawrence et al., 2017]. And the former can be estimated according to the adsorbate in use; for example, the surface area of nitrogen gas is normally assumed $16.2 \times 10^{-20} \text{ m}^2/\text{molecule}$ [Palacios et al., 2016; Lawrence et al., 2017].

The PSD of mesoporous materials, as cement pastes, is determined by assuming that the adsorbate density is the same of the bulk condensed gas in the pore structure [Beaudoin et al., 2001]. Among the capillary condensation methods, the Barret–Joyner–Halenda (BJH) model based on modified Kelvin equation is the most used to compute the volume pore size distribution in cement pastes [Palacios et al., 2016]. This model admits the cylindrical shape for the pores. Nonetheless, the majority of the pores in cement pastes are slit-shaped structures mostly found in $C - S - H$ gel [Metha et al., 2013]. Alternatively, the density functional theory allows to consider different pore geometries, as in shape of slit [Palacios et al., 2016]; notwithstanding Fernández [2008] found no significant changes in the PSD determined between BJH method and density functional theory. Another point to take in consideration is BHJ method is limited to pore radii exceeding 1.6 nm, since that Kelvin formula is not applicable for smaller sizes [Beaudoin et al., 2001]. The PSD can be calculated from the adsorption isotherm or from the desorption isotherm. Usually, desorption curve has been used to obtain PSD in cement pastes [Juenger et al., 2001], though the adsorption branch of isotherm is less affected by the tortuosity and pore shape [Palacios et al., 2016].

Most of the variation found in the results of SSA and PSD of cement pastes by gas sorption technique came from sample preparation and the degassing process. The hydration stoppage and/or the removal of evaporable water from the pores shall be proceeded properly to not interfere in analysis and at the same time preserve the pore structure. The direct drying methods, such as oven drying and vacuum freezing, are less subtle than solvent exchange or P-drying processes. In the solvent exchange process, the free water in the pores is first replaced by an organic solvent miscible with the water and then removed by a mild oven-drying process or by rinsing with diethyl ether [Palacios et al., 2016]. Several solvents may be used (e.g. acetone and methanol), though isopropanol is the least aggressive to the hydrated products of cement [Winnefeld, Schöler, & Lothenbach, 2016; Palacios et al., 2016].

4.3.1.2. Experimental Procedure

The mix design criteria, the prefixed proportion of the raw materials and the mixing procedure of the mixtures are detailed in Section 3.4. Two distinct CNFs were used in the mixes, namely, CNF #0.13 and CNF #1.13.

One cylindrical specimen was cast per mixture of CNF-cement paste. The cylinders were molded in four layers, each one compacted by an external vibrating table at 60 Hz for at least 20 secs to dimensions of 50 mm in diameter and 100 mm in height. Special care was taken during the compaction to not permit excessive bleeding. After that, the specimens were covered with a cap and stored for 1 year in moist room meeting the requirement of ASTM C511 [ASTM, 2013]. At this age, about 1 mm-height of the specimen ends were ground with an abrasive paper (grit P80), in order to ensure a flat surface, with open pores at the surface, and to avoid the influence of bleeding on the analyses.

After that, 10 mm-thick slices were cut with distilled water from the cylinders using a diamond saw cutting machine. Approximately 1 mm outer layer of cut slice was sandpapered out, in order to get rid of any possible carbonation depth which may have occurred. To do so, a sandpaper ISO grit designation P80 was used.

After, this slice was hand ground with a pestle in a mortar, and concomitantly sieved until the entire sample passes through the nominal sieve opening of 0.6 mm (sieve mesh #30). Around 1.5 g of the ground sample retained in sieve standard designation of 0.3 mm (sieve mesh #50) were collected to be submitted to solvent exchange. This procedure aims to remove any residual evaporable water that, by chance, could be in the pore structure. The 1.5-g sieved sample was immersed in isopropanol alcohol at a liquid-to-solid rate of nearly 50 (mL/g) for at least 30 minutes. After that, the alcohol in excess was poured into a crucible with filter paper and the wet sample residue vacuum aspirated for 3-5 minutes. Figure 4.10 and Figure 4.11 illustrate part of this sample preparation procedure.

Immediately after, the degassing of sample was initiated in *Autosorb Quantachrome IMP* analyzer – see Figure 4.12.(a). About 0.9 g of sample was vacuum degassed at 105 ± 5 °C in the first 5 ± 0.25 hours and then at room temperature for more 15 ± 0.5 hours. After the sample is degassed, the gas sorption analysis was finally proceeded with the same analyzer. The nitrogen with a purity of 99.9% was used as adsorbate gas. The adsorption isotherm was constructed with 20 points, so as the desorption isotherm – see Figure 4.12.(b). The SSA and the average pore size was computed

according to BET method based on the adsorption isotherm. The PSD was determined as per BJH method using the data from desorption isotherm. These results served as the basis for calculating the accumulated pore size distribution and the overall porosity.

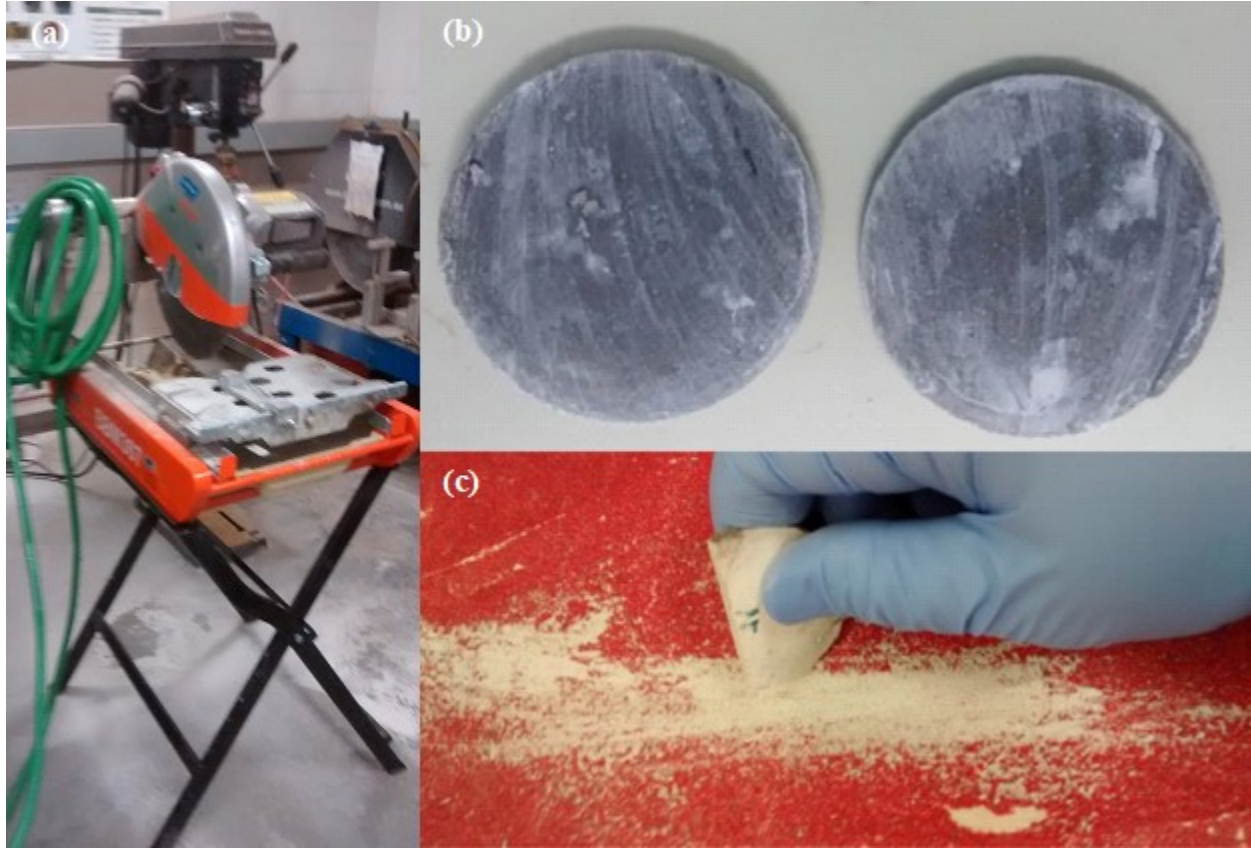


Figure 4.10 View of (a) the cutting machine used to slice the cylinder made of hardened CNF-based cement paste. View of (b) the cut slices and (c) the sandpapering process.

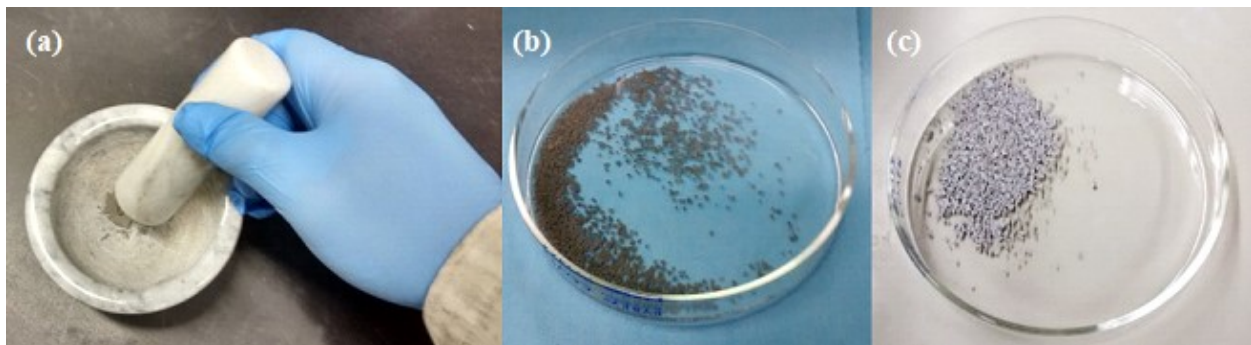


Figure 4.11 View of (a) the manual crushing of CNF-based cement pastes and the ground sample (b) during and (c) after the removal of free residual water through solvent exchange.

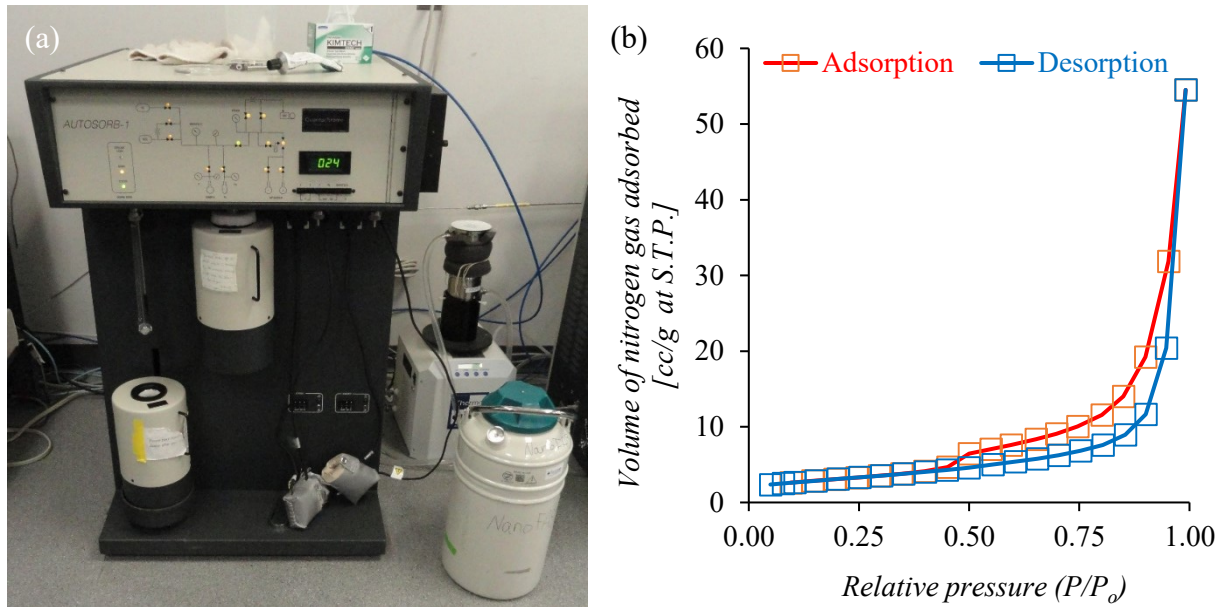


Figure 4.12 View of (a) the gas sorption analyser used, and (b) the adsorption-desorption isotherm of control paste. P/P_0 is the sample pressure-to-saturation pressure ratio of the adsorbed nitrogen.

4.3.1.3. Results and Discussion

The data of SSA, average pore size, PSD, accumulated PSD and porosity of CNF-cement pastes are tabulated in the plots presented in Figures from Figure 4.13 to Figure 4.16, respectively.

Based on Figure 4.13, CNF increments produced a relatively steady raise in the SSA of cement pastes and (coherently with the SSA behaviour) a decline in the average pore size. It seems that the water retention capacity of CNF modifies the cement hydration kinetics and consequently in the proportion of hydrated cement products. Likely due to that, the higher capacity of CNF #1.13 has boosted these numbers, not only compared with CNF #0.13 range (i.e. up to 0.4 vol.%), but also over the entire range of loadings. As a result, the addition of CNF (principally CNF #1.13) enhanced the pore volume, as shown in the PSD plots of Figure 4.14.(a) for CNF #0.13 and Figure 4.14.(b) for CNF #1.13. This systematic growth in the pore volume occurred specially in the pore range of 3-4.5 nm in diameter, as can be perceived in the PSD plots magnified to pore sizes less than 50 nm of Figure 4.14.(c) and Figure 4.14.(d). And even easier to notice in the zoom in for the range of 0-10 nm shown in Figure 4.14.(e) and Figure 4.14.(f). It is worth noting that the pore size in Figure 4.14 is expressed in terms of radius, not in diameter. This nano-sized pore is mostly found in $C - S - H$ gel, what reinforces the hypothesis of changes in the cement hydration

mechanism caused by CNF. This pore refinement effect promoted by CNF (and in special by CNF #1.13), and already observed in Figure 4.14, is more evident in the plots of accumulated pore volume by pore size exhibited in Figure 4.15.

The overall porosity of CNF-cement pastes displayed in Figure 4.16.(a) shown approximately two distinct conducts: (i) an initial uptrend for fractions up to 0.4% of both CNFs, and (ii) roughly stable plateau at around 0.109 cc/g from 0.4-1.2 vol.% of CNF #1.13. During the growth stage at low-fraction CNF, CNF #0.13-cement pastes behaved in a relative similar manner than CNF #1.13-cement pastes. Interestingly, the porosity plot of CNF #0.13-cement pastes moves away from the plot of CNF #1.13 mixtures, by degrees, as the pore volume are counted till 50 nm and till 10 nm – see Figure 4.16.(b) and Figure 4.16.(c). It means that the CNF #1.13 loading produced a more intense pore refinement in cement pastes than CNF #0.13.

These findings are going to be recalled in order to understand the CNF role in the shrinkage performance of cement pastes in CHAPTER 5 and in the ingress of aggressive ions in CHAPTER 6 and CHAPTER 7. No error bars are plotted in the Figures due to financial and time constraints.

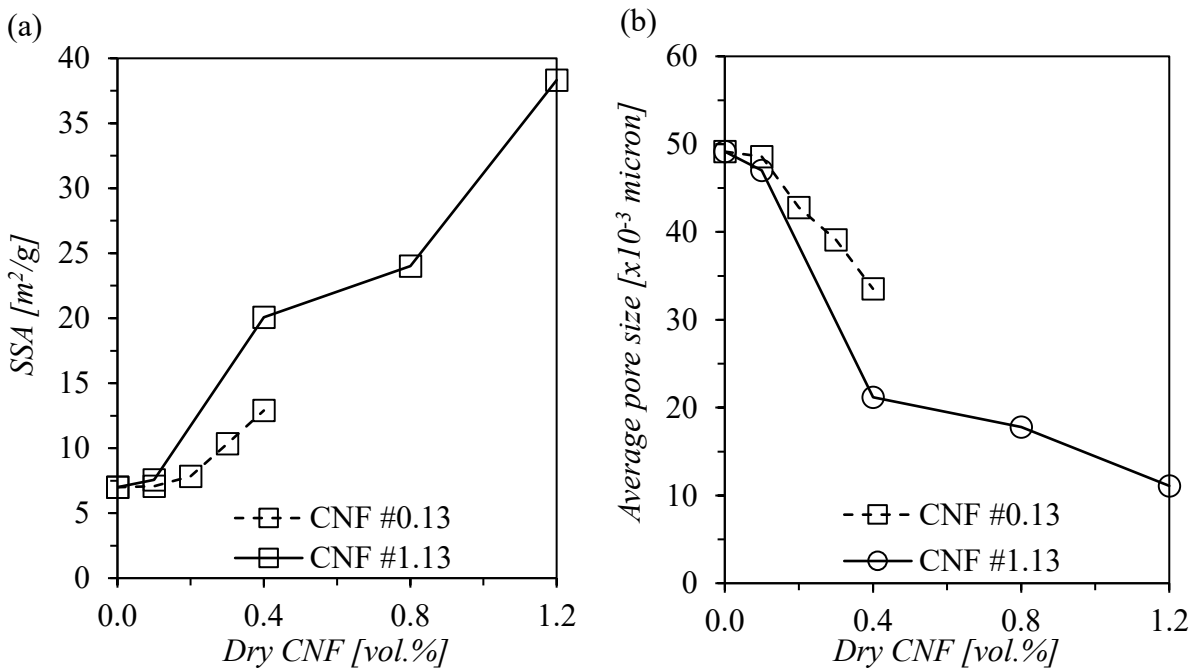


Figure 4.13.(a) Specific surface area (SSA), and (b) average pore size of cement pastes loaded with a range of fractions of CNF #0.13 and CNF #1.13. Both data were based on adsorption isotherms.

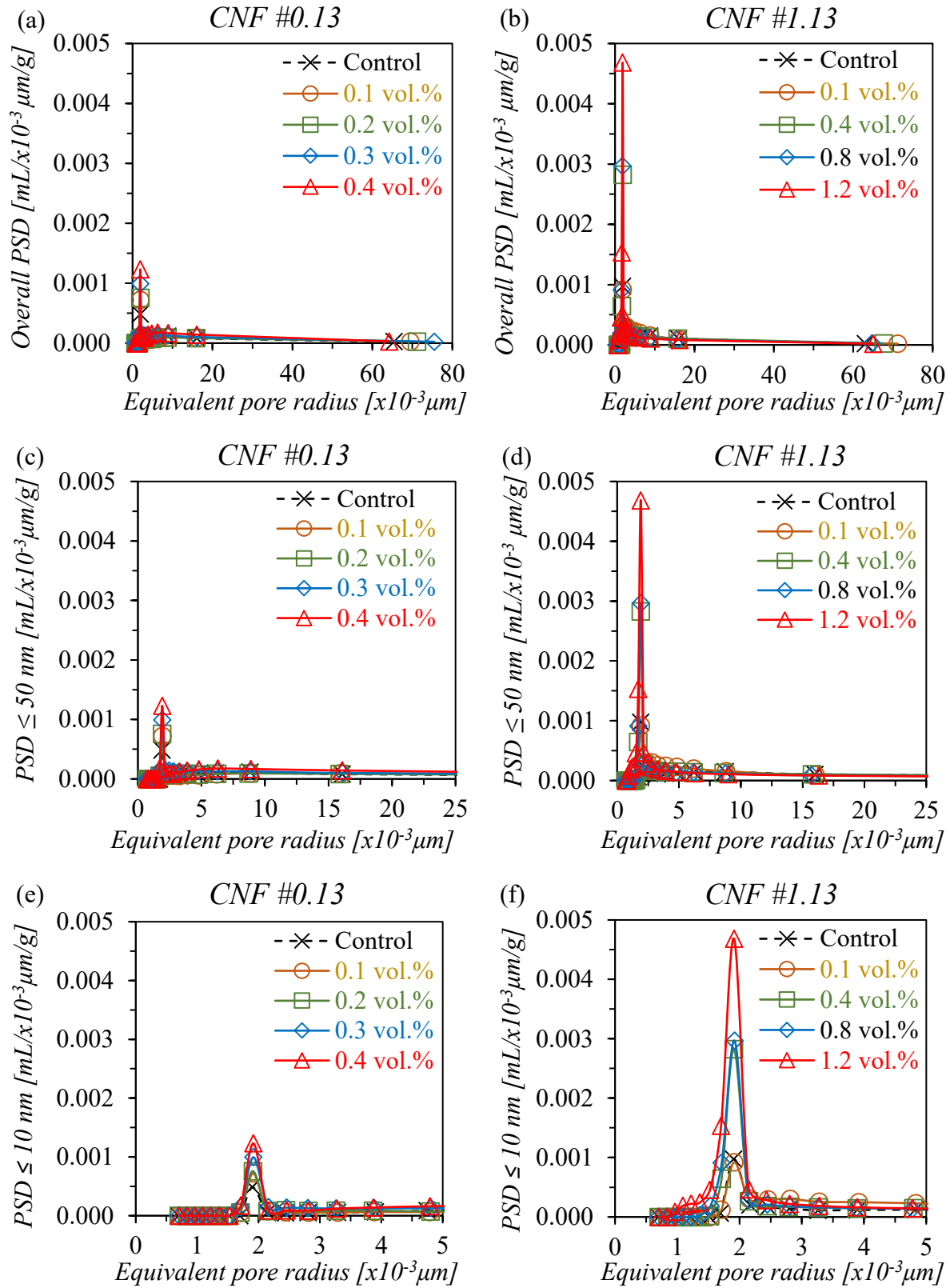


Figure 4.14 Pore size distribution (PSD) of (a) CNF #0.13- and (b) CNF #1.13-cement pastes based on desorption isotherms. Same plots limited to pore sizes less than (c),(d) 50 nm and (e),(f) 10 nm.

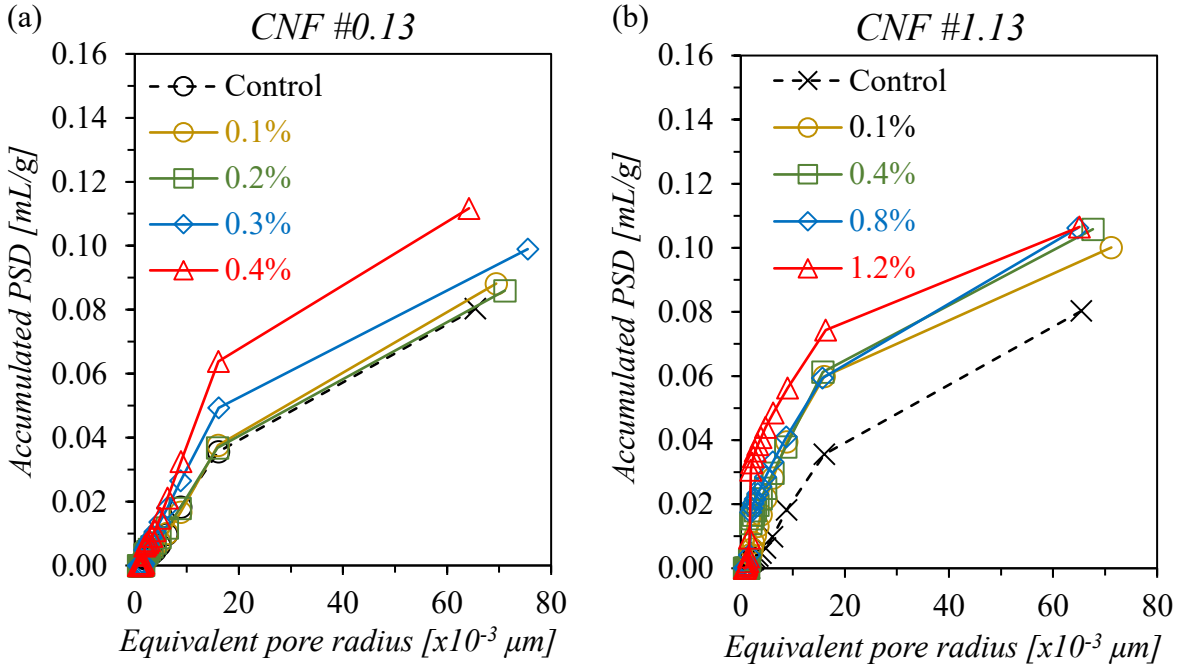


Figure 4.15 Accumulated pore size distribution (PSD) of (a) CNF #0.13-cement pastes, and (b) CNF #1.13-cement pastes based on the desorption isotherms.

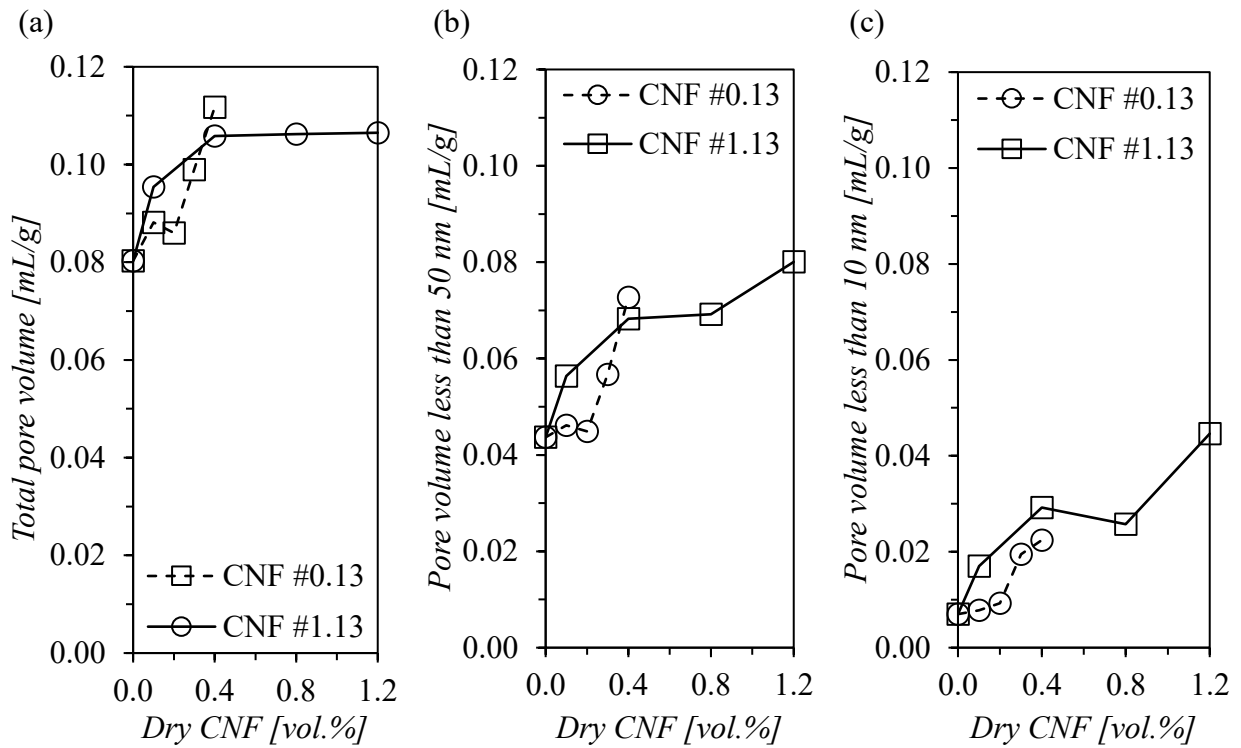


Figure 4.16.(a) Overall pore volume of CNF-based cement pastes. Pore volume less than (b) 50 nm in diameter and (c) 10 nm in diameter. Data based on desorption isotherms.

4.3.2. Scanning Electron Microscope (SEM) Image Analysis

4.3.2.1. Introduction

The complexity of concrete comes from the continuous interaction among the diverse raw materials and, between them and the external chemical elements over the entire lifetime of cement-based materials. The hydration of cementitious materials starts at the very first contact with water, still in fresh concrete. The solid phase evolves gradually as a result of these internal chemical reactions. The initial microstructure of fresh cement paste composed by pores as large as 3 to 5 μm in size [Metha et al., 2013] progressively gives rise to a more refined porous structure in hardened cement-based materials. This gradual refinement of pore structure is an ongoing mechanism that endures as long as the unreacted solid phase interacts with aqueous phase. Overall, the pore structure is formed by a striking variety of pores ranging from millimeter-sized voids to nanometer-sized pores equal to or less than 0.5 μm in diameter, which together constitutes between 25 and 50% of hardened cement paste volume [Jennings et al., 2002]. Nonetheless, the typical PSD of the hydrated products of cement varies from 10 μm to at least 0.5 nm. The capillary pores are defined as those ranging from 10 μm to 2.5 nm, the gel pores of $C - S - H$ phase varies between 10 nm – 0.5 nm and the finest pores lower than 0.5 nm are, in fact, interlayer spaces of $C - S - H$ gel [Jennings et al., 2002].

The pore structure has a large impact on the cementitious materials macroproperties. As discussed in the CHAPTER 2, the pores less than 50 nm determine the shrinkage (as well as creep) of cement pastes. And the permeability (and also, strength) is closely associated with the porosity between 10 μm and 10 nm [Jennings et al., 2002]. Metha et al. [2013] claimed that the capillary pore sizes are permeable only above 50 nm. Neville [1995] suggested that the fluid transport in concrete takes place in the range of 120-160 nm. Gong, Zhang, Sica, Ueda [2013] suggested that the pores greater than 100 nm in diameter should be neglected for permeability analysis. Nonetheless, it is important to recognize that pores greater than 10 μm reduce the impermeability of concrete, but not as much as those in the range of 10 μm and 10 nm. In this regard, pores greater than 1 mm encompasses the entrained air bubbles and entrapped air voids, which occurrence is more related to fresh concrete properties than associated with the cementitious material hydration; the referred fresh properties are low workability, inadequate compaction energy, use of entraining air admixtures,

just to name a few [Neville, 1995; Metha et al., 2013]. Not to mention the voids over 200 μm , as microcracks and the pores from 20-50 μm in the interfacial transition zone between paste and coarse aggregates.

Permeability is a highly relevant property for the purpose of concrete durability evaluation. Many of the detrimental physical and chemical mechanisms in concrete depend on the ingress of aggressive elements from external sources, such as SO_4^{2-} and Cl^- , which are addressed in CHAPTER 6 and CHAPTER 7, respectively. This property involves the flow of gases and/or liquids through the pore structure of concrete. The transport of these substances may occur through: (i) ionic gradient from areas with high concentration of ions toward areas with low concentration; (ii) suction provoked by the surface tension in the capillary pores; or (iii) adsorption-desorption mechanism of vapor in the pore structure. Thus, the characteristics of the pore structure, such as porosity and PSD, are determinant factors in the permeability of SO_4^{2-} and Cl^- in hardened cement pastes [Metha et al., 2013]. However, this relationship is not direct, given that the permeation of fluids and gases in cement pastes is, in part, controlled by the connectivity and tortuosity of pore network, especially among the capillary pores ranging from 10 μm -10 nm [Jennings et al., 2002].

As revealed in CHAPTER 2, the SO_4^{2-} expansive reactions result in cracking and disintegrations of cement paste microstructure, whilst Cl^- is pernicious for the integrity of embedded steel bars; despite the ability of some cement compounds to bind to the Cl^- . In light of this fact, the porosimetry was conducted in samples taken from sawn sections of specimens exposed to sulphate solution.

Silica fume, which are spherical particles of amorphous silica typically 0.1 μm on average, drops the permeability of concrete through a physical micro-filler (or packing) effect on the pore structure; that is, the very finer particles fill the voids hampering the connection among the pores and turning them more tortuous [Neville, 1995; Metha et al., 2013]. Note that CNF is at least ten times smaller than silica fume. Banthia, Sappakittipakorn, and Jiang [2012b] found that loading 0.1-0.3 vol.% of cellulose fibres improved the impermeability of cement pastes by truncating the

porosity network and hindering the flow of fluids, a phenomenon also known as pore-size refinement.

There are several apparatus and analytical techniques to measure the PSD of cement pastes [Juenger et al., 2001]. A list of them is found in Section 3.4 of the thesis. It is tabulated in this Section through the porosimetry of CNF-cement paste mixtures for pores less than 100 nm, using the gas sorption technique. For pore sizes above 100 nm, the analytical technique that best suits this range of pores is the analysis of images taken with the backscattered scanning electron microscope (BSEM). In this technique, a series of magnified images taken from a well-polished cross section of cement pastes are analyzed with the assistance of image processing programs [Scrivener, 1988; Skalny & Hearn, 2001; Scrivener, Bazzoni, Mota, & Rossen, 2018]. This software, first, binarizes and filters the colour of 2D images using appropriate thresholding tools and then analyzes many features of the image, such as PSD and porosity, using the ‘opening method’, for example [Schindelin, Arganda-Carreras, Frise, Kaynig, Longair et al., 2012].

4.3.2.2. Experimental Procedure

The PSD of cement paste mixtures containing various volume fractions of CNF were assessed by means of image analysis of polished sections via backscattered electrons (BSEs). CNF #0.13 was added to cement pastes in the range of 0.-0.4 vol.% fraction. And CNF #1.13 from 0-1.2 vol.% loadings. More details about the mixture proportions and the mixing procedure of these mixes are given in Section 3.4 of this thesis.

The samples used in the BSE image analysis were obtained from cylindrical paste specimens. The casting, demolding, and 28-day moist curing and cylinder-side epoxy resin coating were undertaken as described in Section 6.4.1.2 of CHAPTER 6. The epoxy resin coating aims to ensure unidirectional penetration through the cylinder ends only, in order to avoid sulphate overconcentration at the cylinder corners. Next, the cylinders were submerged in Na_2SO_4 solution (50 g/L) for 12 weeks according to Section 6.2.1. The 10-mm thick slices were cut using distilled water as reported in Section 6.4.1.2. In these Sections are found several Figures illustrating these procedures.

After 12 weeks in Na_2SO_4 solution, smaller prisms of approximately 1 cm^2 of surface area and less than 5 mm in thickness were cropped from the cut slices by wet cutting using a diamond blade, as demonstrated in Figure 4.17.(a)-Figure 4.17.(c). Before initiating the sample impregnation with epoxy resin of low viscosity, the free water was removed from the capillary pores by, first, 1-week immersion in isopropanol alcohol at a liquid-to-solid rate of 100 v./v., then 24 hours of oven dry at $40 \pm 1\text{ }^\circ\text{C}$, and finally more 48 hours in a dissector, as recommended by Scrivener et al. [2018]. The general guidance for epoxy impregnation, polishing, re-polishing and carbon coating followed the recommendations of Scrivener et al. [2018]. Carbon coating the polished surface of the sample eases the electric conductivity through the surface and improves the resolution of the images – see Figure 4.17.(d).

The BSE images scanned throughout 1 cm^2 -surface sample magnified 50x, 600x and 2000x. The *Zeiss Sigma 300 VP-FESEM* with an accelerating voltage of 15 kV, shown in Figure 4.17.(e), was used for taking the BSE images. The total porosity and the PSD of cement pastes were measured after processing the images via an open source software (under general public license) ‘Fiji’ coupled with appropriate ‘plugins’ to PSD analysis based on the opening method [Münch, 2019]. The ‘Fiji’ software was built on top of the image processing program ‘ImageJ’. The ‘Image J’ software was also used to evaluate overall shrinkage, bleeding, and cracking growth in CHAPTER 5 of this thesis. Figure 4.18 exemplifies the image processing step.

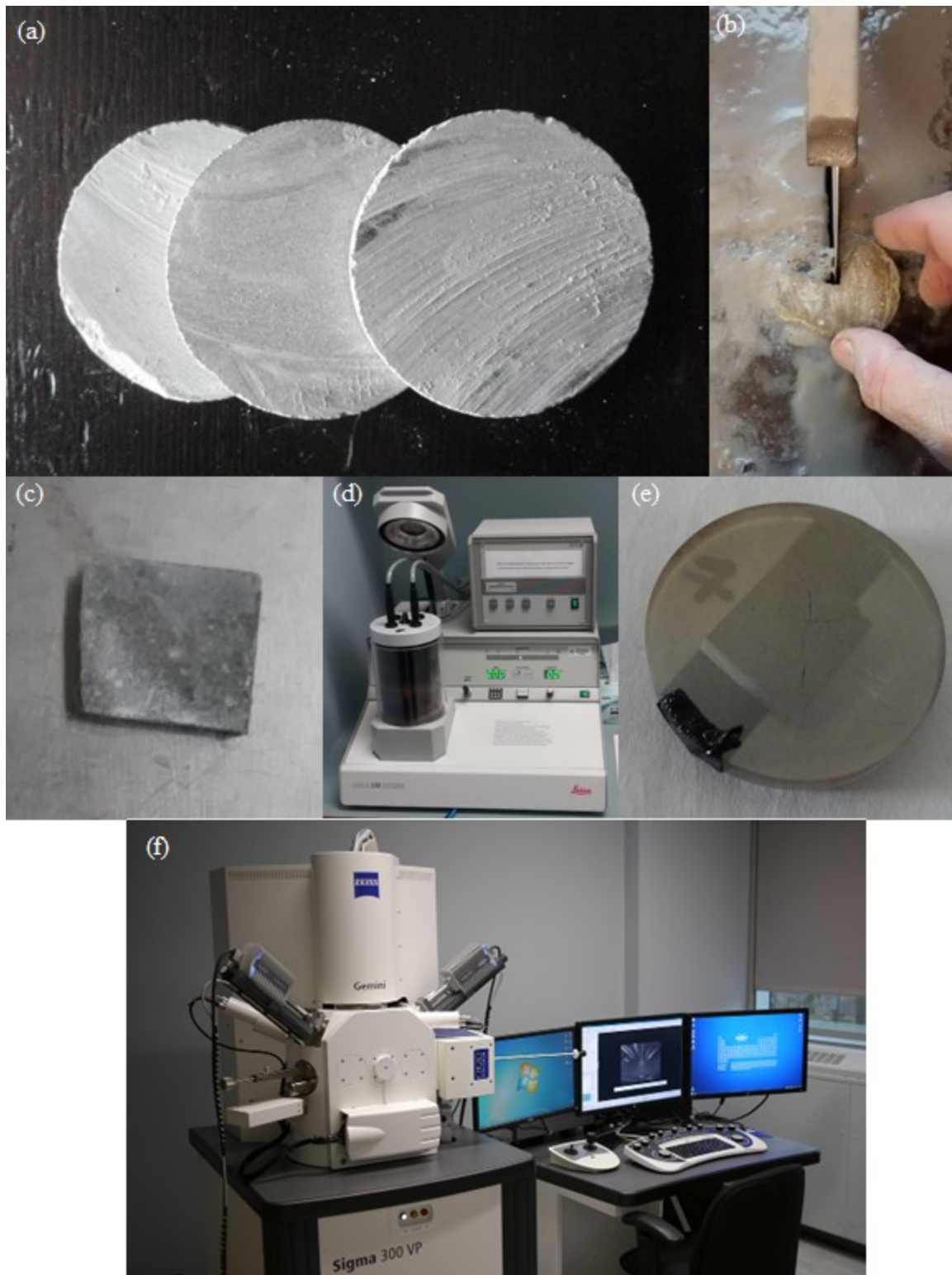


Figure 4.17 View of the (a) cut slices; (b) cutting; (c) sample ready to be embedded in epoxy resin; (d) carbon coat machine; (e) ready-for-analysis sample; and (f) *Zeiss Sigma Field Emission SEM*.

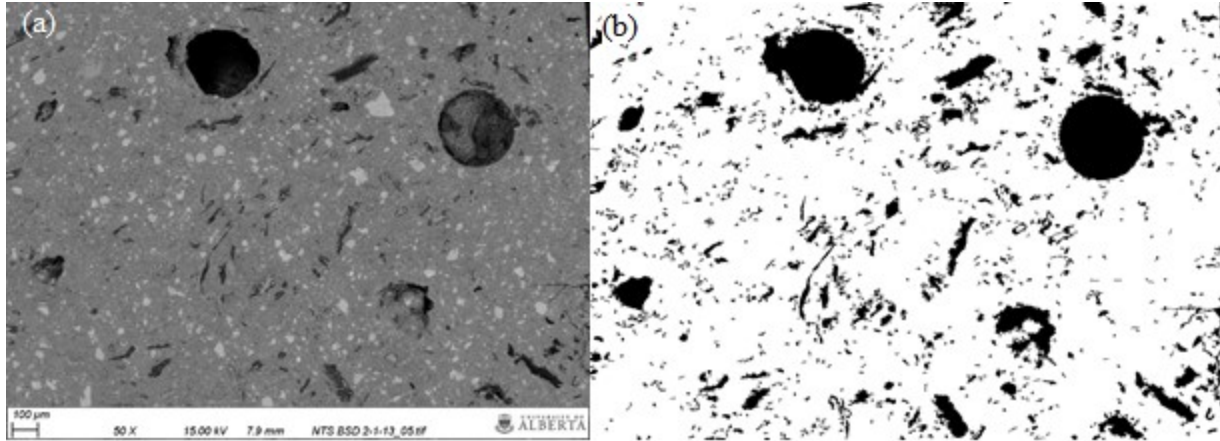


Figure 4.18 View of BES image (a) before and (b) after being processed by 'Fiji' program.

4.3.2.3. Results and Discussion

The pore fraction and the accumulative pore fraction measured in cement pastes containing CNF #0.13 loadings are shown, respectively, in Figure 4.19.(a) and Figure 4.19.(b). And in cement pastes with CNF #1.13 incorporated up to 0.5 vol.% fraction are displayed in Figure 4.20.(a) and Figure 4.20.(b).

Based on the literature review, the permeability of cementitious materials is more related with pores ranging from 10 nm to 10 μm in diameter [Jennings et al., 2002] than above 10 μm . For this reason, the plots of accumulative pore fraction were divided in two ranges, as seen in Figure 4.19.(c) and Figure 4.19.(d) for CNF #0.13 pastes and Figure 4.20.(c) and Figure 4.20.(d) for CNF #1.13. Note that the pore sizes in these graphs are expressed in radius, not diameter. The set of data plotted in these Figures revealed that the majority of the pore volume is accumulated between 10 nm-10 μm in diameter, for both CNF pastes. Besides, the porosity of cement pastes raised with increments of CNF loadings, again for both CNFs and in especial for CNF #1.13 dosages.

In spite of that, each CNF type impacted porosity in pastes in a different way. The growth seen for CNF #0.13-cement pastes was clearly governed by the range of pores between 10 nm to 10 μm . Moreover, the accumulative pore fraction greater than 10 μm maintained at a relative steady plateau of around 1.6% – see Figure 4.21.(a). In contrast, pores above 10 μm in diameter weighed much more in the porosity of mixtures containing CNF #1.13, as shown in Figure 4.21.(a) and

Figure 4.21.(b). It means that the CNF #1.13 paste mixtures incorporated a considerably large volume of air bubbles during the mixing operation of fresh paste than the mixes dosed with CNF #0.13. In numbers, the porosity of the paste containing 0.5 vol.% of CNF #1.13 went up 9.82% compared with the control cement paste. Under constant energy of compaction, the greater viscosity of fresh cement pastes manufactured with CNF #1.13 contents hindered the expelling movements of the entrapped air voids. The higher viscosity of these pastes was induced by the topmost CNF #1.13's water retention capacity among the CNFs used in the study. On the other hand, the CNF #1.13 pastes demonstrated porosity values for the 10 nm-10 μ m pore size interval oscillating in a narrow extension of about 13.01%-14.62%, which is precisely the most relevant pore range in terms of permeability – see Figure 4.21.(b).

These findings will serve as a basis for explaining the penetration mechanism of sulphates and chlorides in CNF-cement based systems in CHAPTER 6 and CHAPTER 7, respectively.

Only one SEM image analysis per mixture was carried out in this study because of cost constraints.

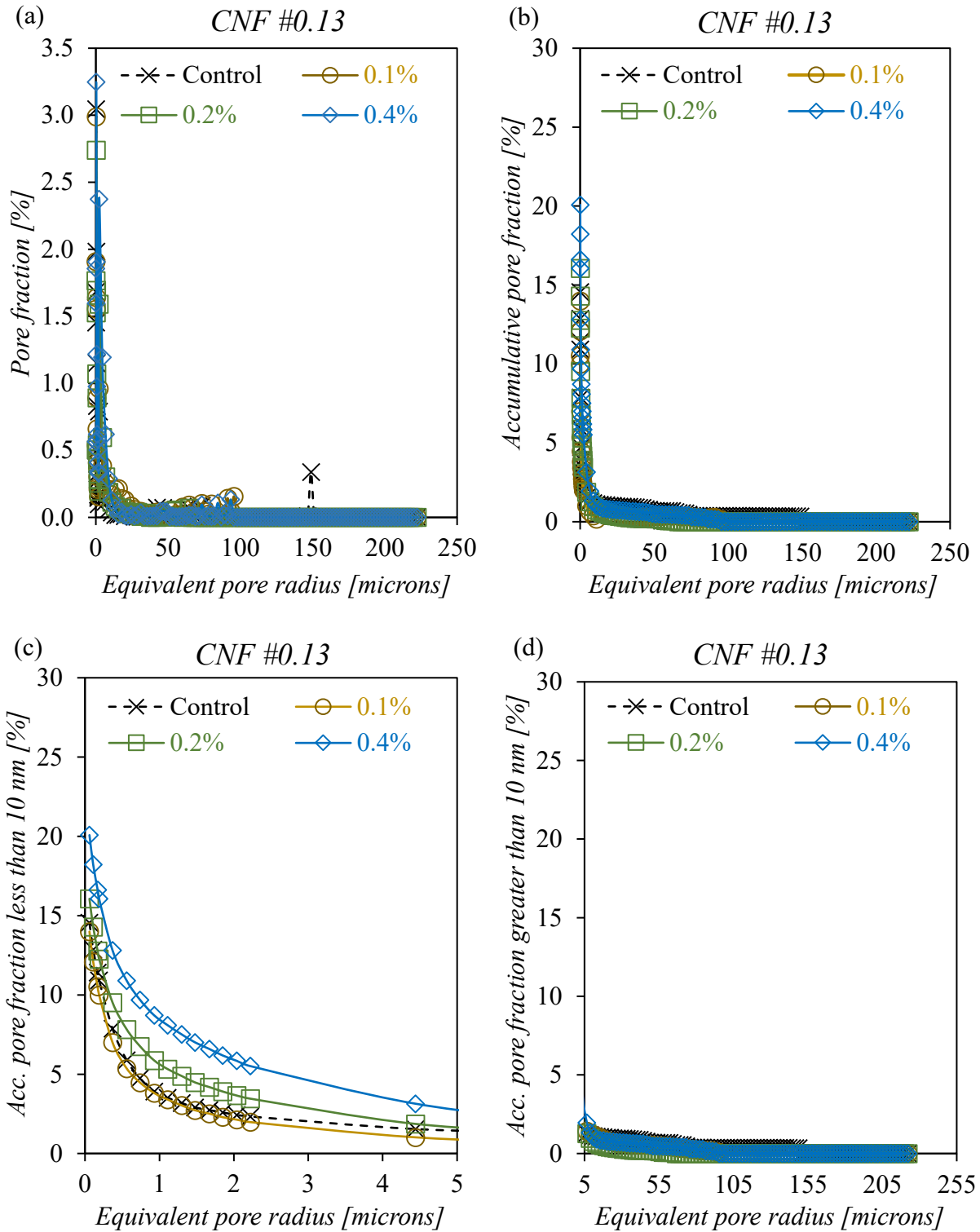


Figure 4.19.(a) Pore fraction and (b) accumulative porosity of cement pastes affected by a range of CNF #0.13 loadings. Accumulative porosity (c) less than and (d) greater than 10 nm in diameter.

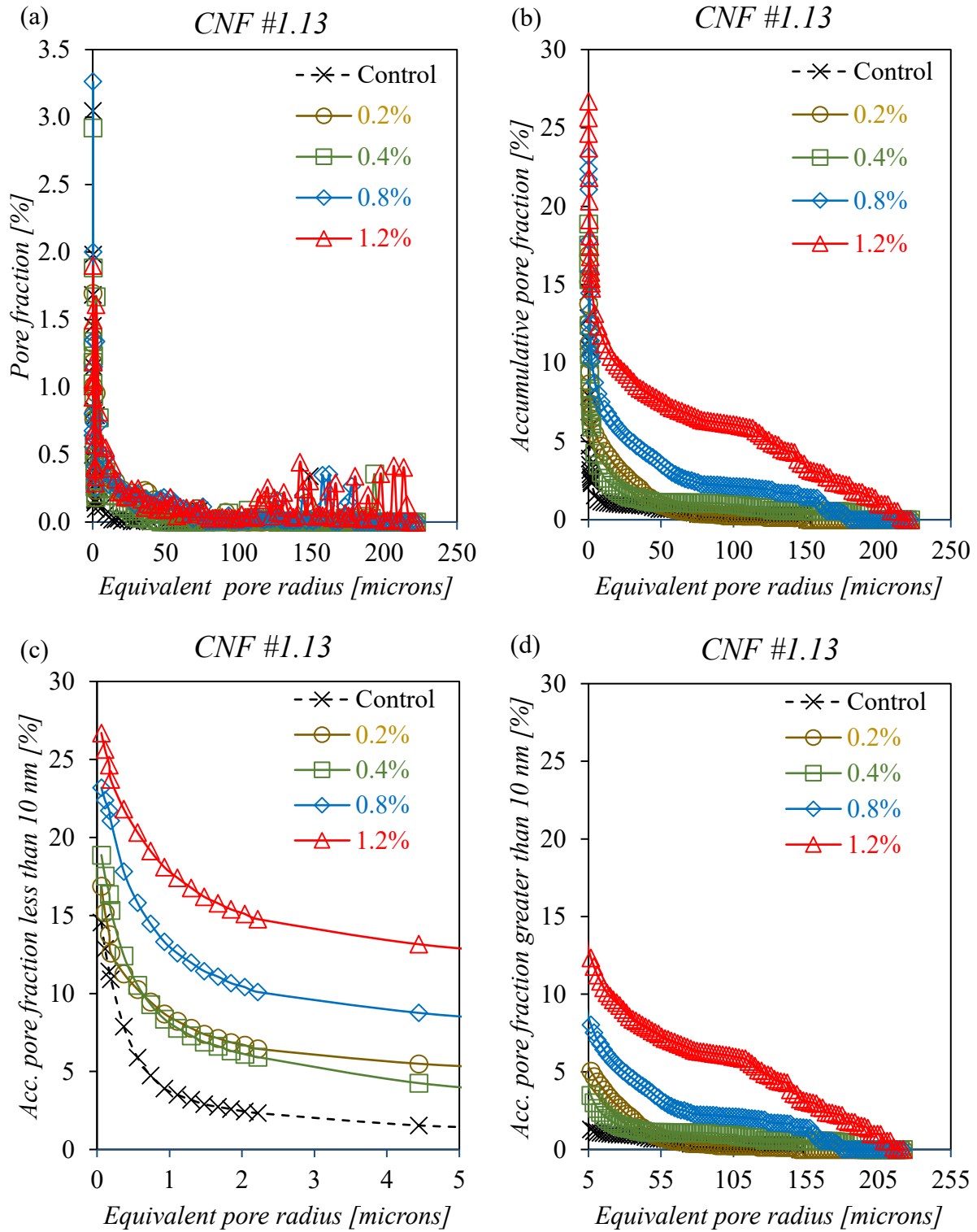


Figure 4.20.(a) Pore fraction and (b) accumulative porosity of cement pastes affected by a range of CNF #1.13 loadings. Accumulative porosity (c) less and (d) greater than 10 nm in diameter.

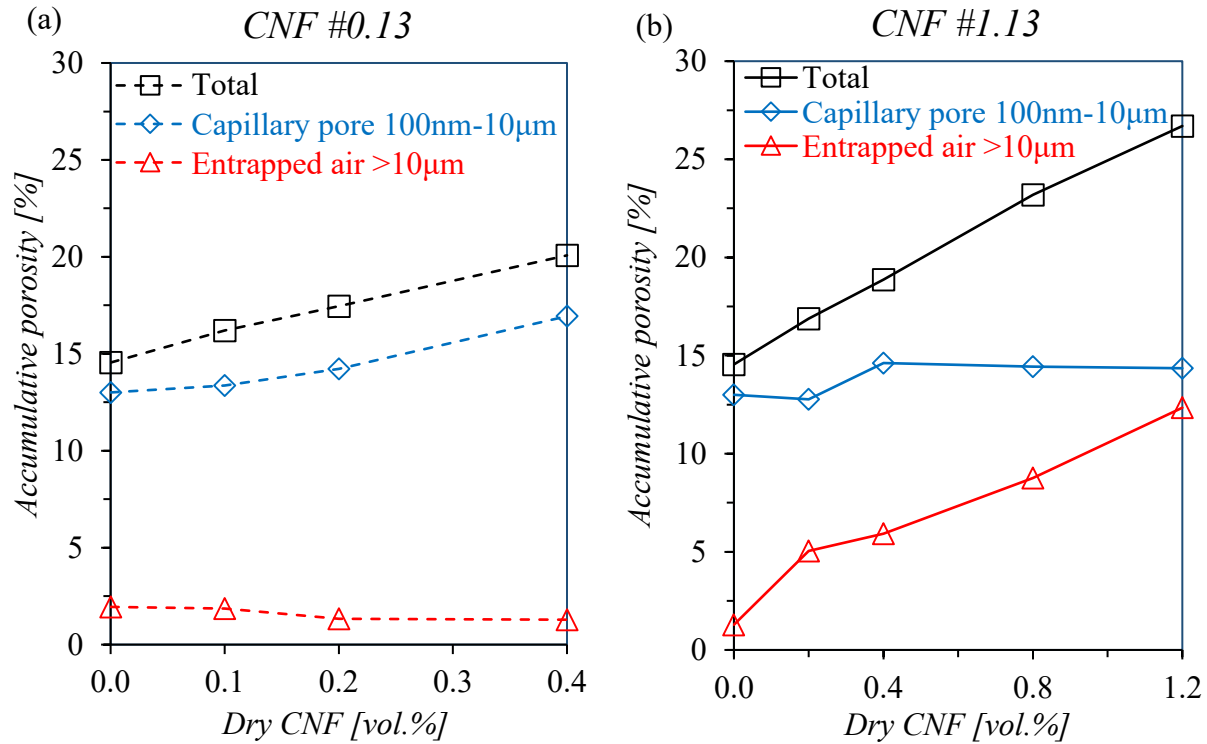


Figure 4.21 Porosity associated to different pore ranges of cement pastes affected by various doses of (a) CNF #0.13, and (b) CNF #1.13.

4.4. Mineralogical Analysis

4.4.1. Introduction

The electron microscopy is a powerful technique for analyzing the microstructure of cementitious materials. The scanning electron microscope (SEM) is a type of electron microscope that provides images of the sample surface magnified tens of thousands of times. Through the SEM images is possible to identify the mineralogy of the compounds of cementitious materials based on their morphology at micro- and nanoscale. The SEM image analysis may reveal significant facts about cement hydration, pathologies and specific chemical reactions, such as the one between CNF and Ca^{2+} . Hime, Marusin, Jugovic, Martinek, Cechner, and Backus [2000] claimed that SEM analysis is an important tool to identify ettringite and investigate the sulphate attack. An accurate analysis requires performing concomitantly SEM images and semi-quantitative elemental chemical analysis in specific spots of the microstructure using the energy dispersive X-ray spectroscopy

(EDS), in order to confirm the findings of morphological analysis [Franus, Panek, & Wdowin, 2015].

4.4.2. Experimental Procedure

Crushed pieces of a slice cut from the top-end of a paste cylinder exposed to 12-week unidirectional Na_2SO_4 solution (at rate of 50 g/1,000 mL) was submitted to SEM analysis. The paste used to cast the cylinder was dosed with 0.4 vol.% fraction of CNF #0.13. More details about this mixture and the cylinder casting are found in Section 6.4.1.2 of this thesis. The use of crushed pieces aimed to expose the internal solid microstructure to better visualize its mineral compounds and explore the core of the sample. The SEM apparatus was a *Hitachi S 4800 HR SEM* utilizing an electron beam accelerated at 30kV; no complementary EDS analysis was carried out. Figure 4.22 shows the SEM and Figure 4.23 an example of the magnification potential provided by SEM. In Figure 4.23, the SEM enlarged the image of the surface of a paste sample from millimeter to micrometer, revealing with clarity details of the cement paste microstructure.

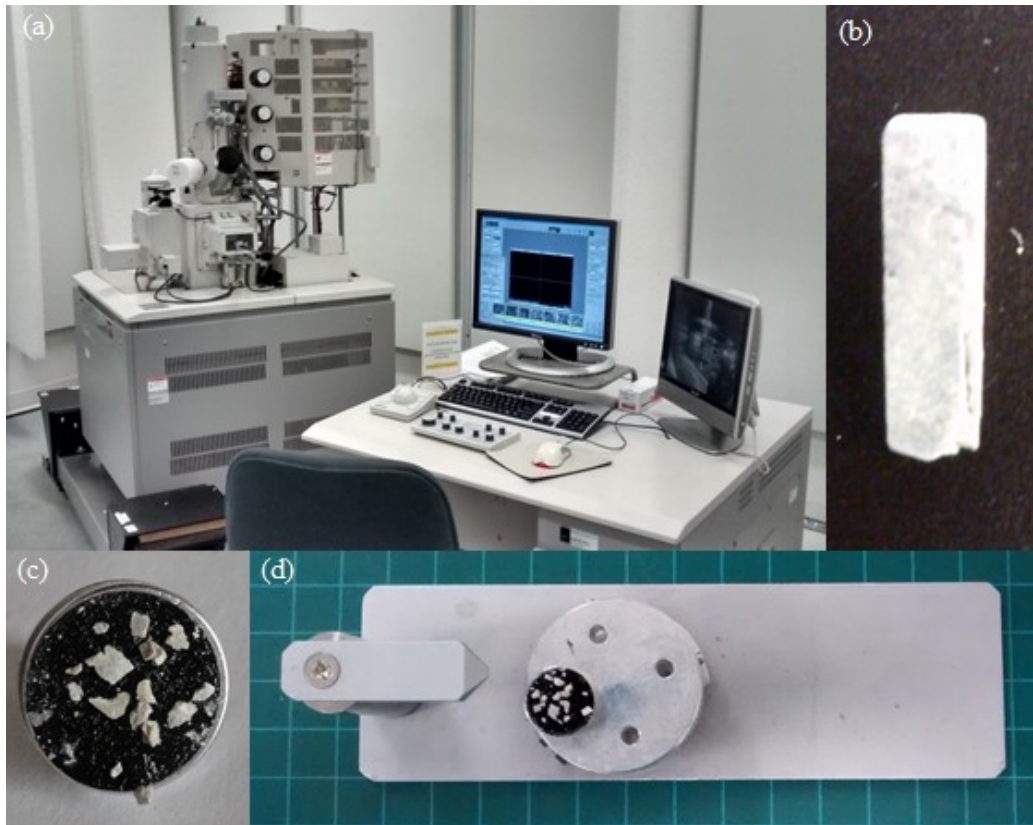


Figure 4.22 View of (a) the SEM; (b) the cut slice; and (c) the crushed pieces of sample used in the SEM analysis. View of (d) the SEM sample holder ready to be inserted in SEM.

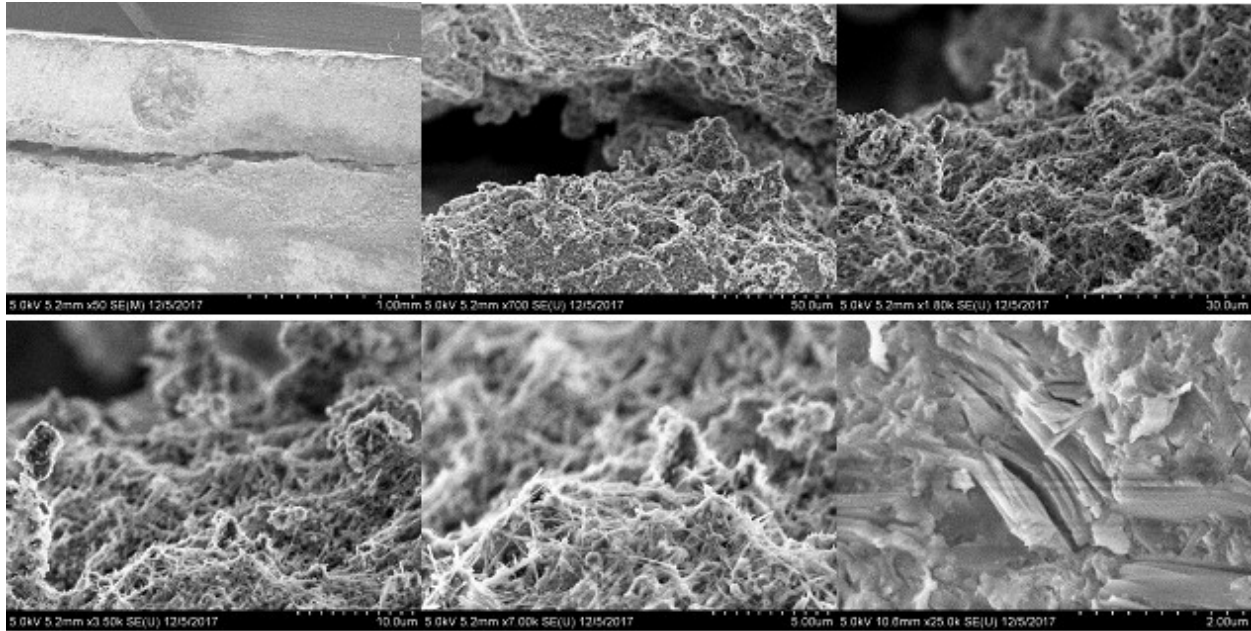


Figure 4.23 Sequence of SEM images increasing the magnification from 1 mm to 2 μm .

4.4.3. Results and Discussion

The SEM images with the pertinent comments about the crystallography and identification of the minerals are reported in Figure 4.24.

As shown in the SEM images, all minerals commonly found in cement pastes were also observed in pastes dosed with CNF, such as $\text{Ca}(\text{OH})_2$ (also known as portlandite), $\text{C} - \text{S} - \text{H}$ and ettringite. Unfortunately, neither CNF nor any sign of the chemical reaction between CNF and Ca^{2+} were visualized in the SEM images. Probably, due to the low content of CNF #0.13 in cement paste (i.e. 3.15 mg of CNF/g of dry cement) and CNF nanometer scale.

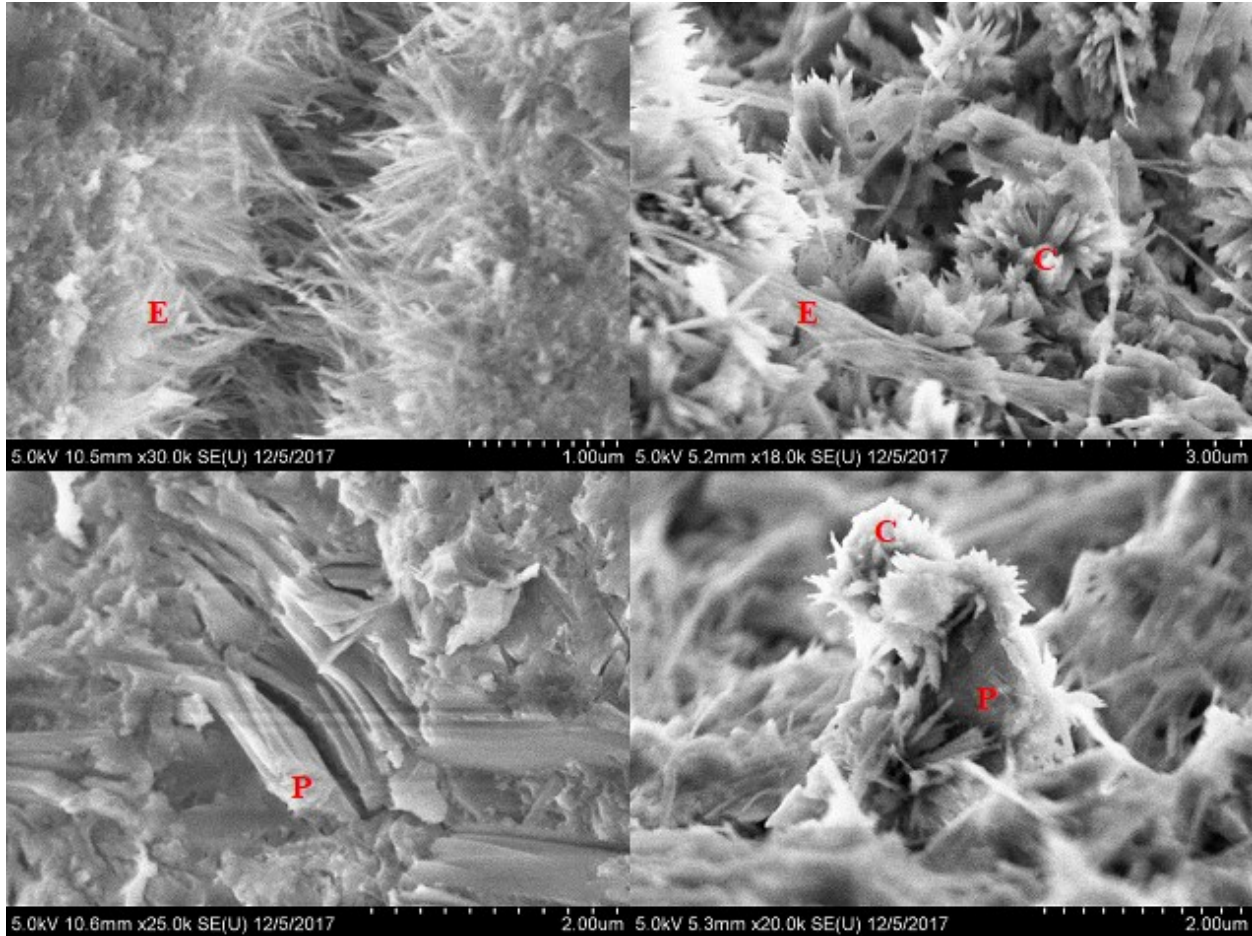


Figure 4.24.(a) Acicular ettringite [E] growing inside of a void. (b). Fibres of ettringite [E] and needle-like $C - S - H$ [C] stacks in the middle of hydrated products of cement poorly crystallized. (c). Columns of hexagonal plates of the $Ca(OH)_2$ crystals [P]. And (d) growth of $C - S - H$ [C] needles on the plate shape of $Ca(OH)_2$ [P].

4.5. Concluding Remarks

LOI measured by TGA and weight-loss method was employed to determine the DOH of GU cement pastes dosed with various CNF fractions. Besides, the porosimetry of these same mixtures was analyzed using gas sorption technique (for nanometric pore sizes) and SEM image analysis (for nano- and micrometric pore sizes). Two CNFs were incorporated to the mixtures, CNF #0.13 and CNF #1.13. Based on the findings revealed in this CHAPTER is the following concluding remarks can be withdrawn:

- The DOH was slightly reduced as CNF loadings were added to the control paste. The DOH drop was governed by decarbonation. The dehydroxylation of $Ca(OH)_2$ phase was slightly

downsized with increments of CNF loadings and the dehydration of ettringite, $C - S - H$ and gypsum was negligible. It seems that hydrophilic nature of CNF retained the water and hence delayed the hydration kinetics of cement, declining more the $Ca(OH)_2$ phase than the other hydration products. Interestingly, the most affected phase was another Ca-phase, $CaCO_3$. It may suggest that CNF's active anionic groups may combine with calcium cations soluble in the aqueous phase of pore system. Judging by DOH data, the 'short-circuit diffusion' phenomenon is an unlikely scenario for mixtures dosed with CNF;

- The volume of pores less than 50 nm in cement pastes was enlarged by CNF loadings till 0.4 vol.%. The CNF #0.13- and CNF #1.13-cement pastes performed similarly up to this fraction. After that, the small-size porosity of cement pastes remained approximately the same. CNF #1.13 generated a more intense enlargement in the small-pore volume than CNF #0.13. The majority of porosity growth occurred in pore sizes about 50 nm or less in diameter. Therefore, the higher availability of water proportioned by CNF's water retention appears to affect more smaller capillary pores and pore gel; and
- The volume of pores greater than 100 nm in size rose as increasingly amounts of CNF were added to cement pastes. This increase was controlled by the porosity range between 100 nm and 10 μm in CNF #0.13-cement based pastes, whereas in pastes containing CNF #1.13 loadings was by unintentional entrapped air, over 10 μm ; the rise in the 100 nm-10 μm range in CNF #1.13 mixes was only marginal. Accordingly, the augment observed for the CNF #1.13-based mixtures is associated with changes in the rheology (workability), as noted in Section 3.4 of preceding CHAPTER.

CHAPTER 5. Shrinkage in CNF-based Cement Pastes

5.1. Introduction

Shrinkage in concrete is inherently associated with the volume changes seen in the hydrating cement paste. This dimensional instability may manifest in diverse ways. Among them, plastic shrinkage and drying shrinkage encompass most of the volume changes. Plastic shrinkage dominates until the setting time of cement paste. After that, drying shrinkage controls. Bleeding and loss of moisture by evaporation are properties directly associated with shrinkage during the early age of concrete. And at later ages, the evaporable water is lost mostly from the gel pores, that is, pores less than 50 nm. All these phenomena are related to free-water movements inside the system or from the inside to the outside of cement-based systems.

Cellulose nanofibres (CNF) have active groups of hydroxyl and carboxyl on their cellulose macromolecules able to retain water [Klemm et al., 2011]. These active groups are accountable for the CNF's hydrophilic nature, which interfere with the water displacement in concrete.

In fresh concrete, the water retention capacity of CNF may hold the free mixing water and thus hamper its upward movement to the surface due to the settlement of solid particles. As a result, the early loss of bleed water from the concrete surface to the environment by evaporation may be prevented. A more favorable bleed-water evaporation relationship may alleviate the undesired effects of plastic shrinkage. In contrast, the inherent hydrophilicity of CNF may also prolong the setting time of cement paste, as observed by Jiao et al. [2016], and accordingly allows an increase in the bleed water rate.

In hardened concrete, CNF may release the free water retained by its active groups to hydrate the unhydrated cement particles exactly when the availability of water in the pore structure is scarce. Besides, the CNF's anionic carboxylate groups may react with alkalis and calcium cations soluble in aqueous solution to form hydrophilic complex adsorbed on cement grains [Jiao et al., 2016]. In this way, CNF can favorably modify the hydration kinetics of cement (as well as its degree of hydration) and hence the porosity is reduced. Drying shrinkage at late ages depends on the pore volume less than 10 nm, i.e. the higher the porosity, the higher the shrinkage [Jennings, Thomas,

Rothstein, & Chen, 2002]. Metha et al. [2013] attributed the shrinkage control to pore sizes less than 50 nm in diameter. Another possibility is that CNF may maintain some free water in the pore gel structure of hardened cement-based system. In this case, it is expected that the drying shrinkage is attenuated as a function of the physical swelling in the gel porosity.

Furthermore, CNF may present reinforcement properties or similar effects, as any other fibre-like material; though with limited action due to its shorter length. This potential extra-factor may theoretically collaborate in reducing the number of cracks and microcracks resulting from the shrinkage processes. Besides that, the ingress of aggressive elements in concrete may also be mitigated. The associated literature is very limited and there is little or no agreement between the results reported, as discussed earlier in Section 2.6.4 of the thesis.

Accordingly, the above hypotheses are examined in this CHAPTER. To this end, the mix proportions used are listed in Table 3.10. A fixed water-to-cement ratio of 0.485, which was kept at the flow range of $30 \pm 5\%$ by a superplasticizer as detailed in Section 3.4. The mixing procedure followed the steps described in Table 3.9.

5.2. Overall Shrinkage

5.2.1. Introduction

One may determine the very-early age shrinkage in cementitious materials through multiple means. Many are based on embedded strain transducers, laser sensors and fibre optic sensors. Nonetheless, all these methods are associated with setbacks, such as high cost of the devices, monitoring only after the initial setting time or difficulties in fixing and placing the targets used as reference for the shrinkage readings in the still-soft concrete [Ong & Myint-Lay, 2006]. Ong et al. [2006] reviewed many such methods. Digital image analysis is a cheap and practical alternative that allows one to read the dimensions just 30 minutes after the cement hydration starts. This technique has already been applied for almost two decades in concrete and other building materials [Ong et al., 2006]. Diamond [2001] analyzed backscatter scanning electron microscope (SEM) images of the interfacial transition zone in concrete. Dequiedt, Coster, Chermant, & Chermant [2001] accessed the air-voids dimensions in concrete through automatic image analysis. The digital

image analysis was used in this thesis to evaluate the overall shrinkage in CNF-cement pastes submitted to 2-day accelerate test. The general steps of the experiment are described by Mamun and Bindiganavile [2012]. As described therein, the overall shrinkage embraces the plastic shrinkage, autogenous shrinkage and drying shrinkage.

5.2.2. Experimental Procedure

The paste specimens were prepared with two distinct CNFs, i.e. CNF #0.13 and CNF #1.13. Recall that they contain, respectively, 0.13 mmol/g and 1.13 mmol/g of the carboxylate content. Before casting, the metallic molds were covered with wax paper in order to facilitate the demolding and avoid friction between the bottom surface of fresh specimen and the mold base – see Figure 5.1.(a). The specimens were cast in a single layer of paste and compacted by an external vibrating table at 60 Hz for about 20 secs to dimensions of 310 mm x 75 mm x 10 mm. The plane surface of the specimens held practically perpendicular to the mold edges. Two specimens were cast per mixture and from the same batch. Immediately after the casting, the specimens were moved without vibration to the environmental chamber and then positioned according to the ink marks on the mold base – see Figure 5.1.(b). In the chamber, the specimens were subjected to 48-hour severe conditions, i.e. temperature of 40 ± 2 °C, relative humidity of air of $12 \pm 2\%$ and wind speed of 0.50 ± 0.05 m/s, as shown in Figure 5.2. These conditions were monitored and (if necessary) adjusted three times per day – see Figure 5.1.(c). The operational details and characteristics of the chamber are described by Mamun et al. [2012]. Thirty minutes after the initial contact of cement and water, the sides of the mold were carefully removed and then the top surface of the specimens photographed with a high-resolution digital camera, 14.1 Megapixels (4599 x 3066). The side of the mold were removed ahead of the initial setting time, which was measured in 80 minutes for the control paste in accordance with ASTM C403/C403M [ASTM International (ASTM), 2016]. At the end of the 48-hour exposure, another image was captured from the unrestrained surface of the specimen – see Figure 5.3.(a) and Figure 5.3.(b). These photos were taken from a fixed distance of 500 mm orthogonally aligned between the line of focus and the specimen surface – see Figure 5.1.(d). The length of the specimen surface was determined using a calibration factor along three target lines defined by ink marks – see Figure 5.1.(b). This calibration factor was obtained through the image analysis software ImageJ 1.50i, as reported by Mamun et al. [2012] – see Figure 5.4. This open source software enabled an accurate image processing and analysis of the target lines in

the captured images [Abràmoff, Magalhães, & Ram, 2004]. The length change was calculated according to the following formula:

$$\Delta_{48\text{ hours}} = (L_{30\text{ min.}} - L_{48\text{ hours}}) \times 100 / L_{30\text{ min.}} \quad (5.1)$$

where ' $\Delta_{48\text{ hours}}$ ' is the overall shrinkage [%], and ' L_x ' is the length at age 'x' [mm].

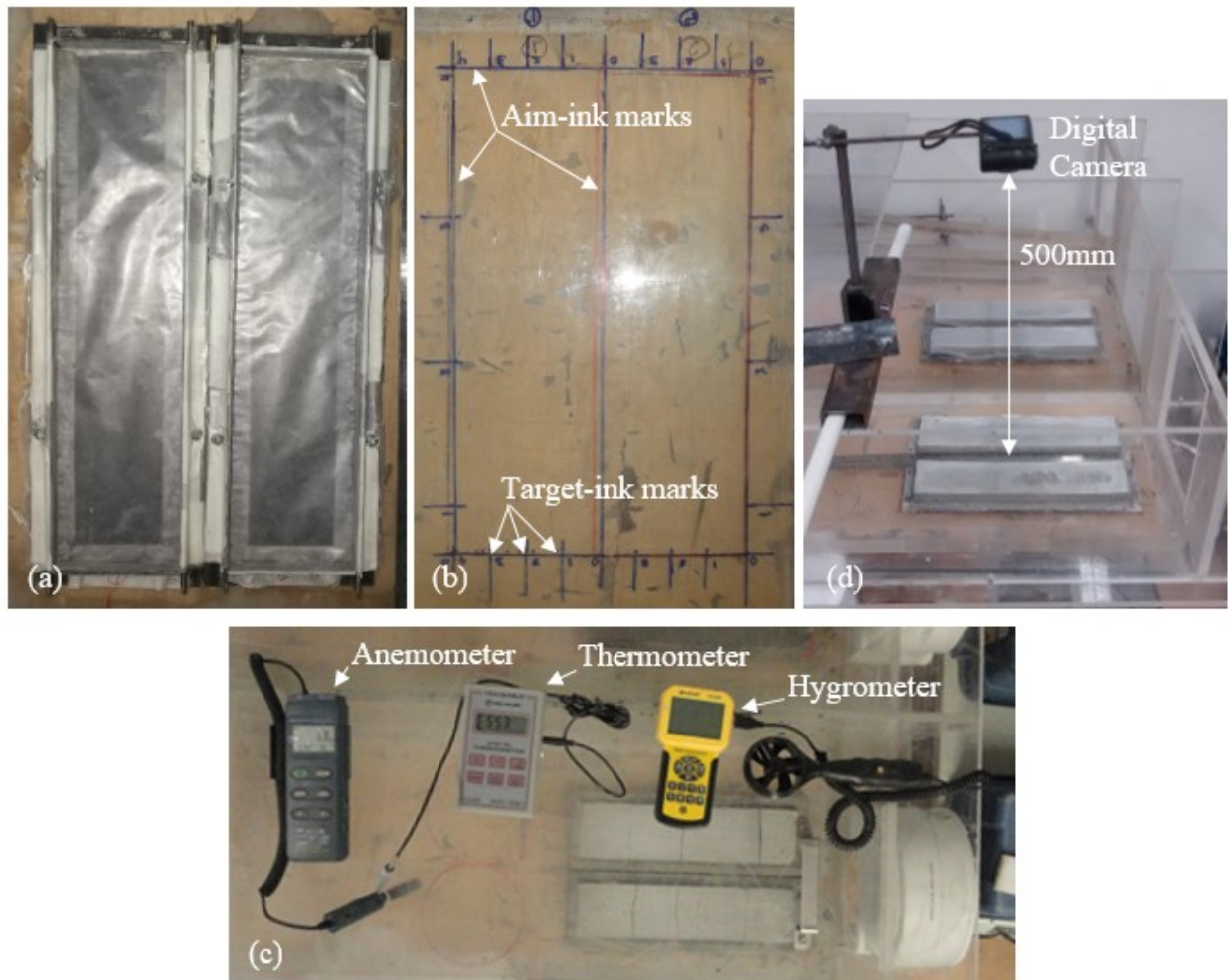


Figure 5.1 Some steps of the overall shrinkage experiment: (a) molds covered with wax paper; (b) ink marks to arrange the specimens and to measure the length change (LC) at specimen surface; (c) instruments used to control the environmental conditions inside the chamber; and (d) apparatus to photograph the specimen surface.

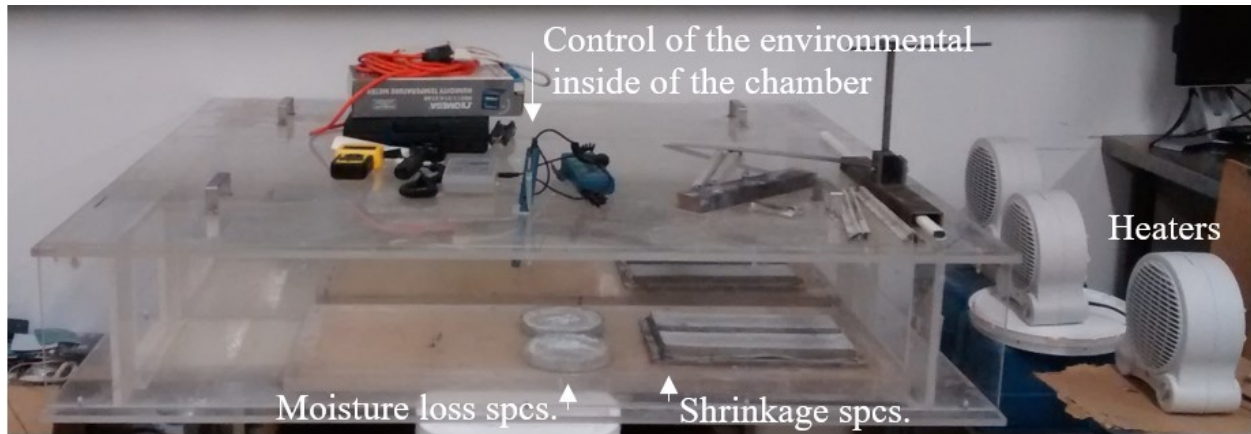


Figure 5.2 View of the chamber equipped with fan-forced heater at one end, which blows heated air into the compartment containing specimens used for overall shrinkage and evaporation rate.

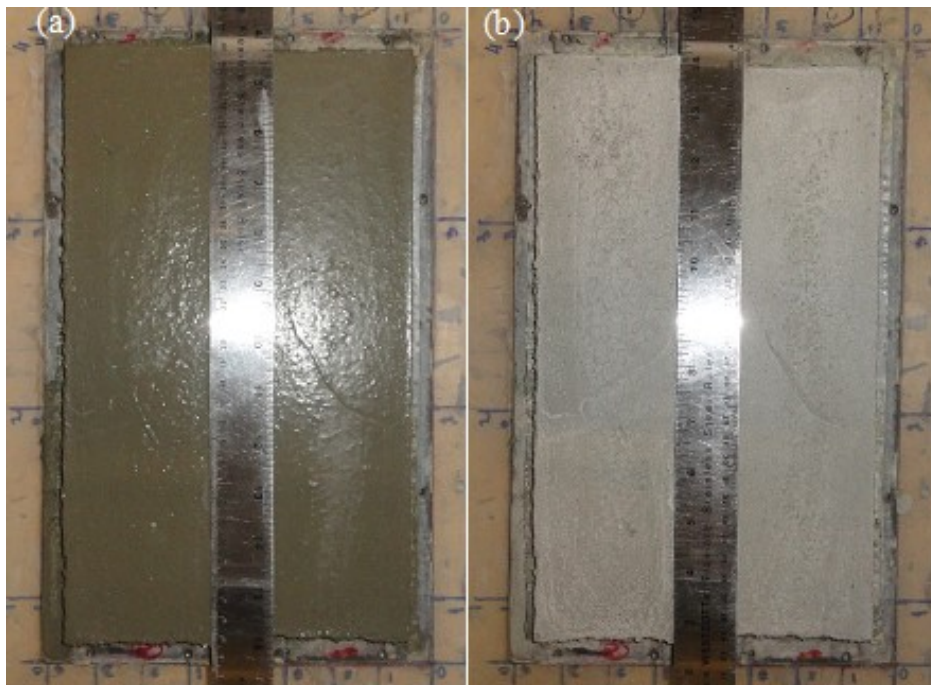


Figure 5.3 Specimen photographs taken after (a) 30 minutes and (b) 48 hours of severe exposure in the chamber used to determine the length change of specimens by image analysis.

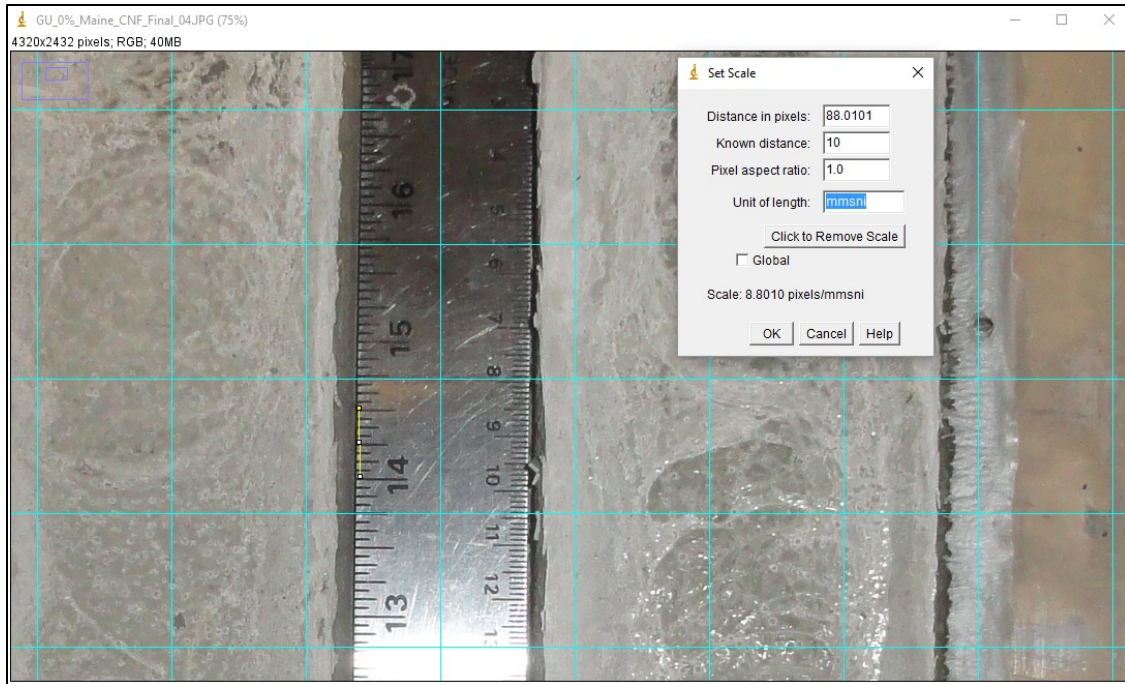


Figure 5.4 Screen-print of the 'ImageJ' software tool used to obtain the calibration factor.

5.2.3. Results and Discussion

The overall shrinkage measurements of CNF-cement mixtures are reported in Figure 5.5. Based on this Figure, two distinct stages of performance may clearly be identified in comparison with the control paste. That is (i) there is no-effect upon the shrinkage from adding CNF #1.13 and (ii) there is an increase with dosing CNF #0.13. The shrinkage roughly remained invariable with increments in the fraction of CNF #1.13; in fact, the shrinkage was very slightly reduced. On the other hand, CNF #0.13 loadings increased the shrinkage; particularly for dosages above 0.1%. The peak shrinkage was attained at 0.3% of CNF #0.13. In this regard, the superplasticizer demand for paste mixtures containing 0.3% and 0.4% of CNF #0.13 exceeded the maximum recommended by the admixture supplier (i.e. 1170 mL/100 kg); according to Table 3.10, the superplasticizer dosage was 1667 mL/100 kg and 5417 mL/100 kg, respectively. This overdosing may have slightly delayed the setting time of these mixtures in relation to the control paste, as visually observed during the experiments. As a consequence, the performance of these mixtures may have been affected by less rigidity of cement paste at the time of removal of the mold sides.

While cement paste is still in a plastic state, the balance between the evaporation rate of the water at the specimen surface and the rate at which the free water moves toward the surface, that is, bleeding governs the plastic shrinkage. If the evaporation rate is higher than the bleeding rate, sooner or later the surface will shrink. Hypothetically, the water retention capacity of CNF should in fact preserve the free water inside of the fresh mixture and hence reduce the bleeding. As a consequence of a low volume of bleed-water evaporated, the plastic shrinkage may have been enhanced. El-Bakkari et al. [2019] demonstrated that the CNF's capacity of retaining water is nearly proportional to the CNF's carboxyl group content, as noted in Section 2.5. Therefore, it is expected a better performance of CNF #1.13-cement mixtures over that of the CNF #0.13 mixes; given that CNF #1.13's higher carboxylate content, i.e. 1.13 mmol/g.

However, it must be considered, as well, the hypothesis of CNF may have functioned in a contrary direction to what was intended. In other words, CNF may have speeded up the bleeding process. Jiao et al. [2016] found an increase in the setting time as growing fractions of CNF are added to cement pastes. This rise reached 100 minutes and 90 minutes, respectively, for the initial and final setting times. These authors [Jiao et al., 2016] attributed this postponement to a delay in the induction period of hydration caused by reactions between the anionic groups of CNF and the soluble cations (calcium and alkalis) in the pore solution of fresh cement paste. Extended setting time prolongs the bleeding period along with the bleed-water volume, which may be lost by evaporation. And for this reason, the plastic shrinkage increases.

Despite the controversy, the chemical admixture dosage required to keep the workability of CNF-based cement pastes equal to the control paste may also have contributed to boost the bleed water rate, as commonly observed in conventional cementitious materials [Ramachandran, 1996; Peschard, Grosseau, Guilhot, & Guyonnet, 2004; Wiliński, Łukowski, & Rokicki, 2016; Halim, Kusuma, & Hardjito, 2017]. Notably for overdosing, as occurred for mixtures loaded with 0.3% and 0.4% of CNF #0.13.

The bleed water layer must contain a parcel of CNF carried out together with water during the bleeding mechanism. The Figure 5.6 shows the colour contrast in gray colour as seen on the surface of specimens made of pastes with growing fractions of CNF #0.13; the higher the CNF fraction in

paste, the darker the shade. This Figure also shows an interesting surface cracking pattern observed in paste containing 0.4% of CNF #0.13; this pattern is typically found in concretes with high amount of bleed water. A similar process may have occurred in CNF #1.13 reinforced cement pastes.

The accelerated conditions imposed upon the shrinkage experiment speeded up the progress of cement hydration and the scarcity of free water in pore structure of hydrated paste. For this reason, contractions in the solid microstructure gradually prevails over volumetric changes caused by early loss of moisture. Drying shrinkage now controls the process. At this stage, any change in the paste volume are mostly related to the slow loss of adsorbed water from pore size less than 50 nm to the environment [Metha et al., 2013]; not mentioning the water consumed by hydration reactions. This range of pore size comprises the (medium and small) capillary pores and the gel pores; the first varies from 10-50 nm and the second from 0.5-10 nm [Jennings et al., 2002]. This pore range also includes the smallest hydrated cement compound, calcium silicate hydrate particles, $C - S - H$ gel, which represents 50-60% of the volume of solids in a fully hydrated cement paste [Metha et al., 2013]. The water retention capacity of CNF must initially promote an internal environment rich in water, so that the particles of $C - S - H$ gel are separated by a water film, as occurs in pastes with elevated water-to-cement ratio [Neville, 1995, Metha et al., 2013]. With the decline in the abundance of water, CNF may remove the adsorbed water from $C - S - H$ gel in order to balance its own moisture loss; hence, it shrinks the solid phase and in particularly the $C - S - H$ gel. Or CNF may act in opposite way. In other words, CNF may gradually release water to hydrate the unhydrated cement particles to compensate a gradual depletion in the pore water. Any enhancement in cement hydration will reduce the porosity with clear benefits for mitigating the drying shrinkage.

However, as demonstrated in Figure 4.6 and Figure 4.7 and explained in Section 4.2.3, adding CNF slightly decreased the degree of hydration of cement pastes; most likely because CNF's active hydroxyl and carboxyl groups (perhaps associated with the high range water reducer action) prolongs the setting time [Jiao et al., 2016]. More importantly, the increase in the volume of pores less than 50 nm and 10 nm shown, respectively, in Figure 4.16.(b) and Figure 4.16.(c) explains the growth in shrinkage observed for CNF-cement pastes; notwithstanding not justify the worst

shrinkage performance checked for mixtures incorporating CNF #0.13 in comparison with those with CNF #1.13. In this regard, it appears that the CNF #1.13's better ability to hold water played a decisive role in attenuating more vigorously the shrinkage of cement pastes at early ages (by means of an improved bleeding-evaporation balance) than at late ages.

The outcome of the interaction of some of these hypotheses was the overall shrinkage reported in Figure 5.5. For now, it can be stated that additions of CNF were ineffective to mitigate the shrinkage of cement paste; And, in fact, CNF #0.13 contents above 0.1% intensified the shrinkage. The higher water retention capacity or the finer morphological characteristics of CNF #1.13 enhanced the shrinkage of cement pastes.

In addition, a close visual exam of the post-test specimens revealed a clear curling at the slab ends, as portrayed in Figure 5.7. This type of deformation is observed in fibre concrete and alleviates the cracking in cement pastes [Banthia & Gupta, 2009]

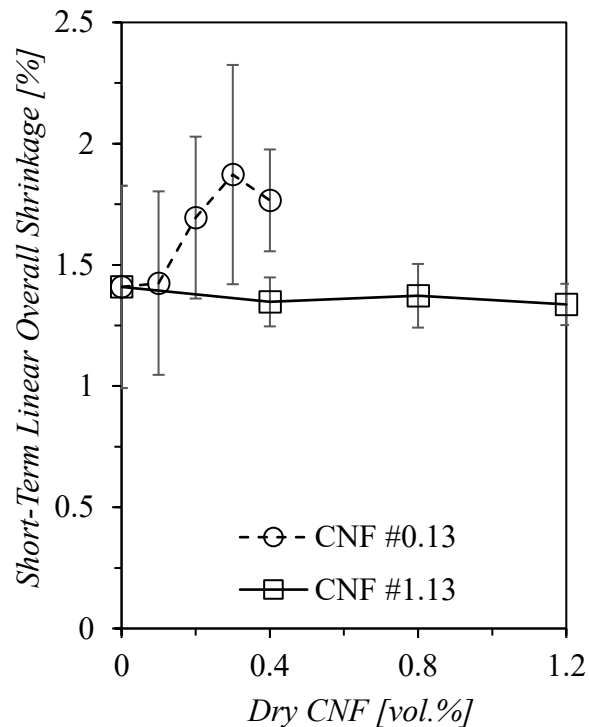


Figure 5.5 Overall shrinkage of CNF-based cement pastes exposed to 48-hour severe environment.

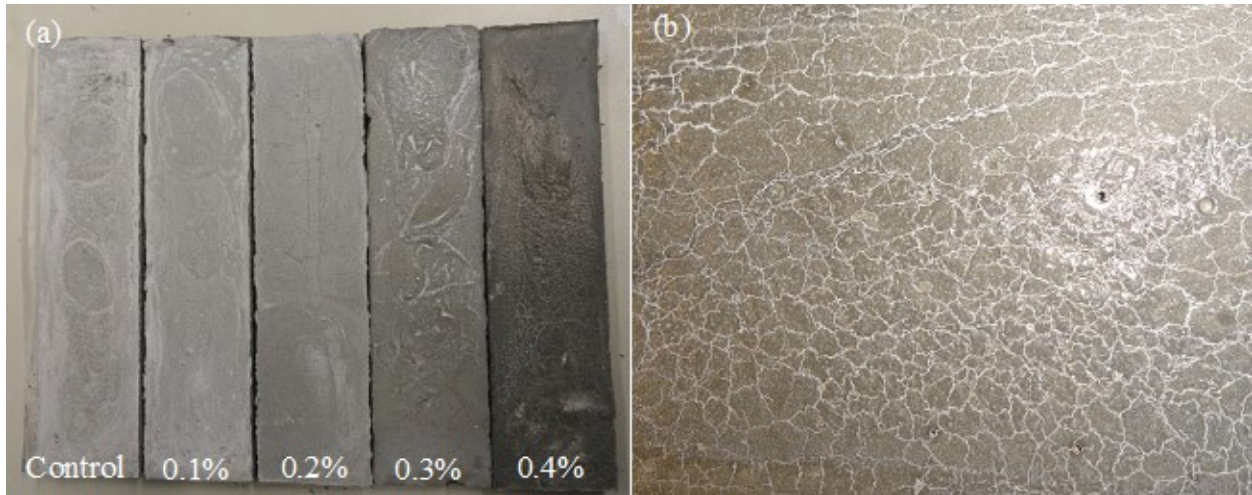


Figure 5.6.(a) View of the gradual darkening in shades of gray presented by slab-specimens loaded with CNF #0.13. (b) View in detail of the alligator skin-like cracking pattern observed in the surface of paste specimen containing 0.4 vol.% CNF #0.13 and overdose of superplasticizer.



Figure 5.7 Curling observed in the slab-like specimen: (a) side view, and (b) end view.

5.3. Drying Shrinkage

5.3.1. Experimental Procedure

The specimens were prepared, then demolded, cured, stored and the readings of specimen length were recorded in accordance with ASTM C596 [ASTM, 2009]. Cement pastes with various contents of CNF #0.13, CNF #0.7 and CNF #1.13 was used, instead of control mortar. Unlike the previous shrinkage experiments, the specimens were first exposed to 3-day water saturated cure and afterward, to air storage in the environmental chamber for 12 weeks. The temperature in the

chamber was $23 \pm 1^\circ\text{C}$ and the relative humidity $50 \pm 1\%$. Figure 5.8 shows the chamber. The readings of specimen length were taken inside the chamber at 1, 2, 4, 8 and 12 weeks of air storage. The drying shrinkage was calculated as per ASTM C596 [ASTM, 2009].



Figure 5.8 Environmental chamber used to expose the specimens to a controlled mild condition.

5.3.2. Results and Discussion

An account of the results is listed in Figure 5.9. Based on this Figure, both CNFs led to poor drying shrinkage performances compared with the control cement paste. It was least effective in CNF #0.13 reinforced mixtures, whereas both CNF #0.7 and CNF #1.13 behaved in a similar way. Actually, the results obtained by pastes loaded with CNF #0.7 were very slightly better than with CNF #1.13; presumably due to its lower concentration of nanofibrils. The increase in drying shrinkage was evidenced for the full range of CNF loadings examined. Interestingly, the shrinkage behaviour of CNF-cement pastes was relatively similar independently of the CNF content; this

finding was applicable for all CNF types. Another intriguing occurrence was the greatest difference of the pastes dosed with CNF in relation to the control paste at the very first week. This ‘first-week increase’ was common for all CNF types. Among them, CNF #1.13 displayed the lowest growth with respect to the control paste. After that, the dissimilarities between the performance of paste mixtures dosed with CNF and control paste was progressively diminishing in the remaining 11 weeks of the trial. Considering that, the CNF mixes plots apparently tend to meet the control curve in some weeks.

The 3-day curing prior to actual measurement, as required by the standard prevented the early-age loss of free water by evaporation, which is responsible for the plastic shrinkage in fresh cement pastes. Concomitantly, it allowed the formation of an initial solid microstructure of hardened cement paste. Immediately after the cessation of curing, the free water from the saturated capillary pores near the specimen surface is continuously taken out to environment by evaporation. Once the capillary pores were empty, the adsorbed water is then drained and so forth. As a result, the pore contracts as well as the paste microstructure. For the environmental conditions of exposure established in the standard test method, the removal of evaporable water from pores under 50 nm dictates the rhythm of drying shrinkage in hardened cement paste [Ramachandran et al., 2001; Jennings et al., 2002; Metha et al., 2013]. This range roughly covers the smallest capillary pores and the pores in $C - S - H$ gel, as reported in Section 4.3. Bearing this condition in mind, CNF likely rearranged the pore size distribution of cement pastes into a more refined pore structure. Jiao et al. [2016] found a progressive pore refinement as increasingly fractions of CNF were added to cement pastes; there was a growth in the cumulative pore volume less than around 20 nm in diameter and simultaneously a decline in the porosity over 20 nm. In addition, the authors [Jiao et al., 2016] reported a slight drop in the average pore size. Both findings were ascribed to the water release by CNF in the hardened microstructure of cement pastes.

With this regard, Figure 4.13 exhibited in Section 4.3.1.3 revealed that adding CNF to cement pastes refines the pore system. More importantly, Figure 4.16.(c) and Figure 4.16.(b) in this same Section display an enlargement in pore volume, respectively, up to 10 nm and (mainly) less than 50 nm as increasingly amounts of CNF fractions are added to cement paste. As reported earlier in Section 5.1, this range of porosity governs (the increase in) drying shrinkage [Jennings et al., 2002;

Metha et al., 2013]. The enhanced behavior presented by CNF #1.13 mixes in comparison with those containing CNF #0.13 (as observed for overall shrinkage – see Section 5.2.3) must be linked with CNF's highest water retention capacity, which slowed down the bleeding and, as a consequence, the moisture loss by evaporation.

The CNF's hydrophilicity modified the rheology of pastes, as witnessed during the preparation of CNF-cement pastes. Tang, Huang, Mei, Sun, Zhou et al. [2019] revealed that adding increments of CNF raised the yield stress and the plastic viscosity of oil well cement slurries. The higher viscosity of these mixes must have slowed down the sedimentation of cement particles and as a result, hampered the bleeding mechanism. For this reason, more free water is available in the saturated and thus swelled pore structure of CNF-cement paste than in the control paste. At the outset of the drying process, the evaporation of this greater volume of water contained inside of the pore structure is likely to have escalated the initial shrinkage. It may be the response to the first-week increase in the shrinkage observed in Figure 5.9. This elevated opening contraction is likely decisive to maintain the shrinkage of CNF-cement pastes at higher level than the control paste over the 12-week trial. As referred earlier in this Section, and noticed in Figure 5.9, it seems that the plots will concur to a common point in the future. The slightly better performance of CNF #1.13-cement pastes may be credited exactly to their smaller first-week increase in the shrinkage than other CNF-cement mixtures. Which in turn must be associated with CNF #1.13's higher ability to conserve water.

One these hypotheses or a combination of them may have become the CNF-cement pastes more susceptible to drying shrinkage.

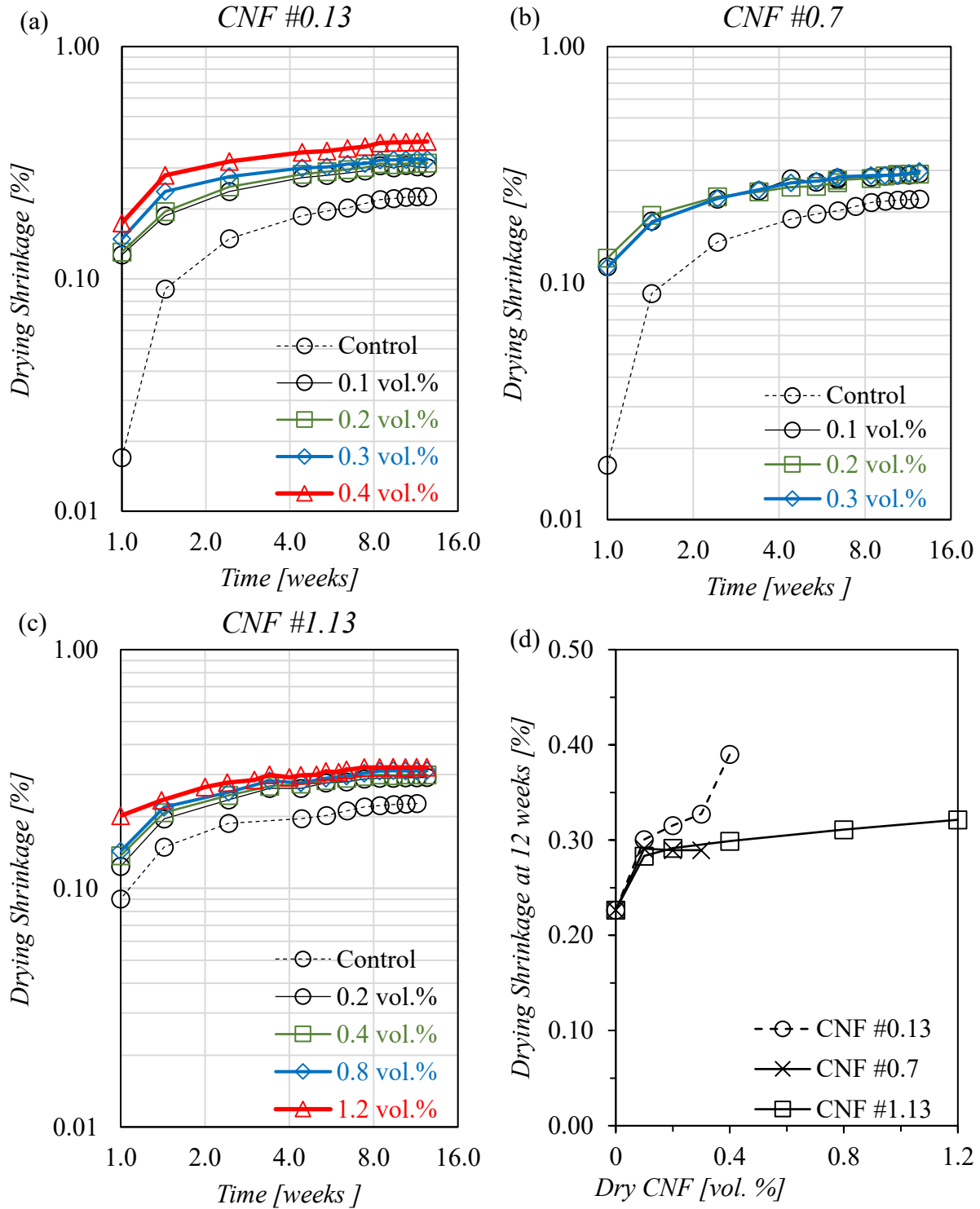


Figure 5.9 Drying shrinkage of cement pastes containing (a) CNF #0.13, (b) CNF #0.7, and (c) CNF #1.13. CNFs effect on (d) 12-week drying shrinkage. Error bars covered by markers.

5.4. Further Investigations

Several hypotheses to explain the shrinkage performance of CNF-cement pastes were raised in the previous Sections 5.2.3 and 5.3.2. Now, this Section tries to shed some light on CNF's role upon the relevant mechanisms for shrinkage. The resistance to cracking due to shrinkage, evaporation rate, and bleeding rate of CNF-cement pastes were examined in order to verify CNF's ability to preserve free water in pastes, as well as the influence of superplasticizer on these two last characteristics.

5.4.1. Cracking Analysis

5.4.1.1. Experimental Procedure

Cement pastes containing an increasing fraction of CNF #1.13 were used to cast, compact and left to air dry in the environmental chamber. Recall that the mixtures are detailed in Section 3.4. Two slab specimens, 310 mm x 75 mm x 10 mm in size, were examined per mixture. The specimens were prepared as described in Section 5.2.2. The internal ambient monitoring and the photographic documentation were carried out as depicted by Mamun et al. [2012]. Figure 5.10 provides an example of the specimens at the beginning and at the end of exposure time in the chamber. Figure 5.11 gives a general view of the crack patterns observed in all mixtures. Hitherto, the apparatus and the procedure for cracking analysis were identical to the overall shrinkage study, excluding two fundamental differences. Instead of wax paper, a layer of fresh paste was placed on a sandpaper CAMI grit designation 36 attached to the mold base – see Figure 5.12. The roughness of sandpaper holds the specimen bottom inducing a uniform restraint along the specimen thickness. And the photos of specimen surface were taken at 24 hours of exposure in the chamber, as recommended by Banthia et al. [2009]; not at 48 hours as when measuring the overall shrinkage.

In order to analyze the shrinkage-induced cracking in the first 24 hours of cement hydration, the total area and the maximum width of the cracks were measured. The maximum crack width was determined from at least 10 readings of the crack width taken equally spaced along each crack. For this purpose, the open-source software ImageJ 1.50i was used to process the images, as depicted by Mamun et al. [2012]. The calculation of the total crack area and the maximum crack width

followed the guidance established by Banthia and Gupta [2007b], as well as the CNF's efficiency rate to mitigate cracking in relation to the control paste.

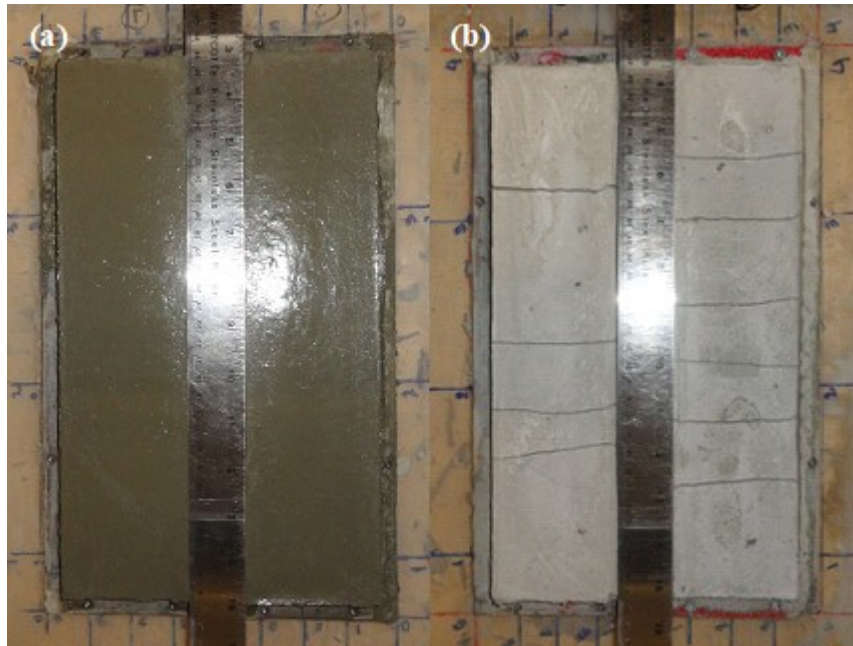


Figure 5.10 Slab specimens after (a) 30 min. and (b) 24 hours of severe exposure in the environmental chamber.

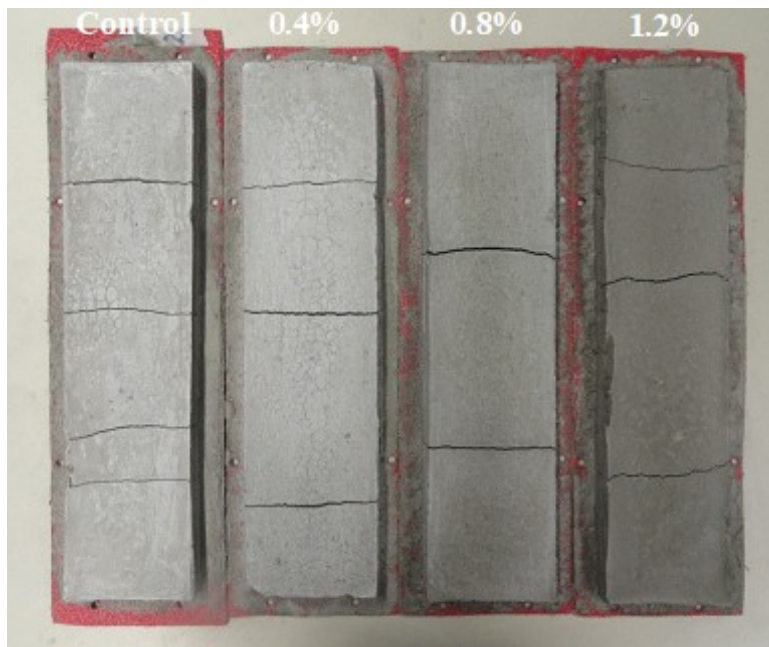


Figure 5.11 Cracking patterns exhibited by the pastes with various CNF #1.13 dosages after trials.



Figure 5.12 View of (a) the sandpaper, (b) the mold ready for casting, and (c) the paste specimen without the mold sides and the sandpaper ends fastened with screws to mold base.

5.4.1.2. Results and Discussion

The cracking analysis of the CNF-cement mixtures are tabulated in Figure 5.13. The efficiency of each fraction of CNF #1.13 in mitigating the cracking in cement pastes due to shrinkage is listed in Table 5.1. Based on the Figure, it is noticeable that CNF #1.13 declined moderately not only the total crack area, but also the maximum crack width. This affirmative is applicable to the entire range of CNF #1.13 loadings. The CNF #1.13's efficiency in improving the cracking behaviour grew with increments of CNF in cement paste, as reported in Table 5.1. The best performance was attained at the maximum dosage possible of CNF #1.13 (i.e. 1.2 vol.%). Kawashima et al. [2011] claimed that cellulose fibres having average size of 2.1 mm in length and 16 μm in diameter did

not affected the drying shrinkage, however, decreased the shrinkage-induced cracking with a suitable fibre dispersion.

The visible curling observed in the CNF-cement pastes specimens used in the overall shrinkage study (and shown in Figure 5.7) was an indicative of the potential nanofibre reinforcement and/or crack control. Similar findings were observed for cellulose microfibrils. Banthia et al. [2007b] obtained a crack-free concrete specimen at 0.2% of volume fraction of cellulose fibres. And Banthia et al. [2014] reported that concretes, when incorporating cellulose microfibrils up to 0.2 vol.% controls the cracking and increases the curling with respect to the reference plain mix; at the dosage of 0.3 vol.%, the cracking was completely arrested by the cellulose microfibrils. However, the crack-free condition found for mixtures with microfibrils was not reached by CNF-cement pastes. The main reason for that is the longest length of cellulose microfibrils, which confers to a better crack bridging effect. Bear this in mind, the crack control provided by CNF #1.13 in cement pastes occurred but must have been limited if compared with that of microfibrils. And even with that of CNF #0.13, since the morphological analysis of both CNFs shown in Section 4.4.2 demonstrated that CNF #0.13 is longer than CNF #1.13. Despite this fact, CNF #1.13-cement pastes exhibited the best shrinkage performances among all mixtures containing CNF. Therefore, it is likely that CNF #1.13 leads to a more favorable evaporation-bleeding balance and/or a smaller volume of pores less than 50 nm in cement pastes.

Table 5.1 Efficiency of each CNF #1.13 fraction in mitigating the cracking caused by shrinkage.

<i>Dry CNF #1.13 [vol.%]</i>	<i>0</i>	<i>0.4</i>	<i>0.8</i>	<i>1.2</i>
<i>Crack Width Control Efficiency [%]</i>	0	0.0374	0.0607	0.1449
<i>Crack Area Control Efficiency [%]</i>	0	0.0365	0.2055	0.1900

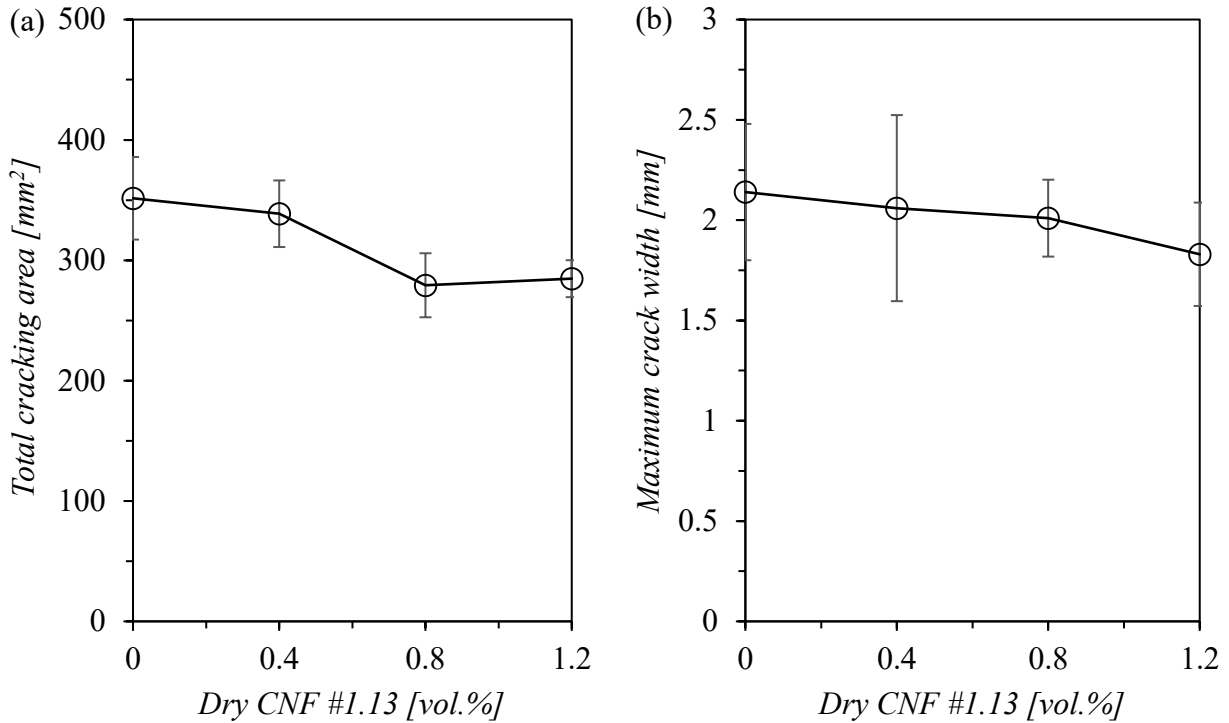


Figure 5.13.(a) Cracking area and (b) max crack width of CNF #1.13-cement pastes.

5.4.2. Bleeding

Bleeding can be visually detected in concrete. Initially, it develops at an accelerated rate that progressively slows down until becomes negligible at about the final setting time. Traditional standard test methods, as ASTM C232/C232M [ASTM, 2014], monitor and determine the bleeding depth in concrete based on naked eyes measurements. Yet, the accuracy of visual measurements requests a clear front of bleed water. Jossierand and De Larrard [2004] and Peng, Lauten, Reknes, & Jacobsen [2017] described four possible zones for bleeding based on different stages of sedimentation presented by the solid particles in fresh concrete. First, a bleeding zone at the top composed by a layer of clear water coming from bleeding flux. Secondly, a somewhat turbid homogeneous zone containing a flux of settling solid particles. Thirdly, more cloudy variable concentration zone with depositing particles. And lastly, the sedimentation cake at the bottom. Several factors may influence on the formation and the thickness of the turbid bleeding zone, such as flocculation of fine particles of cement and aggregate. Autier, Azéma, and Boustingorry [2014] demonstrated that medium-high dosages of polycarboxylate-based superplasticizers, as the one used in the research, thickened this supernatant zone of flow sediments and thinned the sediment

cake height – see Figure 5.14. The turbidity observed in some zones makes the determination of the clear-turbid bleeding depth hard by traditional methods. Time-dependent turbidity methods are an alternative to the conventional methodologies. The turbiscanner apparatus provides information over time about the sedimentation mechanism of dispersed particles in emulsions and suspensions. Peng et al. [2017] listed a number of authors that took use of this new technology to evaluate the stability of colloidal dispersions. Autier et al. [2014] was the first to analyze the stability of cementitious mixtures using the Turbiscan technique. More recently, Peng et al. [2017] innovated again using the intensity variation of the transmitted light to study the bleeding in cement pastes with diverse water-to-cement ratios and dosages of lignosulphonate admixtures.

For the purpose of the current research, the clear-turbid layer is defined as the bleeding height, that is, it embraces the clear-water zone at top, the turbid-suspension zone in the middle and the more cloudiness zone at bottom. In practical terms, some of these zones may or may not occur according to the sedimentation mechanism developed in cement paste.

This Section presents the bleeding performance of CNF-cement pastes based on the discussed methods, i.e. the conventional standard ASTM C232/C232M [ASTM, 2014] and the alternative Turbiscan analysis. The bleeding measurements were recorded until 4 hours counted from the first contact of water with cement; when is believed that the specimens reached the final setting time and no further sedimentation will take place.

In this study, CNF #0.13 was added in range of 0.1-0.4 vol.% and CNF #1.13 from 0.2-1.2 vol.% in paste mixes as listed in Table 3.10. As mentioned in Section 3.4, these mixtures show fixed water-to-cement ratio of 0.485 and flow of 6 ± 0.5 secs. And a polycarboxylate-based superplasticizer was utilized to meet design parameters.

In order to understand to what extent this superplasticizer may become involved in the bleeding mechanism, two new series of mix-proportions were designed and examined only by the Turbiscan method. In one series of paste mixes, the CNF #1.13 fractions of 0.2 vol.%, 0.4 vol.%, 0.8 vol.%, and 1.2 vol.% were maintained, but now, without addition of any polycarboxylate-based superplasticizer; consequently, the parameter of constant workability was disregarded. In the other,

growing quantities of superplasticizer were added to the cement paste loaded with a fixed amount of 1.2 vol.% of CNF #1.13; the dosages used were 0.35%, 0.7%, and 0.926%, by cement mass. The chemical admixture dosage of 0.926 wt.% was the max permissible to not modify the water-to-cement ratio of 0.485. These extra mix-proportions studied are reported in Table 5.2.

Table 5.2 Mix proportions of cement pastes incorporating various CNF #1.13 loadings and no superplasticizer and 1.2% CNF #1.13-cement pastes with increments in superplasticizers dosages.

Dry CNF #1.13 [vol.%]	Superplasticizer [wt.%]	Materials [kg/m ³ of paste]					
		Dry CNF	CNF gel	Cement	Water	SP	Deducted Water
0	0	0	0	1246	604.4	0	0
0.2	0	2.806	95.28	1244	510.8	0	100.59
0.4	0	5.602	190.2	1242	417.5	0	200.8
0.8	0	11.16	379.1	1237	231.9	0	400.0
1.2	0	16.47	559.2	1233	54.94	0	597.5
1.2	0	16.47	559.2	1233	54.94	0	597.5
1.2	0.35	17.86	606.5	1231	4.784	4.307	596.8
1.2	0.7	17.84	605.8	1229	1.874	8.605	596.2
1.2	0.936	17.27	605.3	1228	0	11.37	595.1

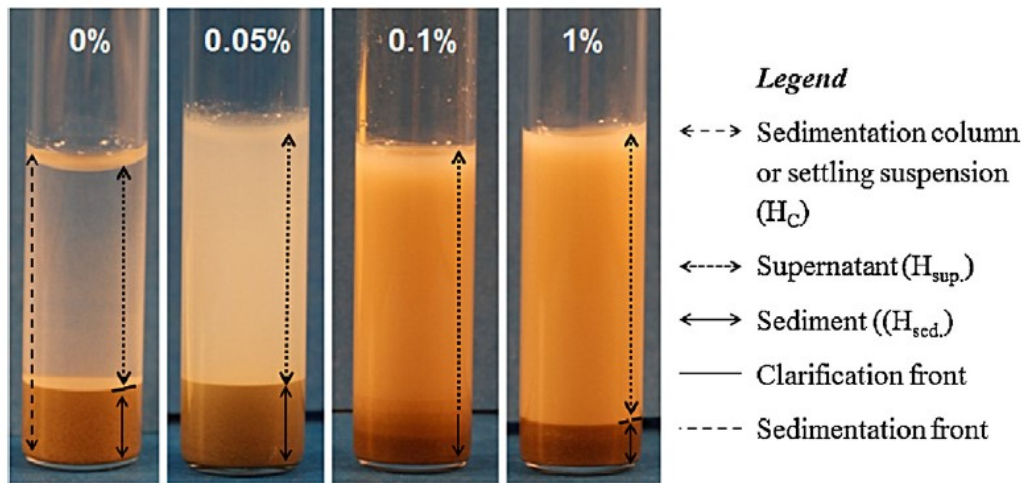


Figure 5.14 View of the different sedimentation levels after 40 minutes as a function of the dosage of polycarboxylate admixtures. Reprinted from Fig. 2 published in Autier et al. [2014] (p. 38).

5.4.2.1. Standard Test Method

5.4.2.1.1. *Experimental Procedure*

The bleeding of cement pastes incorporating growing amounts of CNF was performed in accordance with an adapted ASTM C232/C232M [ASTM, 2014]. The principal deviation from the standard test method were: (i) 750 ± 50 mL of freshly mixed paste was used, instead of 14 litre of concrete, (ii) 1,000 mL glass graduated cylinder replaced the 14 L standard container, and (iii) the monitoring of accumulated bleed-water thickness was made by image analysis of photos taken in the intervals specified by the standard method; no bleed water was pipetted off from the surface of deposited paste over the trial. The images were taken by a 14.1 Megapixels digital camera positioned at a fixed height of 250 mm and at perpendicular distance of 350 mm from the graduated cylinder. The glass cylinder was covered by a paraffin wax film throughout the trial to avoid loss of water by evaporation. Figure 5.15 illustrates the modified standard procedure. At the end of the trials, the 4-hour accumulated bleed water was collected with a pipette and then the bleeding was calculated. Both procedures were carried out according to ASTM C232/C232M [ASTM, 2014]. The idea here was to check the accuracy of the modified method with the standard method.

Three readings of the bleed-water height were obtained nearly from the centre of the graduated cylinder by the open-source software ImageJ 1.50i, as described by Mamun et al. [2012]. The volume of bleed water was determined multiplying the average height by the estimated evaporation area in the graduated cylinder, i.e. 29.8 cm^2 . The accumulated bleed water expressed as percentage of the net mixing water contained within the test specimen was computed in accordance with ASTM C232/C232M [ASTM, 2014]. The evaporation area in the graduated cylinder was smaller than the standard container (i.e. 29.8 cm^2 and 510.7 cm^2 , respectively), but the height of the fresh samples in both containers was roughly the same.

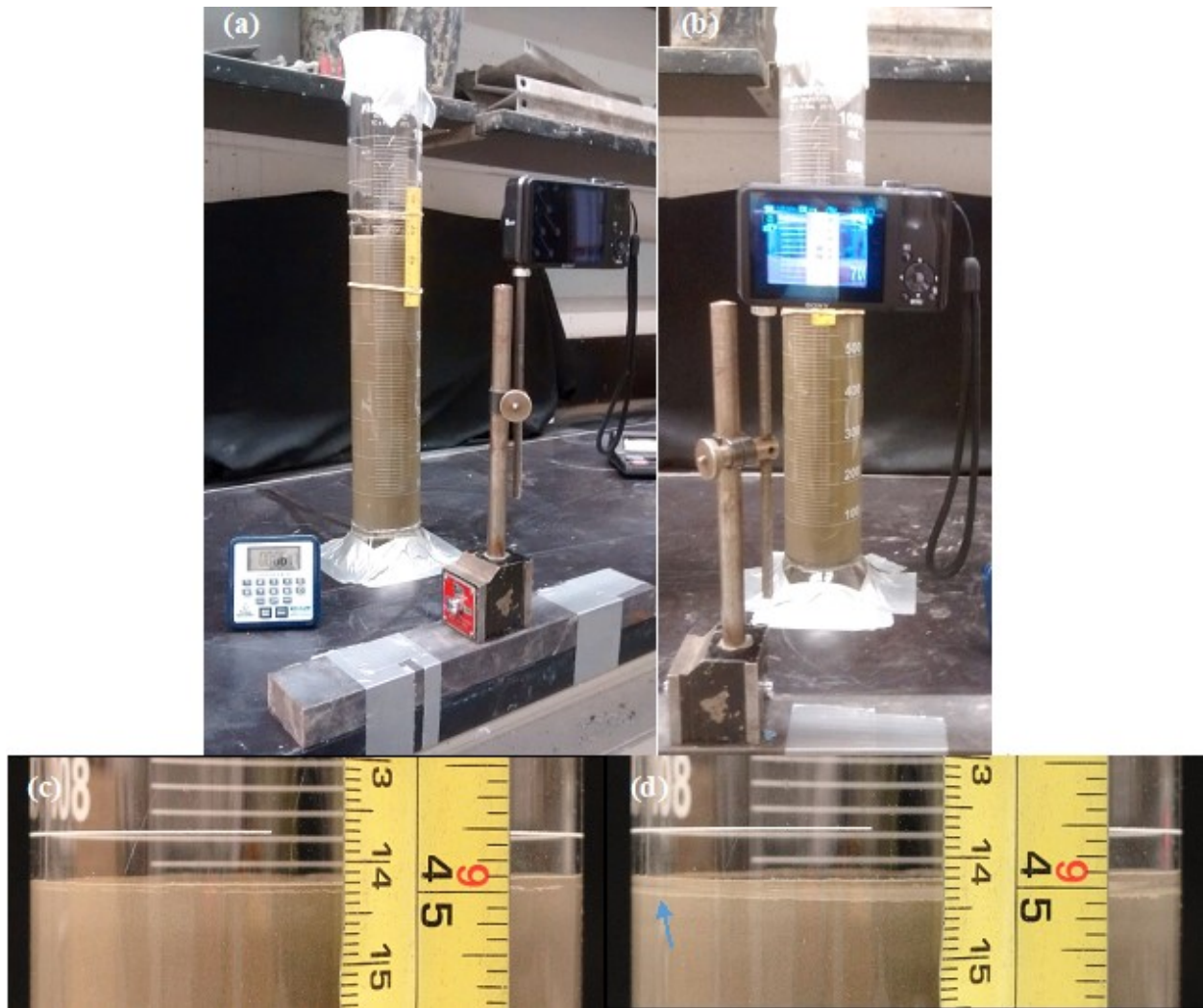


Figure 5.15 View of (a) the adapted ASTM C232/C232M [ASTM, 2014] apparatus, and (b) the system assembled to acquire photos. View in detail of the bleeding heights in cement paste containing 0.8 vol.% CNF #1.13 at (c) 5 minutes, and (d) 240 minutes.

5.4.2.1.2. Results and Discussion

The results of visual bleeding are listed in Figure 5.16. This data clearly evidenced that increments of CNF progressively drops the bleeding rate of cement pastes in relation to the control paste. The reduction was more intense in the very first 30 minutes, as demonstrated by the steep decline in the initial portion of the plots. This behaviour is valid for an environment with a negligible evaporation rate.

The hydrophilic nature of CNF makes the cement paste more viscous. This hampers not only the downward motion of solid particles, but also the upward percolation of water. As a result, the settling rate was considerably reduced, as was the bleeding rate. Nonetheless, the higher water retention capacity of CNF #1.13 was not able to promote better practical impacts on bleeding of pastes containing up to 0.4 vol.% loadings than CNF #0.13; since the performance of both CNFs was about the same, as shown in Figure 5.16.(c). Looking from a different angle, this same capacity of CNF #1.13 was crucial to incorporate larger dosages in cement paste than CNF #0.13 was. Considering that, CNF #1.13 was able to minimize the bleeding rate of cement pastes in high intensity than CNF #0.13, as shown in Figure 5.16.(c). This bleeding performance allows to claim that CNF must reduce the plastic shrinkage of cement pastes in closed-moist systems. Peng et al. [2017] measured the clear and turbid bleedings of cement pastes using one visual standard method and two new test techniques; one of these two is the turbiscanner analysis, which is going to be approached in the next Section. The standard method was performed exactly as described in the previous Section 5.4.2.1.1; except by the sample volume, that is, roughly 650 mL of fresh paste. These authors [2017] found 5 mm in bleeding height after 4-hour trial for a cement paste with 0.5 of water-to-cement ratio (the closest to that used for control paste in this current study, i.e. 0.485) or 8.16% of bleed water as per ASTM C232/C232M [ASTM, 2014]. This value is close to the 6.5% measured for control paste.

A possible finding was the fact that the unhydrated cement particles and/or superplasticizer were able to disrupt the weak ionic bonds of CNF gel to release water not only to hydration, but also to bleeding. This observation is based on the fact that the amount of water liberated by CNF gel to bleed would be contemptable if exposed alone for a short period of time to the same moisture-closed system of the bleeding trials.

It is worth mentioning that the readings of bleeding height were somewhat disturbed by the fine particles of cement floating on the bleed water. Another disturbance factor was the increase in turbidity. It may have interfered in the accurate definition of the limits of bleed water layer, even using image analysis. The bleed water became more turbid as the superplasticizer dosage increased. It corroborates with Autier et al. [2014] findings, as reported earlier in Section 5.4.2. Although, it is highly likely that the deceleration in the particle sedimentation rate provoked by

CNF has also escalated the turbidity of bleed water. Figure 5.15.(d) provides a visual image in this respect. By way of comparison, Figure 5.17 shows a layer with relatively clear-bleed water.

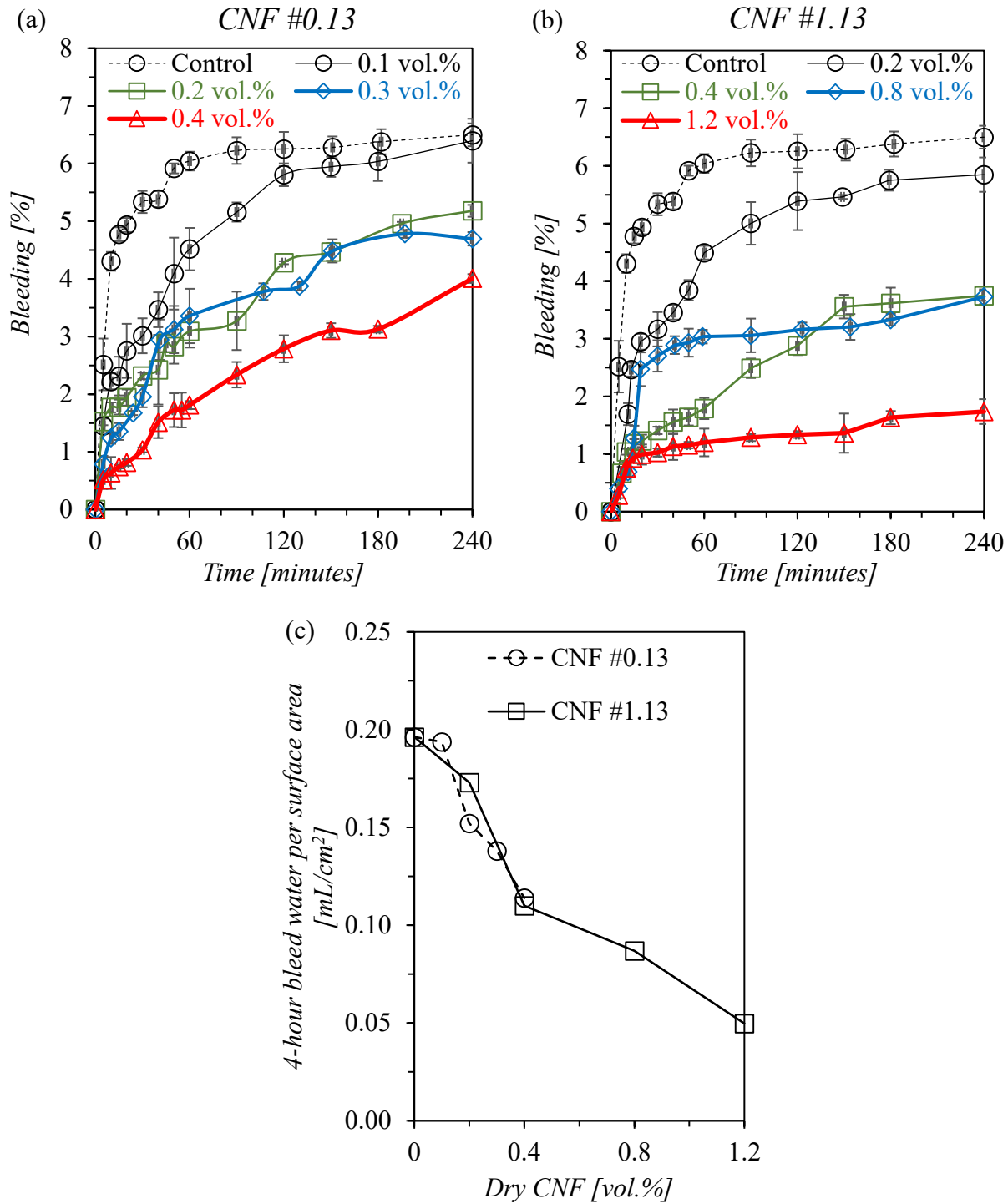


Figure 5.16 Bleeding rates over four first hours of cement pastes loaded with (a) CNF #0.13, and (b) CNF #1.13. (c) Bleeding of CNF-based cement pastes after four-hour trial.



Figure 5.17 View of the clear-light turbid bleed water in the control paste after 4-hour trail.

5.4.2.2. Turbiscanner Analysis

5.4.2.2.1. *Experimental Procedure*

The sedimentation of solid particles and the clear-turbid bleed water measurements were carried out by a Turbiscan[®] analyzer. The apparatus used, a *Turbiscan^{Lab}*, is shown in Figure 5.18. This analyzer detects destabilizations in solid dispersions virtually up to a full concentration range (up to 95% v/v of solids) and in a wide range of particle sizes, that is, from 10 nm to 1 mm.

Only one sample per mixture was analysed. Before undertaking the turbidity analysis, 33 ± 1 g of freshly cement paste was put into 20 mL cell sample. Not more than 6 minutes were spent between the very first contact of water with cement (during the mixing) and the first scan measurements by the Turbiscan apparatus. In this period, a 2-3 mm layer of surfactant-silicone oil mix was put onto the top of cement paste inside of the cell sample, as suggested by Peng et al. [2017] and illustrated in Figure 5.19. This layer lowers the meniscus of bleed water with the internal cell wall, which improves the accuracy in the identification of the bleeding front. From this point on, the procedure to analyse the water migration to the specimen surface followed the methodology proposed by Peng et al. [2017]. In brief, movements in the front of clear-turbid bleed water were monitored analysing variations in the intensity of transmitted light and backscattered light over the entire height of the cell sample in programmed intervals. The measurements were taken every minute for the first hour and every three minutes for the last three hours. If the scanning measurements taken in different times overlap, it means that the cement paste remains stable; though if the intensity of transmission light exceed a pre-defined limit detailed by Peng et al. [2017], the bleeding front is moving. The advance in bleeding height can be observed over time by an increase in the thickness

of this layer, as well as a reduction in its opacity. The clearer the bleed water, the higher the transmission light. And the opaquer the bleed water, the less intense the transmission. The data analysis was performed with the software *Turbisoft v.1.14.0*. The measurement principles of the Turbiscan apparatus are described in detail by Autier et al. [2014]. Figure 5.20 shows the bleeding layer in various post-trial CNF-cement pastes.



Figure 5.18 View of the *Turbiscan^{LAB}* analyser used in the turbidity analysis.

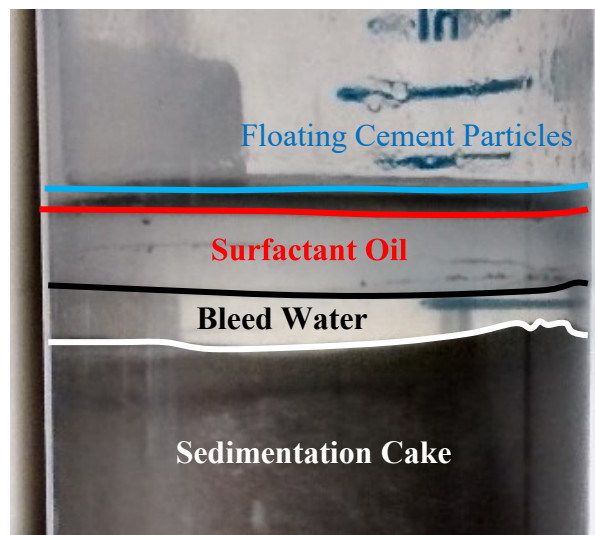


Figure 5.19 The white line demarks the top-limit of sedimentation cake of a cement paste with w/c ratio of 0.5, the black line the top of clear bleed water, and the red line the top of surfactant-oil combination. A thin layer composed by floating fine-cement particles is delineated between the red and blue lines. It is possible to see the meniscus softening in the top of bleed water layer.

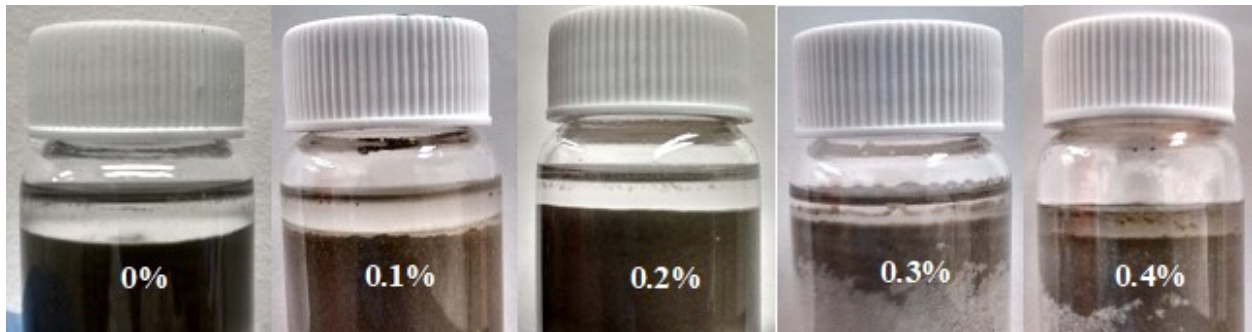


Figure 5.20 Bleeding heights in cement pastes loaded with 0-0.4 vol.% dry CNF #0.13 after 4 hours trial.

5.4.2.2.2. Results and Discussion

The bleed water heights found for cement pastes with various CNF fractions and with superplasticizer to keep the flow constant are reported in Figure 5.21. Figure 5.22 compares the bleeding results obtained by the turbidity method and the standard method. The bleeding of the same mixtures shown in Figure 5.21, but without superplasticizer (hence with different flows) are reported in Figure 5.23. Ultimately, the bleed water heights of paste mixtures with a constant volume fraction of 1.2% of CNF #1.13 and incremental dosages of high-range water reducer are plotted in Figure 5.24. Only one sample per trial was examined in this study principally due to time constraints.

As depicted in the plots of Figure 5.21.(a) and Figure 5.21.(b), the addition of CNF dropped the bleeding in cement pastes for the whole range of CNFs studied. This reduction was quite similar up to 0.4 vol.% of CNF #0.13 or of CNF #1.13. So far, no potential advantage was conferred to CNF #1.13 by its greater water retention capacity. But, this capacity granted to CNF #1.13 the possibility to incorporate till 1.2 vol.% in cement pastes, which is the maximum possible fraction according to the design parameters. For this reason, CNF #1.13 achieved the lowest volumes of bleed water. Nevertheless, it must be noted that the rate at which the water bleeds declined by degrees for cement pastes loaded with 0.8 vol.% and 1.2 % of CNF #1.13, as demonstrated in Figure 5.21.(c). The bleeding rates obtained by the turbidity method demonstrated a high correlation with those from the standard method – see Figure 5.22.

Figure 5.23.(a) and Figure 5.23.(b) display the bleeding behaviour of the same CNF-based paste mixtures shown, respectively, in Figure 5.21.(a) and Figure 5.21.(b) but containing no-admixture.

As discussed in Section 3.4, the absence of water reducers decreased the workability of these paste mixtures with respect to the control paste. Figure 5.23.(c) reveals that the scalling down limit for bleeding was attained at the CNF loading of 0.4 vol.%. That is true for both CNFs, i.e. CNF #0.13 and CNF #1.13. Quantities of CNF #1.13 greater than 0.4 vol.% did not lead to further benefits in minimizing the bleed water volume in cement pastes. In this respect, it seems that the bleeding height reached a minimum plateau at around 1.3 mm. Comparing the performances of CNF-cement mixtures containing no-admixture with those mixes loaded with superplasticizer dosages, both exhibited in Figure 5.23.(c) and Figure 5.21.(c), respectively, evidenced that doses of high range water reducers increased the bleed water volume.

Another interesting finding is seen clearly in Figure 5.24.(a) and Figure 5.24.(b). In these plots, it is noticeable that the chemical admixture played a moderate role in boosting bleeding. As previously highlighted, the overdosage of polycarboxylate-based admixtures may increase the bleeding; notwithstanding the fact that the maximum superplasticizer dosage required by 1.2% CNF #1.13-cement paste (i.e. 883 mL/100 kg of cement) is less than the upper-limit recommended by the supplier (i.e. 1170 mL/100 kg of cement).

As referred in Section 5.4.2.2.1, Peng et al. [2017] used the turbiscanner to compute 4-hour bleeding heights of cement pastes with distinct water-to-cement (w/c) ratios and containing various admixture dosages. Four lignosulphonate-based admixtures with different characteristics were studied. The authors [Peng et al., 2017] reported a bleeding height of nearly 1.8 mm for w/c = 0.5, which value is analogous to that exhibited in Figure 5.21.(c) by control paste (w/c = 0.485), i.e. 2.09 mm. The bleeding after 4 hours trial of pastes with comparable w/c ratio, i.e. 0.5, fluctuated largely (from 0.9 mm to 2.9 mm) according to the lignosulphonate type and dosage; recall that 1.8 mm is the bleed-water height of the no-admixture paste. Differently from Peng et al. [2017], the pastes dosed with a fixed amount of CNF #1.13 and increasingly polycarboxylate-based admixture contents raised moderately the bleeding – see Figure 5.24.(b). In contrast, Perrot, Rängeard, Picandet, and Mélinge [2013] claimed that adding polycarboxylate admixtures increases the flow resistance and decreases the bleeding. Therefore, further research is needed to better explain the effects of doses of CNF and polycarboxylate admixture in the bleeding of cement pastes.

In short, the CNF's capability of hold water raised the viscosity of cement pastes, which in turn slowed down the sedimentation of particles and the bleeding of water.

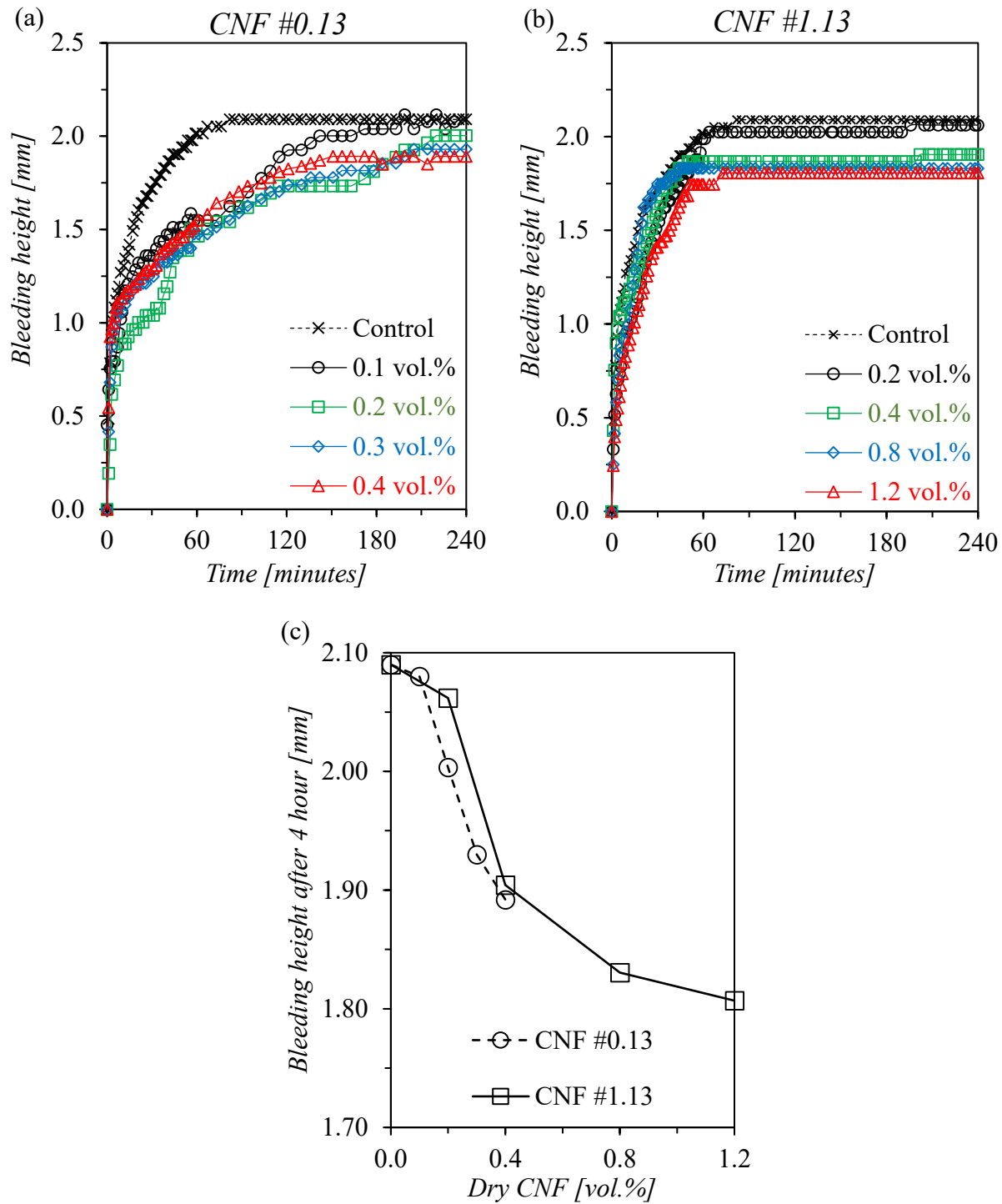


Figure 5.21 Bleeding of cement pastes containing (a) CNF #0.13, and (b) CNF #1.13 over 4 hours. (c) Bleeding of CNF-based pastes after 4 hours. All mixtures contain superplasticizer and show an efflux time in the range of 6 ± 0.5 secs.

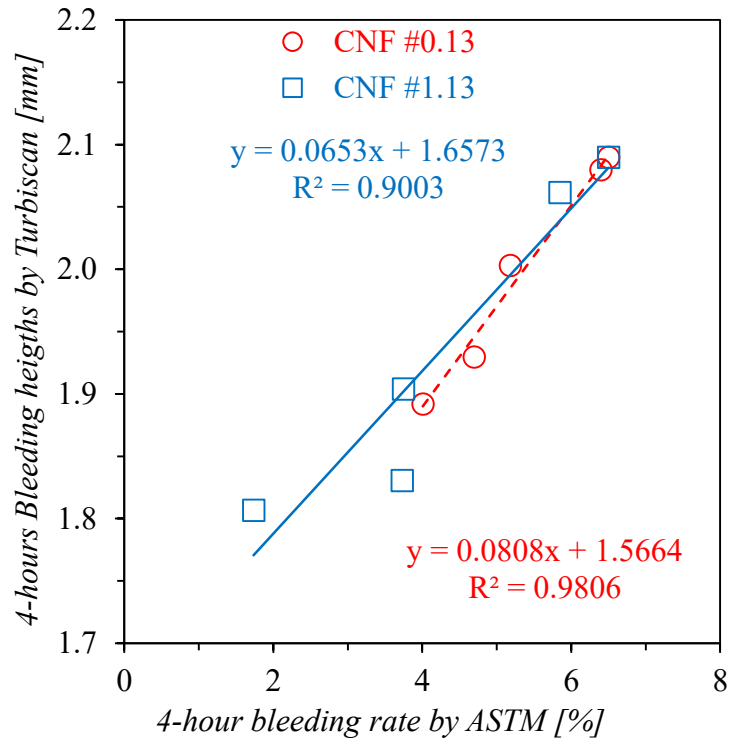


Figure 5.22 Correlation between the bleeding data acquired as per adapted ASTM C232/232M [ASTM, 2014] and Turbiscan analysis.

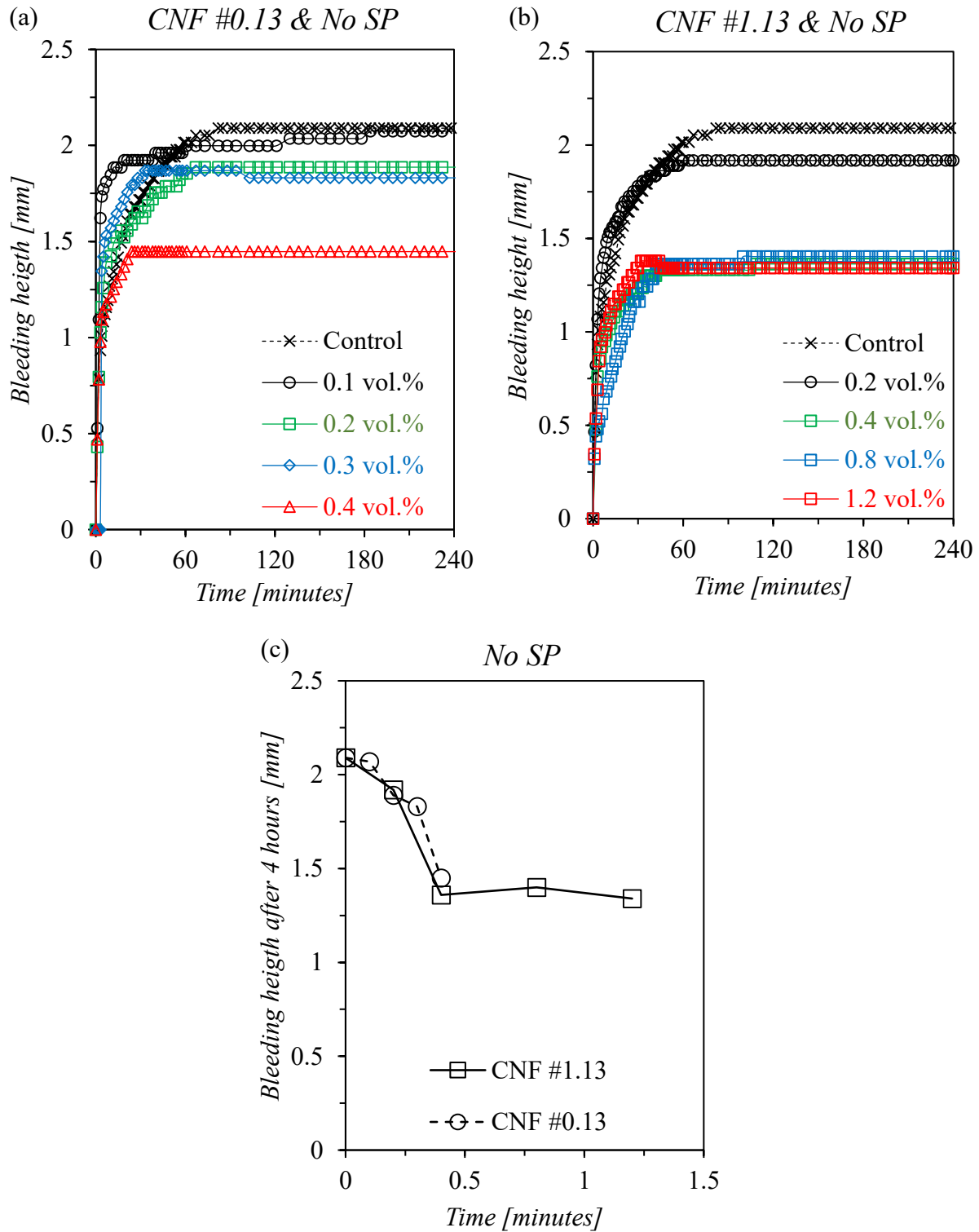


Figure 5.23 Bleeding of cement pastes containing (a) CNF #0.13, and (b) CNF #1.13 over 4 hours. (c) Bleeding of CNF-based cement pastes after four hours. Same mixtures shown in Figure 5.22 without superplasticizer (SP). Paste flows out of the 6 ± 0.5 secs range.

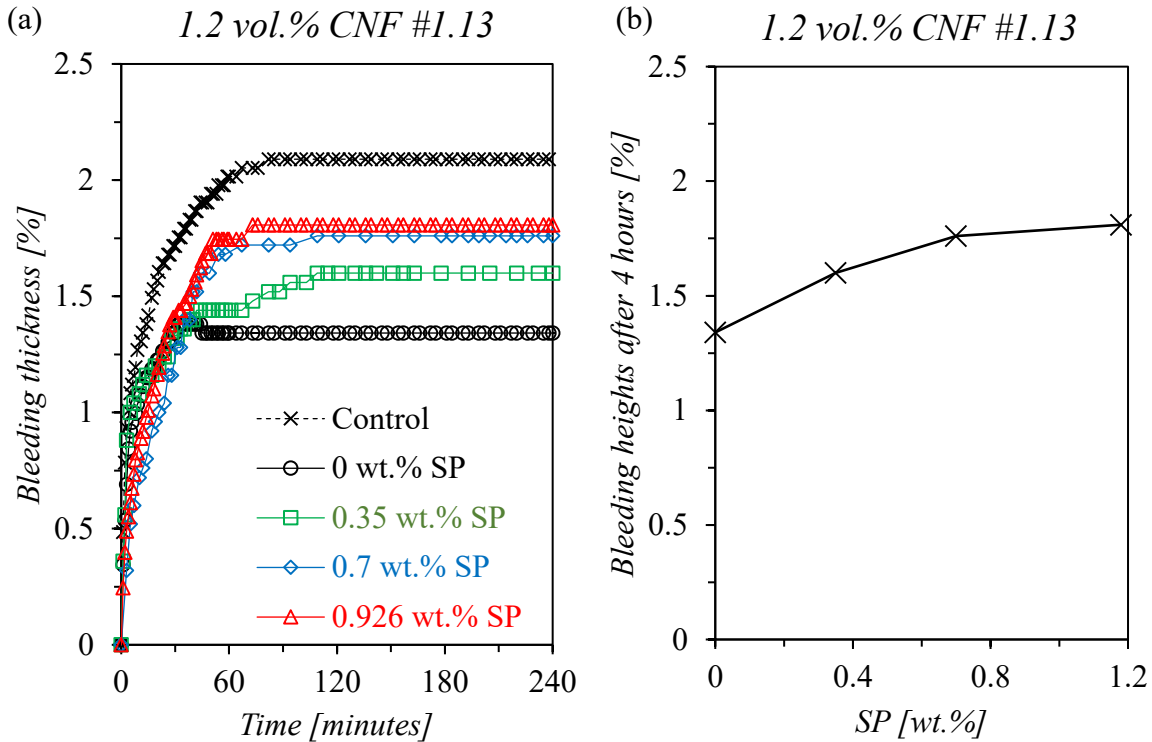


Figure 5.24.(a) Bleeding of cement pastes loaded with a fixed fraction of 1.2 vol.% dry CNF #0.13 and a growing dosage of superplasticizers (SP). (b) Effect of SP on bleeding after 4 hours. Paste flows out of the 6 ± 0.5 secs range.

5.4.3. Evaporation Rate

5.4.3.1. Experimental Procedure

The rate at which water evaporates was examined in pastes and in their respective volatile raw materials, water and CNF. Three distinct pastes with the same water-to-cement ratio of 0.485 were used: (i) a control cement paste, (ii) cement paste loaded with 1.2 vol.% of CNF #1.13 and 0.926 wt.% of superplasticizer to maintain the flow in the range of the control cement paste, and (iii) cement paste loaded with 1.2 vol.% of CNF #1.13 and no superplasticizer; hence the flow of the latter mixture is less than the first two. The flow table of these pastes was measured as per ASTM C1437 [ASTM, 2015]. The volume fraction of 1.2% was chosen because at this dosage the CNF #1.13 replaced completely the mixing water. These mixtures were exposed to a ‘severe’ environment inside of the same chamber referred in Section 5.4.1.1 for 20 hours – see Figure 5.25. Individual samples of CNF #1.13 gel and water were submitted to severe condition and also to two

others, a ‘mild’ and an ‘extreme’. The mild exposure was performed in a room with controlled temperature for 20 hours – see Figure 5.26 – and the extreme exposure in the environmental chamber for 8 hours. The time of exposure to extreme condition was shortened from 20 hours to 8 hours due to the negligible variation in the evaporation rates found after this period of time. The atmospheric temperature, the relative humidity and the air velocity of each of these conditions are listed in Table 5.3.

One single sample for each material was cast to dimensions of 150 mm in diameter and 15 mm in depth. The consolidation of the cement pastes into the molds was made in a single layer by an external vibrating table at 60 Hz for at least 20 secs. And the CNF #1.13 was compacted by small drops of the mold; no compaction energy was applied to the water specimen. On completion of this consolidation, the mixture was levelled to a plane surface with the top edge of the mold. So that the surface area was as flat and perpendicular to the mold sides as possible. Immediately after, the specimens were exposed to the aforementioned environments. Readings of the specimen weight were automatically acquired by the digital balance Ohaus Explorer® each 10 secs during the trial time interval. Figure 5.27 and Figure 5.28 provide a view of the specimens submitted to environmental exposure.

Table 5.3 Environmental exposures.

<i>Condition</i>	<i>Mild</i>	<i>Severe</i>	<i>Extreme</i>
<i>Atmospheric Temperature [°C]</i>	20 ± 1	40 ± 2	55 ± 2
<i>Relative Humidity of Air [%]</i>	40 ± 2	10 ± 2	5 ± 1
<i>Air Velocity [m/s]</i>	0	1 ± 0.1	2 ± 0.1

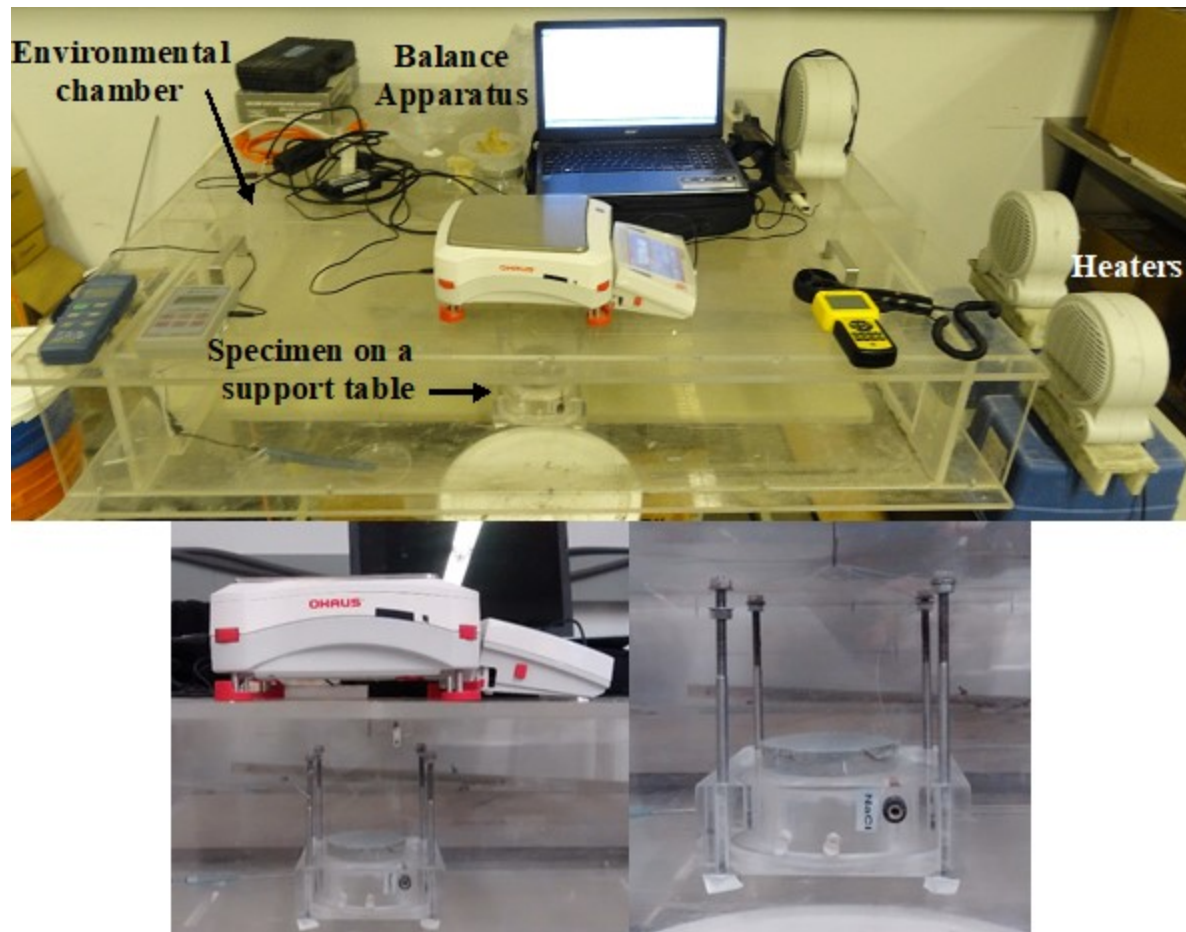


Figure 5.25 Evaporation rate apparatus set for automatic acquisition of weight-sample data in the environmental chamber (top). View of the balance-table weighing system (bottom-left), and in detail of the weighing table in the chamber compartment with a specimen on it (bottom-right).

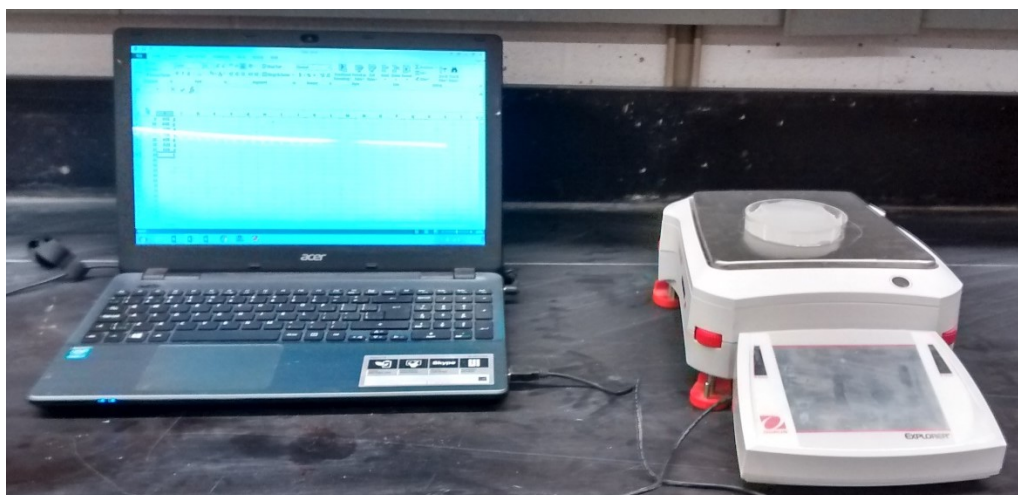


Figure 5.26 Automatic sample weight acquisition system.

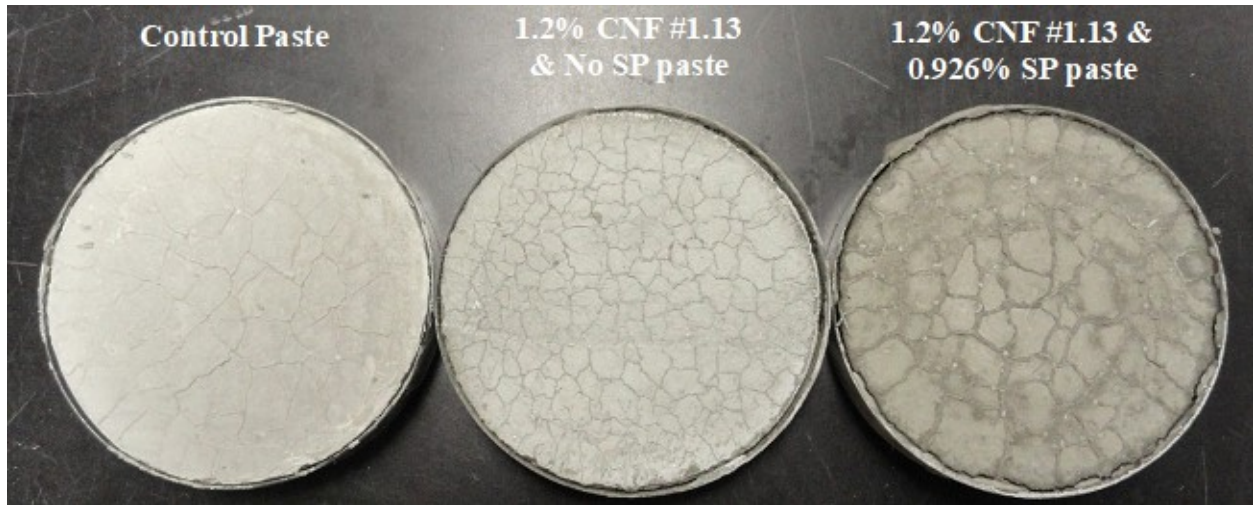


Figure 5.27 Specimen surface after 20 hours trial in severe environment. ‘SP’ = superplasticizer.

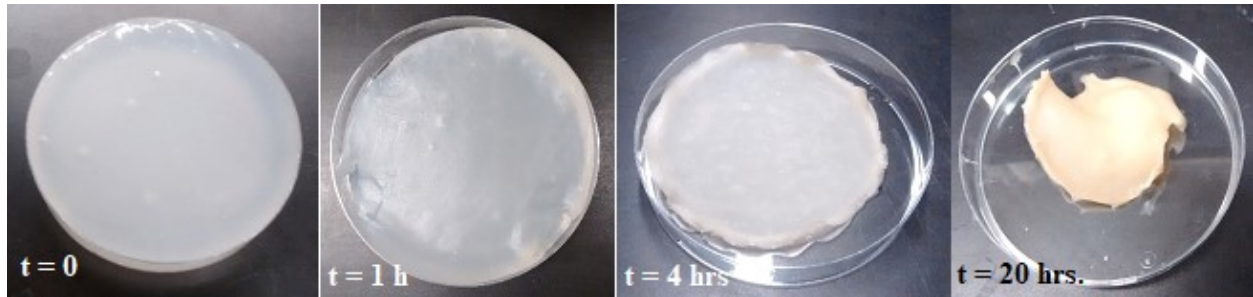


Figure 5.28 View of the CNF #1.13 gel at various times (t) of severe exposure.

5.4.3.2. Results and Discussion

The results of the evaporation rate are plotted in Figure 5.29-Figure 5.33. The 1.2% CNF #1.13-cement paste containing 0.926%, by cement weight, of superplasticizer developed the highest evaporation rates over 20-hour severe exposure, as demonstrated in Figure 5.29.(a). At the end of the trial interval, the growth was of the order of 16.7%, if confronted with the rates of both cement pastes without chemical admixture – see Figure 5.29.(b). A marginal increase of 2.25% was also observed at 4 hours of severe exposure – see Figure 5.29.(c). Even at peak rate, which occurred about 1.5-2 hours of trial, the CNF-cement paste with addition of high range water reducer shows a moderate increase of around 4.49% – see Figure 5.29.(d). Based on that, it is possible to claim that the dosage of superplasticizer magnified the evaporation rate of cement pastes. The slight rise in the evaporation rate during the first 4 hours of trial may be associated with the increase in the 4-hour bleeding rate also observed in CNF-cement pastes containing chemical admixture, as

shown in Figure 5.24.(b). It implies that the effect of the polycarboxylate admixture on plastic shrinkage must have been proportionally low; knowing that plastic shrinkage is the result of the evaporation-bleeding balance until about 4 hours of cement hydration in mild conditions. Interestingly, the difference between the evaporation rates of those mixtures that had no superplasticizer and those that were cast with a superplasticizer gradually increased through the 4 hours to 20 hours trial period; that is, after the estimated plastic shrinkage interval. Considering that, the high range water reducer used to keep the flow constant must have escalated the drying shrinkage more than the plastic shrinkage. It is likely, that the superplasticizer (as well as CNF) modified the pore structure of hardened CNF-cement pastes, so that the rearranged microstructure became more susceptible to moisture loss and consequently long-term shrinkage. However, the 1.2% CNF #1.13-cement paste without high range water reducer displayed a workability (measured by the flow table) considerably smaller than the other two mixes – see Figure 5.30. Such finding was reported in Section 5.4.2.2.2 of the thesis, as well. All in all, despite the higher water evaporation rates found in the paste containing superplasticizer, its absence led to CNF-cement pastes less workable.

The other two pastes, with no superplasticizer, developed roughly similar water evaporation performances, as illustrated in Figure 5.29.(a). In effect, there is a very slight decrease in favour of the paste containing 1.2% of CNF #1.13 in relation to the control paste. At this point, it worth mentioning that the first paste is a mix of cement and CNF #1.13, whilst the second paste was prepared with cement and water. Knowing that, this very small improvement probably reflected the marginal reduction in the evaporation rate exhibited by CNF #1.13 gel in comparison with water. Figure 5.31 (centre) and Figure 5.32 demonstrate that the water contained in CNF #1.13 gel evaporated at a slightly lower rate than pure water. It occurred in trials carried out not only in severe exposure, but also mild and extreme environment – see Figure 5.31. As a result, CNF #1.13 loadings quite moderately mitigated the moisture loss of cement pastes. Bearing this and the findings of Sections 5.4.2.1.2 and 5.4.2.2.2 (about bleeding rate) in mind, CNF #1.13 must improve the bleeding-evaporation balance (so does plastic shrinkage), while the superplasticizer worsens. The former part of this statement is clearly visualized in Figure 5.33. This Figure shows the bleeding rates of CNF #0.13-cement pastes and CNF #1.13-cement pastes obtained in mild exposure after four hours (data from Figure 5.16.(c)) and the evaporation rate of water and of CNF

#1.13 gel subjected to relatively similar conditions; note that 1 mL of bleed water was considered 1 g in weight. The bleed water rates of all mixtures are greater than the water evaporation rates, as shown in Figure 5.33. For this reason, the occurrence of bleeding was visually detected in all experiments developed in mild environment. More importantly though, the bleeding rate of cement paste with 1.2 vol.% of CNF #1.13 loading was very close of the evaporation rate of its volatile raw materials, namely, water or CNF #1.13 gel.

Figure 5.32 also shows a remarkable reduction in the evaporation rate of cement pastes after the peak rate in relation to the rates shown by water and CNF. This behaviour is substantiated by the fact that a parcel of water is consumed during the hydration of cement particles and thus minimizing the availability of evaporable water.

Lastly, it is possible that CNF confers upon cement pastes a restraining capacity. The volumetric contraction of CNF gel by drying takes place in three dimensions (3D), whilst the volume reduction of water is unidimensional from the specimen surface. Figure 5.34 illustrates the 3D contraction sequence over time. Thus, the volumetric reduction of CNF may carry over the solid phase of paste and accordingly, it mitigates the cracking coming from shrinkage as a whole.

Time constraint and limited availability of CNF restricted the number of samples per trial in only one.

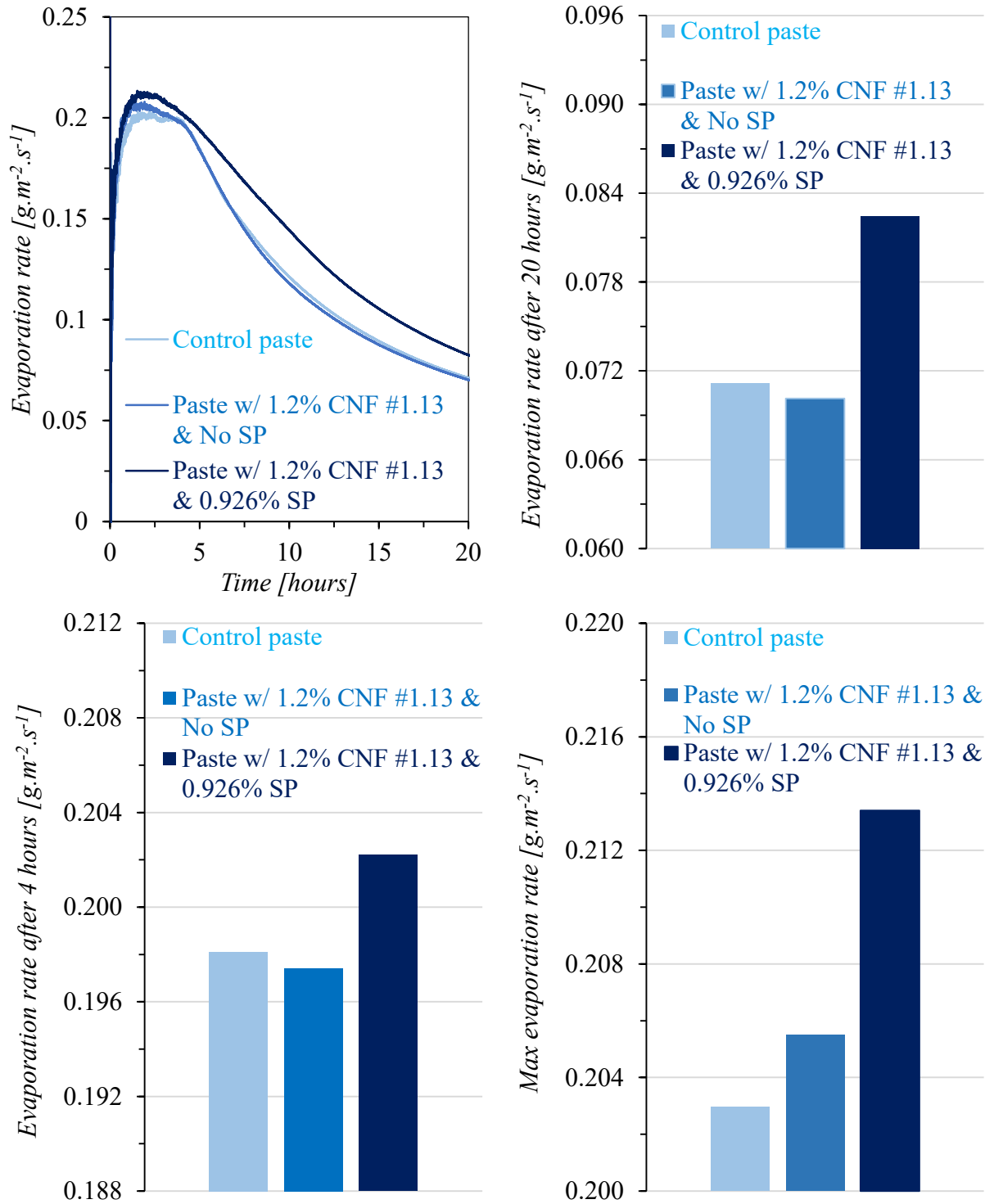


Figure 5.29 Evaporation rates of control paste and CNF #1.13-cement pastes containing and not containing superplasticizers (a) over 20 hours, (b) after 20 hours, and (c) after 4 hours in severe exposure. (d) Evaporation rate at a peak.

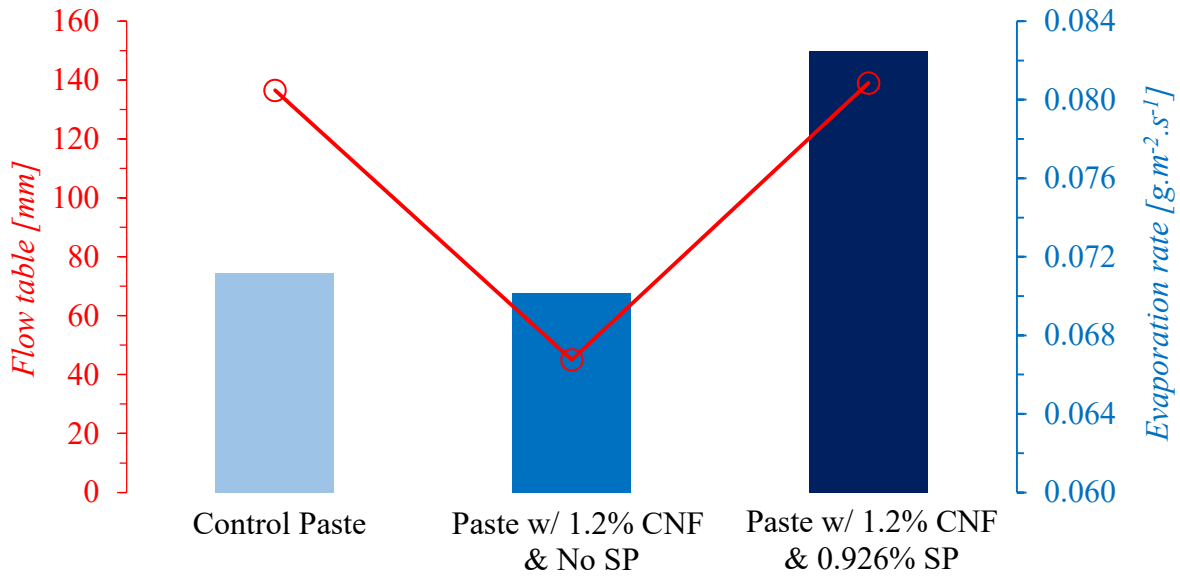


Figure 5.30 Evaporation rates of the control paste and the 1.2% CNF #1.13-cement pastes containing and not containing (SP) after 20 hours in severe exposure and their respective flow.

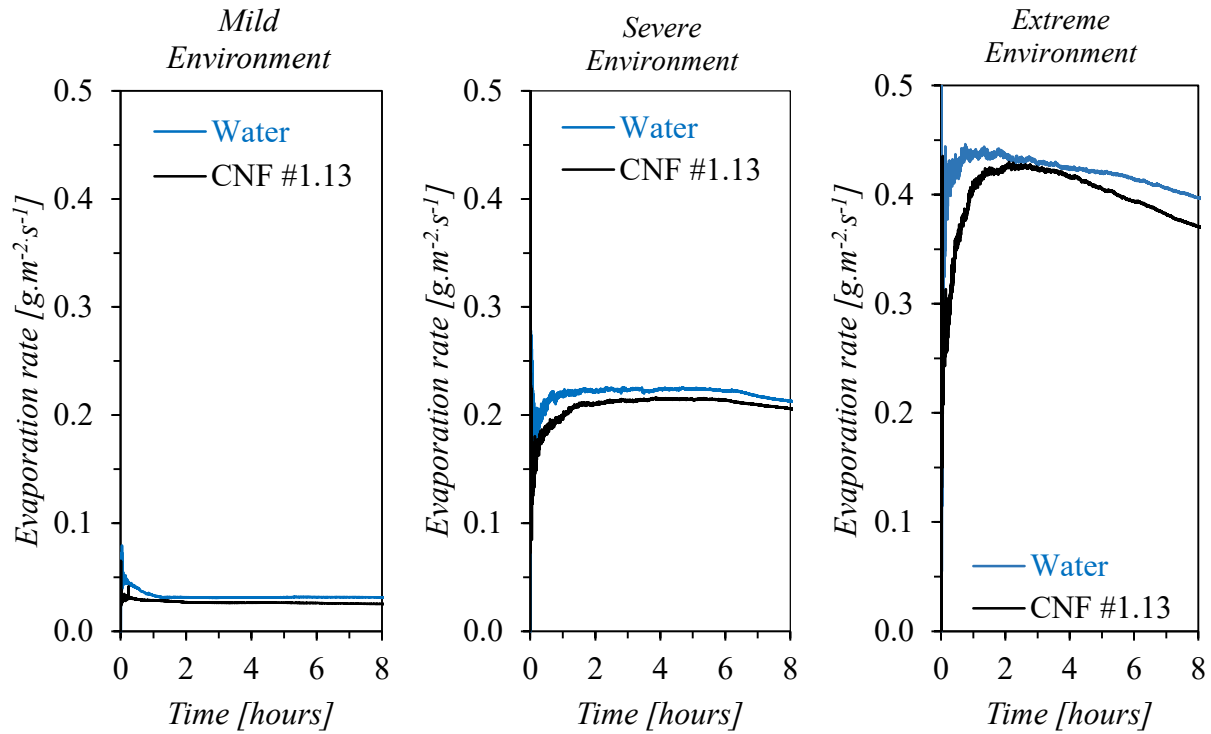


Figure 5.31 Evaporation rates of CNF #1.13 gel and water over 8 hours exposed to mild (left), severe (centre), and extreme (right) conditions.

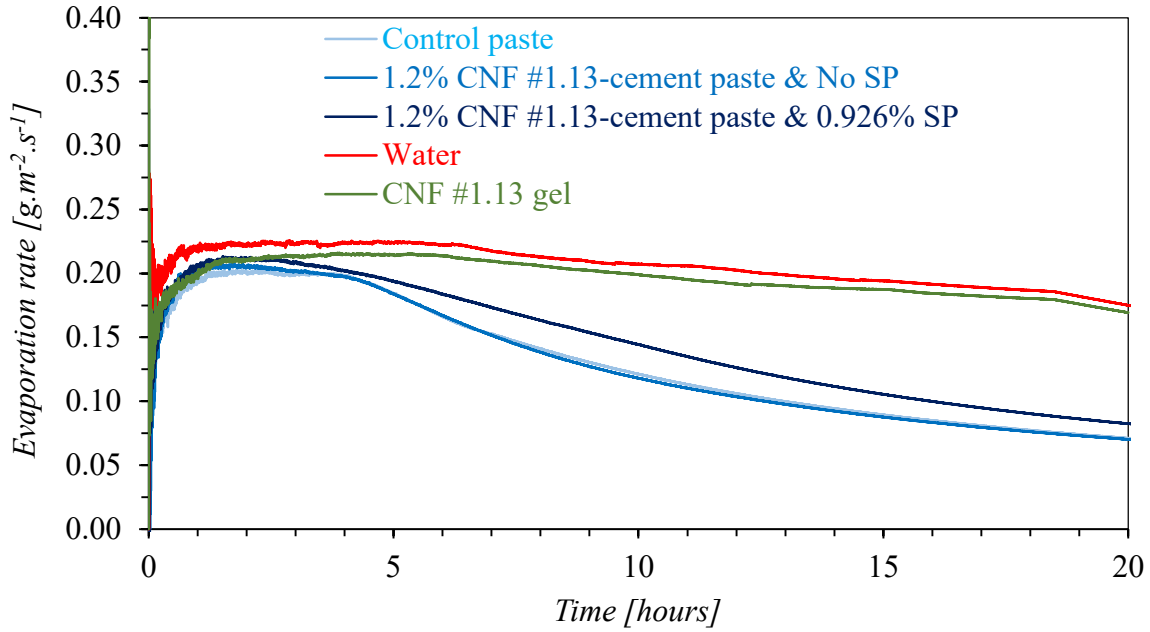


Figure 5.32 Evaporation rates of control paste and 1.2% CNF #1.13-cement pastes containing and not containing superplasticizer (SP) over 20 hours in severe exposure compared with rates of CNF #1.13 gel and water over the same time period and exposure conditions.

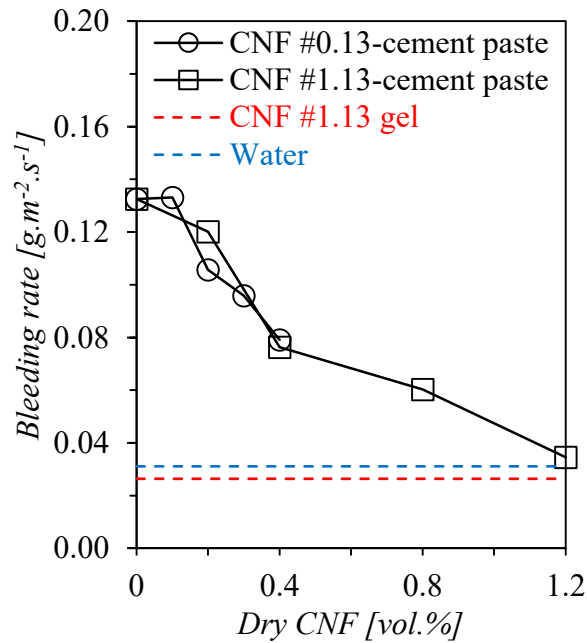


Figure 5.33 Bleeding rates of CNF-based cement pastes after 4-hour trial measured as per standard method – replotted from Figure 5.16.(c) – and evaporation rates of CNF #1.13 gel and water. All samples exposed to mild condition.

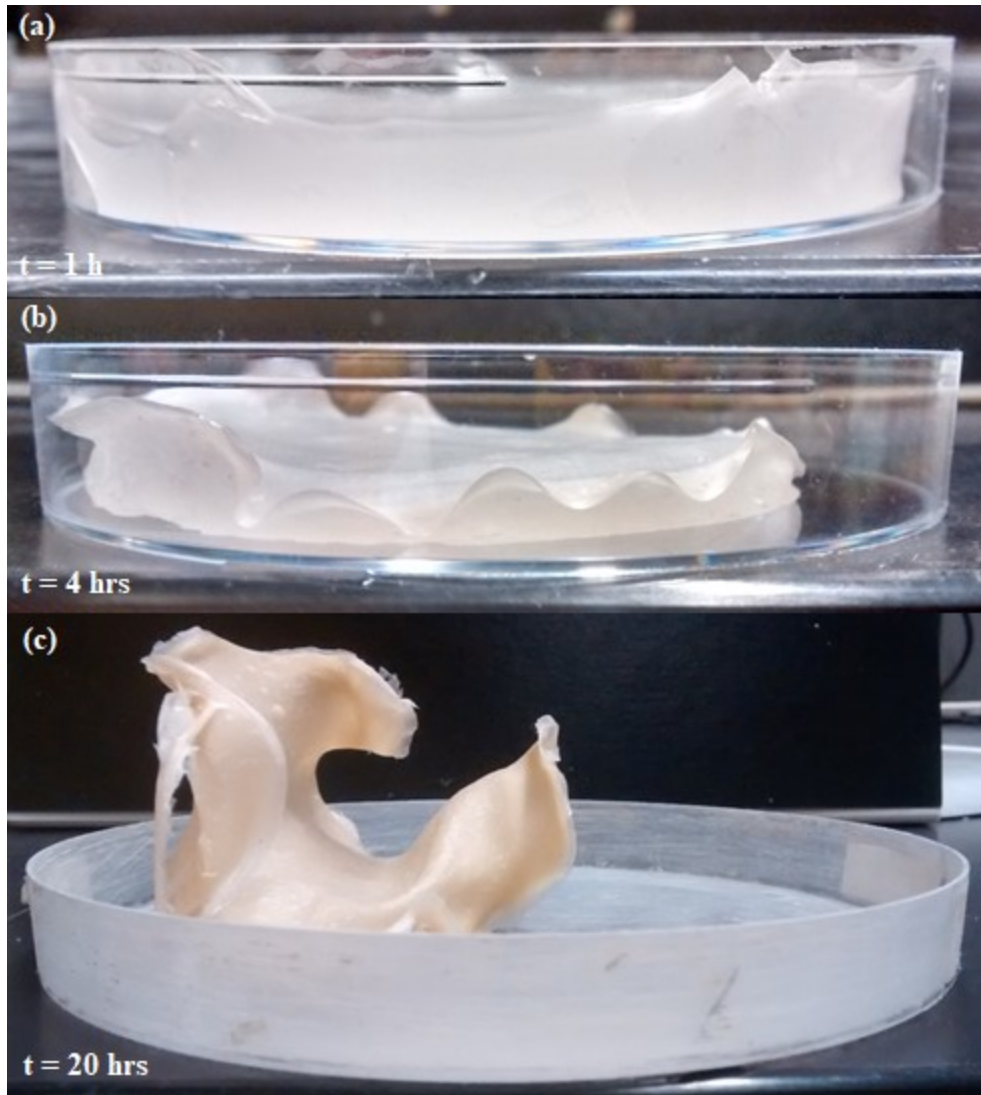


Figure 5.34 Gradual 3D volumetric shrinkage of CNF #1.13 gel (severe exposure) at different times: (a) 1 hour, (b) 4 hours, and (c) 20 hours.

5.5. Concluding Remarks

The shrinkage behaviour of cement pastes containing different fractions of CNF was assessed to examine the effect of CNF with different carboxylate contents (and different water retention capacities). Additional studies of bleeding, water evaporation, and cracking analysis provided support information needed to enlighten the CNF interaction with cement paste.

Based on the study conducted in this CHAPTER and the findings of CHAPTER 4, the following main concluding remarks can be made:

- The overall shrinkage of cement pastes was not affected by the addition of CNF #1.13, but was increased by loadings above 0.1 vol.% of CNF #0.13;
- The drying shrinkage of cement pastes was magnified by increments in CNF fraction, principally after the first week trial. Once again, CNF #1.13-cement pastes demonstrated a better drying shrinkage performance than CNF #0.13-cement pastes. Cement pastes loaded with up to 0.3 vol.% of CNF #0.7 shown similar behaviour to CNF #1.13 mixtures;
- The growth in the drying shrinkage of cement pastes was essentially induced by a pore refinement effect provoked by CNF loadings. The hydrophilic nature of CNF retained free water inside of the fresh cement paste (i) mitigating bleeding, and (ii) boosting the genesis of pores less than 50 nm mainly at early ages – see Figure 4.16.(b). This greater amount of internal water bleeds and evaporates as soon as the moist curing is removed and, as a result, the CNF-cement paste shrinks. This event is accountable for the large first-week increase in the drying shrinkage observed for the pastes containing CNF fractions in relation to the control paste. This initial growth in shrinkage contributed decisively to CNF's ineffective performance in alleviating drying shrinkage over the 12-week trials. And the second CNF's effect became the CNF-cement pastes more responsive to gradients with air moisture at late ages;
- The better shrinkage performance of pastes containing CNF #1.13 fractions in comparison with other CNFs mixes was strongly associated with a more favorable bleeding-evaporation balance of water. This improvement was essentially substantiated by CNF #1.13's greater water retention capacity. However, such benefit was not sufficient to overcome the disadvantage brought about by the increase of the porosity (less than 50 nm) and, consequently, to attenuate the shrinkage;
- CNF loadings ameliorated the bleeding-evaporation balance of water in cement pastes, whilst superplasticizer dosages worsened this relationship;
- Apparently, the advantageous bleeding-evaporation balance of water observed for CNF-cement pastes must have at first reduced the plastic shrinkage of fresh mixtures;
- The cracking caused by shrinkage of cement pastes was slightly mitigated by CNF #1.13 fractions. It explains the slight curling visually verified in the post-trial slab specimens. Taking into account that, the potential refrainment provided by CNF #1.13 may have aided to alleviate somewhat the shrinkage of cement pastes, as well;

- The bleeding rate of fresh cement pastes was significantly reduced with CNF increments. The upward movements of the free water and the sedimentation of the cement particles were inhibited by a raise in the viscosity of fresh cement paste coming from the ability of CNF to retain water. On the other hand, superplasticizer dosages moderately increased the volume of bleed water. However, the literature indicates the contrary. Thus, further studies shall be undertaken to understand the effect of superplasticizers on CNF-based cement pastes. The bleeding performance of CNF #0.13- and CNF #1.13-cement pastes was about the same up to 0.4 vol.% loadings. Nonetheless, the best behaviour was attained by pastes ranging from 0.8-1.2 vol.% of CNF #1.13, exactly because of CNF #1.13 superior water retention capacity;
- The new turbidity method and the standard method demonstrated excellent agreement of bleeding data; and
- The water evaporation rate of CNF #1.13 gel was slightly smaller than the pure water. For this reason, the evaporation rate of the cement paste containing only CNF #1.13 was at least equal to that found for the control paste. Thus, CNF loadings mitigated very slightly the loss of moisture of cement pastes. Both cement pastes without high range water reducer released less evaporable water than mixture containing superplasticizer (i.e. 1.2% CNF #1.13-cement paste). On this account, superplasticizer dosages slightly raised the evaporation rate of cement pastes. Overall, CNF fractions decreased the volume of evaporable water, while doses of superplasticizer rose.

CHAPTER 6. Sulphate Attack in CNF-based Cement Mortars

6.1. Introduction

A number of physically and/or chemically deleterious interactions with internal and/or external agents may significantly shorten concrete lifespan. Sulphate attack is one such principal concern. Here, the loss of durability in concrete is essentially associated with the formation of ettringite. Ettringite is an expansive phase precipitated from the reaction between gypsum, $CaSO_4 \cdot 2H_2O$, and monosulphoaluminate (AF_m). The latter AF_m phase derives from the tricalcium aluminate component within Portland cement. The $CaSO_4 \cdot 2H_2O$ is resulted from the combination of the soluble sulphate, SO_4^{2-} , entering the pore solution and the calcium hydroxide, $Ca(OH)_2$, already present in the pore fluid as a result of the hydration of silicates in the cement. Therefore, the ettringite-induced expansion is strongly dependent upon the internal availability of SO_4^{2-} in the capillary pore structure of cement paste.

The internal source of SO_4^{2-} in concrete are the components of cement itself. For this reason, part of the study was developed with different Portland cement based binders: (i) Type GU Portland cement (or ASTM Type I), known as general use cement (GU), (ii) Type HS Portland cement, known for its high-sulphate resistance (HS), (iii) Type HE Portland cement, known for its high-early strength (HE), and (iv) Type GUb, a blended Portland cement with 70% Type GU and 30% Fly Ash (GUb). The CSA-A3001 [Canadian Standards Association (CSA), 2013] displays the definitions, chemical, physical and uniformity requirements of these cements. The Type GU Portland cement (or its regional counterparts) is, by far, the most consumed hydraulic cement globally; notwithstanding its high aluminate content that makes it vulnerable to sulphate attack. This is usually countered by Type HS Portland cement, manufactured to have the lowest aluminate content among the Portland cements. Type HE Portland cement is ground finer and may contain more tricalcium aluminate than the other cement types. And, as it was just mentioned, high tricalcium aluminate renders it susceptible to sulphate attack. The blended Type GUb, while promoting sustainable practice, is intended to impart sulphate resistance through lower aluminate availability and $Ca(OH)_2$ consumption. The applicable characteristics of these cements from the

point of view of sulfate attack are highlighted in bold in Table 3.2. They are specifically the sulphur trioxide content and the tricalcium aluminate content.

This study takes advantage of the following inherent attributes of cellulose nanofibres (CNFs): (i) high water retention; (ii) abundant amount of chemically active groups; and (iii) nanoscale dimension. These attributes in turn make it possible to function at once, as a physical modifier of microstructure and a chemical sink of SO_4^{2-} . The CNF is enabled therefore, to effectively mitigate the adverse effects of sulphate attack.

The water retention capacity of CNF may reshape the pore structure of cement pastes through altering the hydration kinetics of cement and the composition of hydration products. The solid microstructure of cement pastes may be enhanced through pore and grain size refinement by further hydration coming from an increase in the water supply at late ages and/or by means of the short circuit diffusion. The latter phenomenon, as proposed by Cao et al. [2015], boosts the water transportation through the shell of hydrated products that covers the unhydrated cement grains. In addition, the same active groups able to provide the CNF's hydrophilicity are likely to chemically scavenge calcium cations, Ca^{2+} , from the pore solution [Jiao et al., 2016]. This "cleaning ability" is based on the fact that the unpaired electrons of the primary hydroxyl groups and the oxidized to carboxylate ion, COO^- , groups on the surface of microfibrils may establish hydrophilic complexes with the soluble Ca^{2+} in the pore structure of cement [Jiao et al., 2016], hence retard further ettringite (AF_t) phase formation. The soluble Ca^{2+} are primarily originated from the dissolution of $Ca(OH)_2$ and to a less extent, calcium silicate hydrate, $C - S - H$.

Another feasible consequence of this phenomenon is the reduction of the alkalinity of cement paste. The $Ca(OH)_2$ and alkali hydroxides maintain the pH of aqueous phase over 12.5. A low-pH pore solution turns unstable the hydration products of cement, such as $Ca(OH)_2$, calcium monosulphoaluminate hydrate (or monosulphate) and $C - S - H$ [Skalny et al., 2001]. The instability of $Ca(OH)_2$ and monosulphate may increase the soluble Ca^{2+} in pore solution and activate the ettringite-expansive mechanism. And the decomposition of $C - S - H$, which is the most important cement hydration product [Metha et al., 2013], may decline the mechanical strength (and durability) of cement-based systems.

All these possibilities were examined in the two following steps, as illustrated in this CHAPTER.

To this end, in the first phase, (i) the linear expansion of cement mortars due to ettringite formation, was evaluated over the period of 12 weeks, as per ASTM C1012 [ASTM International (ASTM), 2015]; and (ii) the resistance to unidirectional ingress of soluble SO_4^{2-} in hardened cement mortars was measured over the same time interval. The second experiment involved the extraction of samples from distinct depths of the mortar specimens that were exposed to a sulphate-rich environment at select periods of time. The SO_4^{2-} content in these extracted samples was evaluated by a method similar to ASTM C114 [ASTM, 2015]. The four distinct Portland cements aforementioned, namely, GU, HS, HE and GUb, were used to prepare the mortars loaded with an equivalent amount of dry CNF #0.13 at 0-0.2% as a volume fraction of the mixture. The mortar series made with Portland cement Type GU was dosed with dry equivalent CNF up to 0.5 vol.% fraction. Note that while the dosage is stated in terms of the dry CNF, the actual CNF used in the mixtures was a never-dry CNF gel. This was in order to avoid the hornification of the cellulose nanofibrils, which leads to the complete loss of their hydrophilic properties.

The mix proportions of all cement mortars used in this Section are listed in Table 3.3 (for Type GU cement-based mortars) and Table 3.4 (for mortars having Types HS, HE and GUb as binder). These mortar mixtures were prepared as reported in Table 3.5 and as described in Section 3.3.

Sections 6.2 and 6.3 present these main studies on sulphate attack. Following this, a new battery of experiments was undertaken to investigate chemical changes introduced by CNF in the cement paste microstructure, such as ettringite content, $Ca(OH)_2$ content and pH in order to understand the findings of the first part of the study. In addition, the mechanical strength of the CNF-based cement mortars exposed to sodium sulphate, Na_2SO_4 , solution was examined. More details about these complementary studies are given in Section 6.4.

6.2. Sulphate Penetration

6.2.1. Experimental Procedure

Eleven cylindrical specimens, each 50 mm in diameter and 100 mm in height, were cast per mortar mixture. Each cylinder was molded in four layers, each one compacted by an external vibrating table at 60 Hz for at least 20 secs. The mortar specimens were demolded 23 ± 0.5 hours later and then cured for a further 27 days in a controlled environment, as required by ASTM C1012 [ASTM, 2015]. One out of 11 cylinders per mixture was used to determine the reference sulphate content at 28 days after cast (i.e. at the beginning of sulphate exposure). The remaining ten cylinders were partially covered with an epoxy resin on their lateral surfaces, as illustrated in Figure 6.1.(a) and Figure 6.1.(b), to ensure the unidimensional ingress of SO_4^{2-} . Five out of 10 specimens were submerged for 12 weeks in Na_2SO_4 solution (50g/L) as per ASTM C1012 [ASTM, 2015] and the other five immersed in distilled water for the same time interval – see Figure 6.1.(c). The distilled water met the requirements of ASTM C1012 [ASTM, 2015]. From then on, one cylinder was removed from water and another one from Na_2SO_4 solution at ages of 1 week, 2, 4, 8 and 12 weeks of immersion. Samples were extracted by drilling at various depths from top end of these two cylinders. The extraction depths were function of the immersion time. At ages of 1, 2 and 4 weeks of immersion, one sample were drilled out, every 3 mm from 0-9 mm in depth. At 8 weeks, one sample was extracted every 3 mm in the range of 0-12 mm in depth. And finally, at 12 weeks, one sample was considered every 3 mm from 0-15 mm. The procedure for sample collection is shown in Figure 6.1.(d) to Figure 6.1.(g).

The sulphate content at each depth was determined through chemical analysis. At least 1 gram of a ground sample, dried at $105 \pm 5^\circ\text{C}$ for 24 hours, was first diluted in 20 mL (30 minutes later added more 20 mL) of water at a temperature just below boiling, and then digested in 5mL of 37% hydrochloric acid, HCl , solution for 60 minutes, similarly as depicted in ASTM C114 [ASTM, 2015] – see Figure 6.2.(a). The digested sample was centrifuged at 2,000 g ('1 g' is about 9.8 m/s^2) for 15 minutes at room temperature. Note that everything, except quartz, goes into solution. After that, this solution was filtered through a medium-textured paper, Grade 1, with pore size of 11 μm . The resulting filtrate was titrated with 10 mL of 10% (wt./vol.) barium chloride, $BaCl_2$, aqueous solution and digested for further two hours. The barium sulphate, $BaSO_4$, that precipitated was

filtered using an air-pump and dried at $105 \pm 5^\circ\text{C}$ for 24 hours – see Figure 6.2.(b). The sulphate content was calculated as follows:

$$[SO_4^{2-}] = [w_{BaSO_4} \times (96/233) \times 1000] \quad (6.1)$$

where ' $[SO_4^{2-}]$ ' is the sulphate content [mg/g]; ' w_{BaSO_4} ' is the weight of the dried $BaSO_4$ [g]; and '(96/233)' is the – the molecular mass of $[SO_4]^{2-}$ is 96 g and of $BaSO_4$ is 233 g.

And the sulphate penetration at each depth ('x'= 3, 6, 9, 12 and 15 mm) for a given age ('i' = 1 week, 2, 4 8, 12 weeks) of (Na_2SO_4 solution or distilled water) exposure was computed as the following equation:

$$[SO_4^{2-}]_{i, weeks @ x, mm}^{Na_2SO_4} = [SO_4^{2-}]_{i, weeks in Na_2SO_4 @ x, mm} - [SO_4^{2-}]_{i, 0, week} \quad (6.2)$$

$$[SO_4^{2-}]_{i, weeks @ x, mm}^{water} = [SO_4^{2-}]_{i, weeks in water @ x, mm} - [SO_4^{2-}]_{i, 0, week} \quad (6.3)$$

$$[SO_4^{2-}]_{i, weeks @ x, mm} = [SO_4^{2-}]_{i, weeks @ x, mm}^{Na_2SO_4} - [SO_4^{2-}]_{i, weeks @ x, mm}^{water} \quad (6.4)$$

where ' $[SO_4^{2-}]_{i, weeks @ x, mm}$ ' is the sulphate penetration [mg/g] at a specific depth for a given age 'i'; ' $[SO_4^{2-}]_{i, weeks in sulphate @ x, mm}$ ' is the sulphate content [mg/g] at the same depth and age 'i' of sulphate solution exposure; ' $[SO_4^{2-}]_{i, weeks in water @ x, mm}$ ' is the sulphate content [mg/g] at the same depth and age 'i' of immersion in distilled water; and ' $[SO_4^{2-}]_{i, 0, week}$ ' is the sulphate content [mg/g] prior the specimen is immersed in water or sulphate solution (at 'i' = 0 week'). The value found for ' $[SO_4^{2-}]_{i, weeks in water @ x, mm}$ ' was invariably negligible or equal to 'zero', because SO_4^{2-} uncontaminated water was used.

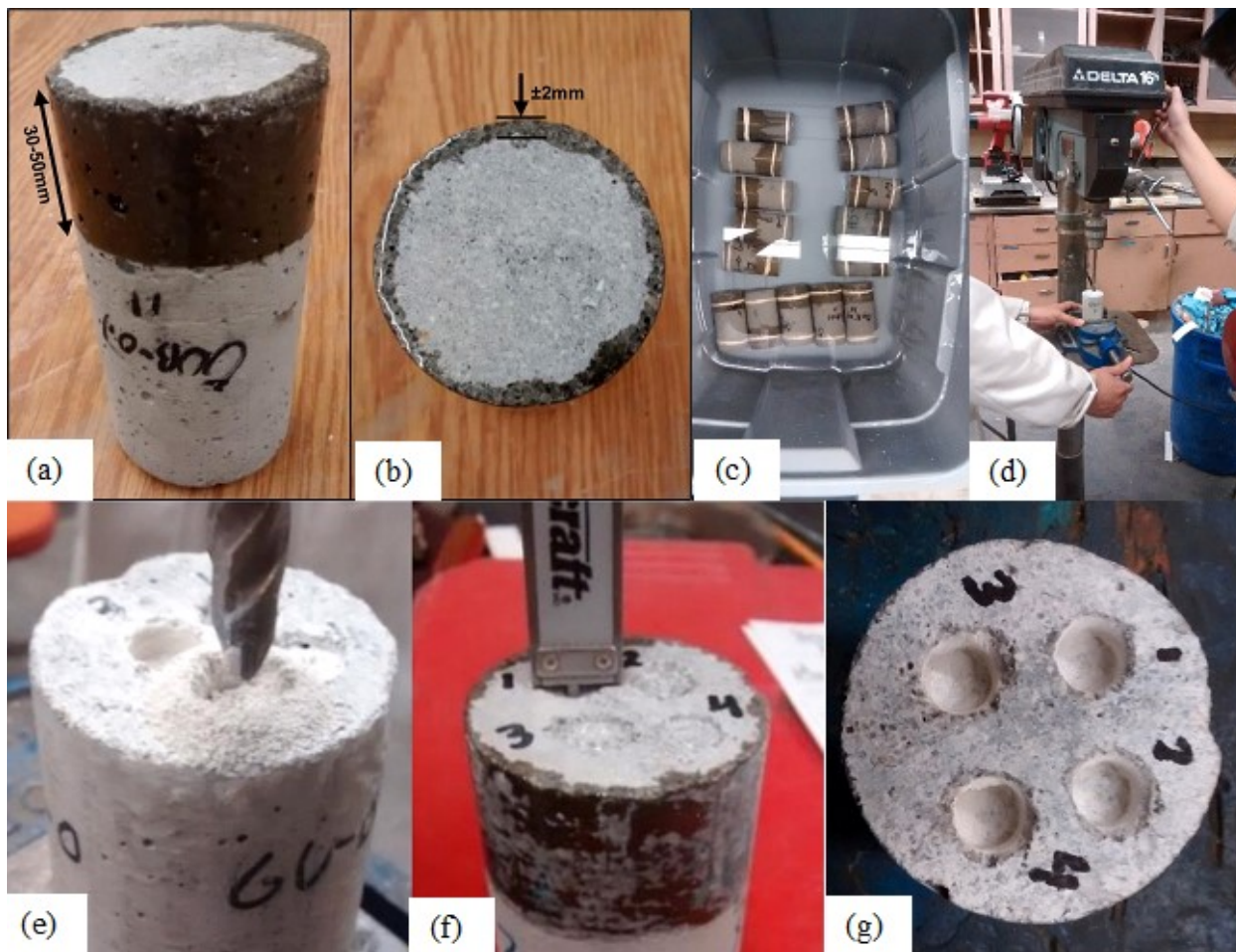


Figure 6.1.(a) Side view and (b) top-end view of the cylinder sides partially coated with epoxy resin. (c) Cylinders immersed in Na_2SO_4 solution. (d) Bench drill press used to (e) drill samples from the top-end cylinder. (f) Measuring sample depths. (g). Top-end cylinder after sample collection up to 9 mm depth.



Figure 6.2.(a) Sample digesting in HCl , and (b) filtrating the $BaSO_4$ precipitate.

6.2.2. Results and Discussion

The ettringite-induced expansion of cementitious materials depends upon the soluble SO_4^{2-} ingress. The penetration of SO_4^{2-} into the mortar matrix was evaluated through chemical analyses of samples extracted at depths up to 15 mm.

The effect of CNF #0.13 dosage on SO_4^{2-} penetration in Type GU cement mortars over the 12 weeks when submerged in Na_2SO_4 solution is shown in Figure 6.3. And, the corresponding penetration in the mortar mixtures prepared with Type HS, Type HE and the blend Type GUb, is plotted in Figure 6.4. The measurements of sulphate content in GU mortar containing various CNF #1.13 contents over the same time interval are displayed in Figure 6.5.

As seen in Figure 6.3 and Figure 6.4, the SO_4^{2-} penetration upon adding CNF #0.13 was minimized over the entire trial interval, even at a depth of only 3 mm. The enhancement of CNF #0.13 is more clearly observed in Figure 6.6.(a). The intrusion of SO_4^{2-} after 12 weeks of exposure was only slightly minimized up to 0.2 vol.% fraction of CNF #0.13 in all mortar series. The decrease was uniform with CNF addition in Type HS, Type HE and Type GUb mortars. However, at higher CNF #0.13 dosages, the SO_4^{2-} ingress was vastly reduced in the Type GU series. The drop reached 50% at dosages of 0.4 vol.% of CNF #0.13 or higher.

The same trend, i.e. a lower SO_4^{2-} penetration for an increase in the CNF dosage, occurred in Type GU series of mortars dosed with CNF #1.13 – see Figure 6.5. As summarized in Figure 6.6.(b), the decline in sulphate content after 12 weeks (and even at 8 weeks) of exposure took place gradually along the entire range of CNF #1.13 increments.

The Type GU cement mortar containing up to 0.3 vol.% of CNF #1.13 demonstrated an enhanced resistance to 12-week SO_4^{2-} ingress than the CNF #0.13 mortar series prepared with the same Type GU cement, as evidenced in Figure 6.7. Above 0.3 vol.% of CNF, the scenario drastically inverts. The CNF #1.13 mortar series maintained roughly a steady reduction in the SO_4^{2-} penetration rate, while the CNF #0.13 mortars plummeted about 50% – see Figure 6.7. As reported in Section 3.3, a higher intensity of compaction energy was necessary to overcome the lower workability shown

exactly by these two mixtures. Figure 3.8.(b) displays the flow of these mixtures outside the design range.

The overall increase in the resistance to SO_4^{2-} ingress is attributed, here, to two factors, both triggered by CNF loadings: (i) a denser pore structure due to further hydration, and (ii) a low-calcium aqueous phase.

Firstly, the nanofibre is inherently hydrophilic due to the presence of active hydroxyl groups on its surface, which are augmented by the introduction of ionized COO^- groups in the process of defibrillation [Saito, Nishiyama, Putaux, Vignon, & Isogai, 2006]. Given its nanometric size, over 30% of the hydroxyl groups appear on the surface of the cellulose nanofibre, which is much higher than in the cellulose microfibre, used hitherto to mitigate shrinkage and curling [Cao et al., 2015]. In conventional cement-based systems, the hydration process slows down over time due to low availability of water. Instead, here, the CNF works like an internal water reservoir. Given their water retention, the nanofibres gradually liberate the retained water to react with the unhydrated cement particles [Jiao et al., 2016]. With this respect, Cao et al. [2015] proposed in regard to cellulose nanocrystals (CNC), that CNC assists in short circuit diffusion, which further promotes hydration. It is therefore likely that CNF too promotes short circuit diffusion. These assumptions may end up increasing the degree of hydration and, as well, changing the pore structure of the cement paste matrix to a more impervious configuration.

In Section 4.2 of CHAPTER 4 was demonstrated, however, that the DOH of cement pastes declined slightly with increments in CNF doses; despite some authors have found opposite results [Sun et al., 2015; Jiao et al., 2016; Mejdoub et al., 2017]. It seems that the CNF's capacity of retaining water delayed the hydration of cement particles. Based on this proposition, the 'short-circuit diffusion' as conceived by Cao et al. [2015] is a phenomenon unlikely to happen in CNF-based cement pastes.

As discussed in Section 4.3, the pore system ranging from 10 μm to 10 nm in diameter of cement pastes controls the penetrability of aggressive ions, such SO_4^{2-} [Jennings, Thomas, Rothstein, & Chen, 2002; Neville, 2011; Metha et al., 2013]. The porosimetry of identical paste mixtures

prepared with procedures relatively similar to those applied in this Section was examined by two analytical techniques in CHAPTER 4. To cover the above-mentioned 10 μm to 10 nm range, the pore size distribution (PSD) from 10 nm to 140 nm was plotted in Figure 6.8 based on the gas sorption analysis of Figure 4.16.(a). And the range between 100 nm and 10 μm revealed in Figure 6.9, according to the SEM image analysis shown Figure 4.21.(a) and Figure 4.21.(b). Based on the Figure 6.8 and Figure 6.9, loading CNF in cement pastes resulted in a modest increase in the porosity ranging from 100 nm – 10 μm in diameter and at the same time, a slight decrease in the pore volume between 10 nm – 140 nm in size. It seems that this decrease in porosity found in smaller pore sizes was enough to compensate the increase in the larger pores. New interfacial transition zones introduced between CNF (which are 5 nm – 20 nm across and at least 2 μm in length) and cement paste likely led to a denser capillary pore structure in the 10 nm – 140 nm range. In fact, the final configuration of the PSD in cement pastes dosed with CNF was a more impervious pore structure taking into consideration the enhancement in the resistance of SO_4^{2-} ingress seen in Section 5.2 and 5.3. Mehta et al. [2013] believed that for pore sizes lower than 100 nm, the connectivity is very low turning the paste more impervious, despite a slight increase in part of the porosity associated with a larger size. Similar phenomenon is seen in cement-based systems when reinforced with micro-fibres [Sappakittipakorn, Banthia, & Jiang, 2010; Bhargava & Banthia, 2008], in that the mean pore size shifts towards a smaller value and restricts permeation. Neville [1995] noted that using very fine particles, such as silica fume, densifies the voids improving the permeability of cementitious materials. Similar phenomenon is expected in mixtures containing CNF, though in lower scale.

Secondly, the same COO^- groups capable of providing the hydrophilic nature to CNF may also combine with soluble cations, such as Ca^{2+} , thus resulting in a low-alkaline pore solution. This proposition is verified in this study as described in the upcoming Sections of this CHAPTER.

There are no error bars in Figure 6.3-Figure 6.7 because the current dataset was obtained from a single trial per mixture. The large number of tests associated with time constraints and limited availability of laboratory facilities to conduct the chemical analysis restricted the number of experiments.

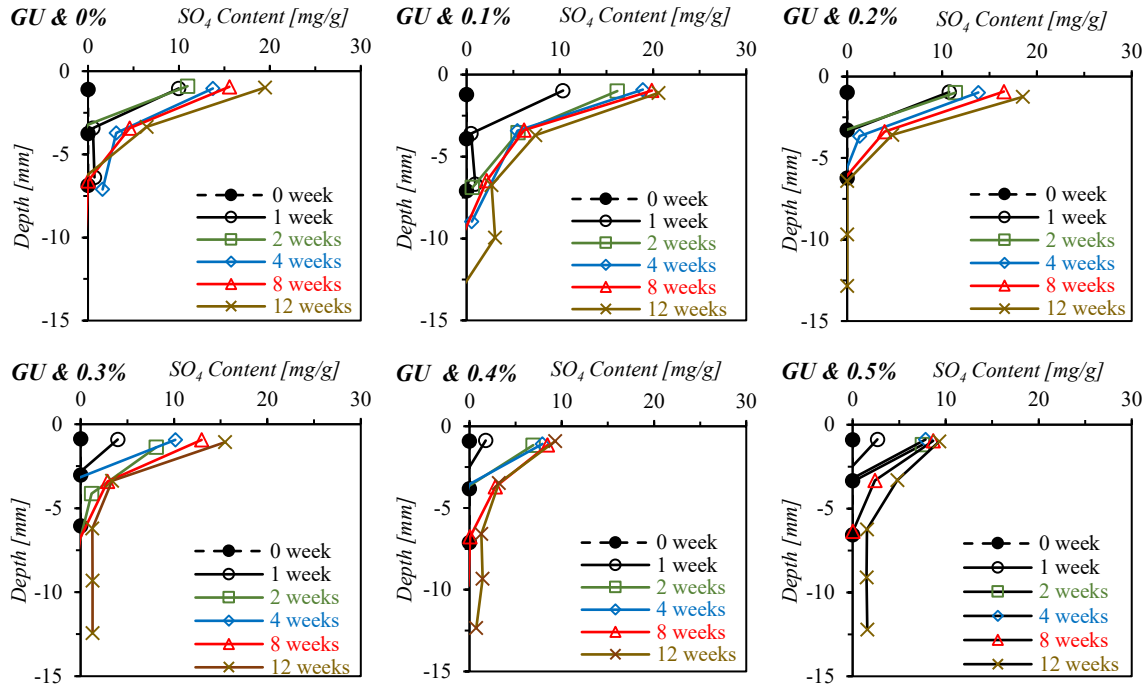


Figure 6.3 Sulphate (SO_4^{2-}) contents at different depths in Type GU cement mortars dosed with 0-0.5 vol.% dry CNF #0.13 over 12 weeks of exposure in Na_2SO_4 solution. The mix identified as 'GU & 0%' is the control mixture prepared with GU cement and no CNF.

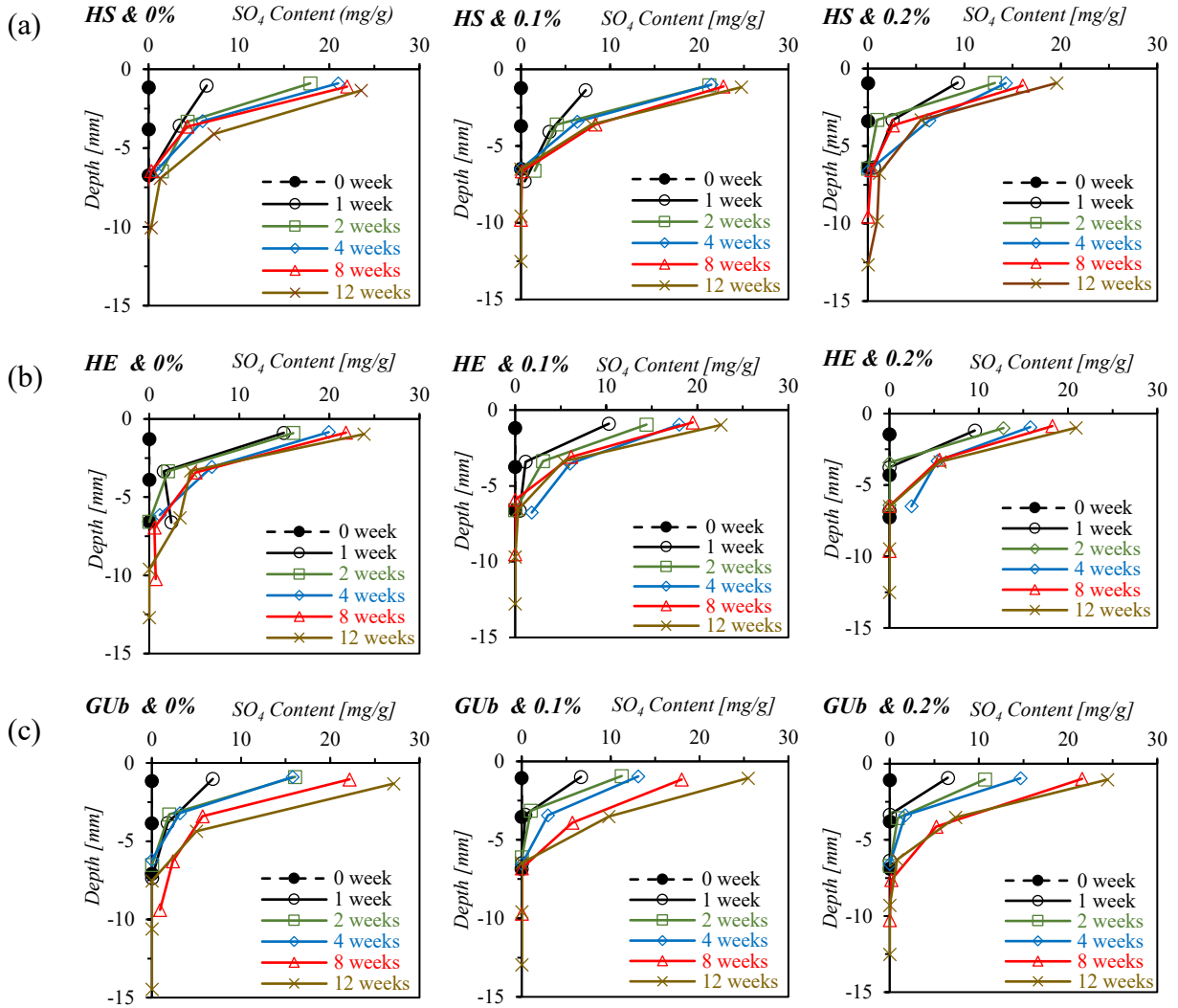


Figure 6.4 Sulphate (SO_4^{2-}) content at distinct depths in mortars as affected by 0-0.2 vol.% dry CNF #0.13 over 12 weeks of exposure in Na_2SO_4 solution for various cement-based binders (a) Type HS cement, (b) Type HE cement, and (c) blended Type GUB cement. The mixes identified as 'HS & 0%', 'HE & 0%' and 'GUB & 0%' are the control mortars prepared with 'HS', 'HE' and 'GUB' cements, respectively.

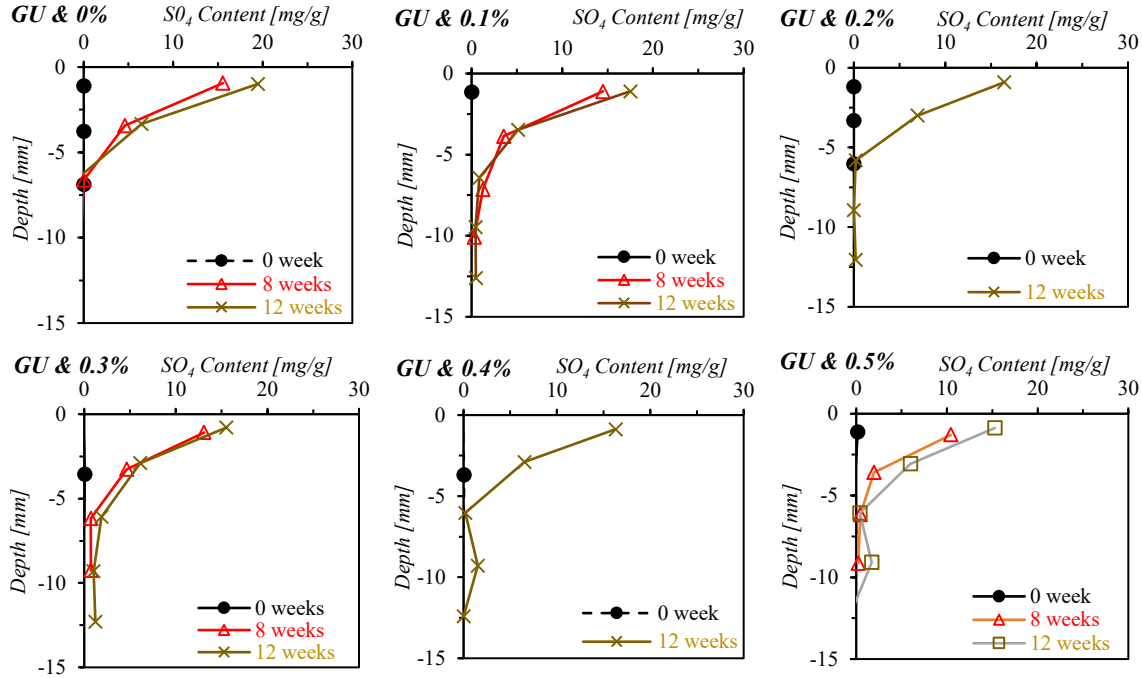


Figure 6.5 Sulphate (SO_4^{2-}) content at various depths in GU cement-based mortars having 0-0.5 vol.% CNF #1.13 over the period of 12 weeks of exposure in Na_2SO_4 solution. 'GU & 0%' is the control mortar.

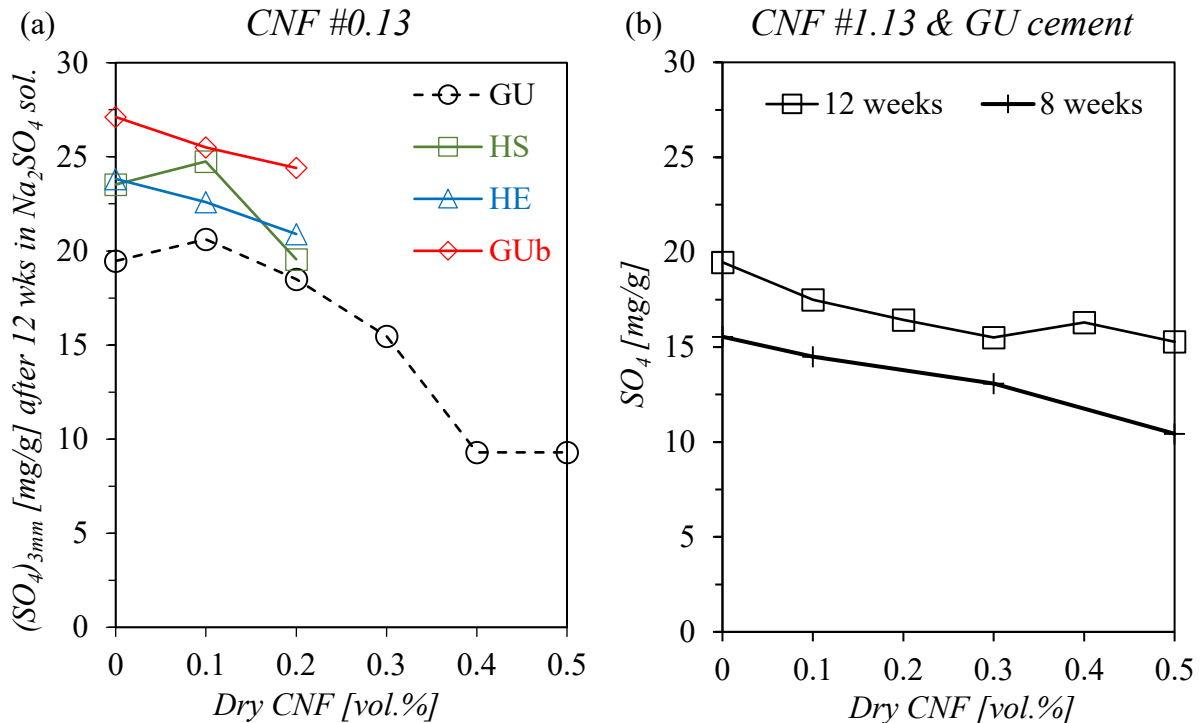


Figure 6.6 Sulphate (SO_4^{2-}) content at 3mm depth in various mortars affected by (a) CNF #0.13 loadings after 12 weeks of exposure in Na_2SO_4 solution, and (b) CNF #1.13 loadings after 8 and 12 weeks of exposure in Na_2SO_4 solution.

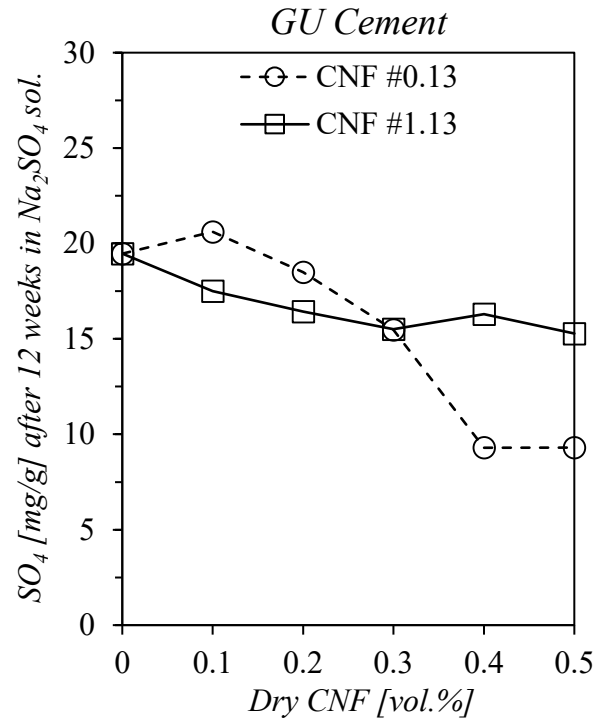


Figure 6.7 Sulphate (SO_4^{2-}) content at 3mm depth after 12 weeks in Na_2SO_4 solution in Type GU mortar series affected by CNF #0.13 dosage compared with those mixtures affected by CNF #1.13.

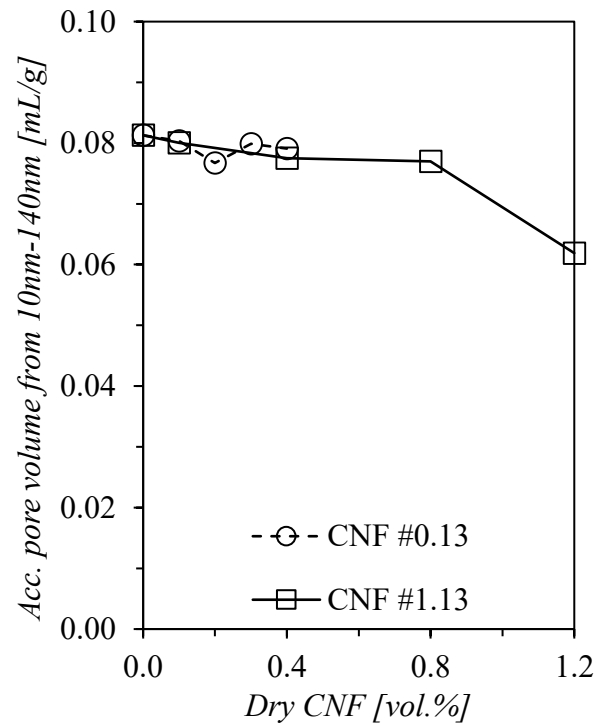


Figure 6.8 Porosity of CNF-based cement pastes in the range of 10 nm-140 nm. Data based on the gas sorption analysis shown in Figure 4.16.(a).

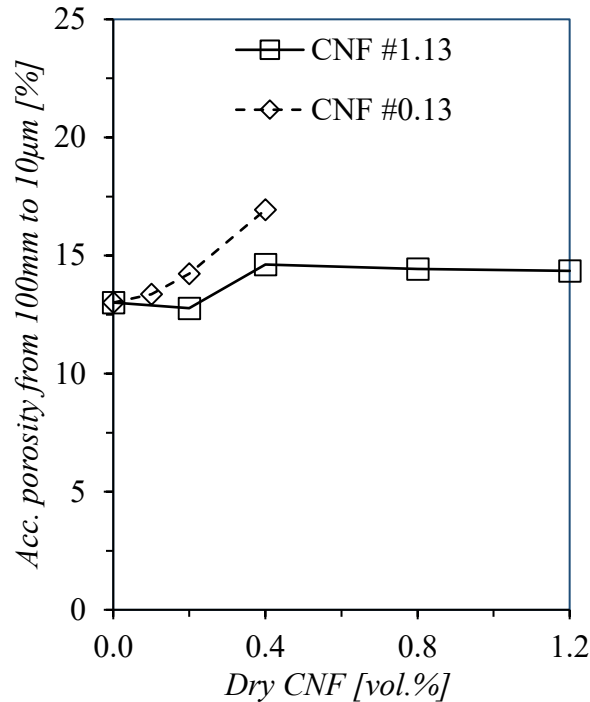


Figure 6.9 Porosity of cement pastes containing several CNF fractions ranging between 100 nm – 10 µm measured by SEM image analysis. Dataset based on Figure 4.21.(a) and Figure 4.21.(b).

6.3. Linear Dimensional Change

6.3.1. Experimental Procedure

Each mortar mixture was cast into nine prisms of dimension 25 mm x 25 mm x 285 mm and demold in the next day in accordance with ASTM C157/C157 [ASTM, 2008]. The specimens were cured in controlled environment for further 27 days on top of the plastic raisers placed inside of sealed containers as recommended by ASTM C1012 [ASTM, 2015]. After the initial curing period, six out of nine prisms were submerged in a standard Na_2SO_4 solution (50g/L) for 12 weeks at $23 \pm 2^\circ C$. The pH of the Na_2SO_4 was held at 7.8 before immersion. Figure 6.10.(a) and Figure 6.10.(b) illustrate these procedures. The remaining three prisms were immersed in water. The purity of this water met the requirements of Type I as per specification ASTM D1193 [ASTM, 2006] – see Figure 6.11. The prisms were submerged in containers at a ratio of 4 ± 0.5 volumes of liquid to 1 volume of mortar specimens. The same proportion of liquid-to-solid was maintained for the baths of Na_2SO_4 solution and water. The readings of the prim length were taken at 1 week, 2, 4, 8 and 12 weeks of immersion using a length comparator according to ASTM C490 [ASTM, 2011] – see

Figure 6.10.(c). The length change (LC) of the prismatic bars submerged in Na_2SO_4 solution and pure water were calculated as per ASTM C1012 [ASTM, 2015]. Thereafter, the difference between them was taken to account for the expansive effect generated by the external SO_4^{2-} ingress in cement mortars.



Figure 6.10 View of (a) the sealed container, (b) the prisms immersed in Na_2SO_4 solution, and (c) the length comparator used to measure the length change of prisms.



Figure 6.11 Water purifier Milli-Q® Integral.

6.3.2. Results and Discussion

Adding CNF to the mixtures uniformly reduced the expansion caused by sulphate attack over the 12-week period of trials, as seen in Figure 6.12 for mixtures containing CNF #0.13 and Figure 6.12.(a) for those mixes dosed with CNF #1.13. The greatest reduction was seen in mortar mixtures having HS as a binder, as expected. Although, even for these mixtures, CNF loadings declined the expansion. In Figure 6.13 and Figure 6.14.(b), the expansion in water has been discounted to showcase the change in length directly attributable to sulphate exposure. Hereafter, this change in length (LC) is referred to in this thesis as ‘absolute length change’. A reduction in the absolute LC was also true for all mixtures, regardless of the binder.

The LC associated with the plain Portland cement Type HS mortar, (i.e. not containing any CNF), was chosen as the reference baseline. This is illustrated through the blue-dashed line in Figure 6.13 for CNF #0.13-cement mixes and Figure 6.14.(b) for mortars loaded with CNF #1.13 doses, whereby, the performance of the unreinforced Type HS mixture was projected onto those of the other mixtures. Note that at a volume fraction of 0.4% or greater, CNF #0.13 when added to Portland cement Type GU meets this performance and in fact, betters it for higher volume fractions. The same superior performance was attained for mortars with 0.5 vol.% of CNF #1.13. This was true for the entire period of exposure.

The change in length after 12 weeks is shown as a function of CNF dosage in Figure 6.14 and Figure 6.15, according to the CNF type. Notice a decrease in length that appears linearly proportionate to the CNF content. Once again, the performance of the Type HS binder with no CNF added, was taken as the benchmark to be met. A blue-dashed line is traced in these Figures to enable a visual evaluation of the mortar performances. Accordingly, it is clear that adding CNF brought the Type GU, Type HE and the blended GUb mortars containing CNF #0.13 closer in sulphate resistance to this benchmark. Again, for CNF volume fractions beyond 0.4%, Type GU mortar depicted a lower LC after 12 weeks of exposure than the benchmark. Similar situation transpires for GU mortars with doses of CNF #1.13, in which a fraction of 0.5 vol.% of CNF led to a linear expansion lower than the benchmark. This is most encouraging as it implies that an alternative to Portland cement Type HS is possible through adding CNF to the Type GU cement.

Note that both Portland cement Type HE (for high early strength) and the blended binder Type GUb are similar to each other in performance. Early strength gain, and high sulphate resistance are required also by specialty cement types such as oil-well cements. The present findings promise a further push towards sustainable alternatives to Portland cement Type HS and oil-well cements, through CNF addition on the blended Type GUb binders. In this regard, the reduced C_3A content to combine with SO_4^{2-} soluble in pore solution and the pozzolanic reactions to refine the pore structure provided by the 30 wt.% fly ash added to blended GUb cement in manufacturing was maximized by the positive mechanisms afforded by the active groups on CNF surface to mitigate the precipitation of expansive ettringite phase and drop the expansion, as seen in Figure 6.15.(b).

A comparative performance of the mortar series prepared with the same binder, GU cement, but different CNFs is reported in Figure 6.17. The normalized data presented in Figure aims to harmonize a small dissimilarity in the LC results of the control mortar used in the trials of CNF #0.13 and in the CNF #1.13, as seen in Figure 6.15 and Figure 6.16. CNF #1.13 loadings led to a lower expansion in Na_2SO_4 solution than CNF #0.13 mixes only up to 0.3 vol.% fraction. Interestingly, above this fraction the behaviour inverts. CNF #0.13 loadings of 0.4% and 0.5% resulted in the best performances among all GU cement-based mortars. This dual behaviour is clearly exposed in Figure 6.17.(a). This sudden drop in the LC of GU cement mortars containing at least 0.4 vol.% of CNF #0.13 was also observed in the expansion trials and as explained in Section 6.2.2, is likely associated with an overcompaction applied to cast the specimens of these two mixtures, in specific. On the other hand, considering the absolute LC plot shown in Figure 6.17.(b), both kinds of CNF led to similar linear reduction in the absolute LC performances.

The mitigation in LC of cement pastes with CNF loadings as seen here and in Section 6.2, is probably due to the combination of an impervious pore structure and a reduced SO_4^{2-} availability in the paste matrix. Another hypothesis to be considered, but in a lower degree (due to CNF's micrometric length), is the crack bridging possibly provided by the nanofibres. Together, they render the material more impervious and chemically resistant.

The hydration kinetics of cement may be altered by the hydrophilic nature of CNF. The retained water by CNF may work as a water reservoir for further hydration of unhydrated cement particles

and promote the short circuit diffusion, as does CNC. Both assumptions can build a denser microstructure with a more impervious pore network. The CNF also functions as a nanofiller. This effect may further decrease the connectivity among the capillary pores and increase their tortuosity, similar to what occurs with microfiller or silica fume [Song, Pack, Nam, Jang, & Saraswathy, 2010]. The physico-chemical changes in the microstructure of cement pastes with incremental fractions of CNF were examined in CHAPTER 4 by means of the porosimetry (see Section 4.3) and the degree of hydration (see Section 4.2). Based on this data, the restriction to ettringite-induced expansion in CNF-based cement mortars is associated with a drop in the sulphate ion ingress (as revealed in Section 6.2.2) due to a rise in discontinuities in the capillary pore network ranging from 10 nm – 140 nm – see Figure 6.8; it is likely that the introduction of transition zones between nanofibres and cement paste partially obstructed the penetration of sulphate ions through this range of capillary pores. However, no enhancement in the DOH was observed, and hence the short circuit diffusion is unlikely. This hypothesis is discussed in Section 6.2.2 too.

The assumption about CNF's ability to scavenge the soluble Ca^{2+} from aqueous phase (which is a necessary ingredient to precipitate ettringite) is examined in detail in Section 6.4.

As for the last assumption, it is well-known that short, discrete fibres provide a bridging effect in transferring stresses across the micro-cracks and in the process, enhance the dimensional stability of concrete due to deleterious chemical reactions [Brandt, 2008; Mohr et al., 2009] and loss of evaporable water [Banthia & Gupta, 2006; Ramakrishnan, Zellers, & Patnaik, 2007; Choi, Park, & Jung, 2011]. Note that the CNFs employed here show approximately 5 nm – 20 nm in thickness with an aspect ratio between 40 and 200. This makes the CNF finer and thinner than the conventional cellulose microfibrils. As mentioned in Section 2.5, the mechanical properties of CNF are superior by far, compared with conventional cellulose microfibrils or synthetic macro and microfibrils [Iwamoto, Kai, Isogai, & Iwata, 2009]. Bhalerao, Wayal, Patil, & Bharimalla [2015] attested to CNF imparting superior fracture resistance to concrete. The curling observed in the post-trial CNF-cement paste specimens (see Figure 5.7) and the enhanced cracking resistance described in Section 5.4.1.2 are evidences of a possible CNF's potential reinforcement.

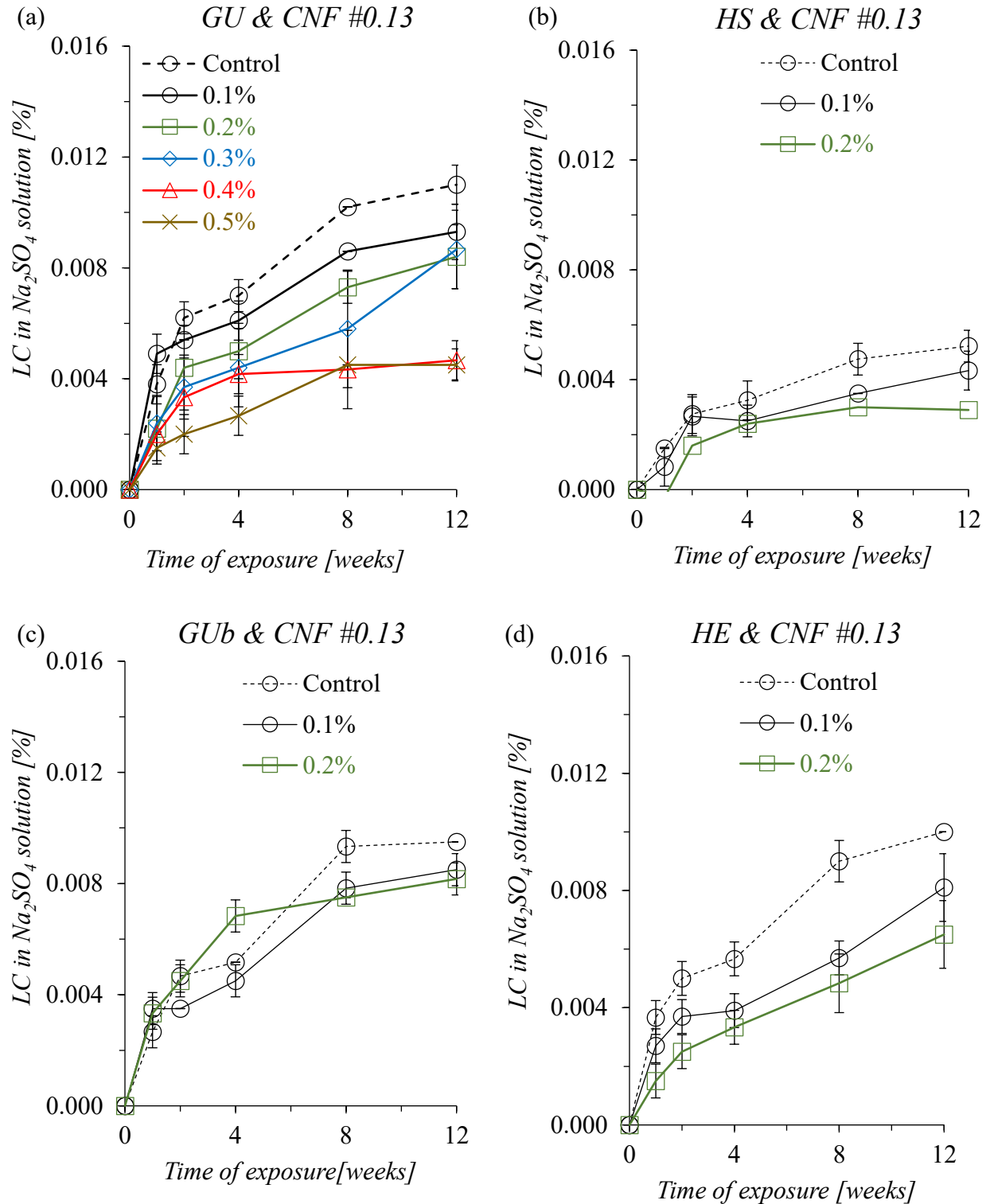


Figure 6.12 Length change (LC) measured in CNF #0.13-mortar mixtures prepared with distinct binders, (a) Type GU cement, (b) HS, (c) HE, and (d) GUb, over 12 weeks of exposure in Na_2SO_4 solution. Note that 'positive' values mean expansion.

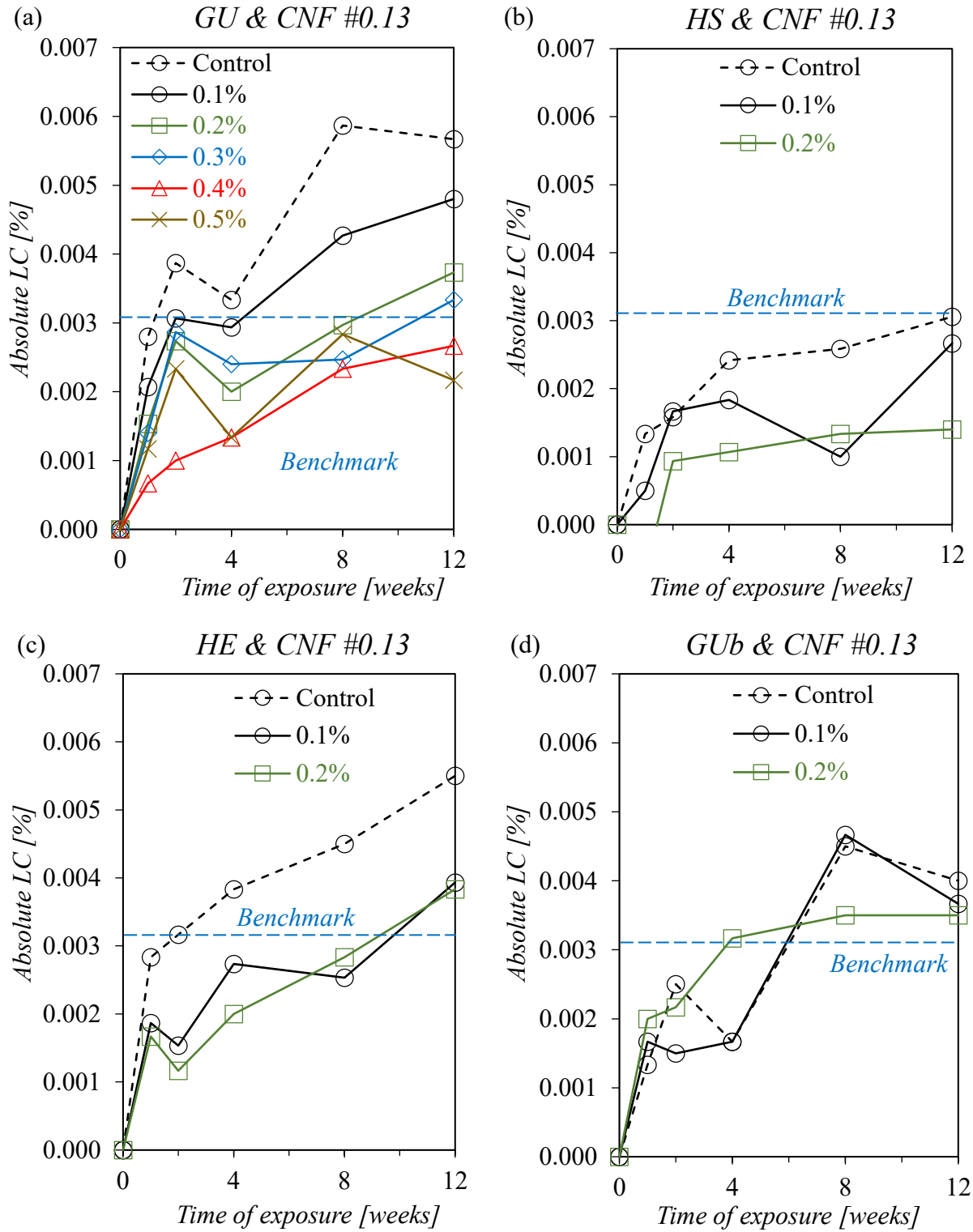


Figure 6.13 Absolute length change (LC) measured in CNF #0.13-cement mortars prepared with (a) Type GU cement, (b) HS, (c) HE, and (d) GUB over 12 weeks in Na_2SO_4 solution. The blue-dashed line shows the benchmark expansion in HS mortars. Note that ‘+’ values mean expansion.

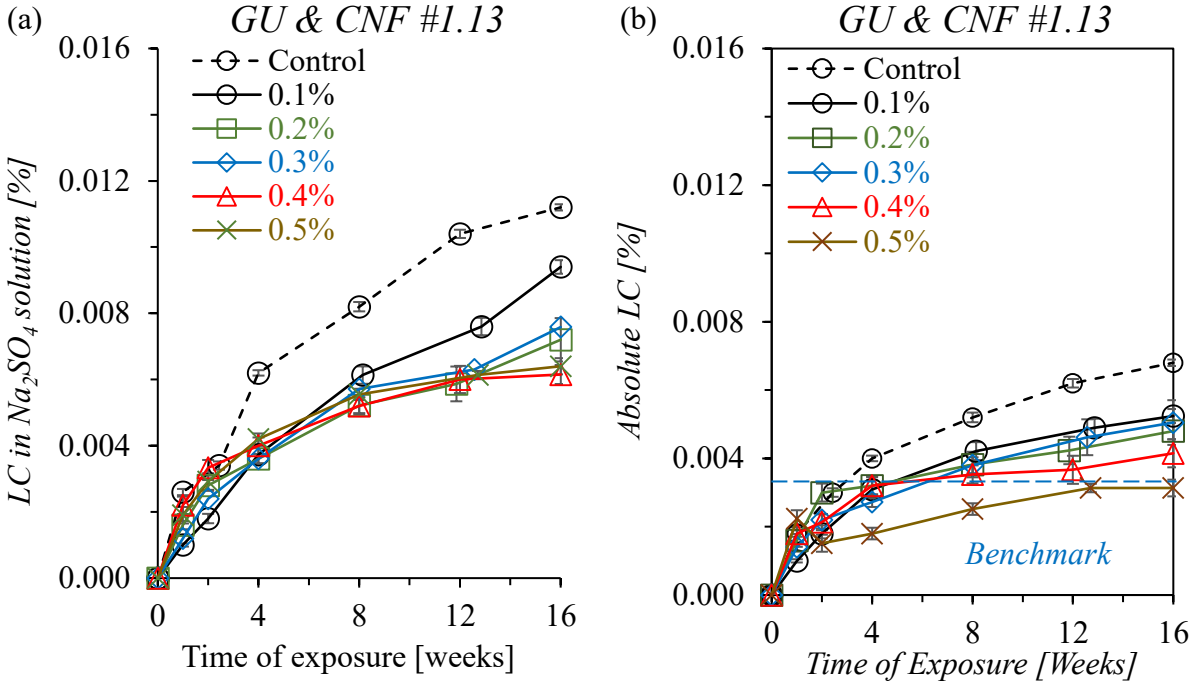


Figure 6.14.(a) Length change (LC) of CNF #1.13-GU-cement mortars over 12 weeks in Na_2SO_4 solution. (b) Absolute LC of the same mixtures. The blue-dashed line shows the benchmark expansion in HS cement mortars. Note that positive values mean expansion.

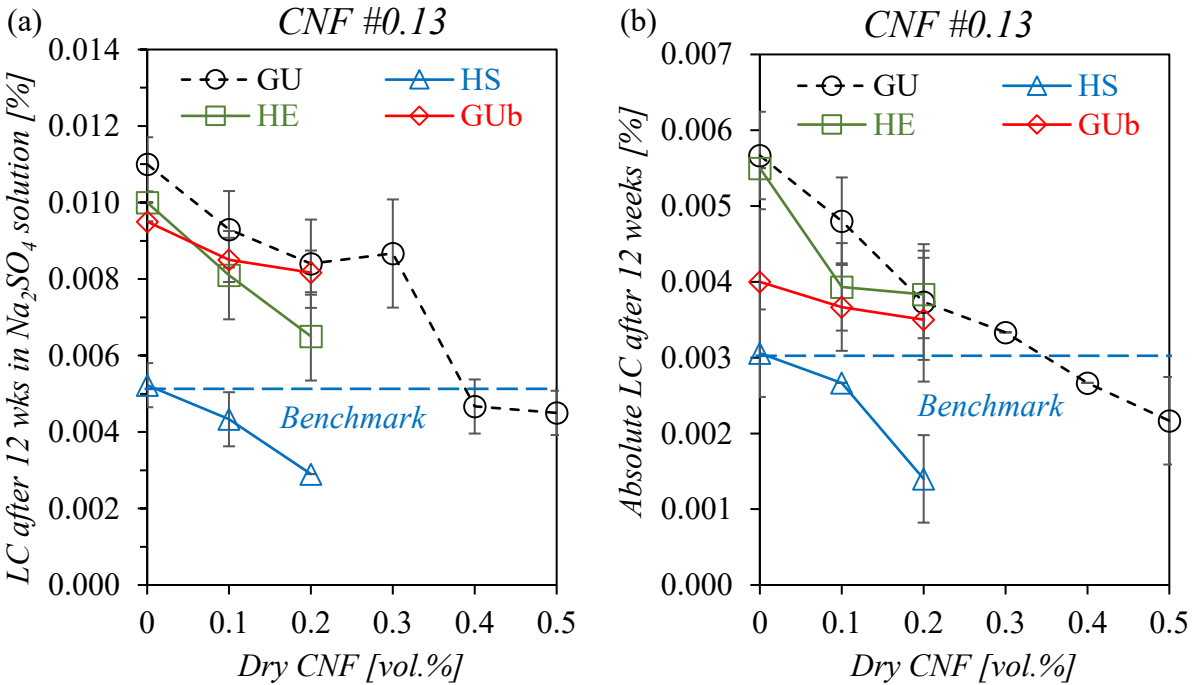


Figure 6.15.(a) Length change (LC) of CNF #1.13-cement mortars prepared with distinct binders after 12 weeks in Na_2SO_4 solution. (b) Absolute LC of the same mixtures. The blue-dashed line indicates the benchmark expansion observed in HS cement mortars. Positive values mean expansion.

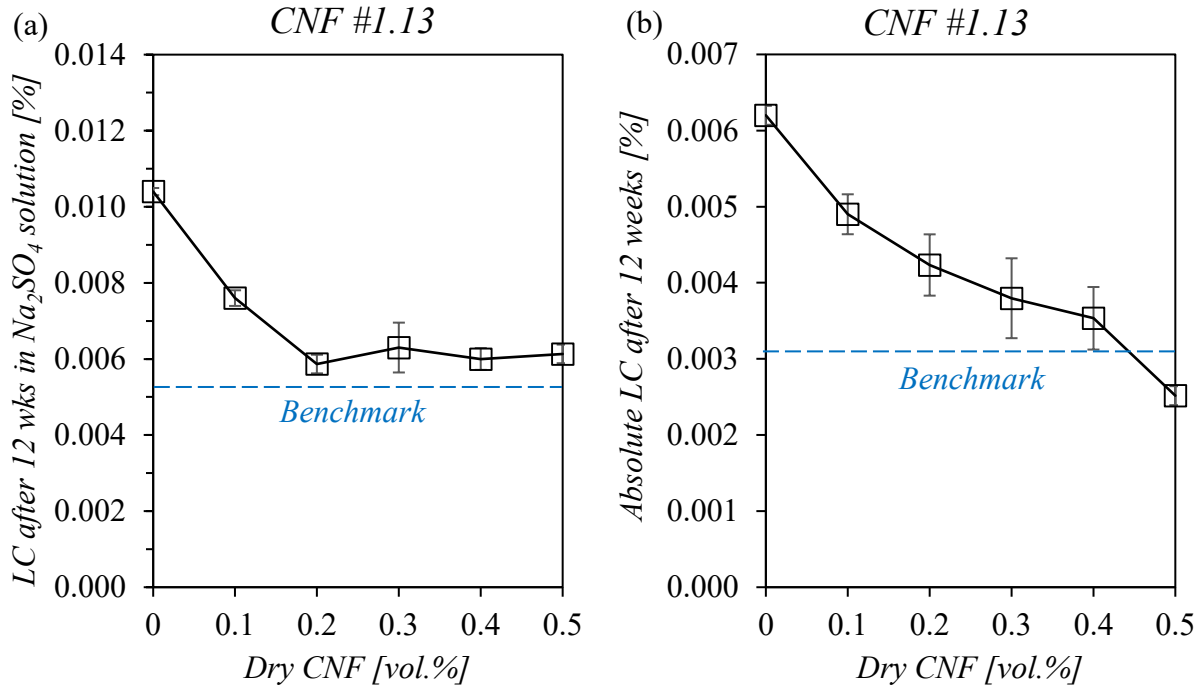


Figure 6.16. (a) Length change (LC) of CNF #1.13-GU cement mortars after 12 weeks in Na_2SO_4 solution. (b) Absolute LC of the same mixtures. The blue-dashed line defines the benchmark expansion verified in HS cement mortars. Note that positive values mean expansion.

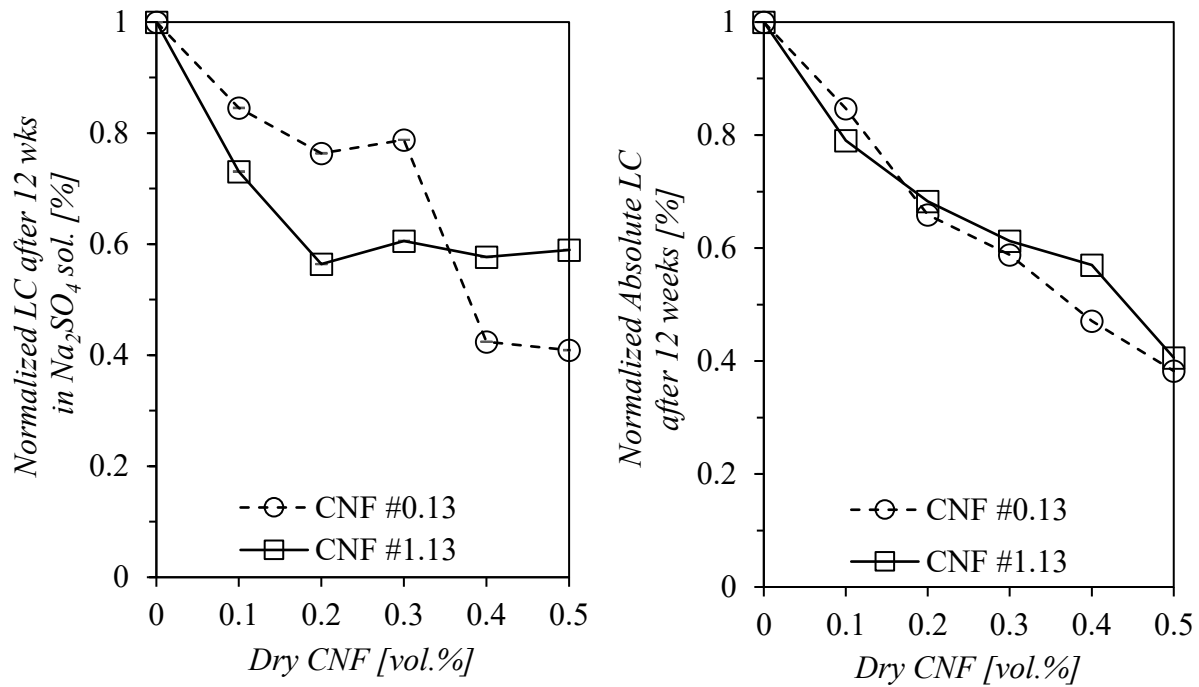


Figure 6.17 Comparison between the normalized (a) length change (LC) of GU-cement mortar mixtures dosed with different CNF types and fractions exposed to 12 weeks in Na_2SO_4 solution, and (b) the absolute LC of the same mixtures. Note that positive values mean expansion.

6.4. Further Investigations

In Sections 6.2 and 6.3 were demonstrated that the addition of CNF strengthened the cement mortars against the sulphate-induced expansion and the resistance to soluble SO_4^{2-} penetration. The possible hypotheses to support such behaviour may be related to: (i) the enhancement in the imperviousness of paste microstructure, and (ii) the chemical scavenging of Ca^{2+} from the pore solution of cement mortar by means of the CNF's COO^- groups. The first hypothesis was evaluated in the preceding Sections of this CHAPTER (and in CHAPTER 4). This Section examines the second hypothesis.

Since the presence of SO_4^{2-} in the matrix does not by itself imply adverse response under sulphate attack, the relative content of ettringite phase per all crystalline phases in CNF-cement mixtures was determined through X-ray diffraction (XRD) analysis as described in Section 6.4.1.

The Ca^{2+} is a crucial input in the chemical mechanism of ettringite-induced expansion of cement paste. The negative charged groups of CNF may bond the Ca^{2+} available in pore solution and hence, mitigate the formation of ettringite. At this point, it is important to recognize that other cationic alkalis, such as Na^+ and K^+ , may also be bound in CNF. Knowing that the most probable internal source of Ca^{2+} in cement pastes is $Ca(OH)_2$, its content was determined through thermogravimetric analysis (TGA) in cement pastes dosed with different fractions of CNF. A decline in Ca^{2+} (and the other alkalis, as well) may in consequence lessen the high values of potential of hydrogen (pH) found in pore solution, usually above 12.5. Sections 6.4.2 and 6.4.3 approach both hypotheses, respectively.

The decalcification of $C - S - H$ and to a lesser extent $Ca(OH)_2$ in low-alkaline microstructures may result in cohesion loss and hence lower mechanical strengths. Section 6.4.4 shows the compressive strength of mortar specimens loaded with various CNF #0.13 fractions after 12 weeks exposed to sulphate attack.

6.4.1. Relative Content of Ettringite

6.4.1.1. Introduction

The X-ray diffraction (XRD) is an analytical technique used to characterize the (un)hydrated crystalline phases of cements. The X-ray powder diffraction provides reliable information about the component phase identifications and their respective quantitative data. The qualitative phase analysis (QPA) is based on the comparison between the peaks of a sample XRD pattern and the peak patterns of known phases of a database.

Anhydrous or hydrated Portland cements are a complex mix of crystalline phases. Powder diffractions of cement phases frequently demonstrate overlapping of the reflection lines, so that the minor phases are hidden by the peak overlapped of the major phases. So that, in order to achieve a quantitative phase analysis, one must apply a pattern-fitting procedure. Snellings [2018] claimed that the Rietveld method is the most commonly used for this purpose in cementitious materials. Unlike other methods, Rietveld method utilizes the least-squares methodology to reduce the deviation between the measured XRD pattern and the calculated XRD pattern-fitting data [Snellings, 2018]. On top of that the Levenberg-Marquardt method is another popular standard nonlinear least-squares curve-fitting routine used to optimize a best-fit approach of the data set points in a chart [Brandt & Brandt, 1999].

6.4.1.2. Experimental Procedure

The samples for XRD were collected from the 10 mm-thick slices cut from the top-end of the 28-day moist-cured paste cylinders exposed to unidirectional SO_4^{2-} attack for 12 weeks. More details about the: (i) cylinder casting is found in Section 6.2.1; (ii) epoxy coating in Section 6.2.1, as well; and (iii) slice cutting, sandpapering, crushing, grinding and sieving of the samples are found in Section 4.3.1.2, excluding the particle size range. A finer range was used instead, that is, smaller than the sieve opening 0.15 (sieve mesh #100) mm and greater than the 0.088 mm (sieve mesh #170). Figure 6.1.(a), Figure 6.1.(b), Figure 6.1.(c), Figure 6.18 and Figure 6.19 show many stages of the sample preparation. These paste cylinders were prepared with Portland cement Type GU and increments of 0.1 vol.% of CNF #0.13 up to a limit of 0.4 vol.% – CNF #1.13 was not used.

The mix proportions of the CNF-cement pastes utilized in this Section are listed in Table 3.10 (see Section 3.4) and their preparation followed the guidance established in Section 3.4. Water Type IV, as per ASTM D1193 [ASTM, 2006], was used to prepare the pastes.

The finger-print XRD diffraction patterns of the cement paste samples were collected with a *Bruker D8 Discover* diffractometer equipped with a theta/theta goniometer a vice with Cu-K α radiation source and *Vantec-500*, 2-dimensional detector. This apparatus is shown in Figure 6.20. The patterns were recorded at a tube voltage of 40 kV and a tube current of 35 mA using a scan rate of 0.02° 2 θ /s over the 2 θ angular range from 5° to 112°. The X-ray powder diffraction data was refined using the Levenberg-Marquardt method [Brandt et al., 1999] associated with the Voigt function for fitting peaks. This function is a convolution of Gaussian and Lorentzian functions [Wells, 1999]. The five highest peaks of ettringite were located in the XRD diffraction patterns according to the peak pattern ranges provided by the diffractometer's database. Individual curves were obtained for each peak by applying fitting functions. This same procedure was applied to all other peak curves in the diffractogram. The nonlinear curve fitting procedure and the peak-area analysis were accomplished through the open source software 'Fityk'. Details about the software 'Fityk' are given by Wojdyr [2010]. The ratio 5-peak ettringite area to total crystalline area, henceforward named relative ettringite 'content', was calculated. This 'content' is, in fact, a relative number equivalent to the majority of the ettringite peak areas relativized with the area found under all peaks of the XRD diffraction patterns. Accordingly, while it is not the actual ettringite content, this methodology is valid to compare performances across distinct mixtures.

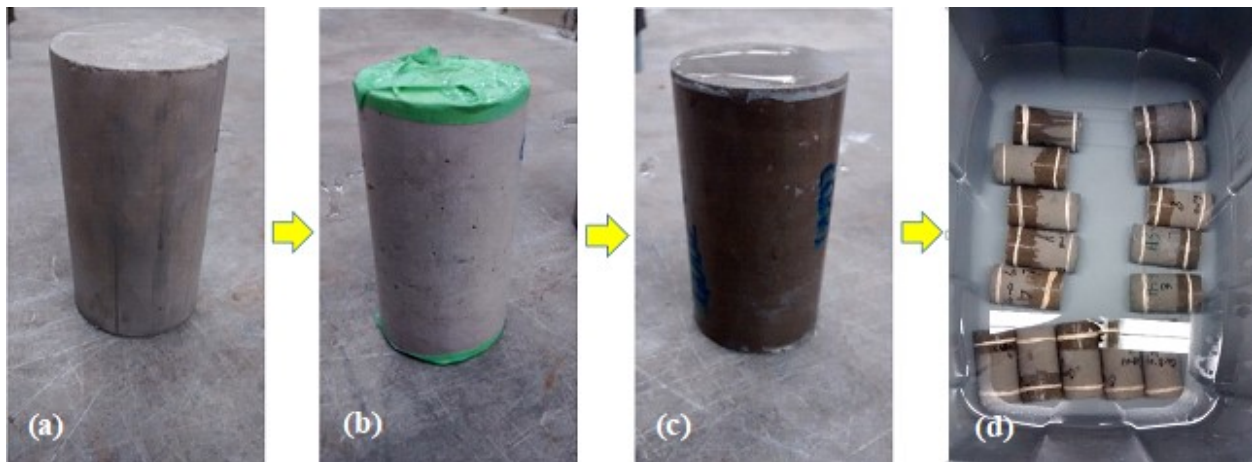


Figure 6.18.(a),(b),(c) Sequence showing the sides of paste cylinder being coated with epoxy resin. (d) Cylinders submerged in Na_2SO_4 solution in a sealed container for 12 weeks.



Figure 6.19 Sequence showing the sample preparation: (a) bench saw cutting machine used to slice the cylinder; (b) cut slices; (c) sandpapering; (d) grinding; and (e) sieving the sample.

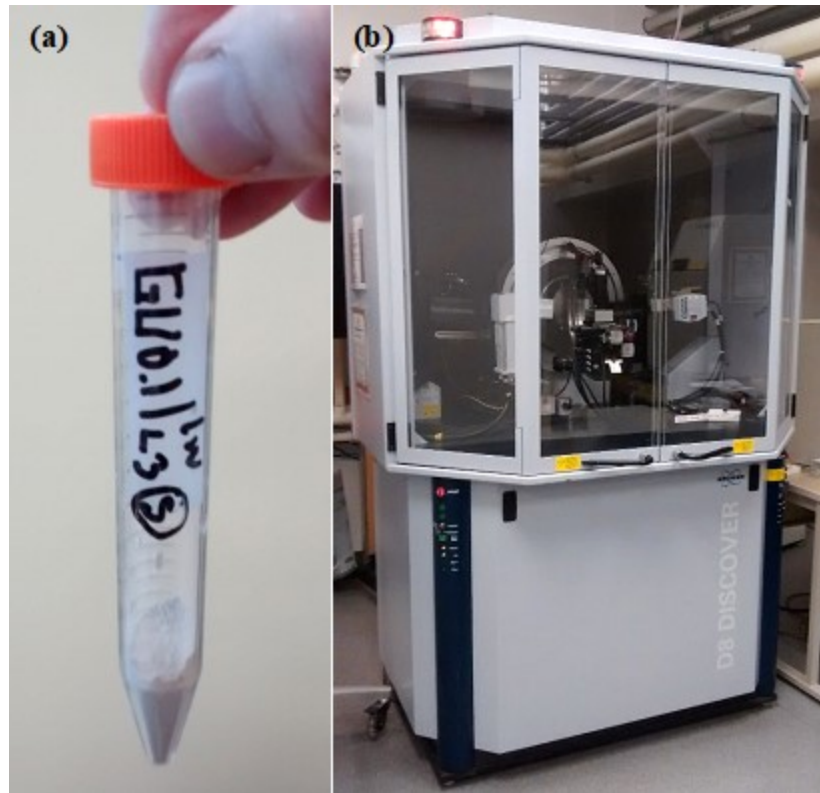


Figure 6.20 View of (a) the powder sample and (b) the diffractometer.

6.4.1.3. Results and Discussion

The sulphate content over various depths shown in Section 6.2 is not, by itself, a threat to the durability of cementitious materials. In fact, sulphate is one of the chemical components of Portland cement and an essential ingredient to control the setting time of cement paste. It is the expansive ettringite that causes concern.

The sulphate-induced expansion is triggered by ettringite precipitated in voids of cement pastes, as described in Section 2.2.2 of the thesis. Figure 6.21.(a) revealed that the 5-peak ettringite area-to-crystalline area ratio in cement pastes drops pointedly with increments in CNF #0.13 loadings after 12 weeks of exposure in Na_2SO_4 solution, inverting drastically the initial trend. The enhancement provided by CNF became factual only after 8 weeks of exposure, as seen in Figure 6.21.(b). Figure 6.21.(c) shows that, from 8 to 12 weeks, the amount of ettringite raised not more than 8.8% in pastes containing 0.5 vol.% of CNF #0.13, whilst in the control cement paste (without CNF) the growth reached 66%.

The ettringite reduction in pastes containing CNF is ascribed to two factors: (i) a lower availability of SO_4^{2-} , as discussed in Section 6.2; and (ii) CNF's ability to chemically scavenge Ca^{2+} from pore solution. Interestingly, the chemical reaction between the Ca^{2+} and the CNF's active anionic groups only was manifested effectively after 8 weeks in Na_2SO_4 solution exposure. Perhaps, this mechanism is exclusively triggered after attaining a certain sulphate concentration in cement pastes.

No further XRD analyses in the mixtures containing CNF #0.13 or other CNF types took place due to time and cost constraints; thus, no error bars were plotted in Figure 6.21.

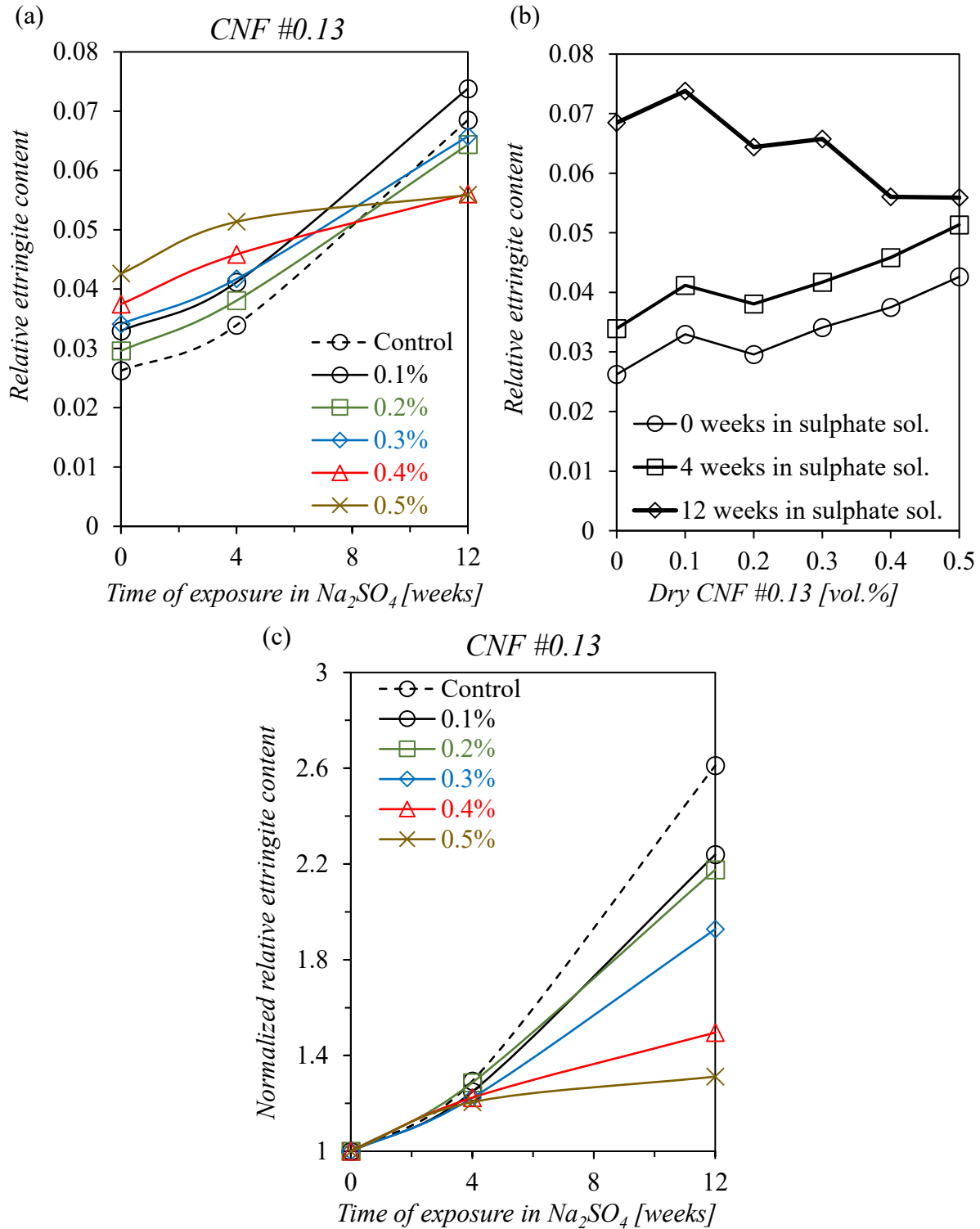


Figure 6.21.(a) Relative ettringite content of cement pastes affected by various CNF fractions in distinct time intervals of Na_2SO_4 solution exposure. (b) Same plot, now, rearranged per CNF dosage. (c) Growth of ettringite content as a function of its initial amount at time zero of exposure.

6.4.2. Portlandite Content

6.4.2.1. Introduction

Sulphate-induced expansion in cement pastes depends on ettringite precipitation. One of the ingredients necessary to ettringite formation is the presence of soluble Ca^{2+} in pore solution of cement pastes. CNF, by means of its COO^- groups, may also compete with ettringite to chemically combine with Ca^{2+} [Jiao et al., 2016]. The feasible chemical relationship that explains this reaction is figured out in Figure 6.22. As noted in Sections 6.1 and 6.4, the main source of soluble Ca^{2+} in pore solution is $Ca(OH)_2$, which is one of the hydrated products of cement.

In order to evaluate the effect of CNF in this chemical mechanism, the amount of $Ca(OH)_2$ phase was measured by TGA. Lothenbach et al. [2016] revealed that TGA is the technique regularly applied to measure the quantity of bound water and $Ca(OH)_2$ in cementitious materials. Besides, TGA is used to follow the hydration reactions in cement or to assess the reactivity of supplementary cementitious materials, such as fly ash and blast furnace slags.

TGA is a method in which modifications in the chemical composition of the cementitious materials are computed as a function of temperature or time. Broadly speaking, thermogravimetric analyzers measure the weight loss of a sample subjected to a continuous increase in temperature at a constant heating rate. In the case of cement paste, the weight loss is related to the loss of bound water or carbon dioxide, CO_2 . During the trials, the readings of sample weight are processed by a highly sensitive low-mass furnace thermo-balance with a purge gas system to minimize chemical changes in the sample due to oxidizing atmospheres. Nitrogen, N_2 , is usually used as a protective purging gas in (un)hydrated cement trials [Lothenbach et al., 2016].

As the temperature increases, the hydrated products of cement undergo several thermal reactions, such as dehydration, dehydroxylation, decarbonation, oxidation, decomposition, phase transition or melting [Fagerlund, 2009; Lothenbach et al., 2016]. During the reactions of dehydroxylation, the $Ca(OH)_2$ is decomposed by losing bound water. It occurs roughly in the range of 400-550 °C [Ramachandran, 2001; Lothenbach et al., 2016]. Hence, the loss of weight during this temperature range is associated with the $Ca(OH)_2$ content. The accuracy of the result improves if the

temperature limits (as the weight at the limits) at which the dehydroxylation of $Ca(OH)_2$ occurs are defined through the derivative plot of TGA data, also known as derivative thermogravimetric DTG curve.

The $Ca(OH)_2$ content calculated on the basis of the dehydroxylation phase can be corrected using the Ca^{2+} content held during the surface carbonation of the sample. This phenomenon may occur when the sample is exposed to air during its preparation or storage. In short, carbonation is the chemical reaction between the soluble Ca^{2+} available in pore solution and the CO_2 existent in the air that precipitates calcium carbonate, $CaCO_3$. This additional Ca^{2+} content is measured through the CO_2 content released during the decarbonation of the sample, which occurs roughly from 550-750 °C [Lothenbach et al., 2016].

The TGA data is strongly affected by sample pretreatments and the TGA parameters chosen to run the trials. The more common source of errors in TGAs come from the hydration stoppage and the removal of residual free water from cement paste samples. In this regard, solvent exchange using isopropanol is the least aggressive technique to the microstructure of cement paste. Alternatively, oven drying at 105 °C is an easy procedure that not affects directly the determination of $Ca(OH)_2$ content, given that the dehydroxylation phase occurs between 400-550 °C; notwithstanding this, a part of the bound water evaporates from the sample, particularly from the $C - S - H$, ettringite and monosulphate [Lothenbach et al., 2016]. Other relevant factors in TGA are the amount and the particle size of the solid sample. For the thermal analyzer, the sample weighing device, heating rate, gas flow rate and the type of purging gas are other important parameters for TGA [Lothenbach et al., 2016].

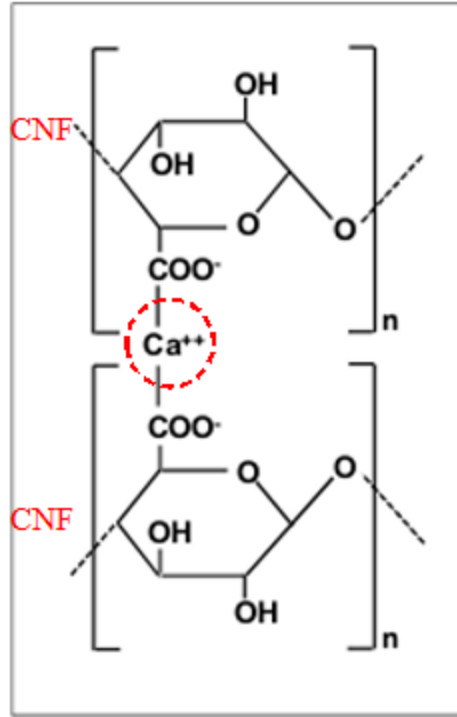


Figure 6.22 Schematic representation of the chemical reaction between the COO^- groups on the CNF surface and the soluble Ca^{2+} in pore solution of cement pastes.

6.4.2.2. Experimental Procedure

Only CNF #0.13 was added to cement pastes. The mix designs of the CNF #0.13-based paste mixtures are reported in Section 3.4 and the proportions listed in Table 3.10. Table 3.9 displays the mixing procedure.

One cylindrical paste specimen was cast, demolded, moist cured, coated with epoxy resin, and exposed to Na_2SO_4 solution as described in Section 6.2.2. This Section also discloses the sequence of TGA sample preparation viz., the slice cutting, the sandpapering, the grinding and the sieving.

The amount of $Ca(OH)_2$ phase in the samples was determined by TGA using the *TA Instruments TA Q50* shown in Figure 4.4 in Section 4.2. The software used for data acquisition was *TA Universal Analysis 2000 version 4.5A*. The TGA trials were performed in a sample of 50 mg previously oven-dried at $105 \pm 5^\circ C$ for 24 hours poured in high temperature platinum crucible of 100 μL . The sample was heated at a ramp rate of $10^\circ C/min$ from room temperature to $850^\circ C$, having nitrogen at a flow of 60 mL/min as purging gas. The dehydroxylation of $Ca(OH)_2$ phase

generally occurs between 400 and 550°C. The $Ca(OH)_2$ content was calculated according to the following equations [Lothenbach et al., 2016]:

$$w_{Ca(OH)_2} = [(w_{400^\circ C} - w_{550^\circ C})/w_{550^\circ C}] \times (74/18) \quad (6.5)$$

where ' $w_{Ca(OH)_2}$ ' is the $Ca(OH)_2$ content in sample [g/100 g of anhydrous cement]; ' $w_{400^\circ C}$ ' and ' $w_{550^\circ C}$ ' are, respectively, the sample weight at 400°C and 550°C [mg]; and the ratio (74/18) is the molecular mass ratio of $Ca(OH)_2$ (74 g/mol) to water (18 g/mol). A 'blank trial' revealed a fictitious weight gain of 0.001 mg/°C, which was discounted from all TGA results, as a zero-error.

There exists the possibility that the carbonated surface of the sample has not been sufficiently sandpapered out. Thus first, the $CaCO_3$ content was calculated and then the $Ca(OH)_2$ content corrected based on the Ca^{2+} present in the $CaCO_3$, as previously explained. The following equations were used:

$$w_{CaCO_3} = [(w_{550^\circ C} - w_{750^\circ C})/w_{750^\circ C}] \times (100/44) \quad (6.6)$$

where ' w_{CaCO_3} ' is the $CaCO_3$ content [g/100 g of anhydrous cement]; ' $w_{550^\circ C}$ ' and ' $w_{750^\circ C}$ ' are the sample weights [mg] at 550°C and 750°C, respectively; and the ratio (100/44) is the molecular mass ratio of $CaCO_3$ (100 g/mol) to CO_2 (44 g/mol); and

$$w_{Ca(OH)_2,corrected} = [w_{CaCO_3}] \times (74/100) \quad (6.7)$$

where ' $w_{Ca(OH)_2,corrected}$ ' is the $Ca(OH)_2$ content corrected [g/100 g of anhydrous cement]; and the ratio (74/100) is the molecular mass ratio of $Ca(OH)_2$ (74 g/mol) to $CaCO_3$ (100 g/mol).

As the hydrated product of cement, the CNF also experiences weight loss between 200-330 °C [El Bakkari, Bindiganavile, Goncalves, & Boluk, 2019]. To assess if the CNF's weight loss interfered in the TGA data of the cement pastes, a DTG of CNF samples, oven-dried at 40 ± 0.5 °C, was performed using the same weight and parameters assumed for the cement paste trials.

6.4.2.3. Results and Discussion

The TGA curves of the CNFs are shown in Figure 6.23. Its derivative, DTG, revealed that practically all weight loss correspondent to the volatile parcel of the microfibrils took place in the

temperature range of 244-383°C for CNF #0.13 and 196-356°C for CNF #1.13 – see Figure 6.24.(a) and Figure 6.24.(b). Against the above, no correction of the $Ca(OH)_2$ content was necessary, since that the weight loss relative to the CNF decomposition occurred in a temperature range smaller than the one assumed for the dehydroxylation of cement pastes, i.e. 400-550°C.

The Figure 6.25.(a) displays the TGA data of all CNF-based cement pastes. Interestingly, adding CNF postponed the onset of the dehydration phase of the control cement pastes from 100 °C to at least 150 °C, even for mixtures containing 0.1 vol%.

The $Ca(OH)_2$ content of cement pastes containing 0.1 vol.% fraction of CNF #0.13 was slightly reduced in about 6.5% in comparison with the reference cement paste, as is perceptible in Figure 6.25.(b). Above 0.1% dosage, the decrease of $Ca(OH)_2$ content remained marginal all over the range of CNF loadings, attaining a cutback of 8.8% for cement pastes dosed with 0.4% of CNF. The value of 22 g of $Ca(OH)_2$ per 100 g of dry cement found for the control cement paste kept a good agreement with those reported by Kim and Olek [2012] and Lothenbach et al. [2016] using the TGA technique and the same sample pretreatments. Identical reduction trend was observed in the $Ca(OH)_2$ contents corrected with the amount Ca^{2+} from the carbonated pastes, as shown in Figure 6.25.(c). Similar slight reduction as the dosage of CNF in cement pastes increases is verified in the $Ca(OH)_2$ content calculated as per equation 6.5 (referred in Section 6.4.2.2) using the weight loss data from the dehydroxylation phase shown in Figure 4.9.(c) of Section 4.2.3 – see Figure 6.26. This data was obtained using TGA and samples prepared as described here, but not exposed to Na_2SO_4 solution.

Both SO_4^{2+} and Ca^{2+} are crucial inputs for sulphate attack. Without them, the internally unstable monosulphoaluminate does not convert into the expansive ettringite. The presence of active hydroxyl and carboxyl groups on CNF surface make it active in the hydrating cement paste. One possibility is that the COO^- of CNF chemically traps the soluble Ca^{2+} through hydrogen bonds or bridging compounds and lessens the amount of $Ca(OH)_2$ phases in pore solution [Jiao et al., 2016]. Due to the hydrophilic nature of COO^- groups, the pore water is likely trapped on the surface of CNF, adding to the water reservoir around the CNF. Again, while this likely promotes hydration, it is equally likely to capture the Ca^{2+} ions and reduce their further diffusion. As is well

known, the conversion of $Ca(OH)_2$ and SO_4^{2-} ions into gypsum, $CaSO_4 \cdot 2H_2O$, is an essential step in the sulphate attack [Marchand et al., 2003].

It worth noting that the loss of $Ca(OH)_2$ and the low alkalinity in cementitious materials are also chemical symptoms of ongoing sulphate-induced expansion, since Ca^{2+} is consumed during ettringite phase formation [Skalny et al., 2001]. For this reason, the pH of cement pastes containing CNF was evaluated in the next Section of this thesis.

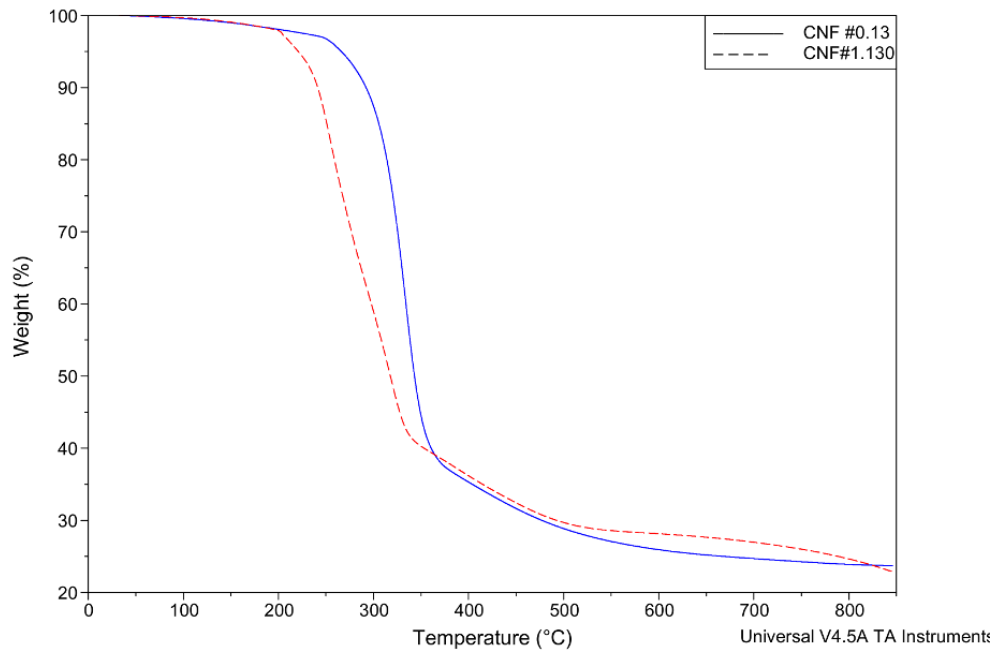


Figure 6.23 TGA curves of dry CNF #0.13 and dry CNF #1.13.

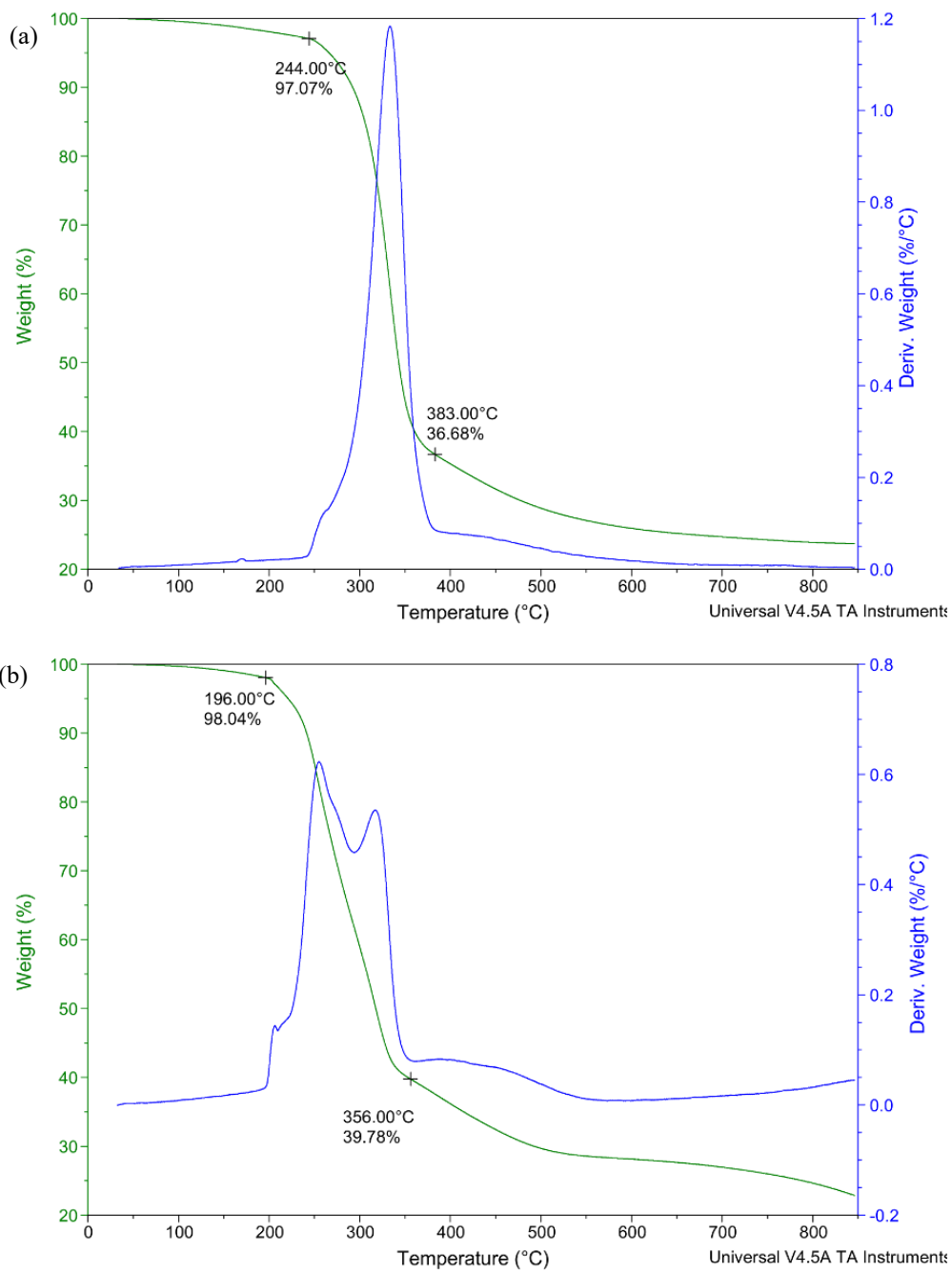


Figure 6.24 TGA/DTG curves showing the temperature limits for decomposition of (a) dry CNF #0.13 and (b) dry CNF #1.13.

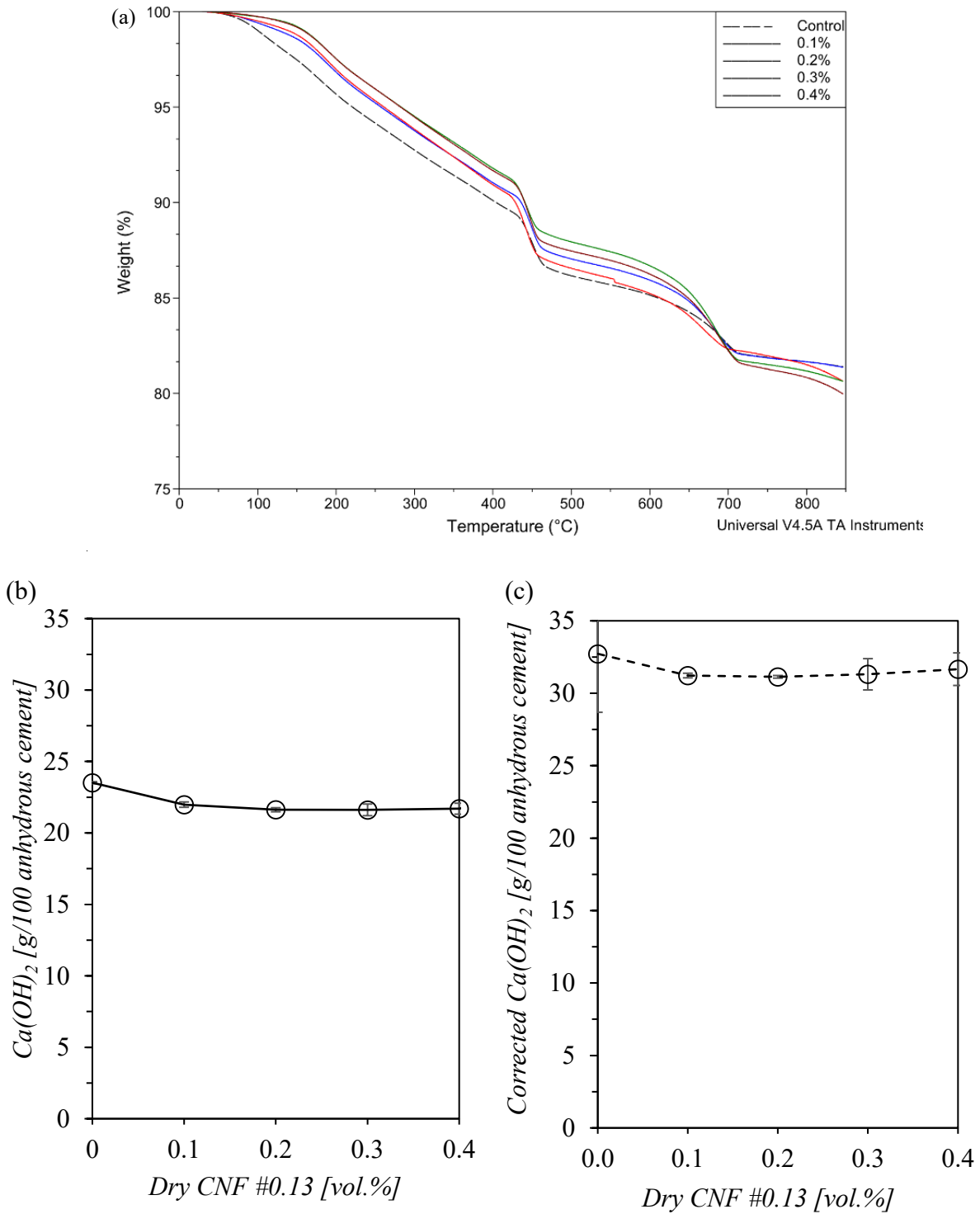


Figure 6.25 View of the TGA plots of (a) the cement pastes dosed with 0-0.4 vol.% of CNF #0.13. (b). Ca(OH)_2 content of pastes affected by various dosages of CNF #0.13. (c). Ca(OH)_2 content corrected with the parcel of Ca^{2+} from the carbonation phase of cement pastes.

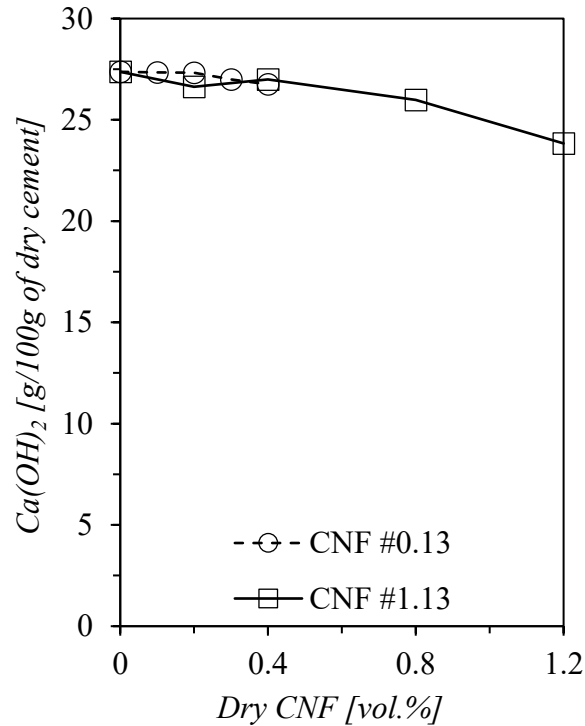


Figure 6.26 Calcium hydroxide, $Ca(OH)_2$, content in cement pastes affected by CNF dosage based on the dehydroxylation data shown in Figure 4.9.(c).

6.4.3. Evaluating the pH

6.4.3.1. Introduction

Water performs a vital role in cement hydration, dissolving several chemical elements of anhydrous cement particles. In the first few hours of hydration, the water surrounding the solid microstructure still in formation is considerably rich in cations and anions [Longuet, Burglen, & Zelwer, 1973], which maintain the high pH of the pore solution. Grubb, Limaye, and Kakade [2007] estimated the pH of cement pastes in 13, and Andersson, Allard, Bengtsson, and Magnusson [1989] in the range 12.4-13.5. The high pH is an essential factor to the ongoing dissolution-precipitation processes of hydration, as well as the stability of the hydrated products of cement. Nonetheless, the initial abundancy in the concentration of calcium, Ca^{2+} , sodium, Na^+ , potassium, K^+ , magnesium, Mg^{2+} , sulphate, SO_4^{2-} and hydroxide, OH^- , among others, gradually decreases with the progress of hydration reactions [Longuet et al., 1973; Andersson et al., 1989; Lothenbach & Winnefeld, 2006]. After this period, the concentration of these soluble elements

boils down to hundreds mmol/L of alkalis (i.e. Na^+ and K^+), some Ca^{2+} , an even smaller amount of SO_4^{2-} and trace of the others [Barneyback Jr & Diamond, 1981; Khadra, Burlion, Rougelot, Carlier, & Lataste, 2017]. As a result, the pH of pore solution may diminish up to 12, depending on the raw materials and environmental exposure of concrete. In hardened cementitious materials, the balance between the level of cations – alkalis and Ca^{2+} – and anions – OH^- – is crucial to keep low the content of hydrogen, H^+ , and hence, the high pH of pore solution.

Manso Blanco and Aguado de Cea [2017] revealed that the pH of pore solution may be reduced by several phenomena of de-calcification and/or de-alkalization of cement pastes, namely, carbonation, leaching and the presence of aggressive sulfates. The carbonation phenomenon described in Section 2.2.1.3 involves the combination of soluble Ca^{2+} with atmospheric carbon dioxide, CO_2 . Grubb et al. [2007] claimed that the carbonated fronts in concrete may reach pH values as low as 8.5. This issue is particularly relevant for electrochemical corrosion of embedded steel bars in concrete. Leaching is a phenomenon in which Ca^{2+} and OH^- dissolved by external acid or de-alkaline water are taken out of concrete. As explained in detail in Section 2.2.2, SO_4^{2-} combines with Ca^{2+} mostly sourced from $Ca(OH)_2$. All these phenomena have in common the consumption of Ca^{2+} from aqueous phase and hence the scaling down of the pH in cement pastes [Manso Blanco et al., 2017]. For this reason, Khadra et al. [2017] stated that the pH is a relevant indicator of concrete durability. Low-pH pore solution destabilizes, among others calcium-based hydration products, $Ca(OH)_2$ and $C - S - H$ gel, which may lead to more sulphonation of Ca^{2+} and material strength loss, respectively [Skalny et al., 2001]. This can be particularly important for mixtures prepared with Type GUB binders containing low-calcium cementitious materials, such as silica fume. Besides, low alkalinity decays the passive film that protects steel bars from the electrochemical corrosion [Neville, 2011; Metha et al., 2013]. This was an additional reason for evaluating the pH of these mixtures

One of the hypotheses raised in this thesis is the plentiful anionic active groups existent on CNF surface possibly combine with part of the Ca^{2+} (so as other cations, such as Na^+ and K^+) available in pore solution [Andersson et al., 1989] and consequently minimize the sulphate-induced expansion. At this point, it is worth refreshing that Ca^{2+} and SO_4^{2-} are the basic inputs for ettringite phase formation. Bearing this in mind, it is important to assess if the alkalinity of pore solution

declines with the addition of CNF to cement-based pastes. The relevance of that is applicable not only to the deleterious effects of sulphate attack, but also to the corrosion of steel bars in concrete.

The pH expresses the acidity and the basicity of a solution on a negative logarithm scale ranging from 0 to 14 of the H^+ concentration [Grubb et al., 2007]. Low concentrations of H^+ leads to high pH, so as alkalinity, and vice-versa. The pH equal to 7 is neutral. There are several methods to measure the pH of fluids, though the access to the solution contained in the pore structure of hardened cementitious materials is a challenging task. Behnood, Van Tittelboom, and De Belie [2016] categorized the extraction techniques of pore solution as destructive methods and non-destructive methods. These authors indicated the expression method, the in-situ leaching and the ex-situ leaching techniques as the most usual destructive methods. And among the non-destructive methods, the embedded potentiometric electrodes and the optic fibre sensors. Behnood et al. [2016] and Manso Blanco et al. [2017] described, in detail, all these methods and discussed about the advantages and the drawbacks of each one.

The methodology to measure the pH of CNF-cement pastes was largely based on the ex-situ leaching techniques. In short, this technique determines the pH in a given quantity of powder in solvent suspension (usually distilled water) after achieves the alkaline equilibrium. The powder sample is obtained by crushing, grinding and sieving the hardened cementitious material to a specific particle size range. The ex-situ leaching methods are widely used to evaluate the pH of soils and the chloride content of concrete [Behnood et al., 2016].

6.4.3.2. Experimental Procedure

CNF #0.13 and CNF #1.13 were used in the preparation of GU cement-based pastes. The range of CNF loadings, the mix design criteria and the mixing procedure of these paste mixtures are defined in Section 3.4 of the thesis. In this Section, Table 3.10 lists the mix proportions, once again.

One cylinder per mixture was cast, demolded and 28-day moist cured as depicted in Section 6.2.1 of the thesis. These cylinders had the sides painted with epoxy resin of low viscosity and after that submerged in (5 wt.%) Na_2SO_4 solution for additional 12 weeks, in order to allow only unidirectional penetration of SO_4^{2-} through the cylinders ends. The procedure for the 10-mm slice

cutting, the removal of the 2-mm carbonated outer layer of the cut slices by sandpapering and the 20-g sample grinding are reported and illustrated in Section 6.4.1.2. About 5 g of ground sample passing through sieve mesh opening 150 μm and retained in sieve mesh 74 μm were collected. And immediately after, immersed in distilled water Type I as per ASTM D1193 [ASTM, 2006] at a liquid-to-solid rate of 5 (mL/g). The particles dispersed in distilled water were subsequently stirred at 650 r.p.m. for 15 minutes and then, left resting for 60 minutes at room temperature, that is, $22 \pm 1^\circ\text{C}$. At end of this soaking period, the solid parcel of the dispersion was removed with a quantitative filter paper grade Q2 and ultimately, the pH determined in at least 15 mL of the filtrate. Figure 6.27 shows many of the aforementioned sample preparation steps.

Two devices were used to acquire the pH readings: (i) an *Accumet*[®] basic pH-meter AB15, and (ii) a pH-indicator strips (non-bleeding) with a pH scale running from ‘0’ to ‘14’ and resolution of ‘1’. Figure 6.28 exhibits both pH apparatus. Ten readings of the stable values of pH were recorded using the pH-meter. And at the end of that, one more measurement of the pH was accomplished with the pH-indicator strips.

The method described herein for measuring pH of cement pastes was developed principally on the basis of the findings of Grubb et al. [2007]. These authors studied a variety of testing parameters, such as dilution rate, sample gradation, sample amount, soaking period and temperature.



Figure 6.27 Sample preparation for pH analysis: (a) grinding; (b) stirring the powder dispersed in distilled water; (c) soaking period; and (g) filtrating the solid part of the dispersion.



Figure 6.28.(a) pH-meter (and the pH-indicator strips). (b) Probe sensor of pH-meter inserted in the filtrated to measure the pH. (c) pH-indicator strips immersed in the filtered. (d) Measurement of pH by matching the colours of the indicator strip with the shades in the colour chart.

6.4.3.3. Results and Discussion

The pH values of the CNF-cement mixtures are tabulated in Figure 6.29. Based on the Figure, the steady value of 12 obtained for all mixtures using the pH-indicator strips reflected the lower accuracy of this device compared with the pH-meter values. Hence, pH-paper strips readings were discarded to evaluate the effect of CNF in the PH of paste mixtures. Bearing this in mind, Figure 6.29 demonstrated that the pH of CNF #1.13-cement pastes oscillated around 12.7-12.77, which

is slightly superior to the control paste, 12.69. The pH values of CNF #0.13-cement mixtures varied from 12.58-12.66, close to the control paste. These results evidenced that CNF loadings did not affect meaningfully the pH of pore solution in cement pastes.

Skalny et al. [2001] pointed out that the concomitant decrease in the alkalinity of pore solution and the $Ca(OH)_2$ content in cement pastes may indicate a potential sulphate-induced expansion. However, the set of data acquired so far addressed to a different cause than the one suggested by Skalny et al. [2001]. In spite of the small decrease in the $Ca(OH)_2$ content shown in Section 6.4.2.3, the ettringite content was downsized in cement pastes with CNF loadings, as depicted in Section 6.4.1.3. This resulted in the enhanced behaviour of CNF mortars under sulphate attack, as disclosed in Sections 6.2.2 and 6.3.2. Moreover, CNF shows itself ineffective in changing the pH of the liquid phase in capillary pores of cement pastes. Therefore, CNF dosages hampered the accessibility of SO_4^{2-} to Ca^{2+} boosting the resistance of cement pastes to ettringite-induced expansion, either by scavenging Ca^{2+} from pore solution or by modifying the pore structure. It worth mentioning once more that the COO^- groups of CNF may react not only with Ca^{2+} [Jiao et al., 2016], but also Na^+ and K^+ [Barneyback Jr et al., 1981; Andersson et al., 1989].

As discussed earlier in this Section, low-pH cement pastes aids to break the protective layer around the steel bars and increment the corrosion mechanism. In view of no effect on the pH of cement paste from CNF, this hypothesis is, for now, put away.

No error bars were plotted in Figure 6.29, since the present dataset was acquired from a single XRD analysis per mixture due to time and cost constraints.

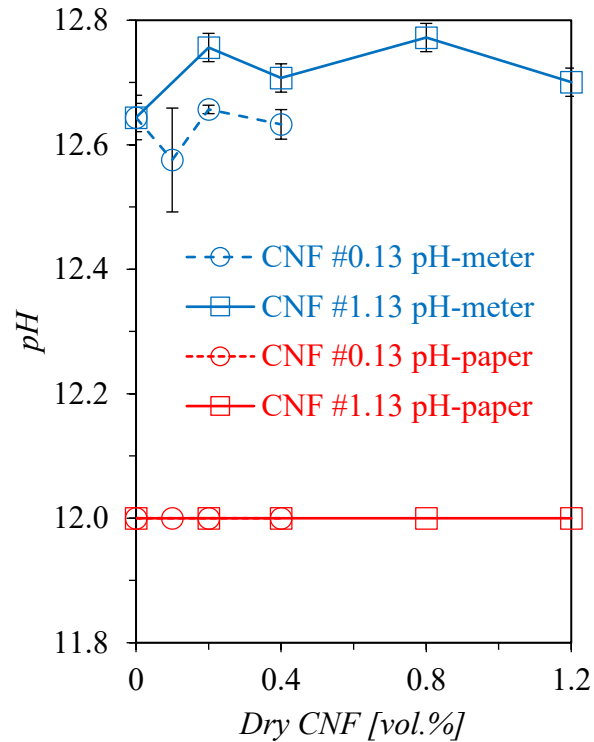


Figure 6.29 Potential of hydrogen (pH) of cement pastes loaded with various dosages of CNF #0.13 and CNF #1.13 measured by ex-situ leaching technique using pH-paper strip and pH-meter.

6.4.4. Compressive Strength Analysis

6.4.4.1. Introduction

The mechanical strength of cement-based systems depends on the pore system and the strength of solid microstructure formed with the progress of cement hydration. Jennings et al. [2002] addressed the strength-porosity relationship of cement pastes to the range of pores between 10 nm and 10 μm ; besides, microcracks and voids in the paste-aggregate interface [Metha et al., 2013]. Calcium silicate hydrate represents 50-60% of the volume of solids in a fully hydrated cement paste [Metha et al., 2013]. And for this reason, it is the most important hydrated compound in the solid phase for mechanical strength.

CNF is a hydrophilic material. This characteristic is strongly associated with the several active hydroxyl and carboxyl groups disposed on CNF's macromolecule, among other factors. These same anionic groups provide chemical reactivity to CNF. Jiao et al. [2016] claimed that the CNF's

active groups and the soluble Ca^{2+} in aqueous phase of cement paste form hydrophilic complex compounds. And for this reason, the precipitation of hydrated products is delayed as well as the setting time. The postponement of the induction period of cement hydration may affect the development of mechanical strength. However, CNF releases water to the adjacent regions at late ages (when the availability of water is scarce), promoting the hydration of unhydrated cement particles and a denser microstructure. Jiao et al. [2016] one found an increase in the mechanical properties of CNF-containing cementitious mixtures provided by a higher degree of hydration. CNF presents some similarities to CNC, as explained in Section 2.4. And Cao et al. [2015] reported an increase in the flexural strength of cement pastes containing CNC in function of the steric stabilization and short circuit diffusion. These phenomena are described in Section 2.4 too. Besides, the mechanical properties of CNF are excellent, as demonstrated in Section 2.5 of this thesis.

The literature review addressing the effect of CNF on the mechanical strength of cement-based system is reported in Section 2.6.3.1. The available literature is divergent in conclusion. Stephenson [2011], Jiao et al. [2016], and Mejdoub et al. [2017] indicated an increase in the compressive strength of cement-based materials dosed with CNF in distinct contents. This increase in the strength varied according to the study. Jiao et al. [2016] and Mejdoub et al. [2017] found the peak strength in cementitious materials containing intermediate CNF contents. These authors imputed the growth in the resistance to a densification of solid microstructure arising from CNF's long-term improvements in the degree of hydration. The drop in the compressive strength was ascribed by Mejdoub et al. [2017] to weaken zones created by CNF agglomeration or inadequate CNF dispersion. In contrast, Landis et al. [2018] and Machado et al. [2017] found that CNF additions decreased the compressive strength of cement mixtures. The nanoscale and the inherent hydrophilicity of CNF were pointed by these authors as the main factors for this reduction.

The literature review of Section 2.2.2 imparts that the sulphate attack provokes the decomposition of cement pastes and respective loss of mechanical properties. This physico-chemical deleterious mechanism is mostly based on the chemical precipitation of expansive compounds, such as ettringite. The Ca^{2+} soluble from the $Ca(OH)_2$ is a key input to form expansive ettringite. As evidenced in Section 6.4.2.3, adding CNF #0.13 slightly downsized the $Ca(OH)_2$ content in

cement pastes. This finding was, therefore, attributed to the CNF capacity to scavenge part of the Ca^{2+} soluble in aqueous phase. Therefore, if growing dosages of CNF gradually mitigated the ingress of sulphate ions and the harmful effects of expansive ettringite on cement pastes, as depicted in Sections 6.2 and 6.3, respectively, it is highly probable that CNF might also attenuate the loss of mechanical strength due to sulphate attack.

6.4.4.2. Experimental Procedure

Four different cement types, GU, HS, HE and GUB, were used in the preparation of mortar mixtures loaded with 0-0.5 vol.% fraction of dry CNF #0.13. The mix-design criteria are detailed in Section 3.3. The mixing procedure and the mix-proportions of these mixtures are listed in Table 3.3, Table 3.4 and Table 3.5. The mortar specimens were tested in compression as per ASTM C109/C109M [ASTM, 2016] at 28 days of moist curing (or zero time of sulphate exposure), and after additional 12 weeks submerged in Na_2SO_4 solution (50 g/L). The specimen exposure to Na_2SO_4 solution followed the recommendations established in ASTM C1012 [ASTM, 2015], which are briefly described in Section 6.3.1.

6.4.4.3. Results and Discussion

Table 3.8 of CHAPTER 3 disclosed the 28-day moist-cured axial compressive strength of specimens prepared with cement mortars dosed with various CNF loadings. These results are replotted in Figure 6.30.(a). As seen in this graph, adding increments of CNF #0.13 to mortar mixtures very slightly decreased the compressive stress, independently of the cement type used. A marginal increase in the strength is noted for CNF #0.13 additions beyond 0.3 vol.%, but the values remain lower than that of the control mortar. This growth must be related to the increase in the compacting energy necessary to cast the mortar specimens, which flowability was out of the acceptable range, as detailed in Section 3.3. It seems that CNF delays the hydration kinetics of cement (because CNF holds a portion of water and the Ca^{2+} at fresh stage, as aforementioned by Jiao et al. [2016]) and as a result, the compressive strength was marginally affected.

The overall behaviour in compression at 28 days roughly agrees with the slight reduction in the degree of hydration occurred in the cement pastes loaded with increasingly amounts of CNF, as demonstrated in Figure 4.6 and Figure 4.7 of CHAPTER 4. And, as well, with the moderate

increase in the 100 nm – 10 µm porosity exhibited in Figure 6.9, despite the drop in the pore volume in the range of 10 nm – 140 nm (see Figure 6.8).

The compressive strength of CNF #0.13 based mortars after 12-week exposure in Na_2SO_4 solution revealed an inverse trend to the foregoing mixtures not exposed to sulphate attack. The compressive stress was moderately enhanced with increments in CNF loadings. The stress at a peak was attained at 0.2 vol.% dry CNF #0.13 – see Figure 6.30.(b). This behaviour was observed in all series, independently of the cement type used.

Figure 6.30.(c) demonstrates the growth rate between the strength of specimens submitted to 12-week sulphate exposure per ‘zero’ exposure. This Figure revealed that the growth rate of HS-cement mixtures containing CNF were higher than those found for GU- and HE-cement mixes. These results were expected, since that HS cement is, among all cements, the one with the highest resistance to sulphate attack. The HS cement possesses a low- C_3A content, which is a fundamental ingredient to form expansive-ettringite. However, the best growth rate was interestingly verified for GUB-cement mixtures containing CNF. Here, this increase is very likely ascribed to a conjunction of factors, that is, the chemical and physical mechanisms provided by CNF to enhance the sulphate resistance associated with the reduced C_3A content in Type GUB cement to react with SO_4^{2-} and the pozzolanic reactions activated by the blends incorporated in this cement at old ages. Beyond 0.2 vol.% dry CNF #0.13, the behaviour of the GU-cement mortars was marked by an initial decline in compression strengths (but the values stayed higher than the control mortar) followed by an increase observed for volume fractions over 0.3% - see Figure 6.30.(b) and Figure 6.30.(c). This drop must be associated with a poor flowability of these mixtures (see Figure 3.8 in CHAPTER 3). Increases in the CNF fraction gradually diminished the amount of free water available to lubricate the solid particles in the fresh mixtures. This phenomenon provoked an increase in the volume of entrapped air incorporated into the mixtures during the mixing stage and for this reason, the strength was reduced. The subsequent growth in the resistance apparently arises from the higher compacting energy demanded for casting the low-workable mortar specimens containing high CNF doses, as also noted earlier for the mixtures not exposed to sulphate – see Figure 6.30.(a).

This overall gain in the compression performance is strongly related to CNF ability to downsize the magnitude of the damages caused by the sulphate attack, as evidenced in Sections 6.2 and 6.3. Jiao et al. [2016] ascribed the enhanced mechanical strength to hydrogen bonds and bridging compounds formed between the CNF's active groups and the cement grains. This improvement reversed the initial trend of force reduction shown by the 28-day moist-cured mixtures.

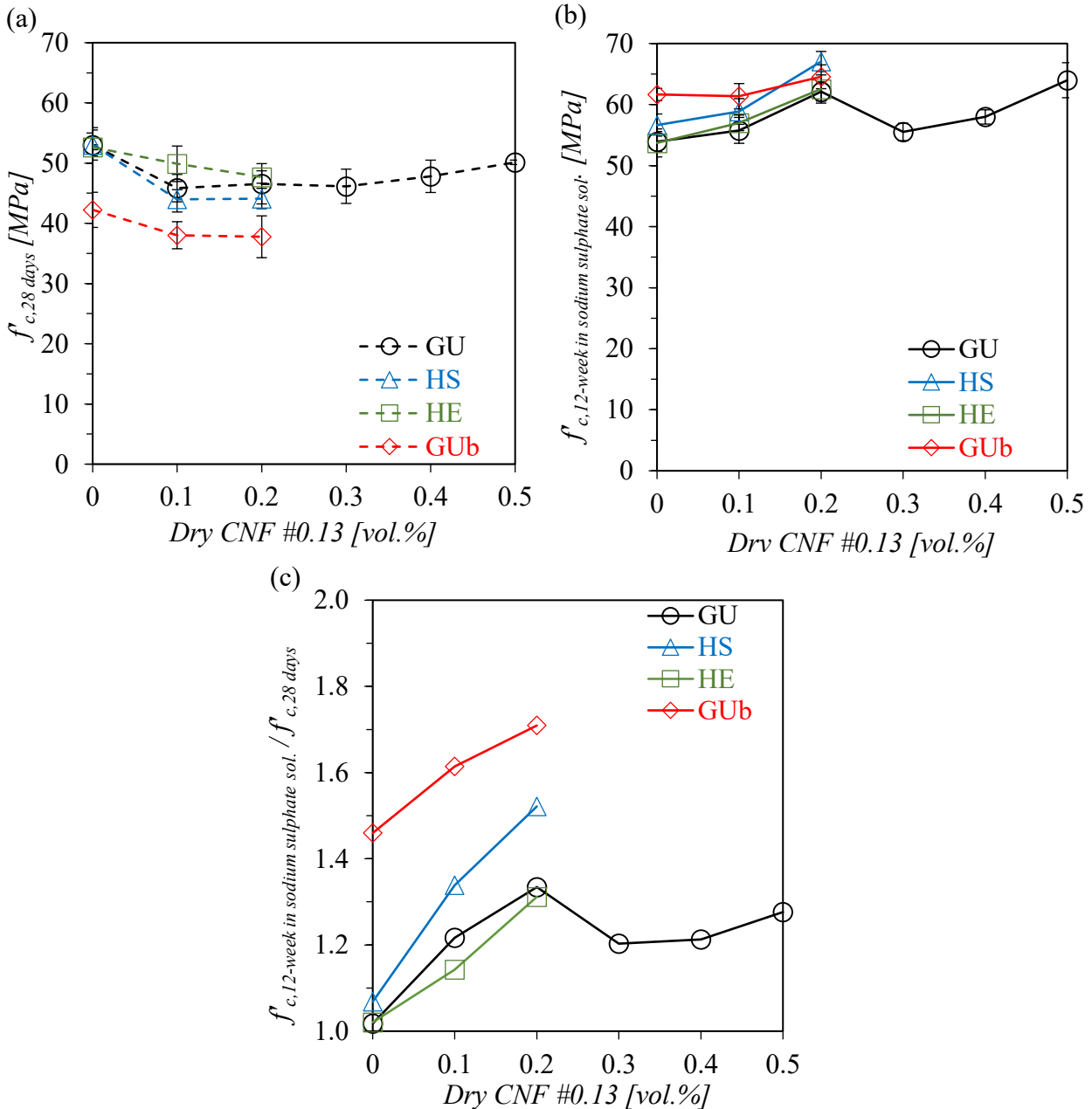


Figure 6.30.(a) Compressive strength at 28 days ($f_{c,28 \text{ days}}$) of mortar specimens prepared with distinct cement types and CNF #0.13 fractions. (b) Compressive strength of these same CNF #0.13-cement mixtures exposed to 12-week Na_2SO_4 solution ($f_{c,12 \text{ weeks in } Na_2SO_4 \text{ sol.}}$). (c) $f_{c,12 \text{ weeks in } Na_2SO_4 \text{ sol.}}/f_{c,28 \text{ days}}$ ratio.

6.5. Concluding Remarks

CNF was added to cement-based materials to address for the first time SO_4^{2-} penetration and subsequent expansion in mortar systems. Using four distinct cements, mortar samples were cast to incorporate up to 0.5% of CNF, by volume. Two CNFs, CNF #0.13 and CNF #1.13, with distinct water retention capacities were used in this study. These mixtures were exposure to sulphate-rich environment (i.e. 5% of Na_2SO_4 per liter of solution) for up to 12 weeks. During this period, the mortar samples were examined periodically to evaluate the SO_4^{2-} penetration and the LC. The compressive strengths of CNF #0.13-based mortars were measured to evaluate CNF as an agent to mitigate the cohesion loss provoked by sulphate attack.

Additional trials to measure the ettringite content, the $Ca(OH)_2$ content, and the pH were undertaken to evaluate the effect of CNF on the alkalinity of cement pastes.

Based on the data obtained in these experiments, besides degree of hydration and porosimetry analysis reported in Sections 4.2 and 4.3, respectively, the following conclusions may be drawn:

- Adding CNF to cementitious systems reduced the SO_4^{2-} penetration. This manifests as a lower SO_4^{2-} concentration at all depths from the exposed surface. This is true for CNF #0.13 and CNF #1.13. Mortars containing up to 0.3 vol.% of CNF #1.13 shown the best performance, whereas above 0.3% loadings, CNF #0.13 mortars. In this regard, an overcompaction during specimen manufacture must have contributed for such outstanding drop in the SO_4^{2-} ingress observed for pastes containing 0.4% and 0.5% of CNF #0.13;
- Upon incorporating CNF, all mixture samples presented a relative steady decrease in the sulphate-induced expansion. With performances very similar to those displayed in the study of SO_4^{2-} ingress. Both CNFs minimized similarly the expansion up to 0.4% loadings, though CNF #1.13 mortars obtained the lowest expansion, when it was dosed up to 1.2% in the cement mortar;
- The higher water retention capacity of CNF #1.13 allowed that a greater amount of CNF is added to cement mortar and in consequence, achieve the best sulphate resistance performance;

- Results show that the CNFs conferred significant sulphate resistance upon cementitious systems. In particular for additions of 0.5% CNF #1.13. With this CNF loading, Portland cement Type GU was seen to display equal or higher resistance to sulphate than Portland cement Type HS, which is specially formulated for this purpose. The same outstanding performance was observed in mortars containing equal to or higher than 0.4% of CNF #0.13, but as observed in the first of the concluding remarks, a specimen overcompaction may have affected the plummet seen in the deleterious effects of sulphate attack. The fly ash contained in Type GUB binder along with CNF additions reduced the ettringite phase (and as a result, the expansion) in mortars. Anyhow, these findings make CNF a replenishable and sustainable admixture to nano-engineer cementitious systems for durability;
- Adding CNF to Portland cement Type GU pastes exposed to 12 weeks in 5 wt.% of Na_2SO_4 solution led to a consistent drop in the amount of ettringite content and a slight reduction in $Ca(OH)_2$ phase, without any change the alkalinity. These findings agree with the aforementioned downsizing trends verified in SO_4^{2-} penetration and expansion of pastes containing growing amounts of CNF. It seems that the introduced TEMPO oxidized COO^- groups on CNF surface lessened the amount of the expansive ettringite phase in cement pastes. Likely, these active groups of CNF chemically trapped the soluble Ca^{2+} in pore solution coming from the $Ca(OH)_2$ phase, mitigating the conversion of Ca^{2+} and SO_4^{2-} into $CaSO_4 \cdot 2H_2O$, which precipitate is an essential input for the ettringite phase formation;
- CNF loading did not enhance the degree of hydration of GU cement pastes. So that, it appears that CNF does not promote the short circuit diffusion as conjectured for CNC in pastes. Nevertheless, a drop in the carbonated phase of hardened cement paste reinforced the likelihood of chemical mitigation of ettringite by CNF. A low availability of soluble Ca^{2+} (due to CNF) minimizes the $CaCO_3$ phase content. Thus, CNF reduced not only the sulphate attack, but also the carbonation of cement pastes. It brings back the hypothesis of CNF scavenging Ca^{2+} from the pore solution of cement pastes, so that not only the $Ca(OH)_2$ phase was mitigated, but also the $CaCO_3$. This idea reinforces even more the fact of the CNF's active groups scavenge Ca^{2+} from aqueous phase. Even with a slight reduction in Ca^{2+} content in pore solution, no change in the alkalinity of cement pastes

was observed with CNF loadings, so that no adverse impact is expected in sulphate attack and in the electrochemical corrosion of steel bars;

- Overall, increments of CNF slightly increased the porosity of GU cement pastes ranging from 100 nm – 10 µm and at the same time, it decreased the pore volume in the range of 10 nm – 140 nm. It seems that CNF hinders the transport of SO_4^{2-} through the pore structure by means of disconnecting the capillary pores and making these pores more tortuous. A pore-size refinement is observed in CNF #0.13 pastes. A nano-filler effect ensues in pastes containing CNF #1.13, which hampers the SO_4^{2-} ingress and subsequent expansion in cement pastes. The amount of entrapped air rose with an increase in the amount of CNF #1.13 in cement paste. Here, the CNF's ability to hold water increased the viscosity of cement paste and simultaneously, impeded the exit of air bubbles incorporated during the mixing operations;
- By and large, the compressive strength of CNF #0.13-based cement mortars exposed to 12 weeks immersed in Na_2SO_4 solution was enhanced. This occurred principally due to CNF capacity to mitigate the harmful expansive effects caused by sulphate attack. However, these same mixtures evidenced a slight reduction trend in the strength at age of 28 days, before the specimens are subjected to sulphate ingress; and
- The pozzolanic activity of fly ash contained in Type GUb cement collaborated with the mitigator mechanisms of CNF to reduce the calcium availability in pore solution and change the pore volume between 10 nm – 140 nm in a more favorable configuration. For this reason, the ettringite-induced expansion was decreased and the compressive strength after a long period of sulphate attack significantly increased in CNF-GUb cement mixtures.

CHAPTER 7. Chloride Penetration in CNF-based Cement Mortars

7.1. Introduction

Helene, Guignone, Vieira, Roncetti, and Moroni [2018] believed that most of the damage seen in reinforced concrete structures are directly related to the corrosion of steel bars. Overall, there are two main reasons for corrosion of steel bars in concrete: chloride attack and/or carbonation. The chloride-induced corrosion is blamed to be the principal cause of corrosion in rebars [Sappakittipakorn et al., 2011]. The sources of chloride ions in concrete may be sometimes internal but mostly external. Their ingress and transport in concrete are controlled by complex mechanisms that involve diffusion, capillary suction, permeation and, convective flow associated with physical adsorption and chemical binding through the coarser part of the pore capillary structure (i.e. greater than 10 nm in diameter) in the progressively microcracking system [Sappakittipakorn et al., 2011; Al-Saleh, 2015; Cao et al., 2019]. Many of these transport mechanisms are identical to those briefly defined for sulphate ion ingress in Section 6.1 of this thesis. The total amount of chlorides can be: (i) physically adsorbed by the calcium silicate hydrate, $C - S - H$, gel; (ii) chemically bound to the calcium aluminate compounds of cement, specifically the tricalcium aluminate, C_3A , and tetra calcium aluminoferrite, C_4AF , forming chloroaluminates, also known as Friedel's salt; and (iii) freely dissolved in pore solution [Angst et al., 2009a; Real, Oliveira, Soares, & Medeiros, 2015]. It worth noting that Type HS cement contains low- C_3A content in order to minimize the sulphate attack. And so, for this same reason, the Type HS cement-based systems are vulnerable to chloride-induced corrosion. Besides, even the bound chlorides may be released into the pore solution depending upon the alkalinity and temperature in concrete. Nevertheless, the main source of chlorides remains the free chlorides in concrete [Real et al., 2015].

Once the free chloride content reaches a critical level around the steel bars, the protective iron oxide film around the rebar is consumed, even if the pH of the pore solution is relatively high, triggering a pitting of electrochemical corrosion [Real et al., 2015]. Several factors can influence this critical value. Alonso, Andrade, Castellote, and Castro [2000] and Angst et al. [2009a] present a detailed review of the critical chloride content measured in field and in the laboratory using different techniques. After the corrosion has begun, the chlorides ions can still accelerate and

spread the corrosion process over many areas of the steel reinforcement [Real et al., 2015], triggering a chain reaction.

Therefore, the chloride ingress and the accompanied rebar corrosion are strongly dependent on the ionic chloride permeability through the capillary pores, typically above 10 nm (so as microcracking) of the concrete cover thickness [Jennings et al., 2002; Metha et al., 2013; Al-Saleh, 2015].

There are several methods to determine the permeation rate of chloride ions in cementitious materials, each one with its advantages and its setbacks. They can be categorized in indirect methods and direct methods. Indirect indicators are the water-to-cement rate, cement composition and compressive strength. By measuring these properties, it is possible to infer the chloride ingress rate. The direct methods are derived from electrical migration or on gravitational permeation. One popular example of the former group of test methods is the electrical indication of concrete to resist the ionic penetration of chloride as per ASTM C1202 [ASTM International (ASTM), 2012], also known as rapid chloride-ion permeability test (RCPT). According to Al-Saleh [2015], this method developed by Whiting [1981] is, nowadays, a standardized method by AASHTO T277 [American Association of State Highway and Transportation Officials (AASHTO), 2015] and ASTM C1202 [ASTM, 2012]. Stanish, Hooton, and Thomas [2001] note the term ‘permeability’ in RCPT is inaccurate, given that the measurements in the method are related to the ionic movement of all ions, and not just the chloride ions. Among the methods in which chloride penetrates more naturally, the most common measurement the resistance of concrete to chloride ion penetration according to ASTM C1543 [ASTM, 2010], which is commonly referred in the literature as ‘salt ponding test’. Stanish et al. [2001] observed that the RCPT is a short-term experiment, but with a low correlation with the gravitational methods; while the ‘salt ponding test’ represents better the real penetrability of chlorides ions in concrete, even though it is a time-consuming test. In order to improve the situation, Kim, Yang, and Yi [2013] proposed the application of colorimetric methods in association with these more representative methods. These are rapid, easy, and less expensive alternatives [Kim et al., 2013]. The silver nitrate-based, $AgNO_3$, colorimetric method is often used in the field to qualitatively measure the chloride ion penetration front in concrete. In this method, an aqueous $AgNO_3$ at a certain concentration solution is sprayed on a newly fracture surface of

concrete and then the chloride ion depth is identified through analyzing the boundaries between the white and brown areas [Kim et al., 2013]. In order to highlight the color difference and to facilitate the identification of the interface between these two areas, the silver nitrate method is associated with other solutions, such as fluorescein, $C_{20}H_{12}O_6$, solution and or potassium chromate, K_2CrO_4 , solution [He, Shi, Yuan, An, & Tong, 2011]. According to Saleh [2015], this method developed in the 1970's by Collepardi, Marcialis, and Turriziani [1972] became a standard, but soon was cancelled without replacement due to low reliability of the results. Real et al. [2015] highlighted that the colorimetric methods may be largely used to assess the penetrability of aggressive elements into concrete with high reliability, such as the phenolphthalein-based colorimetric methods to measure the carbonation depths.

Cellulose nanofibres (CNFs) is a low cost, renewable bio-based nanofibre, naturally found in abundance [Onuaguluchi et al., 2014]. These nanofibrils [Saito et al., 2007; Sun et al., 2015] are covered with plentiful active hydroxyl groups and carboxyl groups [Saito et al., 2007] along with a high aspect ratio [Sun et al., 2015], a high chemical reactivity [Jiao, Su, Chen, Wang, Zhu, & Dai, 2016], ample tunability [Eichhorn, Dufresne, Aranguren, Marcovich, Capadona, Rowan, & Gindl, 2010] and outstanding hydrophilicity [El-Bakkari, Bindiganavile, Goncalves, & Boluk, 2019]. Besides, CNFs also possess excellent mechanical properties [El-Bakkari et al., 2019].

The use of CNF as an additive in cement-based systems is a nascent concept. While reviewing the in Section 2.6 of this thesis, this author found that the majority of the studies have focused on mechanical properties and only a few prior studies address durability issues, specifically shrinkage [Stephenson, 2011; Ferrara et al., 2015; Bindiganavile et al., 2014; Landis et al., 2018].

In this CHAPTER, the ability of CNF in mitigating the chloride ingress in cement mortars is investigated, banking on the nanoscale and hydrophilicity offered by CNF as enumerated above. Based on these features of CNF, it is expected that CNF retains the surplus water added to provide a better resistance to water loss by evaporation of the fresh mixture at early ages and release the water at late ages, when the supply of water is scarce, promoting further hydration of unhydrated cement particles. Recall that there exist some physico-chemical similarities between CNF and cellulose nanocrystal (CNC) – see Table 2.2 in Section 2.4. It is suspected that CNF may promote

hydration through short circuit diffusion, just as CNC. As proposed by Cao et al. [2015], CNC eases the transport of water through a shell of hydrated products that covers the unhydrated cement particles, stimulating additional hydration in hardened cement pastes. These assumptions will likely lead to an increase in the degree of hydration and consequently a reduction in the porosity of cement pastes. If true, both actions will result in a substantially more impervious solid microstructure.

In order to verify such hypothesis, cement paste specimens loaded with various volume fractions of dry CNF were designed, prepared and tested to determine the degree of hydration and the pore size distribution. This is described in Sections 4.2 and 4.3. Two different CNFs were individually added to cement paste mixtures used in the study, CNF #0.13 ranging from 0-0.4 vol.% and CNF #1.13 varying between 0-1.2 vol.%. The larger amount of CNF #1.13 incorporated into the paste is a function of its higher water retention capacity, as explained in Section 3.4 of the thesis.

Another possibility that is examined in this CHAPTER is the lowering of alkalinity in the pore solution of cement paste dosed with CNF. The CNF has active carboxylate ions, COO^- , known for their exceptional hydrophilic nature, which may concomitantly remove the calcium ions from the pore solution. Jiao et al. [2016] claimed that these negatively ionized groups may combine with soluble cations forming hydrogen bonds or bridging compounds with some hydrated products of cement. And as is well known, the removal of these cations will result in a drop in the alkalinity [Andersson et al., 1989]. As mentioned before, a low-alkaline aqueous phase in pore network may damage the passive film around the rebar and as a result, promote the corrosion mechanism, even without the presence of chloride ions. In order to examine this hypothesis, experiments were conducted to measure the calcium hydroxide content and the pH in pore solution of cement pastes containing ranges of 0-0.4 vol.% dry CNF #0.13 and exposed for 12 weeks to sodium sulphate, Na_2SO_4 , solution (50 g/L). More details about the materials, mixtures, and methodology of these experiments can be found in Sections 6.4.2 and 6.4.3.

7.2. Experimental Procedures

7.2.1. Materials, Mix Proportions and Specimens

Recall that the main properties and characteristics of the CNFs, those of Portland cement Type GU and the other raw materials are tabulated, respectively, in Sections 3.2.1, 3.2.2 and 3.2.3.

CNF #0.13 and CNF #1.13, both in water suspension, were separately incorporated in control GU cement mortar in increments of 0.1%, by volume fraction of dry CNF, up to 0.5 vol.%. The control cement mortar met the mix proportion established in ASTM C1012/C1012M [ASTM, 2015], that is, 1 part of cement to 2.75 parts of sand, by mass, and water-cement ratio, by mass, of 0.485. The superplasticizer was added to the mixtures in order to maintain the mortar flow within a specified range of tolerance. Except by the mortar mixtures containing 0.4 vol.% and 0.5 vol.% dry CNF #0.13, which superplasticizer content exceeded the amount recommended by the supplier and, for this reason, developed a smaller workability than all other mixes – see Figure 3.8.(b) and Figure 7.1. The mortar mix design and respective criteria for dosing the CNFs and the superplasticizer are detailed in Section 3.3. In the same Section is found the mixing procedure of these mixtures, as well as their respective mix-proportions, which were reported in Table 3.3. Note that in this Table, CNF is expressed as a volume fraction of the mortar mixtures and as well, by mass in the gel form per 1 m³ of mortar.

Two cylindrical mortar specimens of 100 mm in diameter per 200 mm in height were prepared per mixture and moist cured for an extended time of 56 days in accordance with ASTM C192/C192M [ASTM, 2016]. After curing, a 100 ± 3 mm slice was cut from one cylinder using a water-cooled diamond saw machine, while from other cylinder were sawn two slices of 50 ± 3 mm height. These slices were cut from the central section of the cylinder and its ends discarded, in order to eliminate any effect of bleeding and segregation in the results. The occasional burrs on specimen face ends left after sawing procedure were removed using a belt sander. After 1 hour of drying at room temperature, cut the slices had their sides brushed and then, coated with epoxy resin of low viscosity and fast cure. Note however that the face of the slice ends was kept free of any coating. All these procedures are in accordance with ASTM C1202 [ASTM, 2012]. At the end of this stage, three slices per mixture were made ready for testing further to determine the resistance to chloride

penetration, i.e. two slices with 50 mm height for the RCPT method and subsequently tested by colorimetric method, whilst the one with 100 mm used only for the colorimetric method. Figure 7.2 shows these stages.

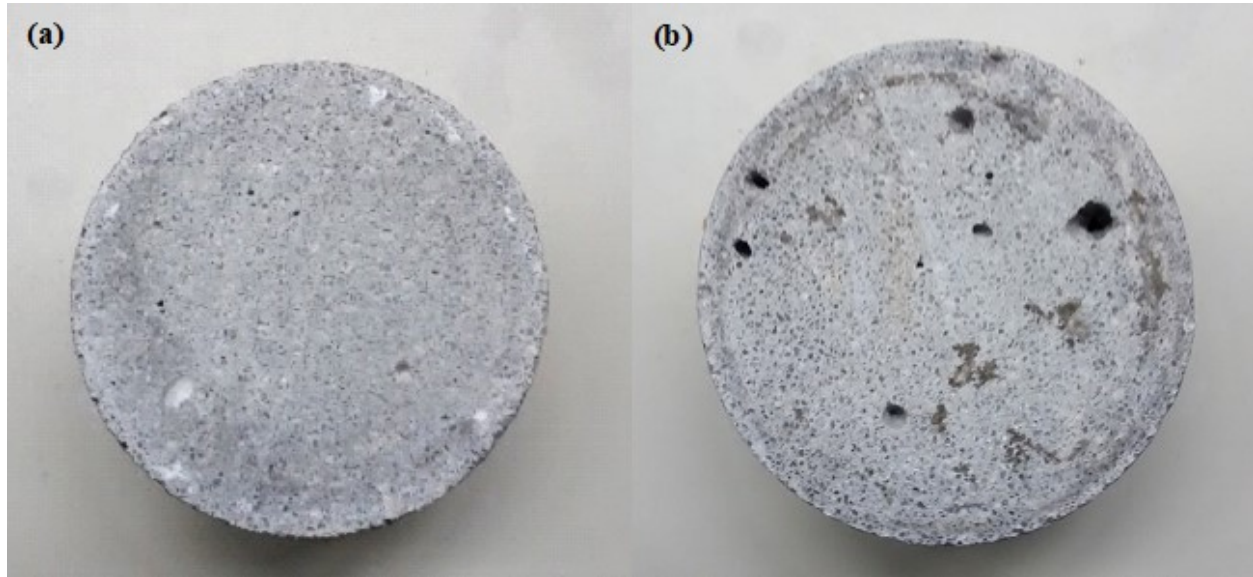


Figure 7.1.(a) Marginal amount of macro entrapped air voids seen in the specimen surface cast with mortar dosed with 0.2 vol.% dry CNF #0.13; and (b) Large number and size of entrapped voids in the mortar slice containing 0.5 vol.% dry CNF #0.13.

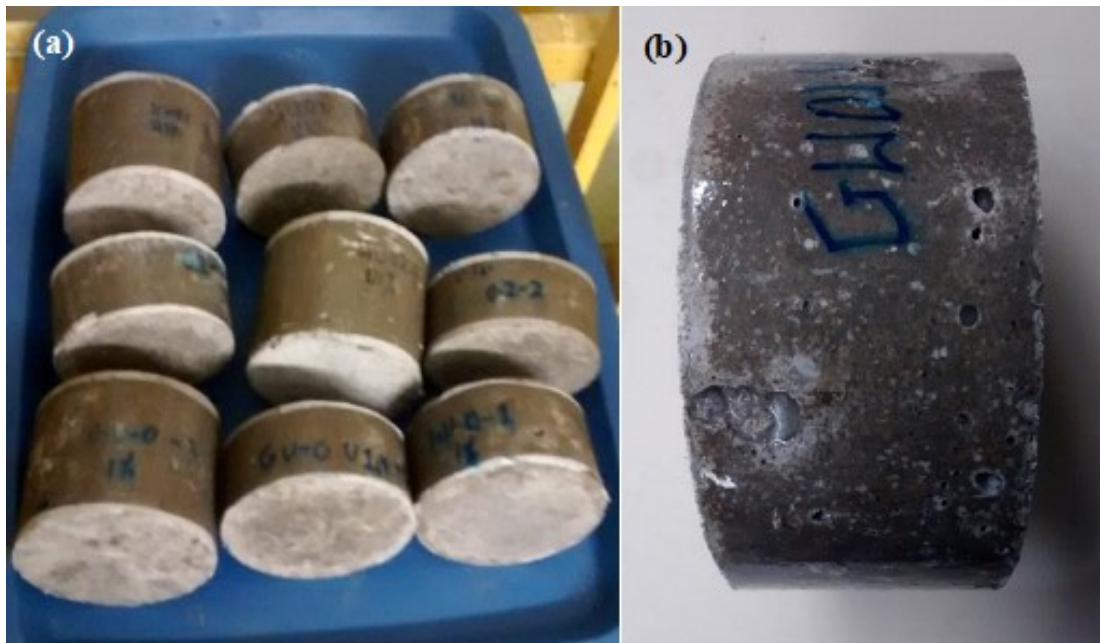


Figure 7.2.(a) Two cut slices with 50 mm height for RCPT and one with 100 mm height for colorimetric method. (b) View in detail of the cut slide sides coated with epoxy resin.

7.2.2. Rapid Chloride-Ion Permeability Method

The RCPT was performed according to ASTM C1202 [ASTM, 2012] to measure the electrical migration of chlorides ions through the specimens prepared with GU cement mortars added with several dosages of CNF, as related in previous Section. The RCPT procedure is described here in brief. After the epoxy-resin was cured, the 50-mm slice was dried at 50 mmHg for 3 hours inside a vacuum desiccator, in order to remove all free water from the capillary pores. Next, the vacuum-dry slices were submerged in de-aerated distilled water with the vacuum pump still running for 1 extra hour, followed by a water soaking period of 18 ± 2 hours. This step intends to fill the permeable capillary pores of the mortar with a water exempted of any kind of ions. Next, the sample slice was placed in two half-acrylic cells with one half filled with 3 wt.% of sodium chloride per liter solution and the other half with 0.3N of sodium hydroxide solution. A constant potential difference of 60 ± 0.1 V was applied to the cell-slice system for 6 hours to promote the electric migration of chlorides ions from the sodium chloride solution through the pore structure of the mortar slice filled with a standard aqueous phase. The electrical current was recorded at the beginning of the trial and at each 30-minute interval over the next 6 hours. The electrical resistance to the chloride diffusion through the mortar slice is expressed in terms of the charge passed in Coulomb (C), as follows:

$$Q = 900(I_0 + 2I_{30} + 2I_{60} + \dots + 2I_{300} + 2I_{330} + I_{360}) \quad (7.1)$$

where ' Q ' [C] is the total electrical charge that crosses the specimen over the 6 hours of testing; and ' I_0 ' [Ampere] and ' I_t ' [Ampere] are, respectively, the electrical current immediately after the voltage is applied and at time ' t ' [minutes] after initial reading. The results were corrected for a standard slice diameter of 95 mm according to the following equation:

$$Q_{95mm} = Q \times (95/x)^2 \quad (7.2)$$

where ' Q_{95mm} ' [C] is the electrical charge passed through the specimen with the standard diameter of 95 mm; and ' x ' [mm] is the actual diameter of the specimen. Figure 7.3 illustrates the experimental scheme.

The apparent coefficient of chloride ion diffusion can be estimated on the basis of the RCPT data – obtained as per ASTM C1202 [ASTM, 2012] – according to the empirical equation developed

by Andrade and Whiting [1996] and by de Medeiros, Gobbi, Groenwold, and Helene [2013], as follows:

$$D_{app} = 0.0103 \times 10^{-8} \times Q^{0.84} \quad (7.3)$$

where ' D_{app} ' [cm^2/s] is the apparent coefficient of chloride ion diffusion, which is equivalent to the total chloride, not only the free chloride.

As soon as the accelerated chloride ion diffusion test ended up, the slice was removed from the half cells and then, performed the $AgNO_3$ -based colorimetric method as detailed in next Section.

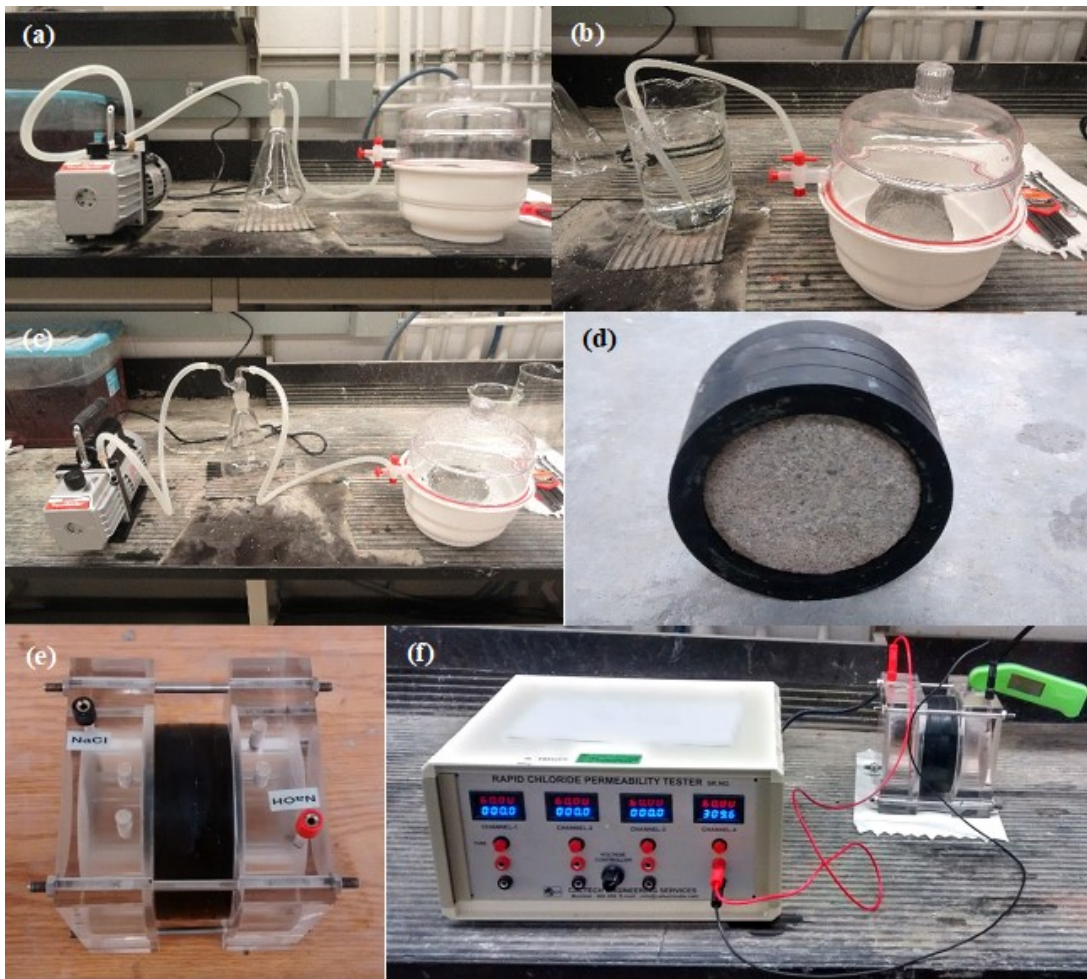


Figure 7.3 Some stages of RCPT: (a) sample drying with a vacuum pump; (b) sample soaking in de-aired distilled water; (c) sample soaking in vacuum; (d) ready-to-test sample in a rubber gasket; (e) specimen in the two half-acrylic cells, one filled with $NaCl$ solution and the other with $Na(OH)$ sol.; and (f) $60 \pm 0.1V$ applied to the solutions in the half-cells, which temperature is continuously monitored by a thermometer.

7.2.3. Silver Nitrate-Based Colorimetric Method

The $AgNO_3$ -based colorimetric method was applied to measure the maximum depth in which the chloride ions can penetrate unidirectionally through the end face of mortar specimens dosed with different fractions of CNF, over 90 days of exposure to a 20-mm height pond of sodium chloride solution, according to a modified ASTM C1543 [ASTM, 2010].

The 100-mm thick mortar slice coated with epoxy on the side according to Section 6.2.1 of the thesis were diked with a plastic wall along the specimen perimeter, in order to retain 20 ± 1 mm high of a ponding solution composed by 3 wt.% of sodium chloride in distilled water. These specimens were stored in an environmental chamber at 20 ± 1 °C and $50 \pm 1\%$ for 90 days. During this period of time, the specimen bottom was exposed to air to allow moisture migration and evaporation of the solution. This procedure, so far, was mostly based on ASTM C1543 [ASTM, 2010] – see Figure 7.4.(a)-Figure 7.4.(d).

At the end of the 90-day storage, the 100-mm mortar slices were split in two halves using a testing machine and then, an aqueous solution of 0.1N $AgNO_3$ was sprinkled to cover the entire broken faces of the specimens. Few minutes later, the free chloride ions in the contaminated area of the specimens will chemically react with the sprayed solution, precipitating a whitish compound of silver chloride, $AgCl$, on the mortar specimen cross-section, whereas the zones rich in free-chlorides zone will become brownish due to the formation of silver oxide, Ag_2O [He et al., 2011; He, Yuan, Chen, & Zheng, 2012; Yuan, Deng, Shi, & De Schutter, 2012; Kim et al., 2013; Real et al., 2015] – see Figure 7.4.(e)-Figure 7.4.(g). Indeed, besides the chlorides, the $AgNO_3$ solution may also combine with other soluble elements commonly dissolved in pore solution of mortar, such as hydroxide, OH^- , and sulphate, SO_4^{2-} ; from the reaction with these two anions will precipitate a brownish silver hydroxide, $AgOH$, compound and a whitish silver sulphate, Ag_2SO_4 , phase, respectively [He et al., 2011].

Usually, the boundary between the contaminated-chloride white zone and the chloride-free brown zone defines the chloride penetration depths. The colour intensity of the precipitates depends on innumerable factors, indulging the cement type, pH of pore solution, contaminants present in the

concrete and concentration of $AgNO_3$ solution. This issue is well-detailed by He et al. [2011], Kim et al. [2013] and Real et al. [2015].

The limit between these two zones is not a uniform line. The free chloride depth [mm] is the area [mm^2] of the whitish zone determined by image analysis of a photography taken at a fixed distance of 250 mm, as illustrated in Figure 7.4.(h) and Figure 7.4.(i), divided by the specimen diameter [mm], i.e. 100 mm. The open source image analysis software ImageJ 1.50i was used to processing the photos.

This same $AgNO_3$ -based colorimetric method was applied to determine the chloride ion depths in the 50-mm thick mortar slices post-RCPT analysis. Besides the preceding image analysis, the chloride depth [mm] was the average of seven depth readings [mm] of contaminated-chloride white zone taken by a 0.01 mm accuracy digital caliper at every 10 mm over the diameter of the specimen cross-section, as proceeded by Real et al. [2015].

The Figure 7.5 shows a schematic representation of both calculation methods.

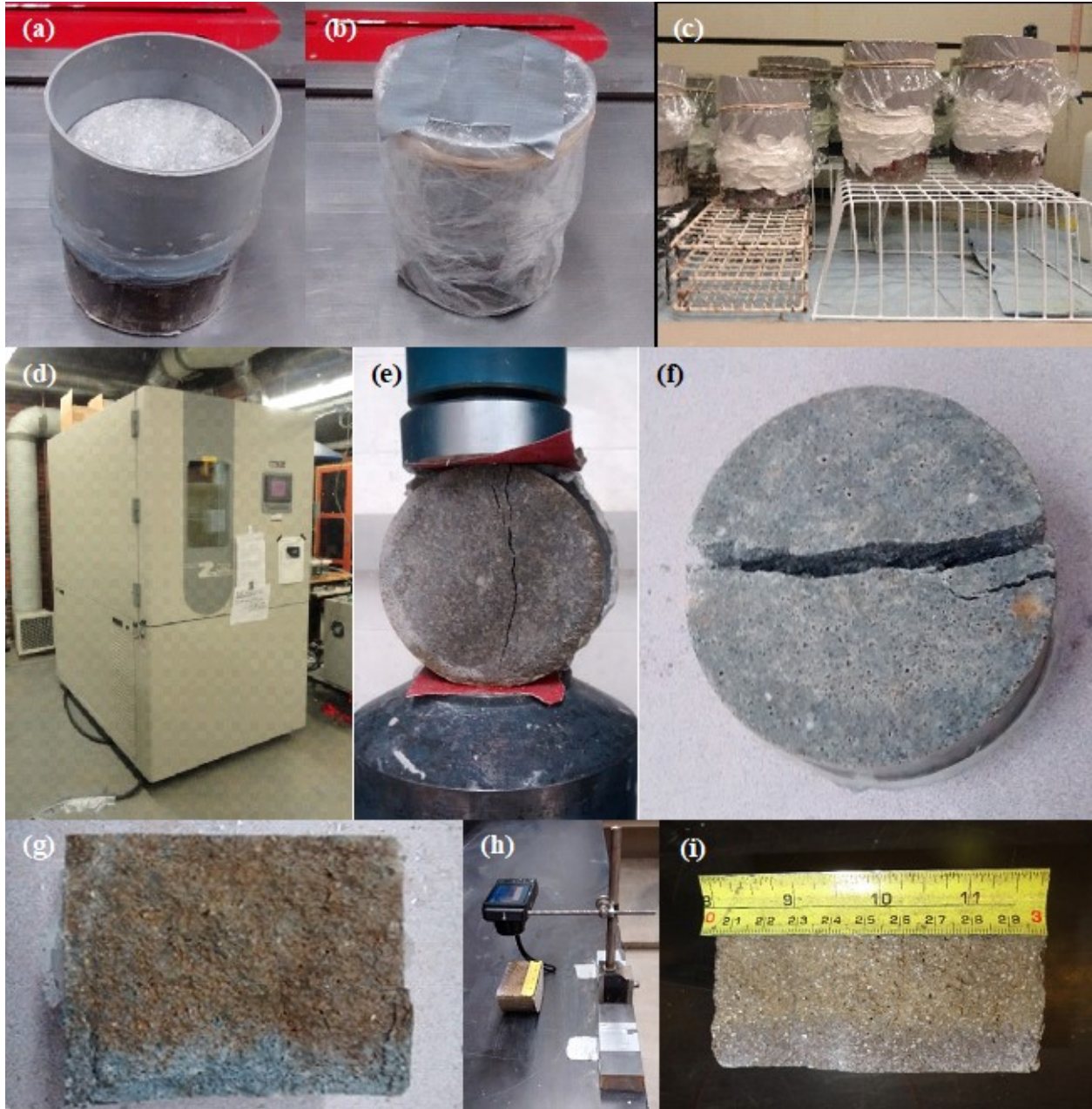


Figure 7.4 Stages of the $AgNO_3$ -based colorimetric method: (a) 100-mm mortar slice diked; (b) specimen top-end covered with wax film to avoid evaporation of the 20-mm height dike of $NaCl$ solution; (c) specimen free bottom face to allow moisture evaporation; (d) environmental chamber; (e) splitting the slice 90-day exposure in $NaCl$ solution; (f) slice split in two halves; (g) fractured surface after spraying $AgNO_3$ solution, showing the chloride-contaminated white zone and the chloride-free brown zone; (h) apparatus to take photos of specimen cross-section; and (i) image used to measure the chloride depth by image analysis.

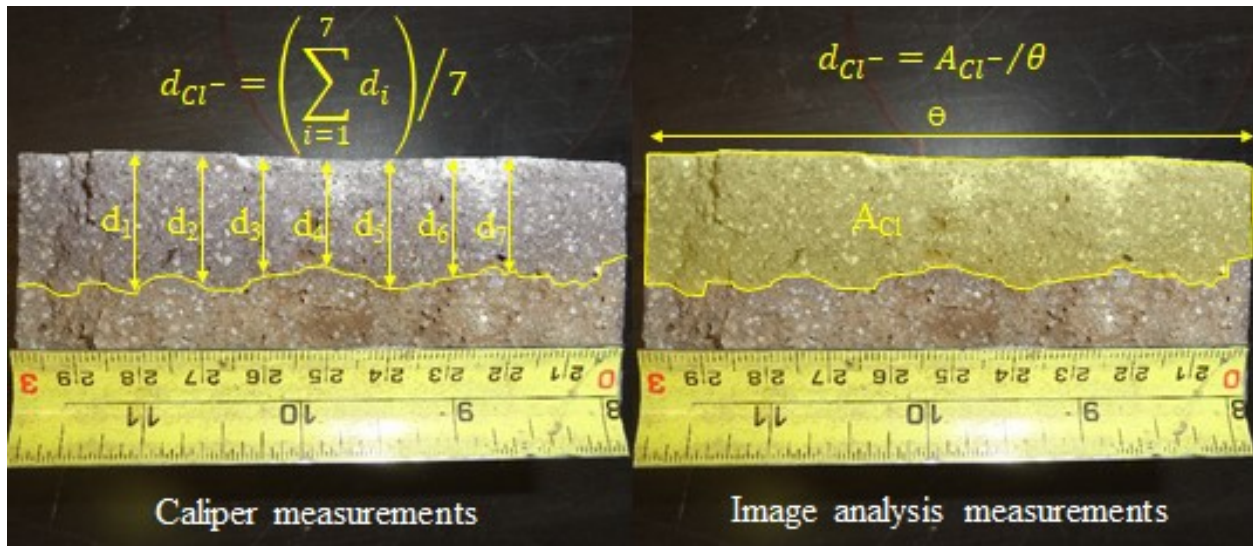


Figure 7.5 Schematic representation of the readings taken from the chloride ion front by the caliper method (left) and the image analysis (right).

7.3. Results and Discussion

Adding increments up to 0.2 vol.% of CNF to cement mortars linearly decreased the electrical charge passed through the cement mortar slices, as illustrated in Figure 7.6.(a). This was valid for all kinds of CNF (CNF #0.13, CNF #0.7 and CNF #1.13). The maximum amount of CNF #0.7 added to the mortar mixes was 0.2%. However, CNF #1.13 and CNF #0.13 were incorporated individually up to 0.5%; notwithstanding the mixtures containing 0.4% and 0.5% of CNF #0.13 demonstrated a significant lower workability than all other mixtures. Above 0.2 vol.%, increasingly doses of CNF #1.13 up to 0.5% caused a progressive decrease in the electrical diffusion of chloride ions, as per the RCPT data. In opposite, CNF #0.13 loadings raised the total charge crossing the specimens in the RCPT.

The post-RCPT specimens containing CNF #1.13 exhibited the same reduction trend for the free chloride depths evaluated by the colorimetric method – see Figure 7.6.(b). The chloride depth data acquired by image analysis displayed a lower standard deviation (as well as values systematically less) than caliper method. For this reason, the image analysis was chosen to quantify the chloride depth by colorimetric method.

The behaviour observed in the free chloride ion penetration measured as per $AgNO_3$ spray method in these two series of CNF-based mixtures was considerably analogous to that displayed by the RCPT, but in a more attenuated manner, as shown, respectively, in Figure 7.7 and Figure 7.6.(a). This is likely because the latter method is based on gravitational penetration of chlorides, while the RPCT is in an accelerated electrical test. In this regard, the colorimetric method revealed roughly similar findings, except by the fact that the CNF #1.13-cement mortars exhibited the best resistance to chloride ingress over the entire dosage range – see Figure 7.7.

Beyond 0.3 vol.%, the chloride penetration begins to increase as is seen in mixtures containing 0.4-0.5 vol.% CNF #0.13. This was found regardless of test methods and is likely due to a poor compaction of the mortar cylinders. The standard energy required by ASTM C1202 [ASTM, 2012] to compact the specimens was insufficient to promote identical densification applied to the other mixtures, given that the low flow shown specifically by these two mixtures – see Figure 3.8 in Section 3.3 of this thesis. And for this reason, the permeability to chlorides ions is worse.

Based on Figure 7.8.(a), the agreement between the measurements as described by Real et al. [2015] using a caliper and by image processing analysis, both on the same specimen, was remarkably good. Similarly, in the present study, the data correlation between the colorimetric method using image analysis and the RCPT, both measured again on the same specimens, was equally in agreement, as demonstrated in Figure 7.8.(b). On the other hand, if the measurements were performed using different methods in distinct specimens, the R-squared of the goodness-of-fit curve was lower than 50%, even if prepared with the very same mortar batch – see Figure 7.8.(c). Therefore, it seems that the specimen preparation caused more effect on the experiment performance than the method by itself.

Metha et al. [2013] showed that the transport of fluid and gases in cement pastes is only possible for capillary pores above 50 nm. Jennings et al. [2002] claimed that the porosity target for evaluating the permeability of cement-based systems purposes is in the range of 10 nm – 10 μ m, as well as the connectivity and the tortuosity of the pore network. Accordingly, the ingress of chloride ions in concrete is a physical process, which is dependent upon the capillary pore network, chiefly on the pore sizes ranging from 10 nm to 10 μ m (not accounting for entrained air, entrapped

air and microcracking) and its connections and sinuosities [Jennings et al., 2002; Metha et al., 2013; Al-Saleh, 2015].

Two analytical methods were used to measure the porosimetry of GU-cement pastes with growing CNF dosage. The pore volume in the range 10 nm – 140 nm determined by gas sorption method is tabulated in Figure 7.9.(a); data compute from the Figure 4.16.(a) in Section 4.3.1.3. And the porosity between 100 nm-10 µm using SEM image analysis shown in Figure 7.9.(b), which data was based on the Figure 4.21.(a) and Figure 4.21.(b) in Section 4.3.2.3 of this thesis. Based on these Figures, the volume of medium capillary pores in cement paste was somewhat reduced with the addition of CNF, while the porosity of large capillary pores up to 10 µm increased, as well. One likely reason for that was the densification of the capillary pore structure ranging from 10 nm – 140 nm in the cement paste around the nanofibres by the active carboxyl and hydroxyl groups on CNF surface; the CNF presents on average 10 nm in width and few microns long. For this reason, the ingress and movement of chloride ions through this range of pore sizes was to some extent hampered, just as it occurred with sulphate ions – see Section 6.2.2.

This finding agrees with the ineffective performance of CNF loadings in enhancing the degree of hydration showcased by identical GU cement paste mixtures, as reported in Section 4.2.3 – see Figure 4.6 and Figure 4.7. Thus, the proposition of ‘short-circuit diffusion’ be also attributed to the CNF, as it was for the CNC by Cao et al. [2015], seems not to be feasible or only applicable for large capillary pores. Nevertheless, as shown in the literature review depicted in Section 2.6.5, many authors [Onuaguluchi et al., 2014; Sun et al., 2015; Jiao et al., 2016; Mejdoub et al., 2017] found enhancements to variable degree in the progress of hydration in cement-based systems dosed with CNF loadings.

Despite that, adding CNF slowed down the penetrability and the mobility of chloride ions into and inside the GU cement mortars containing CNF fractions, likely by a reduction in the apparent chloride diffusion coefficient and/or fluid flow through the medium capillary pore structure. Figure 7.10 displays the scaling-down in the apparent coefficient of chloride diffusion calculated for all mortar mixtures based on the RCPT data. Once again, the exceptions were the mortars loaded with 0.4 vol.% and 0.5 vol.% dry CNF #0.13, for reasons of poor as mentioned above.

Accordingly, a more favourable arrangement of the pore structure in terms of impermeability may be attained through disconnecting the voids and/or making them more tortuous, as occurs in cement-based systems containing cellulose macro- and microfibrils [Banthia et al., 2012b]. Another factor to be considered, although to a lesser extent due to CNF's low-content in the mixtures, is that the nano-sized microfibrils of CNF occupy the nanoscale capillary voids, inhibiting the fluid passage through the pore network in a 'nanofiller effect'. This occurs in a manner similar to the phenomenon induced by silica fume in cementitious materials. Banthia et al. [2012b] found that cellulose fibres loadings of 0.1-0.3 vol.% make cement pastes less permeable to aqueous phase though disabling the connection among the pore structure. According to Metha et al. [2013], very finer particles may also block the link among the capillary pores by filling the voids. Sappakittipakorn et al. [2011] found a decrease in the coefficient of free chloride diffusion in concretes containing up to 0.3% cellulose fibres, by volume fraction, which was responsible to delay the corrosion mechanism. And more importantly, these prior studies also ascribed such behaviour to a possible chloride binding capacity of cellulose fibres, which will inhibit the movement of chloride ions in concrete.

Figure 6.25.(b) and Figure 6.26, shown in Section 6.4.2.3, discloses that increasing amounts of CNF #1.13 resulted in a gradual decrease in the calcium hydroxide phase of GU-cement pastes. The same trend was observed in the paste mixtures dosed with CNF #0.13 loadings, although to a lesser extent. This reduction may be associated with the ability of the active anionic groups located on the CNF surface to combine with the soluble calcium cations coming from calcium hydroxide as discussed in Section 6.1. The calcium loss may drop the alkalinity in the aqueous phase of CNF-based cement mixtures up to critical levels, in which the breakdown of the protective layer against corrosion of the embedded steel bars occurs [Silva, 2013]. Thus, the CNF can potentiate the corrosion mechanism, in spite of hindering the transport of chloride ions. However, Figure 6.29 in Section 6.4.3.3 revealed that the alkalinity of GU cement pastes with various CNF fractions maintained steady, despite the slight decrease in the calcium hydroxide phase. Therefore, as discussed in Section 6.4.3, clearly, adding CNF in cement pastes will not trigger the rebar corrosion due to low pH of pore solution.

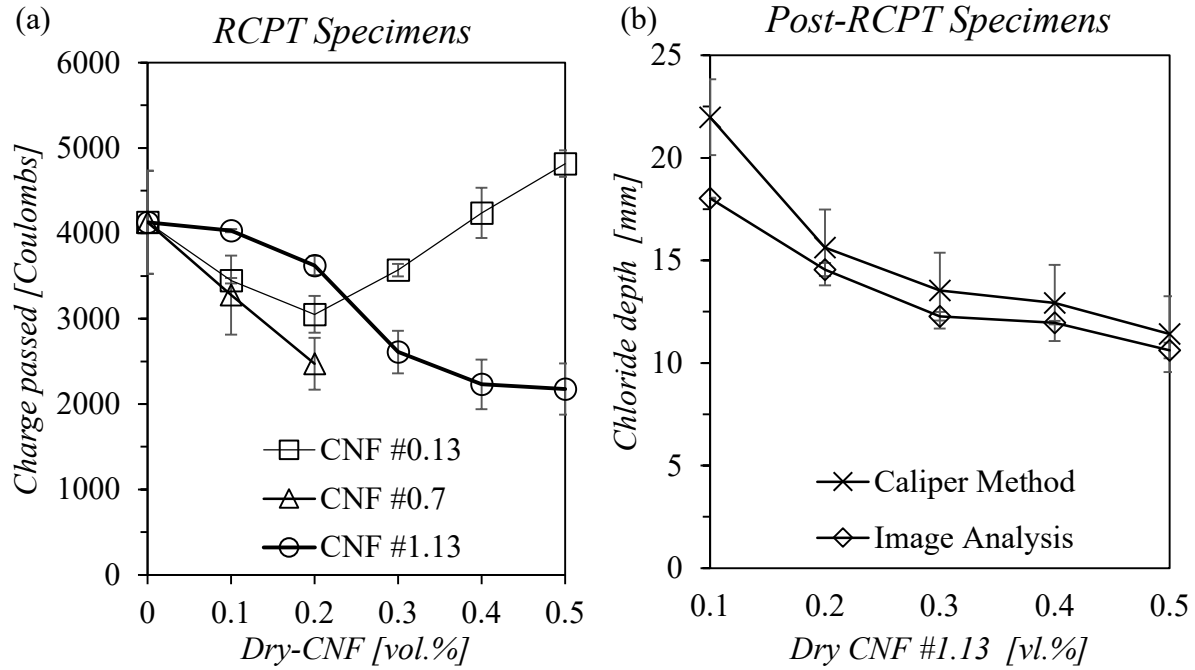


Figure 7.6.(a) Electrical resistance to chloride ion ingress (RCPT) in mortars dosed with various CNF fractions and CNF types. (b) Free chloride depths of CNF #1.13-based mortars measured by $AgNO_3$ -based colorimetric method in post-RCPT specimens.

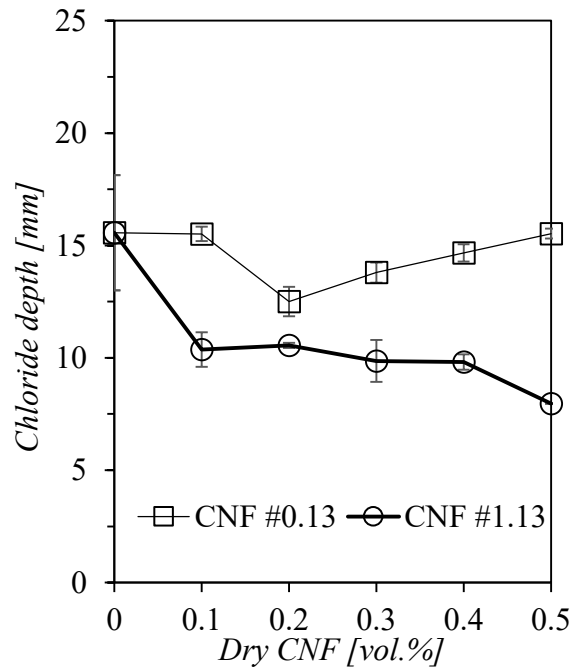


Figure 7.7 Free-chloride depth in mortars dosed with various CNF fractions as per $AgNO_3$ -based colorimetric method.

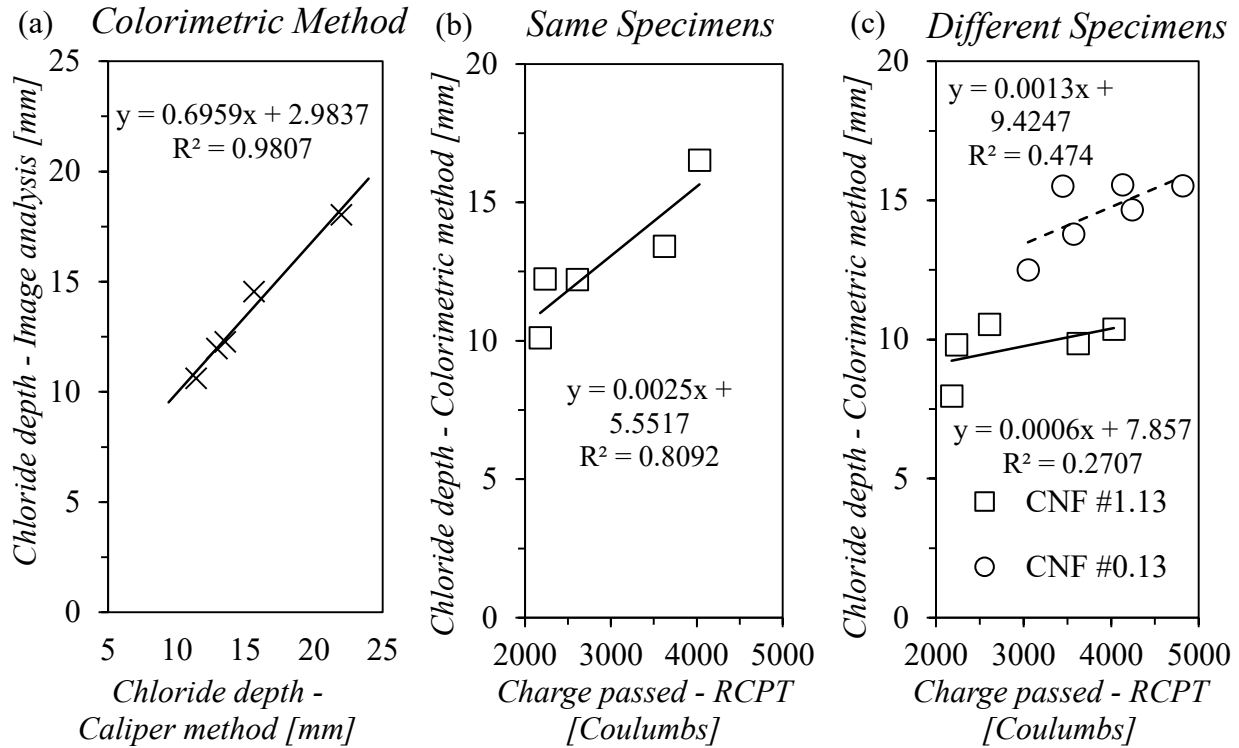


Figure 7.8 Agreement between (a) the data based on the two colorimetric methods: image analysis and caliper method. Comparison between the data acquired by RCPT and colorimetric method in (b) the same specimen, and (c) different specimens.

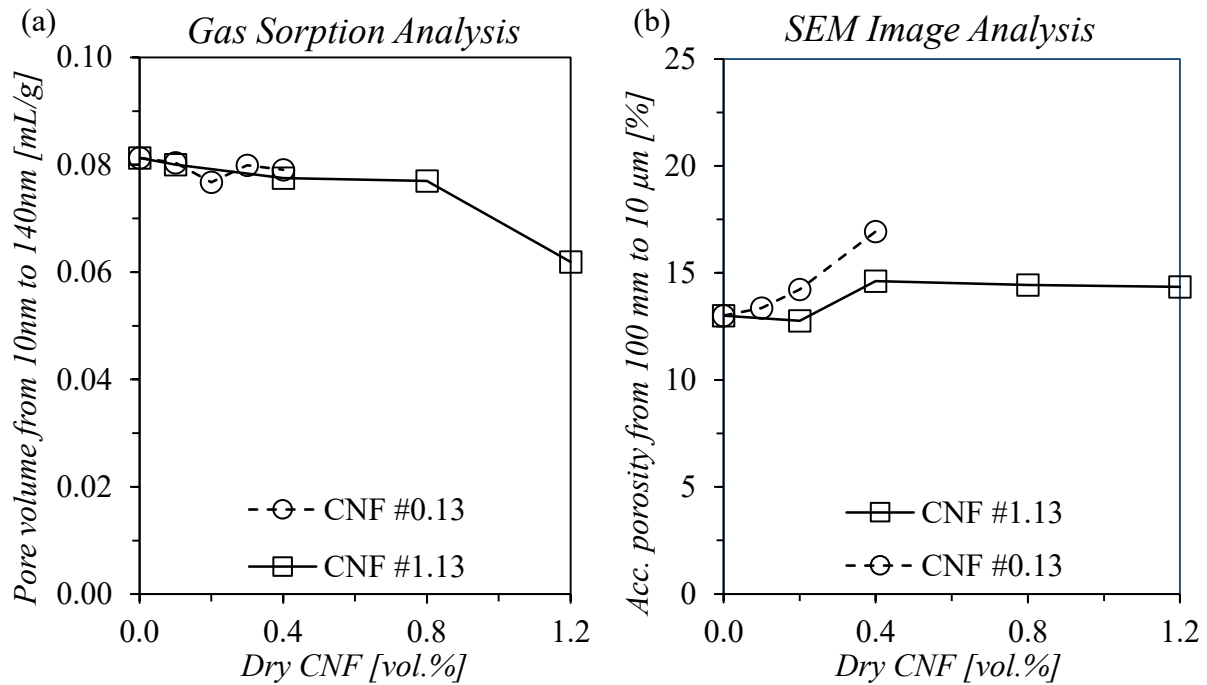


Figure 7.9 Porosity of cement pastes containing various CNF fractions measured by (a) gas sorption analysis in the 10 nm – 140 nm range, and (b) SEM image analysis in the 100 nm – 10 μm range.

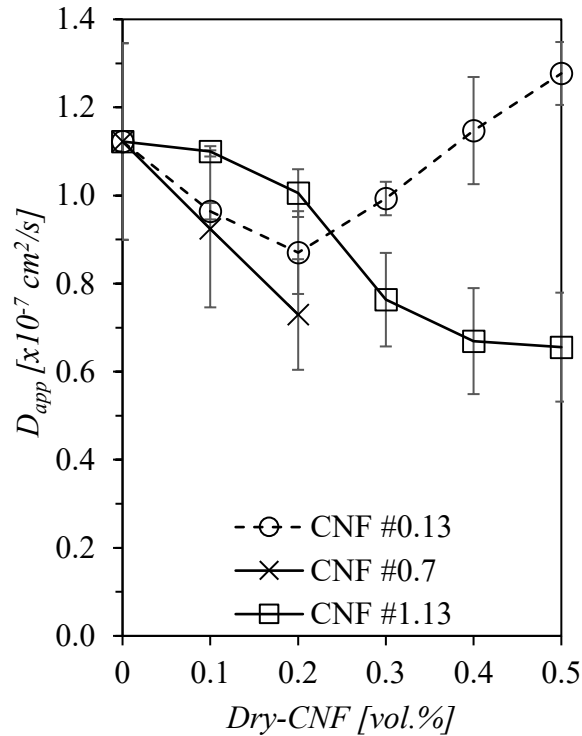


Figure 7.10 Apparent coefficient of chloride diffusion (D_{app}) of cement mortars as affected by CNF additions and types.

7.4. Concluding Remarks

Three different CNFs with varying carboxyl group content (CNF #0.13, CNF #0.7, and CNF #1.13) were added to GU cement mortars in various fractions in order to examine the effect of CNF on the transport of chloride ions using the RCPT. In addition, the resistance of CNF-based cement mortars to the penetrability of chloride was evaluated by a colorimetric method, which is based on spraying 0.1 N $AgNO_3$ solution on the fractured surfaces of the specimens. Only CNF #0.13 and CNF #1.13 were added to cement mortars and examined through colorimetry. The examination of the effect of CNF additions on the calcium hydroxide content and the pH analysis of GU cement pastes dosed with distinct CNF loadings were performed as described in Sections 6.4.2 and 6.4.3, respectively. This data associated with the experimental investigation of degree of hydration and porosimetry analysis of CNF-based cement pastes (both disclosed, respectively, in Sections 4.2 and 4.3 of CHAPTER 4) imparted the key findings summarized as follows:

- CNF addition slowed down the gravitational ingress and the electrical transport of chloride ions into cement mortars. The enhanced performance was evident from the RCPT test and

again, repeated in the $AgNO_3$ -based colorimetric methods. This statement is valid for addition of all three types of CNF, except for dosages of 0.4 vol.% and 0.5 vol.% of CNF #0.13. The low-performance developed by these two mixtures, in specific, rely on the considerable number of voids entrapped into these less-workable fresh mortars during the mixing stage, which were not properly removed by the standard low-energy method of compaction;

- Overall, adding CNF #1.13 high water retention capacity to cement mortars resulted in the best performance among all CNF types and as well, the lowest values of chloride ions transport in cement mortars. This is likely due to its high-water retention, associated with the highest carboxyl group content;
- The enhancement in the capacity of cement mortars to resist to chloride ions transport provided by CNF loadings is likely more associated to a capillary pore network in the range of 10 nm and 140 nm less connected and full of twists and turns than effectively a denser and/or well-hydrated microstructure;
- The RCPT method and the $AgNO_3$ -based colorimetric method demonstrated a high data agreement if the trails were effectuated with the same mortar specimens. Equal scenario was displayed for the two distinct procedures used to measure the contaminated-chloride zone in the $AgNO_3$ -based colorimetric methods; in one procedure the readings of chloride depth were performed by image processing analysis and in the other using a dimensional measuring instrument. However, the data from $AgNO_3$ -based colorimetric method and RCPT portrayed poor correlation. Considering these findings, it seems that the final specimen characteristics impacted on the results of chloride ion penetration more intensely than the experiment method per se, and;
- The rebar corrosion is not affected by adding CNF into cement pastes, despite of a probable decrease in the soluble calcium cation content in pore solution held by the negatively charged carboxyl groups deployed at CNF's surface. The pH of cement pastes maintained unaltered with CNF #0.13 loadings, even with a very slight decrease in the calcium hydroxide, which is the main source of soluble calcium necessary to keep high the pH in pastes.

CHAPTER 8. Conclusions and Recommendations

8.1. Summary of the Findings

The primary targets of this thesis were to examine CNF as an agent to mitigate shrinkage in fresh cement-based pastes, as well as upon sulphate attack and chloride penetration in hardened cement-based mortars. The secondary goals were to evaluate the effect of CNF's anionic groups on the aforementioned durability issues and disclose the interaction between CNF and cement paste. As a result, the following findings can be summarized:

- Adding CNF #1.13 at 0-0.5 vol.% did not affect the overall shrinkage of cement paste, but CNF loadings above 0.1 vol.% of the dry CNF #0.13 did have a negative effect. The drying shrinkage of cement paste was higher with an increase in the volume fraction of CNF for all values of carboxyl groups. However, the pastes containing the CNF with the highest level of carboxylate content, CNF #1.13, once again displayed better performance among all CNF types examined here. The higher contraction of CNF-based cement pastes is associated with an increase in the volume of pores less than 50 nm, i.e. a pore refinement effect. This pore range governs the shrinkage in hardened cement pastes. The hydrophilic nature of CNF made the fresh cement paste more viscous and hence hindered the free water movements toward the surface. It provides a more favourable balance between bleeding and evaporation in cement pastes. However, the higher internal moisture availability kept the calcium silicate hydrate gel particles away from each other. As a result, the solid microstructure became more susceptible to moisture-loss and consequent shrinkage;
- Adding CNF significantly declined the bleeding rate of fresh cement pastes. The evaporation rate of cement pastes containing CNF #1.13 fractions should be at least equal to the control paste, since the water evaporation rate of CNF #1.13 gel was slightly smaller than the mixing water. Both findings suggested to a favorable bleeding-evaporation balance for CNF-based cement pastes and for this reason, to a low plastic shrinkages. However, superplasticizer dosages moderately increased the volume of bleed water and slightly raised the evaporation rate of cement pastes. Accordingly, superplasticizer may have contributed to the growth of plastic and drying shrinkages;
- The resistance of cement mortar mixtures to sulphate attack was uniformly better with increasing dosage of CNF. This was true for the entire range of CNF loadings examined

here across all three levels of carboxyl groups grafting. Adding CNF reduced the depth of ingress and transport of soluble sulphate ions through the capillary pore structure of cement paste. As a result, a smaller sulphate-induced expansion was developed by the cementitious mortars, and this dropped progressively with an increase in the CNF loading. This microstructure most preserved for ettringite expansion led to a moderate increase in compressive strength of CNF #0.13-based cement mortars (mainly up to 0.2%). The present study shows that an increase in the carboxyl groups grafting leads to still lower sulphate ingress and associated expansion. In particular, the amount of ettringite produced in CNF loaded mixtures prepared with Type GU Portland cement was lower than that seen in Type HS cement-based mixtures at the same level of sulphate exposure. The improved resistance under CNF loadings to the sulphate attack of mortars are ascribed both to the physical and the chemical interactions between the CNF and the hydrated products of cement. Contrary to expectation, the CNF did not cause an increase in the degree of hydration. However, adding CNF refined the pore network of cement paste, resulting in a more impervious microstructure. This may be attributed to the hydrophilicity in the CNF, which noticeably dropped the pore volume ranging from 10 nm-10 μ m. Moreover, the CNF's negatively ionized carboxyl groups likely trapped the calcium ions dissolved in the aqueous phase of pore structure of cement pastes. The calcium ions mostly sourced from calcium hydroxide crystals are an essential ingredient in the formation of the ettringite phase, and CNF addition resulted in lower ettringite. Besides, the hindrance to ingress and internal movement of sulphate ions in CNF-based pastes may be associated to the development of disconnections and tortuosities in the capillary pore network likely induced by a nano-filler effect of CNF similar to that provoked by silica fume in cement pastes;

- The chloride penetration in cement mortars was also minimized with increasing fractions of CNF. At both extremes of carboxylate contents namely, CNF #0.13 and CNF #1.13, a progressively high resistance to the penetrability of chloride ions was seen at increasing levels of fibre dosage. Once more, CNF #1.13 led to the lowest values of chloride ion penetration and equally low electrical transport of chlorides ions through the mortar specimens. These improvements to chloride resistance were attributed exclusively to the CNF effectively disconnecting the pore network, and thus extending the path for chloride ions ingress in the cement-based mortars;

- The pH of cement pastes remained unaltered with increments in CNF fractions, despite the CNF's active groups scavenge some calcium ions from aqueous phase and hence drop slightly the calcium hydroxide content. Therefore, it is expected that no rebar corrosion (due to breakdown of the protective passive film) will occur by adding CNF in cement-based systems;
- CNF additions provoked moderate changes in the microstructure of cement pastes. Unexpectedly, CNF loading had little or no effect on the degree of hydration of cement pastes. Therefore, the short circuit diffusion phenomenon (i.e. enhancement of cement hydration) is unlikely to occur in CNF-cement mixtures as conceived for CNC. The capillary porosity in the 100 nm-10 μm range, which it is important to evaluate the permeability to deleterious agents (such as sulphates and chlorides), increased as growing amounts of CNF were added to cement pastes; despite the decrease verified in the range of 10 nm-140 nm. The total volume of small capillary pores and gel pores (less than 140 nm) increased with CNF loadings, as well; a rise in this porosity range grows the drying shrinkage. Overall, CNF induced a pore-size refinement of cement pastes.
- CNF increments dropped the workability of pastes and mortars; the rise in viscosity was visually observed in pastes with growing amounts of CNF. Superplasticizer was added to the CNF-cement mixtures to keep the workability similar to the fresh control mixtures (i.e. without CNF);
- The rise in carboxylate content of CNF allowed the incorporation of higher CNF fractions in pastes and mortars (maintained the flow), as well as the reduction of superplasticizer content. The mortars containing loadings of CNF with the highest carboxylate content, CNF #1.13, displayed better shrinkage behaviour than the low-carboxylate CNF-cement mixtures; despite the best performance showed by the control mortar. The sulphate ingress and the ettringite-induced expansion were minimized with the addition of CNF with increasingly amounts of carboxyl groups. The scenario was verified for the penetration of chloride ions; and
- Apparently, CNF demonstrated a potential micro- and nanofibre reinforcement, as evidenced by the enhanced performance of CNF-based pastes in the cracking analysis and the curling displayed by the slab samples (see Figure 5.7).

8.2. Applications of the Findings

CNF is a relatively new material. The use of CNF gel as an additive in cementitious materials is still more recently. The literature available about the behaviour of cementitious materials containing CNF gel is quite reduced and mostly limited to mechanical properties. Therefore, the practical applications of CNF gel listed in this Section are restricted to the findings acquired in this research. Based on that, CNF gel demonstrated a tendency to extend the durability of concrete or to lessen the destructive effect of some chemical element. Thus, the main application of CNF gel is to enhance the concrete durability. Concrete is one of the most consumed materials by humankind, with an estimated production of 5-7 billion tons per year. If considered only 50% of the total demand of CNF gel dosed from 0.1-1 %, by weight, in concrete, the required consumption of CNF gel may achieve 3-30 million tons per year. Thus, concrete is clearly a large-scale application for CNF gel.

To take advantage of that, CNF gel shall be added to cement-based systems always together with high range water reducers. The CNF gel addition may replace partially or even completely the mixing water initially estimated in the mix design. The ideal CNF gel content to be incorporated into concrete must be in accordance with the aggressiveness of the environment in which concrete is going to be exposed. The concrete guides and correlate national standards disclose an extensive information about the aggressiveness of several environments to concrete. The expected effects on concrete are an enhancement in the lifespan of concrete in service, a more sustainable structural material and a low-cost maintenance material, among others.

The main drawback associated with the large-scale application in concrete is that more than 95 wt.% of the CNF gel is water. This poses two challenges to its large-scale usage. Firstly, the weight and volume of CNF suspension is disproportionately large, making transport to the end user difficult. Secondly, its incorporation is limited by the water-to-binder ratio required by the mix design. Therefore, the following two options must be developed further: (i) a powder version of CNF gel perhaps through spray-drying should be produced for large-scale concrete applications; and/or (ii) a ready-to-use product targeting specific aggressive chemical elements to the concrete durability, such as chloride ions, for small-scale applications. The latter application takes advantage of the high chemical tunability of CNF, whereby predefined chemicals strategically

inserted in the anionic groups of CNF show high affinity to combine with the target elements, such as chlorides ions.

8.3. Recommendations for Further Studies

The macroproperties of fresh and hardened cement-based mixtures studied in this thesis were found affected considerably by CNF loadings. However, many other properties remained only superficially evaluated or even unexplored, because they were peripheral issues to the main goals of the present study. Based on that and on the literature review, the suggestions for further studies are outlined under three different angles: (i) the first, addressing fresh properties of concrete; (ii) the second, to focus on the hardened properties of concrete; and (iii) the third, to expand the fibre efficiency:

- The water retention capacity provided by the anionic carboxylate groups in CNF altered the kinetics of cement hydration as well as the fresh paste rheology. Therefore, it is strongly recommended that the impact of CNF, suitably grafted with anionic groups, upon fresh properties including concrete segregation, the setting time and the plastic shrinkage in the very first 4-8 hours of cement hydration, be examined systematically;
- The nanosized scale, hydrophilic nature and chemical reactivity of the anionic groups of CNF rearranged the pore network of cement-based mixtures in a more impervious configuration. Besides that, CNF potentially scavenged the calcium ions dissolved in the aqueous solution of capillary pores. Through these findings, CNF was able to mitigate the detrimental action of sulphate ions and chlorides ions to concrete integrity. However, there are several other harmful mechanisms. Based on the CNF enhancements, the water permeability of CNF-based cement mixtures should firstly be examined and then, their resistance to aggressive natural or industrial aqueous environments must be investigated, such as those caused by ammonium nitrate and organic acids. Taking advantage of the CNF's ability to combine not only with the calcium ions soluble in the pore solution, but also with the alkalis in general, the damaging mechanisms dependent on these cations, specifically carbonation, alkali-aggregate reaction and electrochemical corrosion of embedded steel bars are likely to be mitigated. These should be explored further;
- The chemical tunability of the anionic groups deployed on CNF surface should be taken advantage of. The microfibrils may be custom-grafted with various chemicals that bear

high affinity with specific pernicious agents that otherwise adversely affect the durability of cement-based systems. A good start would be to develop a product to hold free chloride ions dissolved in the pore solution. Further, CNF drying techniques must be refined to achieve a much drier version of the CNF than used here, without attendant hornification. That will ease the transport and usage of CNF-based products as concrete additives;

- The Type GUb cement may contain different amounts of various types of supplementary cementitious materials, such as fly ash, blast furnace slag or silica fume. Depending on the blends, the low-calcium content in these blended cements and the accompanying pozzolanic activity that converts the calcium hydroxide to calcium silicate hydrate, may drop the alkalinity in the aqueous phase. Low-alkaline pore solutions may induce electrochemical corrosion in the embedded rebar and sulphate attack, as described in CHAPTER 2. For this reason, further examination of the alkalinity, corrosion and sulphate attack in blended Type GUb cement mixtures should be undertaken; and
- Ongoing imaging effort undertaken by the supervisor's group have showcased that innovative emerging techniques can be used to identify, locate and analyze the dispersion of cellulose nanocrystals in the crystalline structure of cement paste. Further studies, therefore, may apply these techniques with the same purpose in CNF-cement pastes.

REFERENCES

- Abe, K., Iwamoto, S., & Yano, H. (2007). Obtaining cellulose nanofibers with a uniform width of 15 nm from wood. *Biomacromolecules*, 8(10), 3276-3278. <https://doi.org/10.1021/bm700624p>.
- Abràmoff, M. D., Magalhães, P. J., & Ram, S. J. (2004). Image processing with ImageJ. *Biophotonics international*, 11(7), 36-42.
- ACI Committee 201. (2016). *Guide to durable concrete. ACI 201.2R-16*. Farmington Hills, MI: American Concrete Institute.
- ACI Committee 222.3. (2011). *Guide to design and construction practices to mitigate corrosion of reinforcement in concrete structures. ACI 222.3 R-11*. Farmington Hills, US: American Concrete Institute.
- ACI Committee 305. (2014). *Specification for hot weather concreting. ACI 305R-14*. Farmington Hills, US: American Concrete Institute.
- ACI Committee 318 (2014). Building code requirements for structural concrete (ACI 318-14) and commentary. Farmington Hills, US: American Concrete Institute.
- Alyaseen, E. H. (2017). *Effects of cellulose nanofibrils on the rheological properties of cement paste*. Master of Science dissertation, University of Maine. Orono, ME, U.S. Retrieved from <https://digitalcommons.library.umaine.edu/etd/2821/>.
- Al-Saleh, S. A. (2015). Analysis of total chloride content in concrete. *Case Studies in Construction Materials*, 3, 78-82. <https://doi.org/10.1016/j.cscm.2015.06.001>.
- Alonso, C., Andrade, C., Castellote, M., & Castro, P. (2000). Chloride threshold values to depassivate reinforcing bars embedded in a standardized OPC mortar. *Cement and Concrete research*, 30(7), 1047-1055. <http://dx.doi.org/10.21041/ra.v5i2.84>.
- American Association of State Highway and Transportation Officials (AASHTO). (2015). *Standard Method of Test for Electrical Indication of Concrete's Ability to Resist Chloride Ion Penetration (AASHTO T277)*.
- American Society of Civil Engineers (ASCE) (2016). The Report Card for America's Infrastructure: Failure to Act: Closing the Infrastructure Investment Gap for America's Economic Future. Economic Development Research Group Virginia, US.

- Andersson, K., Allard, B., Bengtsson, M., & Magnusson, B. (1989). Chemical composition of cement pore solutions. *Cement and Concrete Research*, 19(3), 327-332. [https://doi.org/10.1016/0008-8846\(89\)90022-7](https://doi.org/10.1016/0008-8846(89)90022-7).
- Andrade, C., & Whiting, D. (1996). A comparison of chloride ion diffusion coefficients derived from concentration gradients and non-steady state accelerated ionic migration. *Materials and Structures*, 29(8), 476-484. <http://dx.doi.org/10.21041/ra.v5i2.84>.
- Angst, U., Elsener, B., Larsen, C. K. & Vennesland, Ø. (2009a). Critical chloride content in reinforced concrete - A review. *Cement and Concrete Research*, 39(12) 1122-1138. <https://doi.org/10.1016/j.cemconres.2009.08.006>.
- Angst, U., Vennesland, Ø. & Myrdal, R. (2009b). Diffusion potentials as source of error in electrochemical measurements in concrete. *Materials and Structures*, 42(3) 365-375. <https://doi.org/10.1617/s11527-008-9387-5>.
- Ardanuy, M., Claramunt, J., García-Hortal, J. A., & Barra, M. (2011). Fiber-matrix interactions in cement mortar composites reinforced with cellulosic fibers. *Cellulose*, 18(2), 281-289. <https://doi.org/10.1007/s10570-011-9493-3>.
- Ardanuy, M., Claramunt, J., Arévalo, R., Parés, F., Aracri, E., & Vidal, T. (2012). Nanofibrillated cellulose (NFC) as a potential reinforcement for high performance cement mortar composites. *BioResources*, 7(3), 3883-3894. <http://hdl.handle.net/2117/16392>.
- ASTM international. (2016). *Standard Test Methods for Bulk Density ("Unit Weight") and Voids in Aggregate* (ASTM C29/C29M). Retrieved from <https://compass-astm-org.login.ezproxy.library.ualberta.ca/download/C29C29M.37998.pdf>.
- ASTM international. (2016). *Standard Specification for Concrete Aggregates* (ASTM C33/C33M). Retrieved from <https://compass-astm-org.login.ezproxy.library.ualberta.ca/download/C33C33M.31260.pdf>.
- ASTM international. (2016). *Standard Test Method for Compressive Strength of Hydraulic Cement Mortars (Using 2-in. or [50-mm] Cube Specimens)* (ASTM C109/C109M). Retrieved from <https://compass-astm-org.login.ezproxy.library.ualberta.ca/download/C109C109M.10424.pdf>.
- ASTM International. (2015). *Standard Test Method for Chemical Analysis of Hydraulic Cement* (ASTM C114). Retrieved from <https://compass-astm-org.login.ezproxy.library.ualberta.ca/download/C114.15121.pdf>.

- ASTM international. (2015). *Standard Test Method for Relative Density (Specific Gravity) and Absorption of Fine Aggregate* (ASTM C128). Retrieved from <https://compass-astm-org.login.ezproxy.library.ualberta.ca/download/C128.34811.pdf>.
- ASTM International. (2008). *Standard Test Method for Length Change of Hardened Hydraulic-Cement Mortar and Concrete* (ASTM C157/C157M). Retrieved from <https://compass-astm-org.login.ezproxy.library.ualberta.ca/download/C157C157M.35043.pdf>.
- ASTM International. (2016a). *Standard Practice for Making and Curing Concrete Test Specimens in the Laboratory* (ASTM C192/C192M). Retrieved from <https://compass-astm-org.login.ezproxy.library.ualberta.ca/download/C192C192M-17A.38096.pdf>.
- ASTM International. (2009). *Standard Test Method for Bleeding of Concrete* (ASTM C232/C232M). Retrieved from <https://compass-astm-org.login.ezproxy.library.ualberta.ca/download/C232C232M.19455.pdf>.
- ASTM international. (2014). *Standard Practice for Mechanical Mixing of Hydraulic Cement Pastes and Mortars of Plastic Consistency* (ASTM C305). Retrieved from <https://compass-astm-org.login.ezproxy.library.ualberta.ca/download/C305.23339.pdf>.
- ASTM International (2016). *Standard Test Method for Time of Setting of Concrete Mixtures by Penetration Resistance* (ASTM C403/C403M). Retrieved from <https://compass-astm-org.login.ezproxy.library.ualberta.ca/download/C403C403M.37894.pdf>.
- ASTM International. (2011). *Standard Test Method for Use of Apparatus for the Determination of Length Change of Hardened Cement Paste, Mortar, and Concrete* (ASTM C490/C490M). Retrieved from <https://compass-astm-org.login.ezproxy.library.ualberta.ca/download/C490C490M.5584.pdf>.
- ASTM International (2013). *Standard Specification for Mixing Rooms, Moist Cabinets, Moist Rooms, and Water Storage Tanks Used in the Testing of Hydraulic Cements and Concretes* (ASTM C511). Retrieved from <https://compass-astm-org.login.ezproxy.library.ualberta.ca/download/C511.36153.pdf>.
- ASTM international. (2009). *Standard Test Methods Drying Shrinkage of Mortar Containing Hydraulic Cement* (ASTM C596). Retrieved from <https://compass-astm-org.login.ezproxy.library.ualberta.ca/download/C596.13919.pdf>.

- ASTM international. (2013). *Standard Test Method for Density, Absorption, and Voids in Hardened Concrete* (ASTM C642). Retrieved from <https://compass-astm-org.login.ezproxy.library.ualberta.ca/download/C642.9462.pdf>.
- ASTM international. (2013). *Standard Specification for Standard Sand* (ASTM C778). Retrieved from <https://compass-astm-org.login.ezproxy.library.ualberta.ca/download/C778.28743.pdf>.
- ASTM international. (2016). *Standard Test Method for Flow of Grout for Preplaced-Aggregate Concrete (Flow Cone Method)* (ASTM C939/C939M). Retrieved from <https://compass-astm-org.login.ezproxy.library.ualberta.ca/download/C939C939M.12582.pdf>.
- ASTM international. (2015). *Standard Test Method for Length Change of Hydraulic-Cement Mortars Exposed to a Sulphate Solution* (ASTM C1012/C1012M). Retrieved from <https://compass-astm-org.login.ezproxy.library.ualberta.ca/download/C1012C1012M.16264.pdf>.
- ASTM international. (2017a). *Standard Test Method for Electrical Indication of Concrete's Ability to Resist Chloride Ion Penetration* (ASTM C1202). Retrieved from <https://compass-astm-org.login.ezproxy.library.ualberta.ca/download/C1202.15029.pdf>.
- ASTM international. (2015). *Standard Test Method for Flow of Hydraulic Cement Mortar* (ASTM C1437-15). Retrieved from <https://compass-astm-org.login.ezproxy.library.ualberta.ca/download/C1437.14229.pdf>.
- ASTM international. (2010a). *Standard Test Method for Determining the Penetration of Chloride Ion into Concrete by Ponding* (ASTM C1543). Retrieved from <https://compass-astm-org.login.ezproxy.library.ualberta.ca/download/C1543.31779.pdf>.
- ASTM International. (2006). *Standard Specification for Reagent Water* (ASTM D1193). Retrieved from <https://compass-astm-org.login.ezproxy.library.ualberta.ca/download/D1193.18194.pdf>.
- Autier, C., Azéma, N., & Boustingorry, P. (2014). Using settling behaviour to study mesostructural organization of cement pastes and superplasticizer efficiency. *Colloids and Surfaces A: Physicochemical and Engineering Aspects*, 450, 36-45. <https://doi.org/10.1016/j.colsurfa.2014.02.050>.

- Banthia, N., Moncef, A., Chokri, K., & Sheng, J. (1994). Micro-fiber reinforced cement composites. I. Uniaxial tensile response. *Canadian journal of civil engineering*, 21(6), 999-1011. <https://doi.org/10.1139/194-105>.
- Banthia, N. & Gupta, R. (2006). Influence of polypropylene fiber geometry on plastic shrinkage cracking in concrete. *Cement and Concrete Research*, 36(7) 1263-1267. <https://doi.org/10.1016/j.cemconres.2006.01.010>.
- Banthia, N., & Bhargava, A. (2007a). Permeability of stressed concrete and role of fiber reinforcement. *ACI Materials Journal*, 104(1), 70.
- Banthia, N., & Gupta, R. (2007b). Test method for evaluation of plastic shrinkage cracking in fiber-reinforced cementitious materials. *Experimental Techniques*, 31(6), 44-48. <https://doi.org/10.1111/j.1747-1567.2007.00191.x>.
- Banthia, N., & Gupta, R. (2009). Plastic shrinkage cracking in cementitious repairs and overlays. *Materials and Structures*, 42(5), 567-579. <https://doi.org/10.1617/s11527-008-9403-9>.
- Banthia, N., Bindiganavile, V., Jones, J., & Novak, J. (2012a). Fiber-reinforced concrete in precast concrete applications: Research leads to innovative products. *PCI journal*, 57(3).
- Banthia, N., Sappakittipakorn, M., & Jiang, Z. (2012b). On permeable porosity in bio-inspired fibre reinforced cementitious composites. *International Journal of Sustainable Materials and Structural Systems*, 1(1), 29-41. <https://dx.doi.org/10.1504/ijsmss.2012.050451>.
- Banthia, N., Sappakittipakorn, M., & Jiang, Z. (2012b). On permeable porosity in bio-inspired fibre reinforced cementitious composites. *International Journal of Sustainable Materials and Structural Systems*, 1(1), 29-41.
- Banthia, N., Bindiganavile, V., Azhari, F., & Zanotti, C. (2014). Curling control in concrete slabs using fiber reinforcement. *Journal of Testing and Evaluation*, 42(2), 390-397. <https://doi.org/10.1520/JTE20120111>.
- Barbhuiya, S., Mukherjee, S., & Nikraz, H. (2014). Effects of nano- Al_2O_3 on early-age microstructural properties of cement paste. *Construction and Building Materials*, 52, 189-193. <https://doi.org/10.1016/j.conbuildmat.2013.11.010>.
- Barhoum, A., Li, H., Chen, M., Cheng, L., Yang, W., & Dufresne, A. (2018). Emerging Applications of Cellulose Nanofibers. *Handbook of Nanofibers*, 1-26.

- Barneyback Jr, R. S., & Diamond, S. (1981). Expression and analysis of pore fluids from hardened cement pastes and mortars. *Cement and Concrete Research*, 11(2), 279-285. [https://doi.org/10.1016/0008-8846\(81\)90069-7](https://doi.org/10.1016/0008-8846(81)90069-7).
- BASF Corporation (2018). *MasterGlenium® 3030 Full-Range Water-Reducing Admixture*. v 06/18 v DAT-0055. Retrieved from <https://assets.master-builders-solutions.basf.com/shared%20documents/eb%20construction%20chemcials%20-%20us/admixture%20systems/data%20sheets/masterglenium/basf-masterglenium-3030-tds.pdf>.
- Beaudoin, J. J., & Marchand, J. (2001). Pore structure. In V. S. Ramachandran and J. J. Beaudoin (Eds.), *Handbook of analytical techniques in concrete science and technology: Principles, techniques and applications* (pp. 528-628). Elsevier.
- Behfarnia, K., & Salemi, N. (2013). The effects of nano-silica and nano-alumina on frost resistance of normal concrete. *Construction and Building Materials*, 48, 580-584. <https://doi.org/10.1016/j.conbuildmat.2013.07.088>.
- Behnood, A., Van Tittelboom, K., & De Belie, N. (2016). Methods for measuring pH in concrete: A review. *Construction and Building Materials*, 105, 176-188. <https://doi.org/10.1016/j.conbuildmat.2015.12.032>.
- Berodier, E., Bizzozero, J., & Muller, A. C. (2016). Mercury intrusion porosimetry. In: K. Scrivener, R. Snellings & B. Lothenbach (Eds.), *A practical guide to microstructural analysis of cementitious materials* (pp. 419-442). New York: CRC Press.
- Bertolini, L., & Redaelli, E. (2009). Depassivation of steel reinforcement in case of pitting corrosion: detection techniques for laboratory studies. *Materials and corrosion*, 60(8), 608-616. <https://doi.org/10.1002/maco.200905276>.
- Bindiganavile, V., Boluk, Y., Saha, S. & Mamun, M. (2014). Mitigating shrinkage in concrete structures through cellulose nanomaterials. *Tappi International Conference on Nanotechnology for Renewable Materials*, 30-354.
- Birgisson, B., Taylor, P., Armaghani, J., & Shah, S. P. (2010). American road map for research for nanotechnology-based concrete materials. *Transportation Research Record*, 2142(1), 130-137. <https://doi.org/10.3141/2142-20>.
- Bhalerao, N., Wayal, A. S., Patil, P. G., & Bharimalla, A. K. (2015). A Review on Effect of Nano Cellulose on Concrete. *Int. J. Civ. Struct. Eng. Res. ISSN*, 3(1), 251-254.

- Bhargava, A., & Banthia, N. (2008). Permeability of concrete with fiber reinforcement and service life predictions. *Materials and Structures*, 41(2), 363-372. <https://doi.org/10.1617/s11527-007-9249-6>.
- Bhatty, J. I. (1986). Hydration versus strength in a Portland cement developed from domestic mineral wastes - a comparative study. *Thermochimica acta*, 106, 93-103. [https://doi.org/10.1016/0040-6031\(86\)85120-6](https://doi.org/10.1016/0040-6031(86)85120-6).
- Boghossian, E., & Wegner, L. D. (2008). Use of flax fibres to reduce plastic shrinkage cracking in concrete. *Cement and Concrete Composites*, 30(10), 929-937. <https://doi.org/10.1016/j.cemconcomp.2008.09.003>.
- Boluk, Y., & Danumah, C. (2014). Analysis of cellulose nanocrystal rod lengths by dynamic light scattering and electron microscopy. *Journal of nanoparticle research*, 16(1), 2174. <https://doi.org/10.1007/s11501-013-2174-4>.
- Brandt, S., & Brandt, S. (1999). *Data analysis* (pp. 113-114). New York: Springer.
- Brandt, A. M. (2008). Fibre reinforced cement-based (FRC) composites after over 40 years of development in building and civil engineering. *Composite structures*, 86(1-3), 3-9. <https://doi.org/10.1016/j.compstruct.2008.03.006>.
- Broomfield, J. P. (2003). *Corrosion of steel in concrete: understanding, investigation and repair*. CRC Press.
- Brouwers, H. J. H. (2003). Chemical Reactions in hydrated Ordinary Portland Cement based on the work by Powers and Brownard. *Proceedings 15th Ibausil (Internationale Baustofftagung), Weimar, 1*, 553-566.
- Cao, Y., Zavaterra, P., Youngblood, J., Moon, R., & Weiss, J. (2015). The influence of cellulose nanocrystal additions on the performance of cement paste. *Cement and Concrete Composites*, 56, 73-83. <https://doi.org/10.1016/j.cemconcomp.2014.11.008>.
- Cao, Y., Gehlen, C., Angst, U., Wang, L., Wang, Z., & Yao, Y. (2019). Critical chloride content in reinforced concrete—An updated review considering Chinese experience. *Cement and Concrete Research*, 117, 58-68. <https://doi.org/10.1016/j.cemconres.2018.11.020>.
- Canadian Standards Association. (2013). *Cementitious Materials Compendium (CSA A3000)*. Canadian Standard Association (GSA Group), Mississauga, Ontario. Retrieved from <http://www.scc.ca/en/standardsdb/standards/27226>.

- Choi, S. Y., Park, J. S., & Jung, W. T. (2011). A study on the shrinkage control of fiber reinforced concrete pavement. *Procedia engineering*, *14*, 2815-2822. <https://doi.org/10.1016/j.proeng.2011.07.354>.
- Claramunt Blanes, J., Ardanuy Raso, M., Arévalo Peces, R., Parés Sabatés, F., & Tolêdo Filho, R. D. (2011). Mechanical performance of ductile cement mortar composites reinforced with nanofibrillated cellulose. In *Strain Hardening Cementitious Composites (SHCC2-Rio). Proceedings of the 2nd International RILEM Conference* (pp. 131-138). RILEM Publications. International Union of Laboratories and Experts in Construction Materials, Systems and Structures.
- Cengiz, A., Kaya, M., & Bayramgil, N. P. (2017). Flexural stress enhancement of concrete by incorporation of algal cellulose nanofibers. *Construction and Building Materials*, *149*, 289-295. <https://doi.org/10.1016/j.conbuildmat.2017.05.104>.
- Chang, T. P., Shih, J. Y., Yang, K. M., & Hsiao, T. C. (2007). Material properties of Portland cement paste with nano-montmorillonite. *Journal of materials science*, *42*(17), 7478-7487. <https://doi.org/10.1007/s10853-006-1462-0>.
- Colleparidi, M., Marcialis, A., & Turriziani, R. (1972). Penetration of chloride ions into cement pastes and concretes. *Journal of the American Ceramic Society*, *55*(10), 534-535.
- Colleparidi, M. (2003). A state-of-the-art review on delayed ettringite attack on concrete. *Cement and Concrete Composites*, *25*(4-5), 401-407. [https://doi.org/10.1016/S0958-9465\(02\)00080-X](https://doi.org/10.1016/S0958-9465(02)00080-X).
- Cowie, J., Bilek, E. T., Wegner, T. H., & Shatkin, J. A. (2014). Market projections of cellulose nanomaterial-enabled products--Part 2: Volume estimates. *TAPPI JOURNAL*, *Volume 13 Number 6, 2014*; pp. 57-69., *13*(6), 57-69.
- Czarnecki, L., Broniewski, T., & Henning, O. (1994). Building chemistry. *Arkady, Warszawa*.
- da Costa Correia, V., Santos, S. F., Teixeira, R. S., & Junior, H. S. (2018). Nanofibrillated cellulose and cellulosic pulp for reinforcement of the extruded cement based materials. *Construction and Building Materials*, *160*, 376-384. <https://doi.org/10.1016/j.conbuildmat.2017.11.066>.
- Deboucha, W., Leklou, N., Khelidj, A., & Oudjit, M. N. (2017). Hydration development of mineral additives blended cement using thermogravimetric analysis (TGA): Methodology of calculating the degree of hydration. *Construction and Building Materials*, *146*, 687-701. <https://doi.org/10.1016/j.conbuildmat.2017.04.132>.

- Dequiedt, A. S., Coster, M., Chermant, L., & Chermant, J. L. (2001). Distances between air-voids in concrete by automatic methods. *Cement and Concrete Composites*, 23(2-3), 247-254.
- Diamond, S. (2001). Considerations in image analysis as applied to investigations of the ITZ in concrete. *Cement and Concrete Composites*, 23(2-3), 171-178. [https://doi.org/10.1016/S0958-9465\(00\)00055-X](https://doi.org/10.1016/S0958-9465(00)00055-X).
- Dousti, M. R. (2018). Effect of cellulose nanocrystal particles on rheology, transport and mechanical properties of oil well cement systems (Doctoral dissertation, University of Alberta). Retrieved from <https://era.library.ualberta.ca>.
- Eichhorn, S. J., Dufresne, A., Aranguren, M., Marcovich, N. E., Capadona, J. R., Rowan, S. J., & Gindl, W. (2010). Review: current international research into cellulose nanofibres and nanocomposites. *Journal of materials science*, 45(1), 1-33. <https://doi.org/10.1007/s10853-009-3874-0>.
- El-Bakkari, M., Bindiganavile, V., Goncalves, J., & Boluk, Y. (2019). Preparation of cellulose nanofibers by TEMPO-oxidation of bleached chemi-thermomechanical pulp for cement applications. *Carbohydrate polymers*, 203, 238-245. <https://doi.org/10.1016/j.carbpol.2018.09.036>.
- European Union Commission. (2011). Commission recommendation of 18 October 2011 on the definition of nanomaterial text with EEA relevance (2011/696/EU). *E.U. Commission (Eds.), Brussels, BE*, 2.
- Fagerlund, G. (2009). *Chemically bound water as measure of degree of hydration: method and potential errors*. Lund, Sweden: Division of Building Materials, Lund Institute of Technology.
- Farzadnia, N., Ali, A. A. A., Demirboga, R., & Anwar, M. P. (2013). Effect of halloysite nanoclay on mechanical properties, thermal behavior and microstructure of cement mortars. *Cement and concrete research*, 48, 97-104. <https://doi.org/10.1016/j.cemconres.2013.03.005>.
- Feng, X., Garboczi, E. J., Bentz, D. P., Stutzman, P. E., & Mason, T. O. (2004). Estimation of the degree of hydration of blended cement pastes by a scanning electron microscope point-counting procedure. *Cement and concrete research*, 34(10), 1787-1793. <https://doi.org/10.1016/j.cemconres.2004.01.014>.

- Fernández, M. M. C. (2008). *Effect of particle size on the hydration kinetics and microstructural development of tricalcium silicate* (Doctoral dissertation). PhD thesis No. 4102, Ecole Polytechnique Federale de Lausanne, Switzerland.
- Ferrara, L., Ferreira, S. R., della Torre, M., Krelani, V., de Silva, F. A., & Toledo Filho, R. D. (2015). Effect of cellulose nanopulp on autogenous and drying shrinkage of cement based composites. In *Nanotechnology in Construction* (pp. 325-330). Springer, Cham.
- Folli, A., Pade, C., Hansen, T. B., De Marco, T., & Macphee, D. E. (2012). TiO₂ photocatalysis in cementitious systems: Insights into self-cleaning and depollution chemistry. *Cement and concrete research*, 42(3), 539-548. <https://doi.org/10.1016/j.cemconres.2011.12.001>.
- Franus, W., Panek, R., & Wdowin, M. (2015). SEM investigation of microstructures in hydration products of portland cement. In *2nd International Multidisciplinary Microscopy and Microanalysis Congress* (pp. 105-112). Springer, Cham. https://doi.org/10.1007/978-3-319-16919-4_14.
- Fu, T., Montes, F., Suraneni, P., Youngblood, J., & Weiss, J. (2017). The Influence of Cellulose Nanocrystals on the Hydration and Flexural Strength of Portland Cement Pastes. *Polymers*, 9(9), 424. <https://doi.org/10.3390/polym9090424>.
- Fujisawa, S., Okita, Y., Fukuzumi, H., Saito, T., & Isogai, A. (2011). Preparation and characterization of TEMPO-oxidized cellulose nanofibril films with free carboxyl groups. *Carbohydrate Polymers*, 84(1), 579-583. <https://doi.org/10.1016/j.carbpol.2010.12.029>.
- Fukuzumi, H., Saito, T., Iwata, T., Kumamoto, Y., & Isogai, A. (2008). Transparent and high gas barrier films of cellulose nanofibers prepared by TEMPO-mediated oxidation. *Biomacromolecules*, 10(1), 162-165. <https://doi.org/10.1021/bm801065u>.
- Gao, Y. (2013). *The Production and Characterization of Cellulose Nanofibrils*. Master of Science dissertation. University of Alberta. Edmonton, AB, Canada. Retrieved from <https://search.proquest.com/openview/e86dc1607f8fa421e9645ce1705503da/1?pq-origsite=gscholar&cbl=18750&diss=y>.
- Garboczi, E. (2009). Concrete nanoscience and nanotechnology: Definitions and applications. *Nanotechnology in Construction*, 3, 81–88. https://doi.org/10.1007/978-3-642-00980-8_9.
- Gdoutos, E. E., Konsta-Gdoutos, M. S., Danoglidis, P. A., & Shah, S. P. (2016). Advanced cement based nanocomposites reinforced with MWCNTs and CNFs. *Frontiers of Structural and Civil Engineering*, 10(2), 142-149. <https://doi.org/10.1007/s11709-016-0342-1>.

- Ghosal, M., & Chakraborty, A. K. (2017). Application of Nanomaterials on Cement Mortar and Concrete: A Study. *IUP Journal of Structural Engineering*, 10(1), 7.
- Gong, F., Zhang, D., Sicat, E., & Ueda, T. (2013). Empirical estimation of pore size distribution in cement, mortar, and concrete. *Journal of Materials in Civil Engineering*, 26(7), 04014023.
- Grubb, J. A., Limaye, H. S., & Kakade, A. M. (2007). Testing pH of concrete. *Concrete international*, 29(04), 78-83.
- Halim, J. G., Kusuma, O. C., & Hardjito, D. (2017). Optimizing polycarboxylate based superplasticizer dosage with different cement type. *Procedia engineering*, 171, 752-759. <https://doi.org/10.1016/j.proeng.2017.01.442>.
- Hamad, W. Y. (2017). *Cellulose nanocrystals: properties, production and applications*. Vancouver, Canada: John Wiley & Sons Ltd.
- Hansen, W. (1987). Drying shrinkage mechanisms in Portland cement paste. *Journal of the American Ceramic society*, 70(5), 323-328. <https://doi.org/10.1111/j.1151-2916.1987.tb05002.x>.
- Hashimoto, K., Irie, H., & Fujishima, A. (2005). TiO₂ photocatalysis: a historical overview and future prospects. *Japanese journal of applied physics*, 44(12R), 8269.
- Henriksson, M., & Berglund, L. A. (2007). Structure and properties of cellulose nanocomposite films containing melamine formaldehyde. *Journal of Applied Polymer Science*, 106(4), 2817-2824. <https://doi.org/10.1002/app.26946>.
- Henriksson, M., Berglund, L. A., Isaksson, P., Lindström, T., & Nishino, T. (2008). Cellulose nanopaper structures of high toughness. *Biomacromolecules*, 9(6), 1579-1585. <https://doi.org/10.1021/bm800038n>.
- Heinz, D. & Ludwig, U. (1986) "Mechanisms of subsequent ettringite formation in mortars and concretes after heat treatment", *Proc. 8th Int. Conf. Chem. Cem.*, vol. 5, Rio de Janeiro, p. 189.
- Heinz, D. & Ludwig, U. (1987) "Mechanism of secondary ettringite formation in mortars and concretes subjected to heat treatment", in J.M. Scanlon (ed.) *Concrete Durability: Katherine and Bryant Mather International Conference ACI SP-100*, 2: 2059–2071
- Helene, P. R. (1993). Contribuição ao estudo da corrosão em armaduras de concreto armado. *São Paulo, Brasil 231*, 14.

- Helene, P., Guignone, G., Vieira, G., Roncetti, L., & Moroni, F. (2018). Evaluation of the chloride penetration and the service time of self-healing concretes activated by crystalline additive. *RILEM-IBRACON Structures and Materials Journal*, 11(3) (in Portuguese). <http://dx.doi.org/10.1590/s1983-41952018000300007>.
- He, F., Shi, C., Yuan, Q., An, X., & Tong, B. (2011). Calculation of chloride concentration at color change boundary of AgNO₃ colorimetric measurement. *Cement and Concrete Research*, 41(11), 1095-1103. <https://doi.org/10.1016/j.cemconres.2011.06.008>.
- He, F., Shi, C., Yuan, Q., Chen, C., & Zheng, K. (2012). AgNO₃-based colorimetric methods for measurement of chloride penetration in concrete. *Construction and Building Materials*, 26(1), 1-8. <https://doi.org/10.1016/j.conbuildmat.2011.06.003>.
- Hewlett, P. C. (Ed.) (2003). *Lea's chemistry of cement and concrete*. Elsevier Ltd.
- Hime, W. G., Marusin, S. L., Jugovic, Z. T., Martinek, R. A., Cechner, R. A., & Backus, L. A. (2000). Chemical and petrographic analyses and ASTM test procedures for the study of delayed ettringite formation. *Cement, concrete and aggregates*, 22(2), 160-168. <https://doi.org/10.1520/CCA10476J>.
- Hisseine, O. A., Omran, A. F., & Tagnit-Hamou, A. (2018). Influence of Cellulose Filaments on Cement Paste and Concrete. *Journal of Materials in Civil Engineering*, 30(6), 04018109.
- Hoyos, C. G., Cristia, E., & Vázquez, A. (2013). Effect of cellulose microcrystalline particles on properties of cement based composites. *Materials & Design*, 51, 810-818. <https://doi.org/10.1016/j.matdes.2013.04.060>.
- Isogai, A., Saito, T., & Fukuzumi, H. (2011). TEMPO-oxidized cellulose nanofibers. *Nanoscale*, 3(1), 71-85. <https://doi.org/10.1039/c0nr00583e>.
- Isogai, A. (2018). Development of completely dispersed cellulose nanofibers. *Proceedings of the Japan Academy, Series B*, 94(4), 161-179.
- Iwamoto, S., Kai, W., Isogai, A., & Iwata, T. (2009). Elastic modulus of single cellulose microfibrils from tunicate measured by atomic force microscopy. *Biomacromolecules*, 10(9), 2571-2576. <https://doi.org/10.1021/bm900520n>.
- Iwamoto, S., Lee, S. H., & Endo, T. (2014). Relationship between aspect ratio and suspension viscosity of wood cellulose nanofibers. *Polymer journal*, 46(1), 73. <https://doi.org/10.1038/pj.2013.64>.

- Jennings, H. M., Thomas, J. J., Rothstein, D., & Chen, J. J. (2002). Cements as porous materials. In F. Schüth, K. S. W. Sing and J. Weitkamp (Eds.), *Handbook of porous solids* (pp. 2971-3028). New Jersey: John Wiley & Sons, Inc. <https://doi.org/10.1002/9783527618286.ch40>.
- Jennings, H. M., Bullard, J. W., Thomas, J. J., Andrade, J. E., Chen, J. J., & Scherer, G. W. (2008). Characterization and modeling of pores and surfaces in cement paste: Correlations to processing and properties. *Journal of Advanced Concrete Technology*, 6(1), 5–29. <https://doi.org/10.3151/jact.6.5>.
- Jiao, L., Su, M., Chen, L., Wang, Y., Zhu, H., & Dai, H. (2016). Natural cellulose nanofibers as sustainable enhancers in construction cement. *PloS one*, 11(12), e0168422. <https://doi.org/10.1371/journal.pone.0168422>.
- Jongvisuttisun, P., Negrello, C., & Kurtis, K. E. (2013). Effect of processing variables on efficiency of eucalyptus pulps for internal curing. *Cement and Concrete Composites*, 37, 126-135. <https://doi.org/10.1016/j.cemconcomp.2012.11.006>.
- Juenger, M. C. G., & Jennings, H. M. (2001). The use of nitrogen adsorption to assess the microstructure of cement paste. *Cement and Concrete Research*, 31(6), 883-892. [https://doi.org/10.1016/S0008-8846\(01\)00493-8](https://doi.org/10.1016/S0008-8846(01)00493-8).
- Kawashima, S., & Shah, S. P. (2011). Early-age autogenous and drying shrinkage behavior of cellulose fiber-reinforced cementitious materials. *Cement and Concrete Composites*, 33(2), 201-208. <https://doi.org/10.1016/j.cemconcomp.2010.10.018>.
- Khadra, M., Burlion, N., Rougelot, T., Carlier, J. P., & Lataste, J. F. (2017). Extraction and analysis of pore solution of cement paste: desaturation and resaturation cycles using a non-destructive method by gas injection. *European Journal of Environmental and Civil Engineering*, 1-11. <https://doi.org/10.1080/19648189.2017.1374881>.
- Khalil, H. A., Bhat, A. H., & Yusra, A. I. (2012). Green composites from sustainable cellulose nanofibrils: A review. *Carbohydrate polymers*, 87(2), 963-979. <https://doi.org/10.1016/j.carbpol.2011.08.078>.
- Kibert, C. J. (1994, November). Establishing principles and a model for sustainable construction. In *Proceedings of the first international conference on sustainable construction* (pp. 6-9). Tampa Florida.

- Kim, T., & Olek, J. (2012). Effects of sample preparation and interpretation of thermogravimetric curves on calcium hydroxide in hydrated pastes and mortars. *Transportation Research Record*, 2290(1), 10-18. <https://doi.org/10.3141/2290-02>.
- Kim, M. Y., Yang, E. I., & Yi, S. T. (2013). Application of the colorimetric method to chloride diffusion evaluation in concrete structures. *Construction and Building Materials*, 41, 239-245. <https://doi.org/10.3141/2290-02>.
- Klemm, D., Kramer, F., Moritz, S., Lindström, T., Ankerfors, M., Gray, D., & Dorris, A. (2011). Nanocelluloses: a new family of nature-based materials. *Angewandte Chemie International Edition*, 50(24), 5438-5466. <https://doi.org/10.1002/anie.201001273>.
- Kline, J., & Barcelo, L. (2012, May). Cement and CO₂, a victim of success!. In *Cement Industry Technical Conference, 2012 IEEE-IAS/PCA 53rd* (pp. 1-14). IEEE.
- Konsta-Gdoutos, M. S., Metaxa, Z. S., & Shah, S. P. (2010). Highly dispersed carbon nanotube reinforced cement based materials. *Cement and Concrete Research*, 40(7), 1052-1059. <https://doi.org/10.1016/j.cemconres.2010.02.015>.
- Kumar, S., Kolay, P., Malla, S., & Mishra, S. (2011). Effect of multiwalled carbon nanotubes on mechanical strength of cement paste. *Journal of Materials in Civil Engineering*, 24(1), 84-91.
- Lam, L., Wong, Y. L., & Poon, C. S. (2000). Degree of hydration and gel/space ratio of high-volume fly ash/cement systems. *Cement and Concrete Research*, 30(5), 747-756. [https://doi.org/10.1016/S0008-8846\(00\)00213-1](https://doi.org/10.1016/S0008-8846(00)00213-1).
- Landis, E. N., Alyaseen, E., Ahmed, M., & Kolour, H. H. (2018). An Investigation on the Effects of Cellulose Nanofibrils on the Performance of Cement Paste and Concrete. *Advances in Civil Engineering Materials*, 7(1), 463-478. <https://doi.org/10.1520/ACEM20180048>.
- Laukkanen, A., Teirfolk, J. E., Leivo, M., Kuosa, H., Kataja, K., & Nurmi, A. (2015). *U.S. Patent No. 9,174,873*. Washington, DC: U.S. Patent and Trademark Office. Retrieve from <https://patents.google.com/patent/US9174873B2/en>.
- Lawrence, M., & Jiang, Y. (2017). Porosity, pore size distribution, micro-structure. In *Bio-aggregates Based Building Materials* (pp. 39-71). Springer, Dordrecht.
- Lazaro, A., Yu, Q. L., & Brouwers, H. J. H. (2016). Nanotechnologies for sustainable construction. In *Sustainability of Construction Materials (Second Edition)* (pp. 55-78).

- Lee, J., Mahendra, S., & Alvarez, P. J. (2010). Nanomaterials in the construction industry: a review of their applications and environmental health and safety considerations. *ACS nano*, 4(7), 3580-3590. <https://doi.org/10.1021/nn100866w>.
- Leitner, J., Hinterstoisser, B., Wastyn, M., Keckes, J., & Gindl, W. (2007). Sugar beet cellulose nanofibril-reinforced composites. *Cellulose*, 14(5), 419-425. <https://doi.org/10.1007/s10570-007-9131-2>.
- Lerch, W. (1957). Plastic Shrinkage. *ACI Journal*, 53(8) 797-802.
- Li, H., Xiao, H. G., & Ou, J. P. (2004). A study on mechanical and pressure-sensitive properties of cement mortar with nanophase materials. *Cement and Concrete research*, 34(3), 435-438. <https://doi.org/10.1016/j.cemconres.2003.08.025>.
- Li, Z., Wang, H., He, S., Lu, Y., & Wang, M. (2006). Investigations on the preparation and mechanical properties of the nano-alumina reinforced cement composite. *Materials Letters*, 60(3), 356-359. <https://doi.org/10.1016/j.matlet.2005.08.061>.
- Longuet, P., Burglen, L., & Zelwer, A. (1973). La phase liquide du ciment hydrate [The liquid phase of the hydrated cement]. *Revue Matériaux Construction Travaux*, 676, 35-41. (in French).
- Lothenbach, B., & Winnefeld, F. (2006). Thermodynamic modelling of the hydration of Portland cement. *Cement and Concrete Research*, 36(2), 209-226. <https://doi.org/10.1016/j.cemconres.2005.03.001>.
- Lothenbach, B., Durdziński, P. & De Weerd, K. (2016). Thermogravimetric analysis. In K. Scrivener, R. Snellings & B. Lothenbach (Eds.), *A Practical Guide to Microstructural Analysis of Cementitious Materials* (pp. 177-211). New York: CRC Press.
- Machado, F. G. D., Pedroti, L. G., Lemes, J. V. B., Lima, G. E. S., Fioresi, L. A. F., Fernandes, W. E. H., & Alexandre, J. (2017). Addition of Cellulose Nanofibers in Reactive Powder Concrete. In *Characterization of Minerals, Metals, and Materials 2017* (Ikhmayies S. et al. Eds.). The Minerals, Metals & Materials Series. (pp. 529-535). Springer, Cham. https://doi.org/10.0007/978-3-319-51382-9_57.
- Maheswaran, S., Bhuvaneshwari, B., Palani, G. S., Nagesh, R., & Kalaiselvam, S. (2013). An overview on the influence of nano silica in concrete and a research initiative. *Research Journal of Recent Sciences*, ISSN2277, 2502.

- Mamun, M., & Bindiganavile, V. (2012). Mitigating shrinkage cracking in stucco through the replacement of fine aggregate with expanded perlite. *Canadian Journal of Civil Engineering*, 39(8), 906-914. <https://doi.org/10.1139/l2012-075>.
- Manso Blanco, S., & Aguado de Cea, A. (2017). A review of sample preparation and its influence on pH determination in concrete samples. *Materiales de construcción (Madrid)*, 67(325), 1-10. <https://doi.org/10.3989/mc.2017.08515>.
- Marchand, J., Odler, I., & Skalny, J. P. (2003). Sulfate attack on concrete. In A. Bentur, S. Mindess (Eds.), *Sulfate Attack on Concrete* (1st Edition). (p. 43-126). CRC Press.
- Marikunte, S., & Soroushian, P. (1995). Statistical evaluation of long-term durability characteristics of cellulose fiber reinforced cement composites. *Materials Journal*, 91(6), 607-616.
- de Medeiros, M. H. F., Gobbi, A., Groenwold, J. A., & Helene, P. (2013). Previsão da vida útil de concreto armado de alta resistência com adição de metacaulim e sílica ativa em ambientes marinhos. *Rem: Revista Escola de Minas*, 66(1). <http://dx.doi.org/10.1590/S0370-44672013000100008>.
- Mejdoub, R., Hammi, H., Suñol, J. J., Khitouni, M., M, A., & Boufi, S. (2017). Nanofibrillated cellulose as nanoreinforcement in Portland cement: Thermal, mechanical and microstructural properties. *Journal of Composite Materials*, 51(17), 2491-2503. <https://doi.org/10.1177/0021998316672090>.
- Metha, P. K., & Monteiro, P. J. (2013). *Concrete: Microstructure, Properties, and Materials* (3rd Ed.) (121-202). New York, NY: McGraw-Hill Professional.
- Mindess, S., Young, J. F., & Darwin, D. (2003). *Concrete*. 2nd Edition. Upper Saddle River, NJ: Prentice Hall.
- Missoum, K., Belgacem, M., & Bras, J. (2013). Nanofibrillated cellulose surface modification: a review. *Materials*, 6(5), 1745-1766. <https://doi.org/10.3390/ma6051745>.
- Mohr, B. J., Hood, K. L., & Kurtis, K. E. (2009). Mitigation of alkali-silica expansion in pulp fiber-mortar composites. *Cement and Concrete Composites*, 31(9), 677-681. <https://doi.org/10.1016/j.cemconcomp.2009.06.006>.
- Münch, B. (2019, February 11). Xlib (ImageJ / Fiji plugins). *ImageJ*. Retrieved from <https://imagej.net/Xlib>.

- Nasir, M., Hashim, R., Sulaiman, O., & Asim, M. (2017). Nanocellulose: Preparation methods and applications. In *Cellulose-Reinforced Nanofibre Composites* (pp. 261-276).
- Natural Resources Canada, Forest Resource, Statistical Data. Retrieved from <https://cfs.nrcan.gc.ca/statsprofile> (accessed January 20th, 2019).
- Neville, A.M. (2011). *Properties of Concrete*. 4th Edition. Essex, UK: Longman, Ltd.
- Nilsson, L. O., Poulsen, E., Sandberg, P., Sørensen, H. E., & Klinghoffer, O. (1996). HETEK, Chloride penetration into concrete, state-of-the-art, transport processes, corrosion initiation, test methods and prediction models. *Denmark, ISSN/ISBN, 0909-4288*.
- Norhasri, M. M., Hamidah, M. S., & Fadzil, A. M. (2017). Applications of using nano material in concrete: A review. *Construction and Building Materials, 133*, 91-97. <https://doi.org/10.1016/j.conbuildmat.2016.12.005>.
- Odler, I. (2003). The BET-specific surface area of hydrated Portland cement and related materials. *Cement and Concrete Research, 33*(12), 2049-2056. [https://doi.org/10.1016/S0008-8846\(03\)00225-4](https://doi.org/10.1016/S0008-8846(03)00225-4).
- Ong, K. G., & Myint-Lay, K. (2006). Application of image analysis to monitor very early age shrinkage. *ACI materials journal, 103*(3), 169.
- Onuaguluchi, O., Panesar, D. K., & Sain, M. (2014). Properties of nanofibre reinforced cement composites. *Construction and Building Materials, 63*, 119-124. <https://doi.org/10.1016/j.conbuildmat.2014.04.072>.
- Onuaguluchi, O., & Banthia, N. (2016). Plant-based natural fibre reinforced cement composites: A review. *Cement and Concrete Composites, 68*, 96-108. <https://doi.org/10.1016/j.cemconcomp.2016.02.014>.
- Otero, J., Charola, A. E., Grissom, C. A., & Starinieri, V. (2017). An overview of nanolime as a consolidation method for calcareous substrates. *Ge-conservación, 1*(11), 71-78.
- Ozyildirim, C., & Zegetosky, C. (2010). Exploratory investigation of nanomaterials to improve strength and permeability of concrete. *Transportation Research Record: Journal of the Transportation Research Board, (2142)*, 1-8. <https://doi.org/10.3141/2142-01>.
- Pacheco-Torgal, F., & Jalali, S. (2011). Nanotechnology: advantages and drawbacks in the field of construction and building materials. *Construction and building materials, 25*(2), 582-590. <https://doi.org/10.1016/j.conbuildmat.2010.07.009>.

- Page, C. L., & Page, M. M. (Eds.). (2007). *Durability of concrete and cement composites*. Washington, US: Woodhead Publishing Ltd.
- Palacios, M., Kazemi-Kamyab, H., Mantellato, S. & Bowen, P. (2016) Laser diffraction and gas adsorption techniques. In: K. Scrivener, R. Snellings & B. Lothenbach (Eds.), *A Practical Guide to microstructural analysis of cementitious materials* (pp. 445-484). New York: CRC Press.
- Pane, I., & Hansen, W. (2005). Investigation of blended cement hydration by isothermal calorimetry and thermal analysis. *Cement and concrete research*, 35(6), 1155-1164. <https://doi.org/10.1016/j.cemconres.2004.10.027>.
- Pei, A., Butchosa, N., Berglund, L. A., & Zhou, Q. (2013). Surface quaternized cellulose nanofibrils with high water absorbency and adsorption capacity for anionic dyes. *Soft Matter*, 9(6), 2047-2055.
- Peng, Y., Lauten, R. A., Reknes, K., & Jacobsen, S. (2017). Bleeding and sedimentation of cement paste measured by hydrostatic pressure and Turbiscan. *Cement and Concrete Composites*, 76, 25-38. <https://doi.org/10.1016/j.cemconcomp.2016.11.013>.
- Peters, S., Rushing, T., Landis, E., & Cummins, T. (2010). Nanocellulose and microcellulose fibers for concrete. *Transportation Research Record: Journal of the Transportation Research Board*, (2142), 25-28. <https://doi.org/10.3141/2142-04>.
- Perrot, A., Rangeard, D., Picandet, V., & Mélinge, Y. (2013). Hydro-mechanical properties of fresh cement pastes containing polycarboxylate superplasticizer. *Cement and Concrete Research*, 53, 221-228. <https://doi.org/10.1016/j.cemconres.2013.06.015>.
- Peschard, A., Govin, A., Grosseau, P., Guilhot, B., & Guyonnet, R. (2004). Effect of polysaccharides on the hydration of cement paste at early ages. *Cement and Concrete Research*, 34(11), 2153-2158. <https://doi.org/10.1016/j.cemconres.2004.04.001>.
- Porro, A., Dolado, J. S., Campillo, I., Erkizia, E., De Miguel, Y., de Ibarra, Y. S., & Ayuela, A. (2005). Effects of nanosilica additions on cement pastes. In *Applications of Nanotechnology in Concrete Design: Proceedings of the International Conference held at the University of Dundee, Scotland, UK on 7 July 2005* (pp. 87-96). Thomas Telford Publishing.
- Postek, M. T., Moon, R. J., Rudie, A. W., & Bilodeau, M. A. (2013). *Production and applications of cellulose*. Tappi Press. Peachtree Corners.

- Quercia, G., Spiesz, P., Hüsken, G., & Brouwers, H. J. H. (2014). SCC modification by use of amorphous nano-silica. *Cement and Concrete Composites*, 45, 69-81. <https://doi.org/10.1016/j.cemconcomp.2013.09.001>.
- Ramachandran, V. S. (1996). *Concrete admixtures handbook: properties, science and technology*. William Andrew.
- Ramachandran, V. S., & Beaudoin, J. J. (2001). Concrete science. In Ramachandran, V. S., & Beaudoin, J. J. (Eds.), *Handbook of analytical techniques in concrete science and technology: principles, techniques and applications*. (pp. 1-62). Elsevier Inc.
- Ramachandran, V. (2001). Thermal analysis. In V. S. Ramachandran and J. J. Beaudoin (Eds.), *Handbook of analytical techniques in concrete science and technology: Principles, techniques and applications* (pp. 127-174). Elsevier.
- Ramakrishnan, V., Zellers, R., & Patnaik, A. K. (2007). Plastic shrinkage reduction potential of a new high tenacity monofilament polypropylene fiber. *Special Publication*, 243, 49-62.
- Real, L. V., Oliveira, D. R. B., Soares, T., & Medeiros, M. H. F. (2015). AgNO₃ spray method for measurement of chloride penetration: the state of art. *Revista ALCONPAT*, 5(2), 149-159.
- Saito, T., & Isogai, A. (2004). TEMPO-mediated oxidation of native cellulose. The effect of oxidation conditions on chemical and crystal structures of the water-insoluble fractions. *Biomacromolecules*, 5(5), 1983-1989. <https://doi.org/10.1021/bm0497769>.
- Saito, T., Nishiyama, Y., Putaux, J. L., Vignon, M., & Isogai, A. (2006). Homogeneous suspensions of individualized microfibrils from TEMPO-catalyzed oxidation of native cellulose. *Biomacromolecules*, 7(6), 1687-1691. <https://doi.org/10.1021/bm060154s>.
- Saito, T., Kimura, S., Nishiyama, Y., & Isogai, A. (2007). Cellulose nanofibers prepared by TEMPO-mediated oxidation of native cellulose. *Biomacromolecules*, 8(8), 2485-2491. <https://doi.org/10.1021/bm0703970>.
- Sanchez, F., & Sobolev, K. (2010). Nanotechnology in concrete—a review. *Construction and building materials*, 24(11), 2060-2071. <https://doi.org/10.1016/j.conbuildmat.2010.03.014>.
- Sappakittipakorn, M., Banthia, N., & Jiang, Z. (2010). Cryoporometry based evidence of pore refinement in cementitious composites. *Indian concrete journal*, 84(6), 17-24.
- Sappakittipakorn, M., & Banthia, N. (2011). Corrosion of rebar and role of fiber reinforced concrete. *Journal of Testing and Evaluation*, 40(1), 127-136. <https://doi.org/10.1520/JTE103873>.

- Sayahi, F., Emborg, M., & Hedlund, H. (2014). Plastic Shrinkage Cracking in Concrete: State of the Art. *Nordic Concrete Research*, 51, 95-116.
- Schindelin, J., Arganda-Carreras, I., Frise, E., Kaynig, V., Longair, M., Pietzsch, T. & Tinevez, J. Y. (2012). Fiji: an open-source platform for biological-image analysis. *Nature methods*, 9(7), 676. PMID 22743772, <https://doi.org/10.1038/nmeth.2019>.
- Scrivener, K. L. (1988). The use of backscattered electron microscopy and image analysis to study the porosity of cement paste. *MRS Online Proceedings Library Archive*, 137.
- Scrivener, K., Bazzoni, A., Mota, B. & Rossen, J. E. (2018). Electron microscopy. In K. Scrivener, R. Snellings & B. Lothenbach (Eds.), *A Practical Guide to Microstructural Analysis of Cementitious Materials* (pp. 353-416). New York: CRC Press.
- Segal, L., Creely, J., Martin Jr, A., & Conrad, C. (1959). An empirical method for estimating the degree of crystallinity of native cellulose using the X-ray diffractometer. *Textile Research Journal*, 29(10), 786–794. <https://doi.org/10.1177/004051755902901003>.
- Serpukhov, I., & Mechtcherine, V. (2015). Early-Age Shrinkage of Ordinary Concrete and a Strain-Hardening Cement-Based Composite (SHCC) in the Conditions of Hot Weather Casting. In C. Hellmich, B. Pichler, & J. Kollegger (Eds.), *In Proceedings of the 10th International Conference on Creep, Shrinkage, and Durability of Concrete and Concrete Structures (CONCREEP 10)*: 1504-1513. Vienna, Austria: American Society of Civil Engineers (ASCE).
- Serra, A., González, I., Oliver-Ortega, H., Tarrès, Q., Delgado-Aguilar, M., & Mutjé, P. (2017). Reducing the Amount of Catalyst in TEMPO-Oxidized Cellulose Nanofibers: Effect on Properties and Cost. *Polymers*, 9(11), 557. <https://doi.org/10.3390/polym9110557>.
- Shatkin, J. A., Wegner, T. H., Bilek, E. T., & Cowie, J. (2014). Market projections of cellulose nanomaterial-enabled products-Part 1: Applications. *TAPPI JOURNAL*, Volume 13, Number 5, 2014; pp. 9-16., 13(5), 9-16.
- Silva, N. (2013). *Chloride induced corrosion of reinforcement steel in concrete - Threshold values and ion distributions at the concrete-steel interface*. Doctoral dissertation, Chalmers University of Technology. Gothenburg, Sweden. Retrieved from <https://research.chalmers.se/publication/171960>.

- Silvestre, J., Silvestre, N., & De Brito, J. (2016). Review on concrete nanotechnology. *European Journal of Environmental and Civil Engineering*, 20(4), 455-485. <https://doi.org/10.1080/19648189.2015.1042070>.
- Skalny, J. & Hearn, N. (2001). Surface Area Measurements. In *Handbook of analytical techniques in concrete science and technology principles, techniques and applications*. V. S. Ramachandran and J. J. Beaudoin (Eds.). (pp. 353-416). Elsevier.
- Snellings, R. (2018). X-ray powder diffraction. In K. Scrivener, R. Snellings & B. Lothenbach (Eds.), *A practical guide to microstructural analysis of cementitious materials* (pp. 107-176). New York: CRC Press.
- Sobolev, K., Flores, I., Hermosillo, R. & Torres-Martínez, L. M. (2006). Nanomaterials and nanotechnology for high-performance cement composites. *Proceedings of ACI Sessions on Nanotechnology of Concrete: Recent Developments and Future Perspectives*. Sobolev, K. and Shah, S.P. (Eds.). SP 254. American Concrete Institute: ACI Special Publication, 91-118.
- Sofla, M. R. K., Brown, R. J., Tsuzuki, T., & Rainey, T. J. (2016). A comparison of cellulose nanocrystals and cellulose nanofibres extracted from bagasse using acid and ball milling methods. *Advances in Natural Sciences: Nanoscience and Nanotechnology*, 7(3), 035004. <https://doi.org/10.1038/pj.2013.64>.
- Sonebi, M., García-Taengua, E., Hossain, K. M. A., Khatib, J., & Lachemi, M. (2015). Effect of nanosilica addition on the fresh properties and shrinkage of mortars with fly ash and superplasticizer. *Construction and Building Materials*, 84, 269-276. <https://doi.org/10.1016/j.conbuildmat.2015.02.064>.
- Sonebi, M., Ammar, Y., & Diederich, P. (2016). Sustainability of cement, concrete and cement replacement materials in construction. In *Sustainability of Construction Materials (Second Edition)* (pp. 371-396). Duxford, UK. <https://doi.org/10.1016/B978-0-08-100370-1.00015-9>.
- Song, H. W., Pack, S. W., Nam, S. H., Jang, J. C., & Saraswathy, V. (2010). Estimation of the permeability of silica fume cement concrete. *Construction and Building Materials*, 24(3), 315-321. <https://doi.org/10.1016/j.conbuildmat.2009.08.033>.

- Stanish, K. D., Hooton, R. D., & Thomas, M. D. (2001). *Testing the Chloride Penetration Resistance of Concrete: A Literature Review* (No. FHWA Contract DTFH61-97-R-00022). United States. Federal Highway Administration.
- Stephenson, K. M. (2011). *Characterizing the behavior and properties of nano cellulose reinforced ultra-high performance concrete*. Master of Science dissertation, University of Maine. Orono, ME, U.S. Retrieved from <https://digitalcommons.library.umaine.edu/etd/1579/>.
- Sun, X., Wu, Q., Ren, S., & Lei, T. (2015). Comparison of highly transparent all-cellulose nanopaper prepared using sulfuric acid and TEMPO-mediated oxidation methods. *Cellulose*, 22(2), 1123-1133. <https://doi.org/10.1007/s10570-015-0574-6>.
- Sun, X., Wu, Q., Lee, S., Qing, Y., & Wu, Y. (2016). Cellulose nanofibers as a modifier for rheology, curing and mechanical performance of oil well cement. *Scientific reports*, 6, 31654. <https://doi.org/10.1038/srep31654>.
- Tang, Z., Huang, R., Mei, C., Sun, X., Zhou, D., Zhang, X., & Wu, Q. (2019). Influence of Cellulose Nanoparticles on Rheological Behavior of Oil Well Cement-Water Slurries. *Materials*, 12(2), 291. <https://doi.org/10.3390/ma12020291>.
- Taylor, H. F. W., Famy, C., & Scrivener, K. L. (2001). Delayed ettringite formation. *Cement and concrete research*, 31(5), 683-693. [https://doi.org/10.1016/S0008-8846\(01\)00466-5](https://doi.org/10.1016/S0008-8846(01)00466-5).
- Tazawa, E. I., Miyazawa, S., & Kasai, T. (1995). Chemical shrinkage and autogenous shrinkage of hydrating cement paste. *Cement and concrete research*, 25(2), 288-292. [https://doi.org/10.1016/0008-8846\(95\)00011-9](https://doi.org/10.1016/0008-8846(95)00011-9).
- Tazawa, E. I. (Eds.). (2014). *Autogenous shrinkage in concrete. Proceedings of the international workshop, June 13-14, 1998 Japan Concrete Institute. Hiroshima, Japan*. CRC Press online.
- Toledo Filho, R. D., & Sanjuan, M. A. (1999). Effect of low modulus sisal and polypropylene fibre on the free and restrained shrinkage of mortars at early age. *Cement and Concrete Research*, 29(10), 1597-1604. [https://doi.org/10.1016/S0008-8846\(99\)00136-2](https://doi.org/10.1016/S0008-8846(99)00136-2).
- Toledo Filho, R. D., Ghavami, K., Sanjuán, M. A., & England, G. L. (2005). Free, restrained and drying shrinkage of cement mortar composites reinforced with vegetable fibres. *Cement and Concrete Composites*, 27(5), 537-546. <https://doi.org/10.1016/j.cemconcomp.2004.09.005>.
- Turbak, A. F., Snyder, F. W., & Sandberg, K. R. (1984). Microfibrillated Cellulose—A new composition of commercial significance. *Atlanta, Ga., USA*, 115-124.

- Ueda, T., & Takewaka, K. (2007). Performance-based standard specifications for maintenance and repair of concrete structures in Japan. *Structural Engineering International*, 17(4), 359-366.
- Ulm, F. J., Jennings, H. M., & Pellenq, R. (Eds.). (2013). *Mechanics and Physics of Creep, Shrinkage, and Durability of Concrete: A Tribute to Zdenek P. Bazant: Proceedings of the Ninth International Conference on Creep, Shrinkage, and Durability Mechanics (CONCREEP-9), September 22-25, 2013 Cambridge, Massachusetts*. ASCE Publications.
- Urkhanova, L. A., Lkhasaranov, S. A., Buyantuev, S. L., & Kuznetsova, A. Y. (2016). About the influence of carbon nanomaterials on the properties of cement and concrete. *Nanotechnologies in Construction*, 8(5).
- Villain, G., Thiery, M., & Platret, G. (2007). Measurement methods of carbonation profiles in concrete: Thermogravimetry, chemical analysis and gammadensimetry. *Cement and Concrete Research*, 37(8), 1182-1192. <https://doi.org/10.1016/j.cemconres.2007.04.015>.
- Walker, H. N., Lane, D. S., & Stutzman, P. E. (2006). *Petrographic Methods of Examining Hardened Concrete: A Petrographic Manual* (FHWA-HRT-04-150). Retrieved from Federal Highway Administration (FHWA) website: <https://www.fhwa.dot.gov/publications/research/infrastructure/pavements/pccp/04150/04150.pdf>.
- Wells, R. J. (1999). Rapid approximation to the Voigt/Faddeeva function and its derivatives. *Journal of Quantitative Spectroscopy and Radiative Transfer*, 62(1), 29-48. [https://doi.org/10.1016/S0022-4073\(97\)00231-8](https://doi.org/10.1016/S0022-4073(97)00231-8).
- Whiting, D. (1981). Rapid determination of the chloride permeability of concrete. *Final Report Portland Cement Association, Skokie, IL. Construction Technology Labs*.
- Wiliński, D., Łukowski, P., & Rokicki, G. (2016). Polymeric superplasticizers based on polycarboxylates for ready-mixed concrete: current state of the art. *Polimery*, 61.
- Winnefeld, F., Schöler A. & Lothenbach B. (2016) Sample preparation. In: KScrivener, K., Snellings, R., & Lothenbach, B. (Eds.). (2016). *A practical guide to microstructural analysis of cementitious materials*. CRC Press.
- Wojdyr, M. (2010). Fityk: a general-purpose peak fitting program. *Journal of Applied Crystallography*, 43(5-1), 1126-1128. <https://doi.org/10.1107/S0021889810030499>.
- Wong, H. S., & Buenfeld, N. R. (2009). Determining the water–cement ratio, cement content, water content and degree of hydration of hardened cement paste: Method development and

- validation on paste samples. *Cement and Concrete Research*, 39(10), 957-965. <https://doi.org/10.1016/j.cemconres.2009.06.013>.
- Wu, Z., Shi, C., Khayat, K. H., & Wan, S. (2016). Effects of different nanomaterials on hardening and performance of ultra-high strength concrete (UHSC). *Cement and Concrete Composites*, 70, 24-34. <https://doi.org/10.1016/j.cemconcomp.2016.03.003>.
- Xu, X., Liu, F., Jiang, L., Zhu, J. Y., Haagensohn, D., & Wiesenborn, D. P. (2013). Cellulose nanocrystals vs. cellulose nanofibrils: a comparative study on their microstructures and effects as polymer reinforcing agents. *ACS applied materials & interfaces*, 5(8), 2999-3009.
- Yang, H. (2011). *Investigation and characterization of oxidized cellulose and cellulose nanofiber films* (Doctoral dissertation, McGill University Libraries).
- Yio, M. H. N., Phelan, J. C., Wong, H. S., & Buenfeld, N. R. (2014). Determining the slag fraction, water/binder ratio and degree of hydration in hardened cement pastes. *Cement and Concrete Research*, 56, 171-181. <https://doi.org/10.1016/j.cemconres.2013.12.002>.
- Yuan, Q., Deng, D. H., Shi, C. J., & De Schutter, G. (2012). Application of silver nitrate colorimetric method to non-steady-state diffusion test. *Journal of Central South University*, 19(10), 2983-2990.
- Zdravkov, B. D., Čermák, J. J., Šefara, M., & Janku, J. (2007). Pore classification in the characterization of porous materials: A perspective. *Central European journal of chemistry* 5(2), 385-395. <https://doi.org/10.2478/s11532-007-0017-9>.
- Zhu, W., Bartos, P. J., & Porro, A. (2004). Application of nanotechnology in construction. *Materials and Structures*, 37(9), 649-658. <https://doi.org/10.1007/BF02483294>.

APPENDIX

Table A.1 Superplasticizer dosage and flow of the CNF-based cement mortars.

<i>Dry CNF #0.13 [vol.%]</i>	0	0.1	0.2	0.3	0.4	0.5
<i>SP [g/kg cement]</i>	0	12.50	22.92	62.52	62.52	62.52
<i>Flow [%]</i>	26.5	25	31.5	25	5	0
<i>Dry CNF #0.7 [vol.%]</i>	0	0.1	0.1551	-	-	-
<i>SP [g/kg cement]</i>	0	2.50	3.80	-	-	-
<i>Flow [%]</i>	26.5	30	25	-	-	-
<i>Dry CNF #1.13 [vol.%]</i>	0	0.1	0.2	0.3	0.4	0.5035
<i>SP [g/kg cement]</i>	0	1.824	4.168	7.555	11.46	15.37
<i>Flow [%]</i>	26.5	32.8	33.4	33.2	26.2	34.1

Note: 'SP' is superplasticizer.

Table A.2 Superplasticizer dosage and flow of the CNF-based cement pastes.

<i>Dry CNF #0.13 [vol.%]</i>	0	0.1	0.2	0.3	0.4	-	-	-	-
<i>SP [g/kg cement]</i>	0	0.52	2.97	17.47	56.77	-	-	-	-
<i>Efflux time [secs]</i>	5.70	5.94	6.05	5.51	6.40	-	-	-	-
<i>Dry CNF #0.7 [vol.%]</i>	0	0.1	0.2	-	-	-	-	-	-
<i>SP [g/kg cement]</i>	0	0.24	0.57	-	-	-	-	-	-
<i>Efflux time [secs]</i>	5.70	5.51	6.02	-	-	-	-	-	-
<i>Dry CNF #1.13 [vol.%]</i>	0	0.1	0.2	0.3	0.4	0.6	0.8	1	1.184
<i>SP [g/kg cement]</i>	0	0.17	0.42	0.67	1.17	1.67	3.33	5.67	8.67
<i>Efflux time [secs]</i>	5.70	5.51	5.61	5.69	5.67	5.7	6.44	6.35	5.62

Note: 'SP' is superplasticizer.

Table A.3 Overall shrinkage of CNF-based cement pastes exposed to a severe environment.

<i>Dry CNF [vol.%]</i>	0	0.1	0.2	0.3	0.4	0.8	1.2
<i>CNF #0.13</i>							
<i>Overall Shrinkage [%]</i>	1.409	1.425	1.695	1.872	1.766	-	-
<i>SD [%]</i>	0.417	0.378	0.334	0.452	0.210	-	-
<i>CNF #1.13</i>							
<i>Overall Shrinkage [%]</i>	1.409	-	-	-	1.347	1.372	1.334
<i>SD [%]</i>	0.4171	-	-	-	0.101	0.131	0.085

Note: 'SD' is standard deviation.

Table A.4 Drying shrinkage for 12 weeks of CNF-based cement pastes with growing CNF fractions.

<i>CNF Type</i>	<i>Dry CNF [vol.%]</i>	<i>Time [weeks]</i>			
		<i>0</i>	<i>4</i>	<i>8</i>	<i>12</i>
<i>Control</i>	<i>0</i>	0	0.197	0.229	0.237
<i>CNF #0.13</i>	<i>0.1</i>	0	0.283	0.317	0.311
	<i>0.2</i>	0	0.292	0.323	0.325
	<i>0.3</i>	0	0.306	0.330	0.333
	<i>0.4</i>	0	0.339	0.371	0.377
<i>CNF #0.7</i>	<i>0.1</i>	0	0.251	0.284	0.296
	<i>0.2</i>	0	0.253	0.284	0.302
	<i>0.3</i>	0	0.248	0.278	0.295
<i>CNF #1.13</i>	<i>0.1</i>	0	0.232	0.268	0.276
	<i>0.2</i>	0	0.262	0.290	0.292
	<i>0.4</i>	0	0.274	0.299	0.299
	<i>0.8</i>	0	0.277	0.310	0.311
	<i>1.2</i>	0	0.298	0.321	0.321

Table A.5 Cracking analysis of the cement pastes with CNF #1.13 loadings.

<i>Dry CNF #1.13 [vol.%]</i>	<i>0</i>	<i>0.4</i>	<i>0.8</i>	<i>1.2</i>
<i>Number of Cracks</i>	4	3.5	2.5	3
<i>Crack Width [mm]</i>	1.20	1.23	1.13	1.04
<i>Maximum Crack Width [mm]</i>	2.14	2.06	2.01	1.83
<i>Standard Deviation [mm]</i>	0.34	0.46	0.19	0.26
<i>Total Crack Area [mm²]</i>	351.5	338.68	279.25	284.71
<i>Standard Deviation [mm²]</i>	34.31	27.66	26.59	15.36

Table A.6 Bleeding of CNF-cement pastes as per a modified ASTM C232/C232M [ASTM, 2014].

<i>CNF Type</i>	<i>Dry CNF [vol.%]</i>	<i>Bleeding [%]</i>	<i>Bleeding rate [g.m⁻².s⁻¹]</i>
<i>Control</i>	<i>0</i>	6.50	0.1326
<i>CNF #0.13</i>	<i>0.1</i>	6.40	0.1345
	<i>0.2</i>	5.18	0.1056
	<i>0.3</i>	4.69	0.09583
	<i>0.4</i>	4.01	0.07907
<i>CNF #1.13</i>	<i>0.2</i>	5.85	0.1201
	<i>0.4</i>	3.75	0.07636
	<i>0.8</i>	3.73	0.06032
	<i>1.2</i>	1.74	0.03453

Table A.7 Bleeding of CNF-cement pastes with and without superplasticizer as per Turbiscan[®] analysis.

<i>CNF Type</i>	<i>Dry CNF [vol.%]</i>	<i>Superplasticizer [wt.%]</i>	<i>Bleeding Height [mm]</i>
<i>Control</i>	<i>0</i>	0	2.09
<i>CNF #0.13</i>	<i>0.1</i>	0.052	2.08
	<i>0.2</i>	0.297	2.00
	<i>0.3</i>	1.747	1.93
	<i>0.4</i>	5.677	1.89
<i>CNF #1.13</i>	<i>0.2</i>	0.044	2.06
	<i>0.4</i>	0.122	1.90
	<i>0.8</i>	0.349	1.83
	<i>1.2</i>	0.926	1.81
<i>CNF #0.13</i>	<i>0.1</i>	-	2.07
	<i>0.2</i>	-	1.89
	<i>0.3</i>	-	1.83
	<i>0.4</i>	-	1.45
<i>CNF #1.13</i>	<i>0.2</i>	-	1.92
	<i>0.4</i>	-	1.36
	<i>0.8</i>	-	1.4
	<i>1.2</i>	-	1.34

Table A.8 Bleeding of cement pastes containing a fixed amount of 1.2 vol.% of dry CNF #1.13 and variable quantities of superplasticizer as per Turbiscan® analysis.

<i>CNF Type</i>	<i>Dry CNF [vol.%]</i>	<i>Superplasticizer [wt.%]</i>	<i>Bleeding Height [mm]</i>
<i>Control</i>	<i>0</i>	<i>0</i>	<i>2.09</i>
<i>CNF #1.13</i>	<i>1.2</i>	<i>0</i>	<i>1.34</i>
	<i>1.2</i>	<i>0.35</i>	<i>1.6</i>
	<i>1.2</i>	<i>0.7</i>	<i>1.76</i>
	<i>1.2</i>	<i>0.926</i>	<i>1.81</i>

Table A.9 Bleeding rate (BR) and evaporation rate (ER) of the control paste and CNF-based cement pastes with and without SP exposed to a different period of severe environment.

<i>Dry CNF #1.13 [vol.%]</i>	<i>SP [wt.%]</i>	<i>Evaporation rate [g/m².s]</i>			
		<i>20-hour BR [g.m⁻².s⁻¹]</i>	<i>4-hour ER [g.m⁻².s⁻¹]</i>	<i>Peak over 20-hour ER [g.m⁻².s⁻¹]</i>	<i>Flow [mm]</i>
<i>0</i>	<i>0</i>	<i>0.071</i>	<i>0.198</i>	<i>0.203</i>	<i>136.5</i>
<i>1.2</i>	<i>0</i>	<i>0.070</i>	<i>0.197</i>	<i>0.205</i>	<i>45</i>
<i>1.2</i>	<i>0.926</i>	<i>0.082</i>	<i>0.202</i>	<i>0.213</i>	<i>139</i>

Table A.10 Evaporation rate of the volatile raw materials used to prepare the CNF-based cement pastes exposed to mild environment (ME), severe environment (SE) and extreme environment (EE).

<i>Raw Material</i>	<i>Evaporation rate [g/m².s]</i>			
	<i>4-hour ME</i>	<i>ME</i>	<i>SE</i>	<i>ESE</i>
<i>Water</i>	<i>0.0311</i>	<i>0.0313</i>	<i>0.2113</i>	<i>0.3938</i>
<i>CNF #1.13</i>	<i>0.0263</i>	<i>0.0251</i>	<i>0.2044</i>	<i>0.3666</i>

Table A.11 Length change (LC) of CNF-based cement mortars after 12 weeks exposure in sulphate solution and the absolute LC (i.e. the LC in sulphate solution deducted from the LC in water). ‘Positive’ values mean expansion.

<i>CNF Type</i>	<i>Cement Type</i>	<i>Dry CNF [vol.%]</i>	<i>LC in Na₂SO₄ sol. [%]</i>	<i>LC [%]</i>
<i>CNF #0.13</i>	<i>GU</i>	<i>0</i>	0.011	0.00567
		<i>0.1</i>	0.0093	0.0048
		<i>0.2</i>	0.0084	0.00373
		<i>0.3</i>	0.00867	0.00333
		<i>0.4</i>	0.00467	0.00267
		<i>0.5</i>	0.0045	0.00217
	<i>HS</i>	<i>0</i>	0.00523	0.00306
		<i>0.1</i>	0.00433	0.00267
		<i>0.2</i>	0.0029	0.0014
	<i>HE</i>	<i>0</i>	0.01	0.0055
		<i>0.1</i>	0.0081	0.00393
		<i>0.2</i>	0.0065	0.00383
	<i>GUb</i>	<i>0</i>	0.0095	0.004
		<i>0.1</i>	0.0085	0.00367
		<i>0.2</i>	0.00817	0.0035
<i>CNF #1.13</i>	<i>GU</i>	<i>0</i>	0.010	0.006
		<i>0.1</i>	0.008	0.005
		<i>0.2</i>	0.006	0.004
		<i>0.3</i>	0.006	0.004
		<i>0.4</i>	0.006	0.004
		<i>0.5</i>	0.006	0.003

Table A.12 Sulphate penetration in CNF-based cement pastes prepared with various binders after 8 and 12 weeks in sodium sulphate solution.

<i>Sulphate Penetration at 3 mm in depth [time of exposure in weeks]</i>						
<i>CNF Type</i>	<i>Dry CNF [vol.%]</i>	<i>Cement Type</i>				
		<i>GU</i>		<i>HS</i>	<i>HE</i>	<i>GUb</i>
		<i>8 weeks</i>		<i>12 weeks</i>		
<i>Control</i>	<i>0</i>	15.5452	19.4704	23.5357	23.8253	27.1161
<i>CNF #0.13</i>	<i>0.1</i>	-	20.6136	24.7508	22.5923	25.4958
	<i>0.2</i>	-	18.5	19.5547	20.8977	24.4082
	<i>0.3</i>	-	15.4687	-	-	-
	<i>0.4</i>	-	9.29575	-	-	-
	<i>0.5</i>	-	9.29829	-	-	-
<i>CNF #1.13</i>	<i>0.1</i>	14.4919	17.4988	-	-	-
	<i>0.2</i>	-	16.4350	-	-	-
	<i>0.3</i>	13.0780	15.5047	-	-	-
	<i>0.4</i>	-	16.2962	-	-	-
	<i>0.5</i>	10.4363	15.2812	-	-	-

Table A.13 Relative ettringite content at different times of exposure in sodium sulphate, Na_2SO_4 , solution.

<i>Dry CNF #0.13 [vol.%]</i>	<i>Relative Ettringite Content after time of exposure in Na_2SO_4 sol. [weeks]</i>		
	<i>0</i>	<i>4</i>	<i>12</i>
<i>0</i>	0.02624	0.03393	0.06849
<i>0.1</i>	0.03297	0.04117	0.07381
<i>0.2</i>	0.02958	0.03807	0.06437
<i>0.3</i>	0.03412	0.04172	0.06576
<i>0.4</i>	0.03747	0.04586	0.05605
<i>0.5</i>	0.04261	0.05135	0.0559

Table A.14 Contents of calcium hydroxide ($W_{Ca(OH)_2}$), calcium carbonate (W_{CaCO_3}) and calcium hydroxide corrected ($W_{Ca(OH)_2,corrected}$) with the calcium from calcium carbonate.

<i>Dry CNF #0.13 [vol.%]</i>	<i>Control</i>	<i>0.1</i>	<i>0.2</i>	<i>0.3</i>	<i>0.4</i>
$W_{Ca(OH)_2}$ [g/100g anhydrous cement]	23.5	22.0	21.6	21.6	21.7
W_{CaCO_3} [g/100g anhydrous cement]	11.9	10.9	12.5	10.7	11.6
$W_{Ca(OH)_2,corrected}$ [g/100g anhydrous cement]	32.7	31.2	31.1	31.3	31.7

Table A.15 Potential of hydrogen (pH) of the pore solution of CNF-based cement pastes.

<i>Technique</i>	<i>Control</i>	<i>Dry CNF #0.13 [vol.%]</i>			<i>Dry CNF #0.13 [vol.%]</i>			
		<i>0.1</i>	<i>0.2</i>	<i>0.4</i>	<i>0.2</i>	<i>0.4</i>	<i>0.8</i>	<i>1.2</i>
<i>pH-Meter</i>	12.64	12.58	12.66	12.63	12.76	12.71	12.77	12.70
<i>pH-strips</i>	12	12	12	12	12	12	12	12

Table A.16 Degree of hydration (DOH) of CNF-based pastes by the conventional method.

<i>CNF Type</i>	<i>Dry CNF [vol.%]</i>	<i>DH [%]</i>	<i>DH_{corrected} [%]</i>
<i>Control</i>	0	0.998	0.900
<i>CNF #0.13</i>	0.1	0.998	0.900
	0.2	0.969	0.871
	0.3	0.892	0.782
	0.4	0.888	0.791
<i>CNF #1.13</i>	0.2	0.957	0.860
	0.4	0.884	0.786
	0.8	0.878	0.784
	1.2	0.911	0.815

Table A.17 Accumulative porosity of CNF-based cement pastes by BSEM image analysis.

<i>CNF Type</i>	<i>CNF [vol.%]</i>	<i>Accumulative Porosity [%]</i>		
		<i>>100 nm</i>	<i>100 nm - 10 μm</i>	<i>> 10 μm</i>
<i>Control</i>	0	14.55	13.01	1.29
<i>CNF #0.13</i>	0.1	16.20	13.36	1.32
	0.2	17.46	14.23	1.87
	0.4	20.08	16.94	1.95
<i>CNF #1.13</i>	0.2	16.88	12.77	5.04
	0.4	18.88	14.62	5.93
	0.8	23.19	14.43	8.76
	1.2	26.70	14.36	12.34

Table A.18 Resistance of cement mortars containing various CNF fractions and different CNF types to chloride ion penetration measured by RCPT and by colorimetric methods.

<i>CNF Type</i>	<i>Dry CNF [vol.%]</i>	<i>RCPT</i>	<i>Silver Nitrate-Based Colorimetric Method</i>		
		<i>Charge Passed [Coulombs]</i>	<i>Image Analysis Method [mm²]</i>	<i>Caliper M. [mm]</i>	<i>Caliper M. [mm]</i>
<i>Control</i>	<i>0</i>	4130	-	-	15.56
<i>CNF #0.13</i>	<i>0.1</i>	3446	-	-	15.52
	<i>0.2</i>	3050	-	-	12.51
	<i>0.3</i>	3569	-	-	13.79
	<i>0.4</i>	4239	-	-	14.67
	<i>0.5</i>	4815	-	-	15.53
<i>CNF #0.7</i>	<i>0.1</i>	3276	-	-	-
	<i>0.2</i>	2473	-	-	-
<i>CNF #1.13</i>	<i>0.1</i>	4032	22.74	16.53	10.37
	<i>0.2</i>	3622	15.63	13.42	9.86
	<i>0.3</i>	2610	13.53	12.21	10.55
	<i>0.4</i>	2231	12.93	12.24	9.81
	<i>0.5</i>	2177	11.41	10.12	7.97